

**VIERS-1 progress report part-2  
completion of the laboratory experiments**

C.J. Calkoen  
D. van Halsema  
B. Jähne  
J.A.M. Janssen  
W.A. Oost  
P. Speer



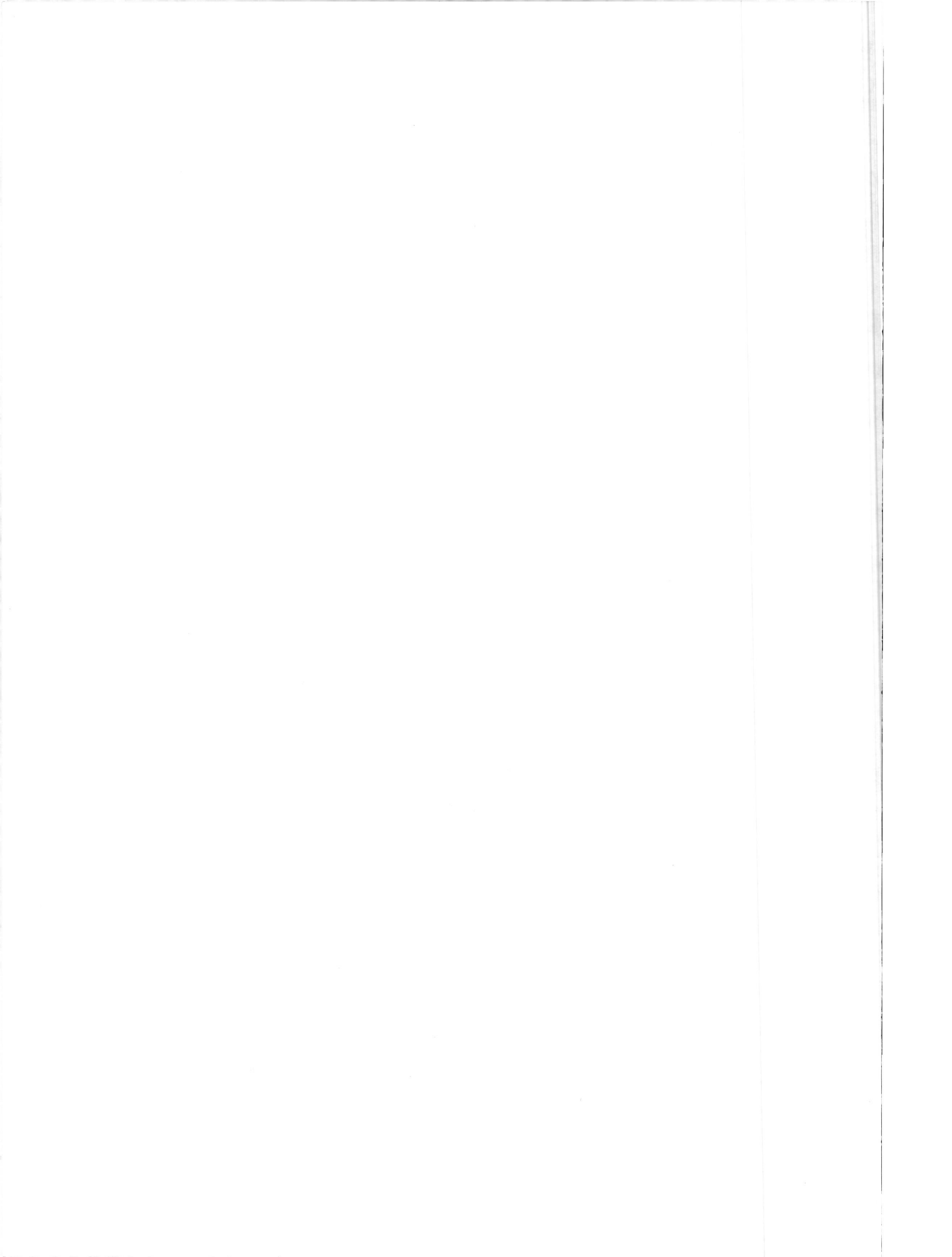
**VIERS-1 progress report part-2  
completion of the laboratory experiments**

C.J. Calkoen  
Delft Hydraulics  
D. van Halsema  
Physics and Electronics Lab. TNO  
B. Jähne  
SCRIPPS Institution of Oceanography  
(on leave from Heidelberg University)  
J.A.M. Janssen  
W.A. Oost  
Royal Netherlands Meteorological Institute  
P. Snoeij  
Delft University of Technology  
J. Vogelzang  
Rijkswaterstaat, Tidal Waters Division

**bcrs report no. 90-27  
bcrs progress report part-2  
of project no. OP-1.26**

**June 1991**

This research is being carried out supported by the Netherlands remote sensing board (BCRS).  
The cooperation with the Institute for Environmental Physics, Heidelberg University was made  
possible by a twinning grant from the European Community (contractno. ST2J-0451-C (GDF)



---

report no. : BCRS  
title : VIERS progress report part-2:  
completion of the laboratory experiments  
author(s) : C.Calkoen, D. van Halsema, B. Jähne, J.A.M. Janssen,  
W.A. Oost, P. Snoeij, J. Vogelzang  
date : November 6, 1990

---

## ABSTRACT/EXECUTIVE SUMMARY

This report is a sequel to BCRS-89-24: "Progress report on the VIERS-1 project, part-1: the Delft experiment", in which the goals of the VIERS-1 project, the programme of activities, and the first laboratory experiment and its preliminary results were presented.

In the first part of the present report the definitive results of the Delft experiment are presented. An important finding is that the relation between the radar backscatter and the friction velocity (as a measure for the wind velocity) is not a simple power law.

The next step in the execution of the project has been the institution of a modeling group to translate the experimentally obtained new insights in the relations between the microwave backscatter, the (water) wave field and the wind into a computer model. The present version of that model is based on an existing state-of-the-art model in which the normalized radar cross-section is calculated as a function of the wave field and a number of atmospheric properties (primarily the wind field). New modules representing new insights will be added to the programme in the course of the project. Finally, to be applicable in the interpretation of ERS-1 data, the model will be inverted to calculate the wind from sets of radar cross-sections. At present three new modules are being implemented, one for the amount and distribution of the short water waves that are mainly responsible for the radar scattering and two for alternative descriptions of the microwave scattering proces. Other activities that at present are being pursued in the modelling group are the interpretation and comparison of the results of the laboratory experiments and the consequences of these results for the parameters in the present model. The actual status can be summarized by stating that the present implementation of the model gives a good basis from which to work; some weak points have been noted and work for improvement is in progress.

Meanwhile the second VIERS-1 laboratory experiment took place in the Deltatank of the "de Voorst" facility of WL. The Deltatank is a large wave tank (230\*5\*5m) which had to be converted temporarily into a wind wave tank, which was succesfully performed. The essential characteristic of the Deltatank for the VIERS-1 experiment is the possibility to generate "life-size" waves, with a height of up to 3 meter. The experiment was performed in March 1989 and consisted of upwind and downwind radar measurements at wind speeds up to 10 m/s with various underlying wave fields. Despite some delays due to unfavourable

weather - the mounting of the radar outside the wave flume proper requested the absence of rain - the full programme could be successfully executed and some results, final as well as preliminary, are already available.

Preparations are well under way for the next step in the programme, the field experiment, which will take place from November 12 until December 7 1990 at the Rijkswaterstaat research platform Meetpost Noordwijk.

---

rapport no. : BCRS  
titel : VIERS voortgangs rapport deel-2:  
afsluiting van de laboratorium experimenten  
auteur(s) : C.Calkoen, D. van Halsema, B. Jähne, J.A.M. Janssen  
W.A. Oost, P. Snoeij, J. Vogelzang  
datum : November 7, 1990

---

## SAMENVATTING

Dit rapport is een vervolg op BCRS-89-24: "Progress report on the VIERS-1 project, part-1: the Delft experiment", waarin het doel van het VIERS-1 project, het programma en het eerste laboratorium experiment en de voorlopige resultaten daarvan zijn beschreven.

In het eerste deel van het huidige rapport worden de definitieve resultaten van het Delftse experiment gepresenteerd. Een belangrijke conclusie is dat het verband tussen de radar werkzame doorsnede en de wrijvingsnelheid (als maat voor de windsnelheid) niet als een machtwet kan worden voorgesteld.

De volgende stap in de uitvoering van het programma was het instellen van een modelgroep die de uit de experimenten verkregen nieuwe inzichten in het verband tussen de ontvangen microgolfstraling, het golfveld (van het wateroppervlak) en de wind moet omzetten in een computer model. De huidige versie van dat model is gebaseerd op een bestaand actueel model waarin de genormeerde radar werkzame doorsnede wordt berekend als functie van het golfveld en een aantal atmosferische variabelen, waaronder op de eerste plaats de windsnelheid. Nieuwe modules die de uit het verdere programma verkregen nieuwe inzichten belichamen zullen in de verdere loop van het project in het model worden ontwikkeld en ingevoegd. Tenslotte moet het model, om toegepast te kunnen worden bij de interpretatie van de signalen van de ERS-1, worden geïnverteerd om uitgaande van gemeten radar werkzame doorsnedes de windsnelheid te kunnen bepalen. Op het moment van schrijven zijn drie nieuwe modules in ontwikkeling, één voor de berekening van de intensiteit van de kleine (water)golven die de grootste bijdrage aan de radar terugstrooiing leveren en twee die alternatieve beschrijvingen van het verstrooiingsproces behelzen. De modelgroep heeft zich verder beziggehouden met de interpretatie en vergelijking van de resultaten van de laboratoriumexperimenten en de gevolgen van deze resultaten voor de modelparameters. De conclusie die op dit moment uit het modelwerk kan worden getrokken is dat het huidige model een goede basis vormt voor verdere ontwikkeling; het model heeft een aantal zwakke punten die thans worden aangepakt.

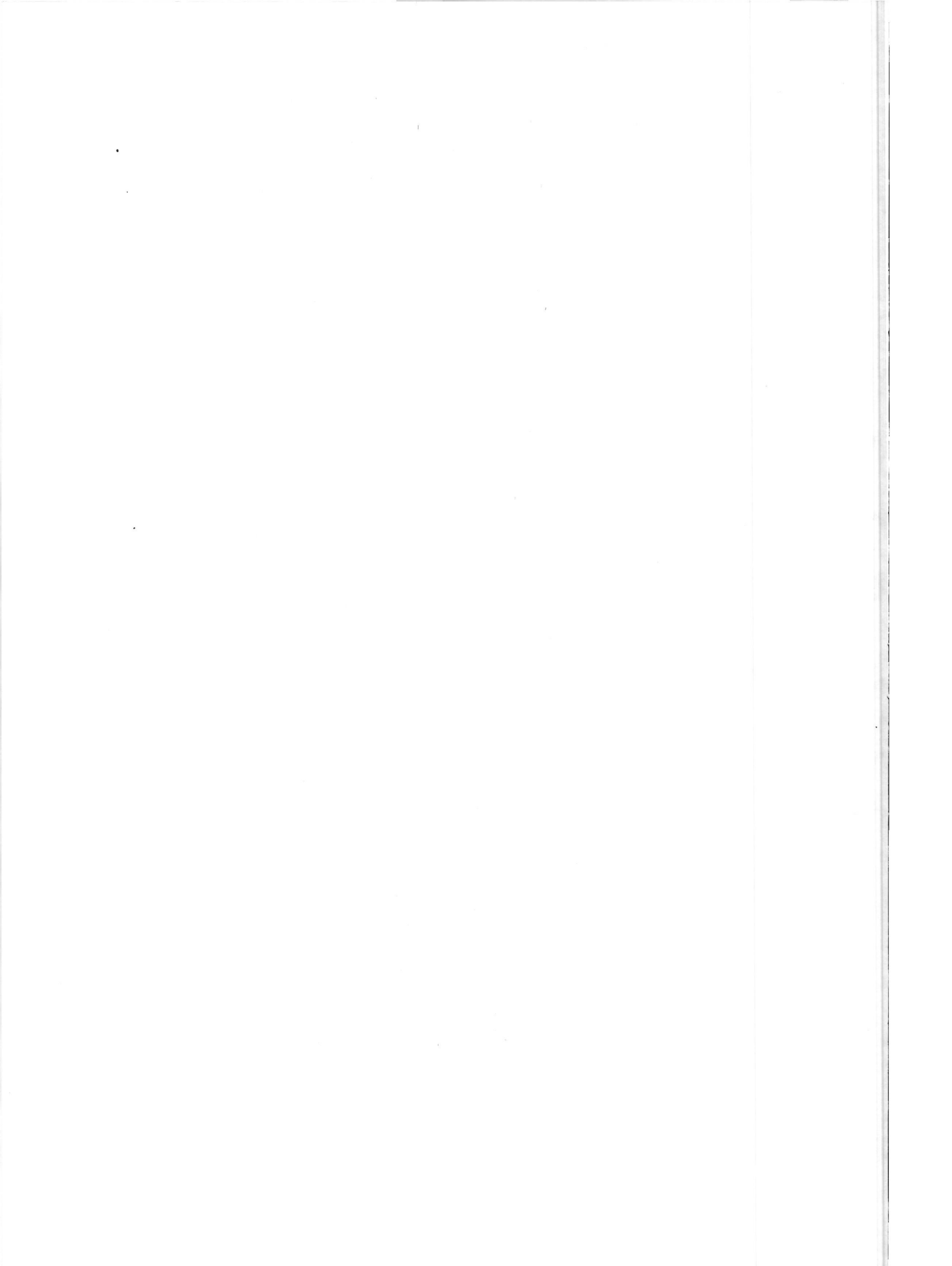
Inmiddels heeft het tweede VIERS-1 laboratorium experiment plaatsgevonden in de Deltatank van WL de Voorst. De Deltatank is een grote golfgoot (230 x 5 x 5m), die voor het experiment tijdelijk in een windgolfgoot moest worden getransformeerd; deze transformatie is

met succes uitgevoerd. De belangrijkste eigenschap van de Deltatank voor het VIERS-1 experiment is de mogelijkheid om "echte" golven, met een hoogte tot 3m te genereren. Het experiment is in maart 1989 uitgevoerd en bestond uit een meetprogramma waarbij, met de radar zowel stroomopwaarts als stroomafwaarts gericht, metingen werden uitgevoerd boven verschillende golfvelden bij windsnelheden tot 10 m/s. Ondanks vertragingen als gevolg van ongunstige weersomstandigheden (de opstelling van de radar buiten de eigenlijk windwatergoot maakte meten bij regen onmogelijk), is het gehele programma met succes uitgevoerd. Een aantal resultaten, voorlopige zowel als definitieve, is inmiddels beschikbaar.

De voorbereidingen voor de volgende fase van het programma, het veldexperiment vorderen goed. Dit experiment zal van 12 november tot 7 december 1990 worden uitgevoerd vanaf Meetpost Noordwijk van Rijkswaterstaat.

# Contents

<b>Abstract/Executive summary</b>	<b>iii</b>
<b>Samenvatting</b>	<b>v</b>
<b>Contents</b>	<b>vii</b>
<b>List of figures</b>	<b>xi</b>
<b>List of tables</b>	<b>xiv</b>
<b>1 Introduction</b>	<b>1</b>
<b>2 Results of the 'Delft' Experiment</b>	<b>3</b>
2.1 Microwave measurements . . . . .	3
2.1.1 Wind speed dependence . . . . .	3
2.1.2 Azimuth angle dependence . . . . .	4
2.1.3 Incidence angle dependence . . . . .	5
2.2 Wind measurements . . . . .	5
2.3 Wave measurements . . . . .	5



---

<b>3</b>	<b>The VIERS-1 model</b>	<b>6</b>
3.1	Description of the model . . . . .	6
3.1.1	Set up . . . . .	6
3.1.2	Developments . . . . .	9
3.2	The wave data . . . . .	13
3.2.1	Measurements . . . . .	13
3.2.2	Intercomparison of results from different gauges . . . . .	17
3.2.3	Comparison between measured data and D&P short-wave model . . . . .	18
3.3	Model parameters . . . . .	19
3.3.1	Long-wave slope distribution . . . . .	19
3.3.2	Short-wave spectrum model . . . . .	20
3.3.3	Hindsight observations . . . . .	20
3.4	Comparison of measured radar data and VIERS-1 model results . . . . .	21
3.5	Conclusions . . . . .	22
<b>4</b>	<b>Experiment 'de Voorst'</b>	<b>24</b>
4.1	Description . . . . .	24
4.2	Tunnel construction and wind machines. . . . .	26
4.3	Microwave measurements . . . . .	27
4.3.1	The acquisition software and measurement procedure. . . . .	29
4.4	Meteo measurements . . . . .	32
4.4.1	Pressure anemometer. . . . .	32
4.4.2	Cup anemometer . . . . .	32

---

4.4.3	Dantec Flowmaster. . . . .	32
4.4.4	Temperature and humidity. . . . .	33
4.4.5	Registration system . . . . .	33
<b>5</b>	<b>Processing and first results "de Voorst"</b>	<b>34</b>
5.1	Microwave measurements . . . . .	34
5.1.1	Microwave data processing and first results. . . . .	35
5.2	Meteo data . . . . .	39
5.3	Discussion . . . . .	40
5.3.1	Modulation of the microwave backscatter by the long waves . . . . .	40
5.3.2	Comparison with models. . . . .	42
5.3.3	Conclusion . . . . .	44
<b>6</b>	<b>Concluding remarks</b>	<b>46</b>
6.1	The 'Delft' experiment . . . . .	46
6.2	The 'de Voorst' experiment . . . . .	47
6.3	The field experiment at MeetPost Noordwijk. . . . .	48
6.4	After the field experiment. . . . .	50
	<b>Acknowledgements</b>	<b>51</b>
	<b>Bibliography</b>	<b>52</b>
<b>A</b>	<b>Presentations</b>	<b>53</b>
<b>B</b>	<b>Organization and finances.</b>	<b>57</b>

Page

x

---

<b>C</b>	<b>“Two-Dimensional Wave Number Spectra of Small-Scale Water Surface Waves”</b>	<b>58</b>
<b>D</b>	<b>The Wind Profile in a Wave Tank</b>	<b>78</b>
<b>E</b>	<b>Tabel: Conditions for all ‘de Voorst’ measurements</b>	<b>89</b>
<b>F</b>	<b>Figures</b>	<b>93</b>
F.1	Figures chapter 2 . . . . .	93
F.2	Figures chapter 3 . . . . .	97
F.3	Figures chapter 4 . . . . .	116
F.4	Figures chapter 5 . . . . .	121



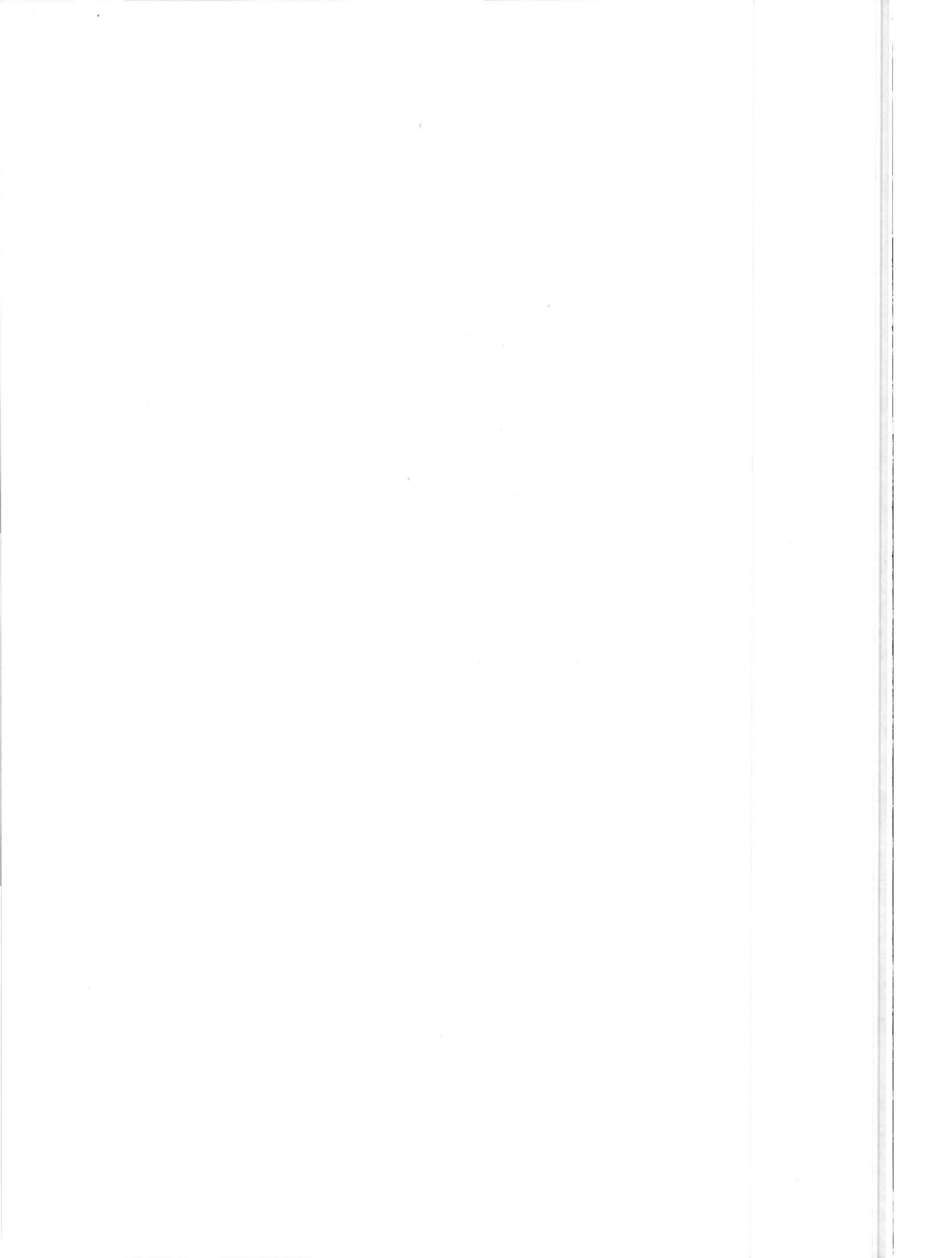
# List of Figures

2.1	Winddependence of the VV polarized microwave backscatter . . . . .	94
2.2	Winddependence of the HH polarized microwave backscatter . . . . .	94
2.3	Difference between VV and HH polarized microwave backscatter as a function of the friction velocity . . . . .	95
2.4	Azimuth dependence of the microwave backscatter . . . . .	95
2.5	Incidence angle dependence of the VV and HH polarized microwave backscatter . . . . .	96
3.1	Lobemeier Wave Gauge spectra for $U_{ref} = 8$ m/s and various fetches . . . .	98
3.2	Lobemeier Wave Gauge spectra for 100 m fetch and various wind velocities	98
3.3	Example of a Laser Slope Gauge spectrum . . . . .	99
3.4	Reproducibility of LSG spectra for $U_{ref} = 3.2$ m/s . . . . .	99
3.5	LSG spectra for $U_{ref} = 3.2$ (drawn), 8.1 (dashed) and 12.3 (dotted) m/s . .	100
3.6	Saturation function $b(f) = f * S(f)$ from LSG measurements . . . . .	100
3.7	Comparison LWG - LSG spectra for $U_{ref} = 8$ m/s . . . . .	101
3.8	Comparison LWG - LSG spectra for various wind velocities . . . . .	102
3.9	Comparison LSG - ISG saturation functions . . . . .	103
3.10	Comparison between LWG spectra and D&P wave model . . . . .	104

3.11	Comparison between ISG saturation functions and D&P wave model . . . .	105
3.12	Comparison between spectral widths from ISG data and D&P wave model .	106
3.13	Examples of directional saturation functions: ISG data and D&P model . .	107
3.14	Long wave slope variances as a function of the cross-over wave number . . .	108
3.15	Long wave slope variances as a function of the wind velocity . . . . .	109
3.16	Fraction of the along-wind slope variance of the total variance versus the wind velocity . . . . .	110
3.17	Tail parameter $\alpha(8)$ as a function of the wind velocity . . . . .	111
3.18	Fraction of the upwind tail parameter $\alpha_u(8)$ of the total $\alpha(8)$ versus the wind velocity . . . . .	112
3.19	Comparison of measured radar data and VIERS-1 model versus wind velocity	113
3.20	Comparison of measured radar data and VIERS-1 model versus incidence angle . . . . .	114
3.21	Comparison of measured radar data and VIERS-1 model versus azimuth angle . . . . .	115
4.1	'De Voorst' wave flume . . . . .	117
4.2	RF-frequency sweep for a FM/CW radar . . . . .	118
4.3	Beat signal for a point target . . . . .	118
4.4	Frequency spectrum of the FM/CW beat signal. . . . .	119
4.5	Schematic overview of the X-band FM/CW scatterometer used. . . . .	120
5.1	Timeseries of the microwave backscatter; HH; wave height 1 m . . . . .	122
5.2	Timeseries of the X-band microwave backscatter; VV; wave height 0.30 m .	123
5.3	Timeseries of the X-band microwave backscatter; HH; wave height 0.30 m .	124
5.4	Timeseries of $\sigma^0(t)$ , HH polarization, $u_* = .33$ m/s, regular long wave ( $\lambda=11.05$ , height .6 m.) . . . . .	125

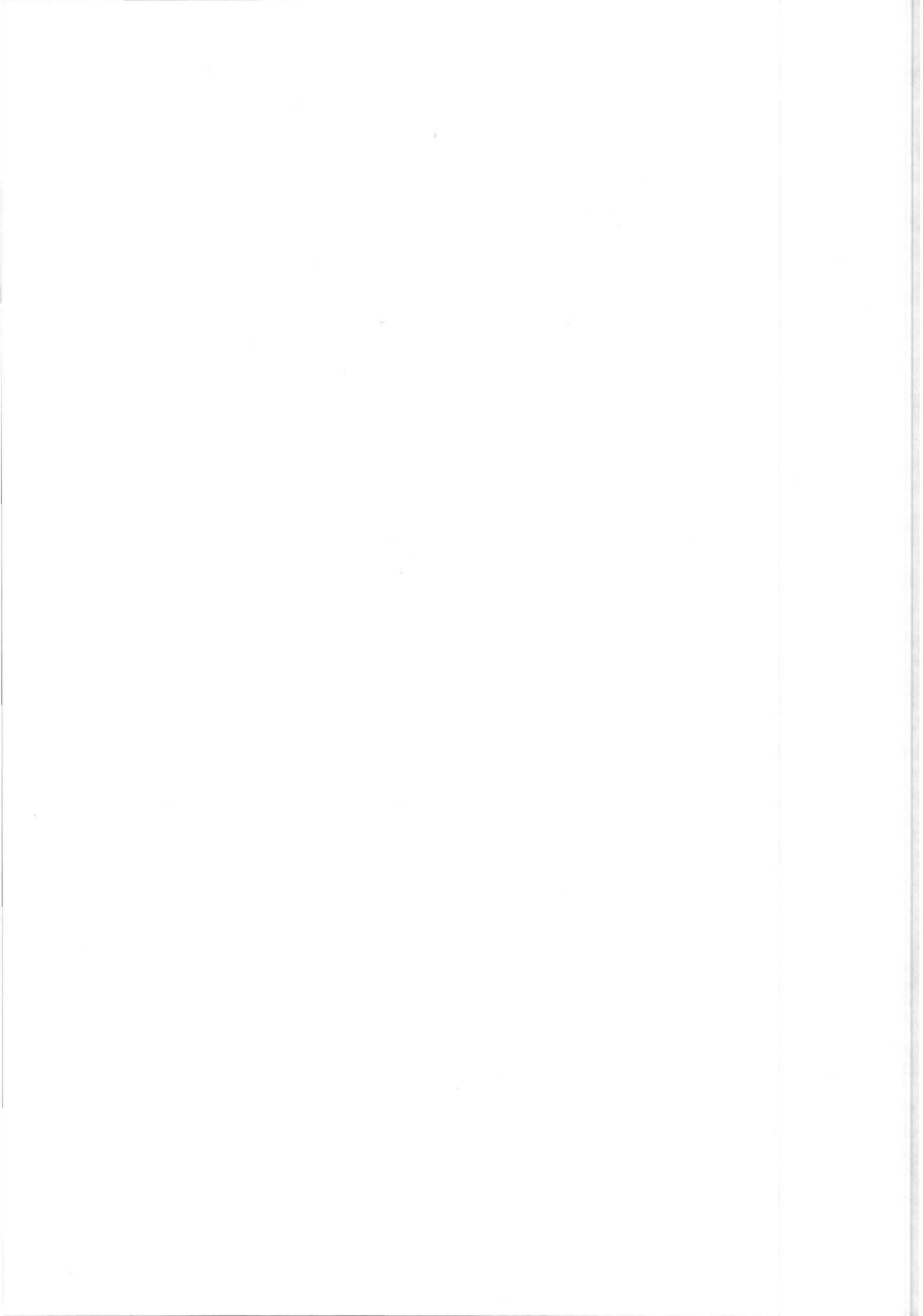
---

5.5	Range (frequency) spectrum of scatterometer data. . . . .	125
5.6	Power spectral density of microwave backscatter for measurement no. 425. .	126
5.7	Power spectral density for three different friction velocities . . . . .	127
5.8	Power spectral density for four different wave heights . . . . .	128
5.9	Power spectral density for HH and VV polarization . . . . .	129
5.10	Autocorrelation function of the VV polarized signal . . . . .	130
5.11	Autocorrelation of the microwave backscatter for different friction velocities	131
5.12	Autocorrelation of the microwave backscatter for different (monochromatic, f = .375 Hz) wave heights . . . . .	132
5.13	Autocorrelation of the microwave backscatter for different polarizations . .	133
5.14	Definition of phase angle of the long wave . . . . .	134
5.15	Microwave backscatter as a function of the long wave phase; HH; mechanical wave height 1.0 m . . . . .	135
5.16	Microwave backscatter as a function of the long wave phase; VV; mechanical wave height 0.6 m . . . . .	136
5.17	Microwave backscatter as a function of the long wave phase; VV; mechanical wave height 0.30 m . . . . .	137
5.18	Microwave backscatter as a function of the long wave phase; HH; mechanical wave height 0.30 m . . . . .	138
5.19	Microwave backscatter as a function of the long wave phase; VV; mechanical wave height 0.30 m . . . . .	139
5.20	Total modulation of the radar cross section for 4 different values of the parameter $\mu$ . . . . .	140



# List of Tables

2.1	Coefficients of fit of azimuth dependence with the ERS-1 empirical azimuth model . . . . .	4
3.1	Conditions for the wave wire measurements. . . . .	15
4.1	Instrumental and environmental conditions "de Voorst" experiment . . . . .	26
4.2	Specifications of the X-band FM/CW scatterometer . . . . .	29
4.3	Conditions radar measurementw, U : upwind measurement with scatterometer, D : downwind measurement, incidence angle : 45 degrees . . . . .	31
5.1	Overview 9 minute averaged $\overline{\sigma^0}$ . . . . .	36
5.2	Overview of the short decorrelation time $t_1$ . . . . .	39
5.3	Backscatter modulation measurements analysed so far. . . . .	42
5.4	Backscatter modulation depth and phase. . . . .	44



# Chapter 1

## Introduction

This report is a sequel to BCRS-89-24: "Progress report on the VIERS-1 project, part-1: the Delft experiment" [1], in which the goals and programme of activities of the VIERS-1 project have been described.

VIERS-1 is a (partly) Dutch acronym for Preparation (Voorbereiding) of the Interpretation (Interpretatie) of ERS-1 data. The programme is aimed at an improved understanding and interpretation of the data from the scatterometer on the oncoming ERS-1 satellite in its wind mode. The reader is referred to [1] for more extensive background information on the project. That report also contains a description of the VIERS-1 experiment in the wind/wave flume of Delft Hydraulics in Delft and the preliminary results of the Delft experiment.

In chapter 2 and annex C of this report the essential experimental results of the Delft experiment are presented.

Chapter 3 describes the first results of the next step in the execution of the project. A modeling group has been installed, headed by Dr. Ch. Calkoen of Delft Hydraulics. In this group the new insights in the relation between the scattering of microwave radiation by a wave field, derived from the literature and tested by comparison with the experiments, are being translated into a computer model. In the present version of that model the normalized radar cross-section is calculated as a function of the wave field and a number of atmospheric properties (primarily the wind field). In a later phase of the programme the model will be inverted to derive the wind from a set of radar cross-sections and some environmental parameters (such as swell and atmospheric stability), as predicted by state-of-the-art operational meteorological and wave models. The modeling group has available now a functioning modular computer programme, based on the so-called two-scale model. As the project continues new modules, based on the experimental results, are being developed and inserted into the model. They present several possible approaches

to the problem. Chapter 3 contains an introduction to the present VIERS-1 model and a first comparison of model result and measured data for the Delft experiment.

Chapter 4 gives a survey of another new phase in the programme, the second VIERS-1 experiment, which took place in and around the Delta tank of Delft Hydraulics at their premises at de Voorst. The preliminary results of that experiment are presented in chapter 5.

Chapters 6 and Annex A,B contain respectively concluding remarks, a review of the future activities in the programme, a list of the presentations members of the VIERS-1 group have made and some remarks about the organization and the finances of the programme.

## Chapter 2

# Results of the 'Delft' Experiment

### 2.1 Microwave measurements

#### 2.1.1 Wind speed dependence

Microwave backscattering has been studied for a range of wind speeds and fetches. We shall report those data at an incidence angle of  $45^\circ$  with the antenna looking upwind. Figure 2.1 (page 94) and 2.2 (page 94) summarize them as a function of wind speed with the fetch as a parameter. The range of the friction velocity was 0.07 till 0.92 m/s and was measured with the pressure anemometer.

Measurements were done at three different fetches: 100, 40 and 25 meter. The backscatter shows a *S*-shaped dependence on the friction velocity, when plotted against the logarithm of  $u_*$ . The largest increase is found at intermediate friction velocities ( $u_* = 0.15$ – $0.25$  m/s). In this region the backscatter increases with friction velocity according to a power law with coefficient of 3.5 for HH and 3.8 for VV polarization at 100 meter fetch. For the shorter fetches this growth rate is of the same order. Beyond a friction velocity of 0.25 m/s and a fetch of 100 meter, this exponential growth suddenly drops to a exponent of 1.3 for HH and 0.8 for VV polarization. This discontinuity of the wind speed dependence coincides with the first occurrence of incipient breaking of the dominant gravity waves.

For the shorter fetches fewer measurements have been done. For both, HH and VV polarization, the reflection coefficient at a fetch of 25 or 40 meter is smaller than at a fetch of 100 meter for the low friction velocities. At  $u_* \approx 0.3$  m/s a cross-over occurs for the small and large fetch signals. For  $u_* \approx 0.45$  m/s the signal at 25 m fetch is larger than the signals at 40 and 100 meter fetch. The occurrence of incipient breaking is dependent of the fetch length. At shorter fetches the breaking starts at higher wind speeds.

	A	B	C
HH	2.96	6.04	4.00
VV	18.7	39.1	26.2

Table 2.1: Coefficients of fit of azimuth dependence with the ERS-1 empirical azimuth model

Figure 2.3 (page 95) shows the ratio of the VV and HH polarized reflection coefficient as a function of the friction velocity at 45° incidence angle, upwind. For friction velocities smaller than 0.25 m/s this ratio slowly increases with  $u_*$  from 3 dB up to 4 dB at  $u_* \approx 0.25$  m/s. Then the ratio rapidly decreases with friction velocity until it is less than 1 dB at  $u_* = 0.92$  m/s. Measurement at shorter fetches show a qualitatively similar behavior though too few measurements have been done to verify this in a quantitative way. Again the sudden change in the VV/HH ratio occurs at the wind speed where incipient breaking starts occurring in the flume. This is an indication that for conditions with breaking waves an additional scattering mechanism with different polarization signature becomes important. Breaking waves within the scatterometer footprint have been observed causing large spikes ( $\approx +15$  dB) in the backscatter.

### 2.1.2 Azimuth angle dependence

For a friction velocity of 0.34 m/s and an incidence angle of 45°, the dependence of the radar cross section on the azimuth angle is shown in figure 2.4 (page 95) for HH and VV polarization.

The cross section shows a familiar dependence on the azimuth angle: for upwind conditions the highest backscatter is found which rapidly decreases with azimuth angle until it reaches a minimum at cross wind. For  $\alpha = 180^\circ$  (downwind) a secondary maximum is found. The upwind/crosswind ratio is 8.0 dB for HH and 7.6 dB for VV polarization. Upwind/downwind ratio is 1.5 dB and 1.6 dB for HH and VV polarization respectively. The dashed curves in figure 2.4 are least squares fits to the original data points with the well known empirical model (also used for present ERS-1 windscatterometer model):

$$\gamma = A + B * \cos \alpha + C * \cos 2\alpha \quad (2.1)$$

$\alpha$  being the angle between the radar 'look' direction and the wind direction. The coefficients found are listed in tabel 2.1.

The results of this model underestimate the cross section for the upwind direction of the radar for as well HH as VV polarization. For VV polarization a good fit is found for

azimuth angles larger than  $90^\circ$ . For HH polarization the overall fit is of a rather poor quality.

### 2.1.3 Incidence angle dependence

The dependence of the radar reflection coefficient  $\gamma$  on the incidence angle has been investigated for the case of a friction velocity of 0.34 m/s and a fetch of 100 m. The azimuth angle was  $0^\circ$  (upwind). The results for HH and VV polarization are shown in figure 2.5 (page 96). The curves show a well known type of behavior for scattering from slightly rough surfaces. For both polarizations the cross section drops rapidly with increasing incidence angle. For small incidence angles, where specular reflections are not negligible, the cross sections of both HH and VV polarizations are nearly the same. Around  $45^\circ$ , the VV polarized cross section reaches a 'plateau region' where the decrease with incidence angle is almost zero. The HH polarized cross section continues to decrease with incidence angle.

## 2.2 Wind measurements

The results of the wind measurements during the Delft experiment, as presented in Annexes B, C and D of [1], are still valid. In this case, contrary to the situation at the 'de Voorst' experiment (see 5.2.), no corrections were needed for the distance between the sensor head of the anemometer, because the sensing head was sufficiently close (25 cm.) to the water surface.

## 2.3 Wave measurements

The wave measurements done with the Imaging Slope Gauge (ISG) and the Laser Slope Gauge (LSG) have all been analysed and published. For completeness, a copy of the publication in the Journal of Geophysical Research is included in appendix C.

## Chapter 3

# The VIERS-1 model

### 3.1 Description of the model

#### 3.1.1 Set up

The purpose of the VIERS-1 model is to provide a framework in which new algorithms to compute radar backscatter on water surfaces, based on a description of the underlying physical processes, can be developed and tested. In this report we discuss the first version of this model, which was designed to correlate wind-, wave- and radar backscatter measurements, obtained in the first VIERS-1 measuring campaign in the Delft wind-wave flume [1].

The starting point for the VIERS-1 radar backscatter model was the two-scale model proposed by Donelan and Pierson [2], (D&P henceforth). The basic idea behind the two-scale model is that the water waves which scatter the radar signal can be separated in two distinct classes: long waves and short waves. The short waves have the same length scale as the radar waves and are mainly responsible for the radar scatter via the Bragg mechanism (for incidence angles between  $25^\circ$  and  $65^\circ$ ). According to Bragg theory the radar backscatter is proportional to the spectral values of the scattering water waves. The short waves ride on the long ones, which tilt the water surface and thus modify the effective radar incidence angle. To take this into account a statistical approach suffices, for which we only need the slope distribution of the long waves. The structure of the two-scale model is thus:

$$\sigma_{pol}^0(\theta, U_{10}, \dots) = \int_{-\infty}^{\infty} P(\mathbf{s}) \widetilde{\sigma}_{pol}^0(\mathbf{s}; \theta, U_{10}, \dots) d\mathbf{s},$$

with

$$\widetilde{\sigma}_{pol}^0(\mathbf{s}; \theta, U_{10}, \dots) = G_{pol}(k_{radar}, \mathbf{s}; \theta, \dots) \Phi(\mathbf{k}(k_{radar}, \mathbf{s}, \theta); U_{10}, \dots).$$

The radar backscatter  $\sigma_{pol}^0$  can be found by integrating the backscatter  $\widetilde{\sigma_{pol}^0}$  tilted in a plane with a slope  $\mathbf{s} = (s_x, s_y)$  times the probability  $P(\mathbf{s})$  that the water surface has that particular slope. In this model we consider horizontal ( $pol = HH$ ) and vertical polarization ( $pol = VV$ ). The backscatter depends on the incidence angle  $\theta$ , the wind velocity and direction  $\mathbf{U}_{10}$ , and other parameters as the water temperature, the air temperature, etcetera. The function  $G_{pol}$  can be derived directly from Bragg theory [3] and mainly depends on the angle parameters and the radar wave number. The wind velocity  $\mathbf{U}_{10}$  only occurs in the wave spectrum  $\Phi$ , which has to be determined for the wave number that satisfies the Bragg condition

$$k = 2k_{radar} \sin(\theta), \quad (3.1)$$

with  $\theta$  the effective incidence angle in the tilted plane. From the above we see that the two-scale model contains three independent components:

1. a model for the slope distribution of the long waves.
2. a model for the short-wave spectrum.
3. a model for the (Bragg) scatter.

The VIERS-1 computer program was designed to have a modular structure, allowing to swap one implementation of a component for another for test purposes. The first version of the program, discussed here, can be considered as the first set of test modules that together form a working program.

To model the slope distribution of the long waves we make the usual assumption of a Gaussian form:

$$P(\mathbf{s}) = \frac{\exp\left(-\frac{(\mathbf{s} \cdot \hat{\mathbf{U}}_{10})^2}{2S_u^2} - \frac{|\mathbf{s} \times \hat{\mathbf{U}}_{10}|^2}{2S_c^2}\right)}{2\pi S_u S_c}, \quad (3.2)$$

with  $\hat{\mathbf{U}}_{10}$  a unit vector in the direction of the wind. The slope distribution is completely determined by the upwind and crosswind slope variances  $S_u^2$  and  $S_c^2$ . The model expression for these parameters, proposed by D&P for fully developed waves, can not be applied to the very young waves in the tank experiment. Since the variances of the wave slopes in the tank have no universal value we did not make a special model but confined ourselves to a parameterization of the slope data, measured in the experiment. The geometrical correction, proposed by D&P to account for the fact that slopes, tilted towards the radar, occupy a larger fraction of the sea surface than slopes, tilted away, was incorporated in the VIERS-1 model.

The short wave spectrum should be known for wave numbers  $k$  that fulfil the Bragg condition (3.1). For X-band radar  $k_{radar} = 201m^{-1}$  and the incidence angles  $\theta$  in this experiment were between  $20^\circ$  and  $45^\circ$ . The region in which we want to know the wave

spectrum is between 140 and 280  $m^{-1}$ . Using the dispersion relation for capillary waves on deep water:

$$\omega^2 = gk + \gamma k^3, \quad (3.3)$$

with  $g = 9.81m/s^2$  the gravitational acceleration and  $\gamma = 7.410^{-5}m^3/s^2$  the surface tension times the air-water density ratio. Since the measured peak frequency of the generated waves was of the order of 1 Hz, the 0.8 m water depth in the Delft wind-wave flume is sufficient to treat all waves as deep water waves. With this dispersion relation the wave number range translates into a frequency domain of  $f$  between 6.2 and 10.7 Hz. For this first version of the VIERS-1 model we choose again to model measured wave data in stead of inserting a wave model based on the energy-balance equation. This way we can evaluate the model components one step at a time. The parameterization of the short-wave spectra, fitted to the measured wave data, had the form:

$$\Phi(k, \psi; U_{10}) = \frac{\alpha_u(k_{radar}; U_{10})}{k^4 \cosh^2(h(k_{radar}; U_{10}) * \psi)}, \quad (3.4)$$

with  $\psi$  the angle between the wind and wave direction, so a  $k^{-4}$ -like spectrum with a spectral width as proposed by D&P. The wave number for X-band radar  $k_{radar} = 201m^{-1}$  corresponds with water waves with a frequency of 8 Hz. Since the analysis was done in the frequency domain, we will refer to  $\alpha_u(8)$ .

The module that computes the backscatter due to the Bragg mechanism is an implementation of the equations given by D&P. Also the cut-off for incidence angles less than 18°, to avoid instabilities due to a singularity for zero incidence angle, was implemented.

The concept of the two-scale model indicates that there is a clear difference between long and short waves. In the wave tank, where the significant wind waves are much smaller than at sea (tank:  $k_{peak} \approx 4m^{-1}$ , sea:  $k_{peak} \approx 0.04m^{-1}$  compared with  $k_{radar} \approx 200m^{-1}$ ), it is more difficult to find a suitable cross-over point between long and short waves. The suggestion of D&P to choose the cross-over wave number  $k_{co}$  at  $k_{bragg}/40$  is not possible in the tank. In stead we have chosen for a fixed value of  $k_{co} = 36m^{-1}$ , ( $f_{co} = 3$  Hz, in the middle between the peak wave number and the radar wave number in the logarithmical sense.

Other differences between the model proposed by D&P and the first version of the VIERS-1 model are:

- no integration over wind variability (because of the steady conditions in the wind-wave flume).
- no model for the specular reflection mechanism was implemented. Specular reflection is important for small incidence angles. At  $\theta = 20^\circ$ , the smallest incidence angle in

the experiment, it is expected that specular reflection still contributes to the total scatter. However, for these small incidence angles the choice of an ad-hoc cut-off parameter in the present model is still dominant. Therefore, we shall leave the modelling of radar scattering at small incidence angles to a special study.

- a model for the modulation of the short waves by the long waves in order to simulate the upwind-downwind scatter difference is not implemented. This too awaits a further study.

Since the long- and short-wave module in the VIERS-1 model consist of parameterized measured wave data, a comparison between measured radar data and model results mainly tests the validity of the scattering module.

### 3.1.2 Developments

Presently, new modules are being developed for future versions of the VIERS-1 model. The parameterized wave data should be replaced by more general models. Also the scatter module should be examined carefully: the strict conditions under which Bragg scatter may be applied theoretically (in terms of wave height and curvature) are seldom satisfied under practical circumstances. Theories exist that solve the problem of scattering electromagnetic radiation on a water surface (almost) exactly, but there are some draw-backs:

1. the theories have been formulated but not yet implemented in operational programs. Nor are these theories easily implemented.
2. these theories require so much computer capacity that their use in operational radar backscatter models is not practical. In this respect there is a wide gap between the more exact theories and the simpler models like the Bragg or Kirchhoff approximation.
3. most exact theories compute the scatter for a given specific water surface in stead of for a given wave spectrum. For application in a radar backscatter model we would have to average the scatter from several water surfaces that are compatible with a given wave spectrum.

In view of these draw-backs we opt for a two-scale Bragg scatter model, but use more exact scatter models to track deficiencies of the Bragg model and (hopefully) correct them.

At the moment we have two candidates for the short-wave module and two alternatives for the scattering mechanism:

### Donelan-Pierson short-wave model

The short-wave model, proposed by D&P [2] is based on the energy-balance equation for waves. This model takes the following physical phenomena into account: energy input through the wind, viscous wave damping and wave breaking. The directional spectrum is parameterized as  $\cosh^{-2}(h(k) * \psi)$ , with the spectral width  $h(k)$  given by the model. An implementation of this model has been made and can be used as a module in the VIERS-1 model.

### The VIERS-1 short-wave model

The VIERS-1 short-wave model: 'Testwa' is also based on the energy-balance equation. Although the ultimate theory still has to be formulated, it has been argued that during the initial stages of wave growth the two dominant energy processes are wind input and nonlinear wave interactions, rather than wind input and wave breaking (D&P). This point of view has been advocated by P.A.E.M. Janssen (K.N.M.I.), who developed the Testwa model on this basis. In this section a brief description of Testwa will be given.

Water waves can be classified into three groups:

- gravity waves:  $f < 5$  Hz; only gravity is important.
- gravity-capillary waves:  $5 < f < 80$  Hz; both gravity and surface tension are important.
- capillary waves:  $f > 80$  Hz; only surface tension is important.

The distinction between the different types of waves is not so sharp as suggested above, rather there is a gradual transition.

In the 'Delft' experiment the dominant waves have a peak frequency in the order of 1 Hz (gravity range), whereas the waves resonant with the radar (Bragg waves) have a frequency in the order of 7 Hz (gravity-capillary range). Hence both the gravity and gravity-capillary range have to be covered if one wants to model the entire frequency spectrum. This poses a problem as the physics of water waves in the different ranges is different. In Testwa this problem is solved by treating the spectrum around the peak and in the gravity-capillary range separately, and subsequently matching them at an intermediate frequency.

The region around the peak is modelled by the empirical JONSWAP expression [4]. It is a universal expression with four parameters:  $\alpha$  (Phillips' constant),  $f_p$  (peak frequency), and the shape parameters  $\gamma$  and  $\sigma$ :

$$E(f) = \frac{\alpha g^2}{(2\pi)^4 (f)^5} \exp(-5/4(f_p/f)^4) \gamma \exp(-\frac{1}{2\sigma^2 f_p^2} (f-f_p)^2) \quad (3.5)$$

$E$  is the one-dimensional frequency spectrum. The parameters depend on friction velocity and fetch. In JONSWAP it is found:

$$f_p = 1.107 g^{2/3} x^{-1/3} u_*^{-1/3} \quad (3.6)$$

$$\alpha = \min(0.05, 0.57(2\pi u_* f_p/g)^{1.5}) \quad (3.7)$$

$$\gamma = \max(1, 1 + 9(1 - (\frac{0.00608}{u_* f_p/g})^2)) \quad (3.8)$$

$$\sigma = 0.08 \quad (3.9)$$

The JONSWAP expression loses its validity outside the gravity range.

In order to calculate the spectral density for frequencies much larger than the peak, it is necessary to consider the energy balance of the water waves. The energy balance is governed by three processes: wave growth by wind input, wave decay by dissipation (breaking, viscous damping and bottom dissipation), and energy exchange among waves of different frequencies by non-linear interactions.

For high-frequency waves dissipation will be primarily due to viscous damping. Therefore Testwa does not take into account breaking and bottom dissipation.

Furthermore it may be assumed that, in the tail of the frequency spectrum, the net wave growth (or decay) resulting from wind input, viscous damping and non-linear interactions is very slow compared to the three constituting processes [5], [6]. This "slow-growth approximation" leads to the following simplified energy balance equation.

$$S_{in} + S_{nl} + S_{vis} = 0 \quad (3.10)$$

Testwa solves 3.10. The various source terms are modelled in the following way.  $S_{vis}$  is proportional to the spectrum; the proportionality coefficient follows from an exact calculation by Lamb [7].  $S_{in}$  is also proportional to the spectrum; in Testwa Plant's expression [8] for the proportionality constant is chosen.  $S_{nl}$  is non-linear in the spectrum. Bold assumptions are needed in order to reduce the complicated exact expressions for three- and four-wave interactions to tractable ones. In Testwa for the three-wave a quadratic (in the spectrum) and for the four-wave interactions a cubic expression is implemented.

The energy balance equation 3.10 has to be supplemented with a boundary condition. This boundary condition has to be provided by the JONSWAP expression 3.5 for the peak. It is more or less arbitrary where to glue together both spectra; in Testwa it is done at twice the peak frequency.

Summarizing: for  $f < 2f_p$ , Testwa generates the JONSWAP expression 3.5; for  $f > 2f_p$ , the simplified energy balance equation is solved; at  $f = 2f_p$  both spectra are joined continuously.

### **The Holliday radar backscatter model**

The problems with two-scale radar backscatter models were discussed already and can be summarized as follows:

1. There is no sound criterium where to make the separation between the long and short wave part of the wave spectrum.
2. First order Bragg scattering is valid only for waves that are much lower than observed at sea.
3. The radar cross section of the sea obtained with first order Bragg diverges when the angle of incidence approaches zero.

Therefore the contribution of Bragg scattering is discarded by Donelan and Pierson in their model for local angles of incidence lower than  $18^\circ$ .

The most fundamental approach to the scattering problem, which adresses all of these shortcomings, is by using the Stratton-Chu equation (Stratton, 1941). This is an integral equation which can be derived directly from the Maxwell equations. It gives the magnetic induction at some point as an integral of the (electromagnetic) surface current over the sea surface. When the surface is precisely known, the Stratton-Chu equation can be solved using standard techniques, like iteration. The problem, of course, is that the sea surface is known only statistically. Holliday, St-Cyr and Woods (1986) show how to solve the Stratton-Chu equation by iteration when only the two-dimensional wave spectrum is given. They derive a relatively simple expression for the radar cross section of the sea in the first iteration. Their approach can be extended to higher iterations. In principle, their model is exact. To keep the calculations feasible, however, some well defined approximations have to be made. The method used by Holliday et al is restricted to small angles of incidence (below  $30^\circ$ ) since in their model the cross section is independent of the polarization. The polarization dependence appears in the second iteration of the Stratton-Chu equation. In this sense, the Holliday et al model is more restrictive than Bragg scattering. However, the advantage is that the effect of long waves on the cross section is taken into account in a completely natural way. Holliday et al use the model to describe modulations in the radar cross section caused by bottom topography. They find that with their model the modulations at X-band are of the same order of magnitude as those at L-band, as indicated by experiments, while first order Bragg underestimates the cross sections at X-band by an order of magnitude. Unfortunately, they make no comparison with scatterometer data.

Giving a good description of the radar cross section at low angles of incidence and being relatively simple, the model of Holliday, St-Cyr and Woods is complementary to two-scale models. Therefore it will be implemented in the VIERS-program to describe scatterometer data at low angles of incidence.

### **The extended Rayleigh method for radar scatter**

The extended Rayleigh method was developed to compute the scatter of radiation in the optical domain on periodic gratings [9]. It uses a Green's function technique in which the outgoing radiation, scattered away from the grating, is expanded in terms of an infinite set of fields, obeying the free Maxwell equation. Almost all of these fields are exponentially damped. A variational method is used to determine the amplitudes of the outgoing fields, such that the boundary conditions on the surface of the grating are satisfied. An implementation of this method was put at our disposal by kind permission of the optical department of the technical university of Delft.

The Rayleigh method has the advantage of still being relatively simple, such that the implementation can run on micro-computer systems. It can not solve all scatter problems but when the computations converge, then the solution is exact (only computational round-off errors, no theoretical omissions). The implementation we have is one-dimensional, i.e. periodic in one direction and constant in the other. This is not a principal restriction, but an extension to a two-dimensional model would require a few orders more computer capacity, making it unpractical in the context of the VIERS-1 model.

The implementation of the Rayleigh method has to be modified a bit to adjust it to the sinusoidal wave surfaces. Tests how to do this have already been completed. This method will not be turned into a VIERS-module, since it still takes too much computer capacity. In stead, we will directly compare its results with those of a pure Bragg model and that way study the effects of finite wave height, non-linear/slanted wave forms and localized wave trains.

## **3.2 The wave data**

### **3.2.1 Measurements**

#### **The gauges**

In the modelling of the radar backscatter from a sea surface on a physical basis, the wave field plays a crucial, intermediary role. The wind drives the wave field, which in turn

determines the radar backscatter. For this reason much attention was paid in the VIERS-1 experiment to the measurement of the wave field. For use in the VIERS two-scale radar backscatter model we were interested in two aspects of the wave field: the wave slope distribution of the long waves ( $< 3$  Hz) and the energy spectrum in the neighbourhood of the Bragg waves (between 6 and 11 Hz for the X-band radar).

During the VIERS-1 experiment in the Delft wind-wave flume the waves were monitored with the help of three different wave gauges: a wave wire, a laser slope gauge and an image slope gauge [1]. These three devices provided complementary information. The wave wire, referred to as the Lobemeier Wave Gauge (LWG), is a relatively simple, well known device. The results were used to compute the frequency spectra, which are expected to be reliable up to about 15 Hz. The LWG was operational during the whole experiment and therefore produced the greatest number of wave spectra (36 time series analyzed for this study). The Laser Slope Gauge (LSG) measured time series of both the along wind and the cross wind wave slopes. The data, analyzed here, were not measured during the VIERS-1 Delft campaign but were obtained by dr. B. Jähne during a later experiment in the Delft wind wave flume (december 1988) and consist of eleven time series covering six wind conditions. The Image Slope Gauge (ISG) produced the most sophisticated wave information: from camera images of the wave surface directional wavenumber spectra were measured. However, the processing of the ISG data is so time consuming that for this study only seven spectra were available.

The data measured with these devices are complementary in two senses. First, with respect to the domain of the spectra. The LWG measures pure frequency spectra, the ISG pure wavenumber spectra and the LSG a kind of mixture: a frequency slope spectrum which is equal to the frequency power spectrum times the wavenumber squared. In most radar backscatter models a simple dispersion relation is used to transform frequencies into wave numbers and vice versa. Doubt has risen whether such an approach can be applied to the small Bragg waves because of their interaction with the orbital currents of the long waves. With the help of the available experimental data we can simply test this approach. The measured wave data are also complementary with respect to the range of validity and the number of spectra measured versus the information content of the spectra. For the description of the high frequency tail of the spectra the ISG data are best suited, but we have too few spectra to obtain a reliable general parameterization. By devising a model for the spectrum tail we can also use the LWG and LSG data to tune the parameter describing the variance, integrated over all directions, and the LSG data for the spectral width. This increases the reliability of the model and allows us to assess its accuracy.

The wave field has been measured as a function of the wind velocity and the fetch. During the VIERS-1 experiment the wind field has been measured extensively. For the details we refer to [1]. What is relevant for the wave analysis in this report is that the wind velocity is given either in terms of the reference velocity  $U_{ref}$ , as measured by a simple gauge in the wind-wave flume, or in terms of  $U_{10}$ , the wind velocity extrapolated to a height of 10

$U_{ref}$ (m/s)	fetch (m)		
	25	40	100
2.1			2
3			2
4	1	2	2
5.3			2
7			2
8	4	2	2
10.5		2	2
12	2	4	2
15			1
15.5		2	

Table 3.1: Conditions for the wave wire measurements.

m. The relation between these two quantities is given by:

$$U_{10} = 1.23U_{ref} + 0.0125U_{ref}^2. \quad (3.11)$$

Also the friction velocity  $u^*$  can be expressed in terms of  $U_{ref}$ :

$$u^* = 0.039 + 0.00823U_{ref} + 0.003779U_{ref}^2. \quad (3.12)$$

In some runs the fetch in the wind-wave flume was limited by connecting a wave barrier to a movable bridge across the flume. The values of the fetch denote the distance between the barrier and the point where the waves were measured. However, since the bridge disturbed the wind flow, the effective fetch may be less.

### The Lobemeier wave data

The data of the Lobemeier wave wire were measured by KNMI at a sampling rate of 35.15625 Hz, no filter applied. Each time series contained about 10000 data points, covering a period of about five minutes. Table 3.2.1 gives the conditions under which the waves were measured. The numbers in this table show how many time series have been used for a certain condition.

We divided the time series in half overlapping segments consisting of 512 data points using a Hann filter to compute the energy spectrum. This should produce discrete spectra with 257 bins from 0 to  $f_{nyq}$  (17.578 Hz, half the sampling frequency). However, the routine used to calculate the spectrum did not compute the spectrum at the Nyquist frequency, so we have 256 bins. The discrete spectra  $E_{dis}(f_i)$  are normalized such that the total variance of the waves  $\overline{\eta^2}$  can be found as:

$$\overline{\eta^2} = \sum_{i=0}^{255} E_{dis}(f_i).$$

The continuous spectrum  $E(f)$ , normalized such that

$$\overline{\eta^2} = \int_0^{17.578} E(f) df \approx \sum_{i=0}^{255} E(f_i) \delta f,$$

with  $\delta f = 17.578 / 256 = 0.0687$  Hz, can be approximated at the frequencies  $f_i$  as  $E(f_i) \approx E_{dis}(f_i)/\delta f$ . In this report we will use the continuous spectra because then we can compare with the results of other gauges, which use a different sampling frequency.

In figure 3.1 (page 98) we compare spectra, calculated from LWG data, measured at a constant wind velocity ( $U_{ref} = 8$  m/s) and varying fetch: 100 m (drawn line), 40 m (dashed) and 25 m (dotted). This plot shows that the tail of the spectra hardly depends on the fetch. The overshoot of the peak is clearly visible. The dotted spectrum (25 m fetch) has an extra peak at 0.95 Hz, which may be attributed to leakage of the fetch limiter. In figure 3.2 (page 98) we give spectra for a constant fetch of 100 m but different wind velocities:  $U_{ref} = 4$  m/s (drawn line),  $U_{ref} = 8$  m/s (dashed) and  $U_{ref} = 12$  m/s (dotted). Here, both the level and the form of the tail of the spectrum depend on the wind velocity.

The spectra show two spurious peaks at 9.48 Hz and at 14.87 Hz. The peak at 14.87 Hz can be identified as 50 Hz noise from the power supply to the wind generators, folded twice ( $f_{samp} = 35.156$  Hz). The second peak has not yet been identified. This peak lies in our region of interest in the spectral tail, 6.2 - 10.7 Hz. and has to be filtered out in the processing. Both spurious peaks in the spectrum disappear when the wind generators are turned off.

### The laser slope data

The laser slope data were measured by dr. B. Jähne with a sample frequency of 1000 Hz. These data were filtered and subsampled with a frequency of 62.9 Hz in order to keep the data set manageable. Each data point consists of two values: an along wind and a cross wind wave slope. Processing these data in a similar way as the LWG data thus yields the along wind and a cross wind slope spectrum  $S_{along}(f)$  and  $S_{cross}(f)$ . These two spectra are moments of the unknown directional slope spectrum  $S(f, \psi)$ :

$$S_{along}(f) = \int_{-\pi}^{\pi} \cos^2(\psi) S(f, \psi) d\psi,$$

$$S_{cross}(f) = \int_{-\pi}^{\pi} \sin^2(\psi) S(f, \psi) d\psi,$$

with  $\psi = 0$  in upwind direction. The one-dimensional slope spectrum  $S(f) = \int_{-\pi}^{\pi} S(f, \psi) d\psi$  can thus be found as  $S(f) = S_{along}(f) + S_{cross}(f)$ . The difference  $S(f) = S_{along}(f) - S_{cross}(f)$  is a measure for the spectral width. The laser slope gauge has measured for six different wind velocities:  $U_{ref} = 3.2, 5.6, 8.1, 10.4, 12.3$  and  $15.2$  m/s.

In figure 3.3 (page 99) we give an example of a slope spectrum for  $U_{ref} = 8.1$  m/s (drawn line =  $S_{along}(f)$ , dashed =  $S_{cross}(f)$ ). Note that between 2 and 4 Hz the crosswind spectrum is larger than the alongwind spectrum. Figure 3.4 (page 99) gives an impression of the reproducibility of the measurements by showing three different slope spectra at the same reference wind velocity of 3.2 m/s. Above 20 Hz the spectra can deviate by as much as a factor of three. The deviation is less than about 20 % between 5 and 10 Hz, the region of interest for the backscatter model for X-band radar. We note that the reproducibility is worst at low wind speeds, which might be due to surface films. In figure 3.5 (page 100) the slope spectra for three different wind velocities are shown (drawn line:  $U_{ref} = 3.2$  m/s, dashed: 8.1 m/s and dotted 12.3 m/s). In figure 3.6 (page 100) we give for the same wind velocities the *degree of saturation*  $b(f) = f * S(f)$  (see [10]).

### The image slope data

For an description of the image slope gauge and its results we refer to the article by Jähne and Riemer [10]. Two-dimensional k-spectra were measured for seven different wind velocities:  $U_{ref} = 2.1, 3.1, 4.2, 5.6, 6.8, 9.1$  and 12.4 m/s, all for a fetch of 100 m.

#### 3.2.2 Intercomparison of results from different gauges

As mentioned above, it is not possible to compare the results of different wave gauges directly since they measure in a different domain (wave number or frequency). To do such a comparison we need to assume that we may apply the standard dispersion relation (3.3) to transform wave numbers in frequencies and vice versa. This dispersion relation does not consider the effect of the orbital currents of longer waves and therefore it is not clear whether it may be applied to capillary waves on long waves. To check this we compare in figure 3.7 (page 101) the the variance spectrum  $E_{LWG}(f)$ , as measured by the Lobemeier Wave Gauge with a variance spectrum computed from the LSG slope spectrum as  $E_{LSG}(f) = S(f)/k(f)^2$ . Here  $k$  is calculated from the frequency  $f$  with the help of the dispersion relation (3.3). The wind velocity for these measurements was  $U_{ref} = 8$  m/s. Figure 3.7 shows an excellent agreement between the two spectra up to at least 14 Hz. This result supports the (frequent) use of the dispersion relation in the two-scale model. In figure 3.8 (page 102) we do the same comparison for reference wind velocities in the range of 3 - 15 m/s. For these cases the wind velocities for LSG and LWG measurements were not exactly the same, but the difference was always less than 0.2 m/s. For  $U_{ref} = 3$  m/s a deviation between the LSG and the LWG spectrum can be observed above about 7 Hz, where the LWG spectrum seems to reach its noise level. At  $U_{ref} = 5.5$  and 10.5 m/s there is again a splendid match between the spectra. For a reference wind velocity of 15 m/s the LWG spectrum is about a factor of 3 higher than the LSG spectrum. Because at this wind velocity there are many breaking waves, the difference may be attributed to the LSG not being able to measure all the slopes.

In figure 3.9 (page 103) we compare saturation functions  $b(k)$  from LSG and ISG data for wind velocities of  $U_{ref} = 5.6$  and  $12.3$  m/s. The LSG functions  $b_{dir}(k)$  were computed from the slope spectra  $S_{dir}(f)$  as  $b_{dir}(k(f)) = f S_{dir}(f) \partial \log(f) / \partial \log(k)$ , with *dir* is *along* or *cross*. The ISG saturation functions were found by numerically integrating the two-dimensional function  $b(k, \psi)$  times  $\cos^2(\psi)$  or  $\sin^2(\psi)$ . From the figure it is clear that the ISG and the LSG saturation functions do not compare as well as the LSG and LWG spectra. In the region of interest ( $140 \leq k \leq 280$ ) the LSG result is lower by a factor of about 2 for  $U_{ref} = 5.6$  m/s and by a factor of 2 - 3 for  $U_{ref} = 12.3$  m/s. It is not clear what causes the discrepancy. It can not be attributed to the omission of the influence of orbital currents of the long waves in the dispersion relation, because that would effect the short waves most. Then one would expect a good match for (relatively) long waves and an increasing discrepancy for shorter waves. In figure 3.9 the opposite turns out to be the case.

### 3.2.3 Comparison between measured data and D&P short-wave model

Later versions of the VIERS-1 model will be compared with radar measurements at sea and therefore the parameterized wave modules should be replaced by more general wave models. One candidate for the short-wave model is the model proposed by Donelan and Pierson [2]. In this section we compare the predictions of the D&P model with measurements in the wind-wave flume. We expect that the short waves in the flume are sufficiently developed to allow for such a comparison with a model for waves at sea. In figure 3.10 (page 104) we compare the D&P model results, integrated over all directions (dashed line), with LWG measurements for wind velocities of  $U_{10} = 5.1, 10.6, 16.6$  and  $21.3$  m/s. In the frequency range between 6 and 10 Hz the model deviates from the measurements by a factor of 5 at most. However, the measured spectral tail seems to increase more with higher winds than the model tail. In figure 3.11 (page 105) we compare the model saturation function in the upwind direction  $b(k, \psi = 0) = E(k, \psi = 0) * k^4$  with the data measured using the ISG. For the latter we use the average over upwind  $\pm 5^\circ$  direction in order to reduce noise. Here too we find deviation up to a factor of five. The width of the directional spectrum is studied in figure 3.12 (page 106). Here we use as a measure for the spectral width the quantity

$$w_s(k) = \int_{-\pi}^{\pi} b(k, \psi) d\psi / b(k, \psi_u),$$

with  $\psi_u$  the wind direction. In the D&P model the directional spectrum is parameterized as  $\cosh(h(k)\psi)^{-2}$  and therefore the width  $w_s$  is related to the parameter  $h(k)$  as  $w_s = (2/h) \tanh(\pi h)$ . From plot 3.12 we see that the measured spectral widths vary significantly less than the model ones. As an example we show in figure 3.13 (page 107) a two-dimensional measured saturation function side to side with a model result.

From the figures we make the following observations:

- the measured data vary less as a function of the wave number and more as a function of the wind velocity than the model results.
- the  $\cosh(h(k)\psi)^{-2}$  parameterization of the directional spectrum does not seem to be optimal for short waves. The measured directional spectrum for capillary waves seems to be more 'square'. For the short gravitational waves the directional spectrum even has a bimodal form with maxima at approximately  $45^\circ$  from upwind, as mentioned by Jähne [10].
- the measured spectral widths vary less than the model values (the high measured values are caused by a local bimodal form).

### 3.3 Model parameters

As mentioned above, the wave modules in the first version of the VIERS-1 model consist of parameterized wave data. In this chapter we deal with the determination of the model parameters.

#### 3.3.1 Long-wave slope distribution

Assuming a Gaussian form, the probability distribution of the long wave slopes is completely determined by the slope variances  $\sigma_{dir}^2$ . For a given cross-over wave number  $k_{co}$  between the long and the short waves we can find the long-wave slope variance by integrating the slope spectrum up to  $k_{co}$ :

$$\sigma_{dir}^2 = \int_0^{k_{co}} S_{dir}(k) dk,$$

with *dir* = along- or crosswind.

For the calculation of the slope variances the measurements with the LSG are ideally suited. In figure 3.14 (page 108) we give the slope variances as a function of the cross-over wave number for several wind velocities. The drawn line is for the along-wind direction and the dashed line for crosswind. The dotted line shows where  $k_{co} = 36m^{-1}$ , the fixed value selected in the model set up. In this figure we see that for low wind velocities the selected  $k_{co}$  is only just in the saturation range, where  $\sigma^2$  is reasonably constant. For high wind velocities  $\sigma^2$  in the saturation range increases significantly with increasing  $k_{co}$ . In figure 3.15 (page 109) we plot the total variance  $\sigma(3) = \sigma_{along}(3) + \sigma_{cross}(3)$ , where the value three denotes the cross-over frequency of 3 Hz, corresponding with  $k_{co} = 36m^{-1}$ . In this plot we also used variances, computed from LWG data according to:

$$\sigma^2 = \int_0^3 E(f)k^2(f) df,$$

with  $k(f)$  given by the dispersion relation 3.3. The fit, drawn through the data points, is given by:

$$\sigma^2 = 6.03 \cdot 10^{-4} U_{10}^{1.39}. \quad (3.13)$$

In figure 3.16 (page 110) the along-wind component of the slope variance over the total slope variance is plotted. Here we used only LSG data. We found the following fit:

$$\sigma_{along}^2 = 0.905 - 0.161 \cdot {}^{10}\log(U_{10}). \quad (3.14)$$

In the long wave module of the first version of the VIERS-1 model the distribution (3.3) was implemented with the fits (3.13) and (3.14).

### 3.3.2 Short-wave spectrum model

In the parameterization of the high frequency spectrum (3.4) we need  $\alpha_u(8)$ , the saturation function in the upwind direction at a frequency of 8 Hz as a function of the wind velocity. We determine this function in two steps: first we make a fit for the function  $\alpha(8)$ , the saturation function at 8 Hz integrated over all directions, using the measured data from all three wave gauges. Next we use the ISG data to relate the upwind saturation function  $\alpha_u(8)$  to the integrated one  $\alpha(8)$ .

In figure 3.17 (page 111) we plot the values of  $\alpha(8)$  or all three wave gauges as a function of the wind velocity  $U_{10}$ . The fitted curve, plotted in the figure, is given by:

$${}^{10}\log(\alpha(8)) = -3.66 + 0.895 \cdot {}^{10}\log(U_{10}) + 0.54 \cdot {}^{10}\log^2(U_{10}). \quad (3.15)$$

We note that the use of all available wave data measurements greatly improved the reliability of the fit.

The upwind saturation function  $\alpha_u(8)$  is related to the integrated  $\alpha(8)$  in figure 3.18 (page 112). The fit

$${}^{10}\log(\alpha_u(8)) = -1.335 - 0.002 \cdot {}^{10}\log(\alpha(8)) - 0.235 \cdot {}^{10}\log^2(\alpha(8)). \quad (3.16)$$

seems to give an excellent agreement. Finally, for the spectral width we found as best fit the constant value:

$$h(k_{radar}; U_{10}) = 0.95. \quad (3.17)$$

The high frequency spectrum module consist of the three fits (3.15) ... (3.17) inserted in the parameterization (3.4).

### 3.3.3 Hindsight observations

On hindsight, a number of choices that we made to parameterize the measured wave data can be improved. We mention:

- the cross-over wave number between the long and short waves can be chosen somewhat higher. Because of the cut-off for small incidence angles in the model the high wave number range is limited by a minimum of about  $120 \text{ m}^{-1}$ . Increasing the cross-over wave number especially affects the slope distribution for low wind velocities (see figure 3.14, page 108).
- for low wind velocities the assumption that the saturation function is approximately constant in the wavenumber range of interest is not correct.
- a better approximation for the directional spectrum can be used. Also, for low wind velocities the directional spectrum is slightly wider than for high velocities.

However, in stead of improving these points it is better to implement more general wave models in next versions.

### 3.4 Comparison of measured radar data and VIERS-1 model results

In this chapter we test the quality of the first version of the VIERS-1 model by comparing its results with data measured in the Delft wind-wave flume campaign. This data set has been discussed extensively in [1]. To quantify the radar backscatter we use the parameter  $\gamma$ , the relative power  $\sigma^0$  normalized for the incidence angle  $\theta$ :  $\gamma = \sigma^0 / \cos(\theta)$ . We repeat that the first version of the model was designed for X-band radar.

In figure 3.19 (page 113) we compare the model radar backscatter as a function of the wind with measured data for a fixed incidence angle of  $45^\circ$  and an azimuth angle of  $0^\circ$  (upwind direction). In this plot the drawn curve denotes the model result for horizontal (HH) polarization and the dashed curve for vertical (VV) polarization. The '\*' symbols give the HH and 'o' the VV measurements. The comparison is not bad (for radar backscatter models): over the wind velocity range of  $U_{10}$  between 2 and 20 m/s the HH model curve shows a bias of -1.4 db with a variance of 1.7 db, and the VV curve has a bias of 2.3 db with a variance of 1.8 db. For wind velocities above 8 m/s the measured data vary less than the model results. Part of the biases can be explained with the calibration error for the backscatter measurements which is estimated at about 1 dB.

When the data is examined more closely, one can see that in the low wind speed range the backscatter increases much more rapidly with wind speed than the model prediction. For wind speeds above 10 m/s this situation reverses. As mentioned in chapter 2.1, at a windspeed of 10-11 m/s the waves start breaking in the flume. Obviously this breaking does have much more influence on the radar backscatter than the model predicts. Especially it shows a large influence in the difference between HH and VV backscatter which is

not predicted by the present model. This may have to do with the fact that for these windspeeds the 'Bragg' backscattering approximation is used outside its validity range.

When the model is used inverse, id est 'given a backscatter value and direction, estimate the wind speed', the average error for HH is  $\pm 1.4$  m/s and for VV  $\pm 2.7$  m/s. Above 10 m/s, the VV-model gives a bias larger than 3 m/s, which is more than the ERS-1 specification.

The dependence of the model on the incidence angle is shown in figure 3.20 (page 114). The wind velocity was fixed at a value of  $U_{10} = 10.6$  m/s and the radar was looking in the upwind direction. The lines and symbols are notated in the same way as in figure 3.19. Here we find that HH polarization curve has a bias of -0.5 db with a variance of 0.8 db and the VV curve has a bias of 2.6 db and a variance of 0.6 db. As can be seen, the dependence on the incidence angle is described rather well, except for the rather large offset for VV polarization. Part of this offset may be caused by calibration errors of the radar (estimated at about 1 dB) but the remaining bias cannot be explained this way.

Finally, in figure 3.21 (page 115) we show the azimuth dependence for a fixed wind velocity of  $U_{10} = 10.6$  m/s and an incidence angle of  $45^\circ$ . The HH curve has a bias of 0.3 db and a variance of 1.6 db, the VV curve a bias of 2.7 db and a variance of 1 db. The upwind/crosswind ratio is accurately estimated for VV polarization (difference only 0.2 dB) and a little less accurate though still quite good for HH (difference 0.8 dB). Part of the high variances can be attributed to the absence of a mechanism in the model that causes the downwind backscatter to be less than the upwind scatter. Such a mechanism should be implemented in a next version of the model.

### 3.5 Conclusions

The main conclusion we draw is that, despite its simplicity, the first version of the VIERS-1 model performs rather good. At least it shows that the two-scale approach works and provides a good basis on which we can build further. The comparison between model and measurements also shows some weak points of the model which need to be improved in later versions:

1. at wind speeds above 10 m/s the VV model cross section predictions are far too large.
2. the model exaggerates the difference between VV and HH polarized scatter (especially at high wind speeds). This is a well-known feature of the Bragg scatter model. To develop an improved scatter algorithm we intend to study test cases with more exact theoretical models as the Rayleigh method.

3. the model backscatter at small incidence angles highly depends on the choice of a cut-off parameter that shields a model singularity at zero incidence angle. The cut-off parameter is an undesired ad-hoc element in the theory. We intend to use the Holliday model as an alternative for small incidence angles and to analyze the singularity with the help of the Rayleigh method.
4. the difference between the upwind and downwind scatter should be explained through an upwind-downwind asymmetry in the waves. The wave data have been searched for such an asymmetry, but as yet nothing has been found.

The weak points mentioned above are caused by the backscatter module, since the wave modules consist of parameterized measured data. The wave modules will be tested separately.

## Chapter 4

# Experiment 'de Voorst'

### 4.1 Description

The "de Voorst" experiment is the second one in a series of three which started in the laboratory environment of the 8 m flume of Delft Hydraulics in Delft and will finish with the field experiment at Meetpost Noordwijk. This second experiment is already in an environment which in some ways, notably the size of the waves, resembles a field experiment.

The Delta tank at the "de Voorst" establishment of Delft Hydraulics, where the experiment took place fig.4.1 (page 117), is a unique facility. With its length of 240 meter and a water depth of 5 meter (or more) it is large enough to study waves with a length of up to about 10 meter without significant distortion due to bottom effects. This tank was available for the second VIERS-1 experiment, which was primarily aimed at studying the change in the radar return from the water surface with and without the presence of large waves. One of the basic drives behind the experiment was the present ubiquitous use of the so-called two-scale model for microwave scattering from the sea surface. In this model the microwave signal is considered to be due to scattering from small (cm) waves, which are modulated by the long waves (see 3.1.1 for a more extensive description). The Delta tank experiment gave a one-of-a-kind possibility to check the assumptions of this model and the deviations between the model and the reality.

Although the Delta tank has an advanced computer controlled hydraulic system for wave generation, it has no wind facility, whereas wind is essential for the experiment. The relation between the wind and the radar signal is, after all, what the VIERS-1 programme is all about. The VIERS-1 team therefore was faced with the problem of converting a wave tank into a wind-wave flume.

Initially attempts were made to board out the design and construction of the necessary hood and ventilation facility to a commercial firm. An important boundary condition in this respect was that the expenses had to remain within the financial limits, posed by the funding of the experiment. Almost all firms contacted considered the problem as outside their competence, mainly because of the required size of both the tunnel hood and the ventilation capacity. Only one firm was willing to consider the problem more seriously, but they too handed in the assignment after a few weeks.

The VIERS-1 team was therefore forced to find an in-house solution for the problem. The construction bureau of the KNMI Instrument Department (INSA) made a design for a temporary hood, based on requirements posed by the team, and found a firm that build it. The ventilators were rented from the Institute for Road transport of the Netherlands Organization for Applied Research (IW-TNO), which has a number of large wind machines, each with a maximum capacity of 100 m<sup>3</sup>/sec available. Two of these were mounted; together they could provide us with a wind speed of up to 10 m/s in our improvised tunnel.

The FM/CW X-band scatterometer of this experiment was the same one as used for the Delft experiment, but with a different set of antennae. This time separate antennae were used for transmission and reception, thus avoiding the use of an circulator. The antennae were mounted on a scaffolding tower outside the tunnel to obtain the required distance of about 30 m from the radar dishes to the water surface (the maximum distance with the dishes under an angle of 45° was 28 m). The mounting of the radar antennae outside the tunnel necessitated that part of its roof was transparent for microwave radiation.

The wind measuring equipment consisted of a pressure anemometer (PA, described in [1]) to determine the mean wind vector as well as the vertical momentum flux, a Dantec Flowmaster and a small cup anemometer. The cup anemometer was mounted in a fixed position and was only used to provide a reference velocity for all participants. The data of the Flowmaster were used as a check on the calibration of the PA.

Other meteorological parameters that were measured were air temperature and humidity, air pressure and water temperature.

Wave measurements were done with a wave wire of the same type as used in the Delft experiment (Lobemeier probe) and an optical system, operated by Heidelberg University and based on the reflection of light from the water surface.

The experiment proper, after the construction of the hood and the installation of the wind machines and the instrumentation, lasted from March 6 until March 30, 1989. During that time a total of 147 data runs were made by KNMI and about 100 by the other institutes. The difference is partly due to the shorter duration of the KNMI runs and partly to episodes with rain, during which the scatterometer could not function, due to the wetting of the radome. This restriction did not apply to the wave and wind measurements inside the

Wind speed (PA)	4 - 10 m/s
Wave height	0 - 1 m
Wave spectrum	monochromatic and JONSWAP type
Wave length (monochr.)	11 m
Air temperature	2.5 - 20 °C
Water temperature	7.8 - 9.2 °C
$T_{air} - T_{water}$	-6.2 - 12.2 °C
Distance PA - water	0.4 - 1.4 m
Scatterometer:	X-band FM/CW
Distance to water	28 m
Elevation	45°
Direction	upwind, downwind

Table 4.1: Instrumental and environmental conditions "de Voorst" experiment

tunnel. The total length of time during which measurements could be made was sufficient to perform at least a single measurement for all situations of the draft programme, but left room for only a restricted number of repetitions. This somewhat limited the possibility to repeat runs to improve the statistical steadiness of the results. Another factor in this respect was the range of air temperatures encountered ( $\approx 17$  °C), which created a large change of the atmospheric stability inside the tunnel (the water temperature hardly varied). In this way the number of situations covered was extended, but the number of measurements that could be considered as identical was reduced. The range of situations covered is presented in Table 4.1. The wind speed given is the one measured by the PA, which was always the instrument closest to the water. The distance from the PA to the water surface was varied for reasons that will be explained in chapter 4.4. The lowest distance of 40 cm was only possible when no mechanical waves were present. The item "wave height" in the table indicates only the mechanical waves.

## 4.2 Tunnel construction and wind machines.

The experiment is, as stated earlier, done in an environment which is more or less intermediate between a laboratory and a field situation. Such a situation does not require an air flow with the usual wind tunnel characteristics of strongly suppressed turbulence and large homogeneity. This enabled us to solve the technical problem of the wind tunnel construction in a relatively straightforward way by mounting wind machines at the (intended) downwind end of a tunnel that consisted of a straight cover with a rectangular cross section, fitted to the existing walls of the Delta tank.

The hood had a length of 150 m and covered the flume from a point 90 m "down wave" from the wave maker to the end of the tank, where it was fitted to the two wind machines. The height of the tunnel ceiling above the water surface was 3.4 m; the width of the Delta flume is 5 m. The cover consisted of plywood sections. Vertical sections were placed on the concrete walls of the Delta tank to link up with the walls in a continuous vertical plane. The vertical sections supported horizontal sections that spanned the tank. To prevent sagging the horizontal sections were supported on the outside by scaffolding material. The whole construction, which was sufficiently sturdy to carry two or three persons, was kept together with scaffolding materials, all mounted on the outside. Through this way of mounting the inside walls of the tunnel were kept sufficiently smooth to prevent adding an appreciable amount of turbulence to the eddies introduced at the inlet of the hood. At the inlet a grid was mounted, consisting of horizontal strips with a mutual distance of a few centimeters, to suppress large eddies in the incoming air. The grid left an opening of some 70 cm above the undisturbed water surface, to allow the free passage of waves with a wave height up to about 1 meter (crest to trough).

A section of the hood, spanning the width of the flume and with a length of 7.2 m was covered with polyurethane foam to provide a radar window. On both sides of this section the tunnel was fitted with a number of hatches through which instruments could be lowered. A special large opening was made to accommodate the optical wave measuring system of Heidelberg University.

The wind facility functioned as desired and wind speeds up to the design velocity of 10 m/s were obtained. The wind profile in the tunnel is described in annex D. During long runs the wind machines, which basically consist of a 160 kW (215 hP) truck motor connected to a fan and regulating equipment, became rather hot, which required a break to prevent their overheating. The machines had no automatic stabilisation, which required monitoring closely the wind speed in the tunnel and regulating the power accordingly. On one occasion a burn-out of an exhaust occurred, which, due to the efficient intervention of the manager of the machines, mr.Lameris of IW-TNO, caused a delay of only a few hours. Apart from this single event the machines functioned as desired, which was an essential contribution to the success of the experiment.

### 4.3 Microwave measurements

The measurement principle of a scatterometer is basically the same as that of a radar, the differences consists in the way in which the information is collected. In 'Delft' and in 'de Voorst' experiments the microwave measurements were performed with a FM/CW X-band scatterometer. For the Delft tank experiment we used one antenna for both transmitter and receiver, whereas in the Delta tank experiment separate transmitting and receiving antenna's were used. In both experiments the resultant -3dB two- way illuminated area

was  $0.6 \times 0.6 \text{ m}^2$ .

In the FM-CW system the transmitter is swept periodically over a frequency band  $B$ . With a distance  $d$  between the radar and the target the received signal will be a replica of the transmitted signal delayed by the time  $t$  (fig. 4.2, page 118), with  $t$  equal to  $2d/c$  and  $c$  the speed of light in m/s. In the receiver the instantaneous frequency difference between the two signals is generated, and from this so-called beat frequency  $f_b$  (fig. 4.3, page 118) the distance can be calculated since

$$f_b = \frac{t}{T} B = \frac{2d}{cT} B \quad (4.1)$$

or

$$d = \frac{cT}{2B} f_b \quad (4.2)$$

The distance resolution is therefore directly related to the accuracy  $\Delta f_b$  in the beat frequency. For the isolated target case this accuracy follows from the consideration that only the time  $T$  is available to measure  $f_b$  and therefore  $\Delta f_b = 1/T$  (fig. 4.4, page 119) and

$$\Delta d = \frac{cT}{2B} \Delta f_b = \frac{c}{(2B)} \quad (4.3)$$

The minimum distance to be measured by the FM-CW system will be zero, corresponding to a zero beat frequency. Similarly the maximum distance corresponds to the maximum beat frequency  $B$ , hence

$$d_{max} = \frac{cT}{2} \quad (4.4)$$

When measuring microwave backscatter from a distributed instead of an isolated target the single beat frequency will be replaced by the beat spectrum.

A simplified block diagram of the VIERS-scatterometer is presented in figure 4.5 (page 120). Some characteristics of this system are listed in table 4.2.

The design of this scatterometer is based on the use of two identical microwave oscillators with frequencies  $F$  and  $F \pm 60 \text{ MHz}$ ; the frequency  $F$  is swept over the range  $9.6 - 9.9 \text{ GHz}$  in case of HH polarization, while for the VV polarization the frequency is swept over the range  $9.3 - 9.6 \text{ GHz}$  in connection with differences in optimum frequencies of the feed.

Radar type	FM-CW
Frequency	9.6 GHz
Modulation	triangular, 300 MHz sweep
Polarization	HH or VV
Range resolution	0.5 m
Antenna	1.1 meter parabolic dish
Azimuth angle	0° or 180° Delta experiment
Angle of incidence	45° Delta experiment

Table 4.2: Specifications of the X-band FM/CW scatterometer

The first oscillator delivers the transmitted signal and the reference signal. By means of the second oscillator and two mixers both the received signal and the reference signal are converted to a constant intermediate frequency of 60 MHz. The frequency difference between the two oscillators is kept constant by an automatic frequency control system. To eliminate amplitude variations of the reference signal both 60 MHz-channels are provided with an automatic gain control. Finally the beat signal is found at the output of a third mixer. All control functions e.g. the choice of polarization states and the choice of an attenuator setting to bring the received signals into the dynamic range of the receiver, are performed by a PC which also handled the digital chirp generation, the data acquisition and the synchronization with other equipment.

#### 4.3.1 The acquisition software and measurement procedure.

For the "de Voorst" measurements an acquisition software package was developed which differed in several ways from the software used for the "Delft" experiment. The main difference is that in "de Voorst" continuous sampling of the scatterometer beat signal was used. The second important difference is that the digitization rate and trigger were controlled by the radar. Continuous sampling is now necessary to avoid range/doppler ambiguities in the FM/CW radar signal.

The beat signal of the scatterometer was connected to a PC-based DT2801a analog to digital conversion board. As mentioned above the sampling trigger of the board was controlled by the internal scatterometer clock, which also steered the triangular RF-modulation signal. This is a major difference with the setup used in the Delft experiment. It could be used now because of the implementation of a digitally generated RF-modulation steering signal in the scatterometer. The advantage of this method is, that a perfect synchronization can be established between the digitized signal and the phase of the RF modulation. This greatly simplifies further data processing. 256 Times per flank of the triangular RF-

modulation, the DT2801a was triggered to sample the scatterometer beat signal. With a 10 ms duration of a single flank, the sample rate becomes 25600 Hz. A 12 bit (2 byte) sampling was performed resulting in a continuous data stream of 51.2 kbyte/s. This data stream was sent to a 64 kbyte buffer in PC-RAM by Direct Memory Access. Once 32 kByte of this buffer was filled (after .6 seconds) the program started transferring the lower part of the buffer to a 27.4 MByte partition on the Winchester hard disk. Meanwhile the second part of the buffer is being filled. Care was taken that hard disk and DMA always operated on separate parts of the buffer. This way continuous measurement could be maintained until the hard disk was full, which occurred after approximately 9 minutes.

The acquisition software consisted of two programmes, both written in PASCAL (Borland Turbo Pascal version 3.0). The first programme, called "hdrmod.pas" was used to examine the beat signal and set the gain and polarization of the scatterometer. Furthermore a header file was configured in which information on the measurement conditions and measurement parameters was saved. The main acquisition programme "acqui.pas" was run after "hdrmod.pas" and performed the acquisition for a user determined amount of time. Just before and after the measurement, the scatterometer quartz-clock was read-out. After the measurement the start and end time of the measurement were added to the header file. Both, header file and data file were then transferred to magnetic tape, the back-up medium.

The beat signal of the scatterometer in the "de Voorst" configuration is a signal with a maximum frequency of approximately 10 kHz, so it lies in the audio range. This signal was also recorded on a commercial Sony Digital Audio Tape recorder (DAT). The second channel of the DAT recorder was used to record the triangular modulation of the scatterometer. Synchronization between the DAT signal and the phase of the RF-modulation can thus still be obtained. Because the DAT digitizes the data in 16 bit before storage on magnetic tape, it is an ideal low-cost backup device. Timeseries of 30 minutes were recorded for the measurements and 5 minute series for the calibration measurements. Therefore we have more DAT data than directly digitized data. If necessary, longer digital timeseries can be generated via digitization of the DAT recordings. Since the Sony DAT recorder does not have a digital output this digitization will have to be performed again with the DT2810a. Software to do so has been developed.

At some stages during the acquisition process errors did occur. Sometimes the DMA process, used by the DT2801a card was interrupted for unknown reasons. This caused a hang-up of the PC. These mysterious DMA errors occurred 9 times (run nrs: 440,441, 464, 469, 475, 476, 480, 481 and 487). In two cases (440 and 441) the digital data was lost and we have to rely on the digitization of the back-up on Digital Audio Tape-unit (DAT). Of the other measurements with DMA errors the exact start and stop times are unknown. This means that no synchronization with the wave measurements can be established. Other errors which occurred too often had to do with the back-up process from hard disk to magnetic tape and were caused by unreliable tape streamers. Although this took us a lot of our time and caused much irritation, no data loss resulted. For the future campaigns we

$u_*$ (m/s)	Single waves wave height ( $cm_{pp}$ )				Irregular waves appr. JONSWAP spectrum		
	0	30	60	100	code A	code B	code C
0		U					
$\approx .15$	U	U	U/D	U			U/D
$\approx .33$	U	U	U/D	U/D	U/D		
$\approx .41$	U	U	U/D	U		U/D	U/D

Table 4.3: Conditions radar measurementw, U : upwind measurement with scatterometer, D : downwind measurement, incidence angle : 45 degrees

will make use of hopefully more reliable optical disks. After the measurement campaign, all data have been backed up on optical disk and on the VAX system at the TU Delft.

At the beginning of each measurement day and after finishing the last measurement of that day, the scatterometer was calibrated. For this calibration a Luneberg lens with a radar cross section of  $10 \text{ m}^2$  was placed on top of the radar window in the tunnel roof in the overlapping region of transmission and receive antenna, at the point of maximum attenuation. The received signals were recorded for approximately 1-3 minutes. Due to small movements of the scaffolding tower the radar antennas variations in the received calibration signal could occur. These variations were of course very dependent on the outside wind speed and direction. In the further processing, the maximum of the recorded calibration signal from the Luneberg lens has been used, as this point corresponds to the measurement at the maximum overlap. A correction has been applied for the difference in range between the calibration spot (tunnel roof) and the water surface. The correction factor was determined after the measurement campaign by a double calibration at the tunnel roof distance as well as at the water surface.

Measurement of the microwave backscatter was synchronized with the measurement of wind speed and waves by KNMI by starting the data acquisition simultaneous which was realized using "acoustical synchronization" for the count-down to start. Wave slope recordings on the U-matic video recorder were mixed with a video signal showing the scatterometer quartz-clock. With this clock a synchronization of about 20 ms can be obtained. The other wave measurements were not precisely synchronized and can only be compared statistically to the microwave measurements. Microwave backscattered signals were recorded under a variety of circumstances. Table 4.3 gives an overview over the measurement conditions during the data take of the scatterometer.

## 4.4 Meteo measurements

The following meteorological instruments were used during the experiment:

### 4.4.1 Pressure anemometer.

This wind meter, developed at KNMI, was also used in the Delft experiment. It is a fast responding instrument (3 dB down at about 30 Hz) that measures the three dimensional wind vector. It was used to measure both the mean wind and its fluctuations in three directions (horizontally along wind, horizontally cross wind and vertical). From the wind speed fluctuations the so-called friction velocity, indicated as  $u_*$ , and a number of other quantities, to be discussed under 5.2., can be derived. The supposition is that the radar signal is more strongly correlated with  $u_*$  than with the mean wind speed  $U$ .

An important characteristic of the PA for the "de Voorst" experiment is its small sensor volume. This allows us to make measurements low above the water surface (down to about 25 cm) without losing significant parts of the frequency spectrum. Although the PA has been designed to survive being hit by an occasional wave, we nevertheless had to mount it higher than the level of the wave crests, as its recuperation time is longer than the period of the long waves. With waves of 1 meter height the distance from the instrument to the undisturbed water surface therefore was at least 60 cm. Measurements were furthermore repeated a number of times with the PA at several levels, for reasons to be explained under 5.2.

### 4.4.2 Cup anemometer

A cup anemometer is a simple instrument with a stable calibration and easy to mount, to use and to register. We put these properties to our advantage by mounting a small cup anemometer at a fixed place near the ceiling of the tunnel to serve as a relative reference instrument. The position of the anemometer was such that its readings didn't give e.g. the mean wind speed in the tunnel, but it gave important on line information about fluctuations of the wind speed during and between runs.

### 4.4.3 Dantec Flowmaster.

This commercial 1-dimensional wind meter was mounted as a possible alternative for the determination of  $u_*$ . Like the PA it was mounted on a movable support to be able to vary the distance between the instrument and the mean water surface.

#### 4.4.4 Temperature and humidity.

The temperature of the air, the water temperature and the atmospheric humidity within the flume were measured. The most important quantity derived from these data was the atmospheric stability. For air temperature and humidity we used a Hygromer sensor; the water temperature was measured with a Pt500 platinum resistance system, designed by KNMI.

#### 4.4.5 Registration system

The meteorological measurements were registered on a new data-acquisition system, that replaced the one used during the Delft experiment. The most important difference is the registration medium: in the new system data are stored on optical disks, which greatly improves both the reliability of the system and the accessibility of the data. The new system also has a greater capacity: it is now possible to register continuously 64 channels with a sampling frequency of 60 Hz/channel. For short times ("events") registration frequencies up to 125 kHz/channel are even possible. A very convenient software feature, developed at KNMI, is the automatic presentation on a PC of a spreadsheet form, immediately after a run has been started. In this form, which is coupled to the data by the automatically generated run number, a number of items (date, start time, end time etc.) are produced by the system, whereas other quantities (e.g. positions and manually selected scales of instruments, run numbers used by the other participants) and remarks can be entered manually. The data of this form are saved in a separate file which made available an overview of all runs of the experiment immediately after it had been finished.

## Chapter 5

# Processing and first results “de Voorst”

### 5.1 Microwave measurements

The processing of the scatterometer data of the ‘de Voorst’ experiment was done in the same way as for the ‘Delft’ experiment but for the subtraction of spurious signals, which was not necessary for this case. The combined antenna pattern of the transmit and receive antennae was measured at the measuring distance during the experiment using a separate receiver. The external calibration measurements were used to derive daily updated calibration factors. The resultant data consists of time series of the scatterdata at the radar footprint in combination with average spectra and average  $\sigma^{\circ}$  values. The ‘de Voorst’ microwave backscatter measurements were all performed with the scatterometer antennae pointing in either the upwind or downwind direction, always with an incidence angle of  $45^{\circ}$ .

Figure 5.1 (page 122) shows a time series of the microwave backscatter at HH polarization, with the radar looking in the upwind direction. The measured wind speed is 7 m/s, and there is a mechanically generated wave with a wavelength of 11 m and a height of  $1m_p$ . The modulation of the backscattered signal due to the underlying wave can clearly be seen. The largest backscattered signals are measured near the point where the wave slope is zero (near the top of the waves).

In figure 5.2 (page 123) and 5.3 (page 124) two more time series are shown of the microwave backscatter. These runs were made under identical conditions with respectively VV and HH polarization. The conditions are the same as for fig. 5.1, but for the wave height which was 0.30 m. The higher response for VV polarization and the higher sensitivity for

the wave modulation in the HH polarization case can clearly be seen.

### 5.1.1 Microwave data processing and first results.

Standard processing consisted of Fourier transforming each sequence of 256 2-byte samples per flank of the triangular RF-modulation of the FM-CW scatterometer. This resulted in one frequency spectrum per 10 ms of data, in which the frequency is proportional to the range with a proportionality constant 1 m/200 Hz. The spectra were then multiplied with their complex conjugate and calibrated. The 7 frequency (range) bins containing the backscattered power of the water surface were linearly averaged. This value was then written to a Direct Access Binary file in real\*4 format. A data reduction of a factor 128 with respect to the original data file was obtained. The result of this processing is a timeseries of radar backscatter values with a time resolution of 10 ms, and a duration of 532 seconds in most cases. An example of part of such a timeseries is shown in figure 5.4 (page 125). It was recorded with a friction velocity  $u_* = .33$  m/s, a long wave frequency of .375 Hz and a height of .6 meter. The modulation of the backscatter by the long wave (slope) can be seen beautifully. Plots like figure 5.4 were generated for all recorded signals. They served as a primary quality control on the data.

When all frequency spectra of the flanks are averaged, we get a spectrum describing the mean microwave backscatter as a function of range (frequency). Figure 5.5 (page 125) is an example of such a spectrum. The scattering from the water surface occurs around 6900 Hz (34.5 meter). Above and below this frequency (range) other reflections can be seen. The lower peak is believed to be caused by the reflection from the radome, the higher one is probably a secondary reflection from the tunnel roof, via the water surface. This second reflection is under some conditions larger than the primary reflection from the water surface. Although they are separated in frequency, care has to be taken when the difference in magnitude becomes too large. Spectral leakage from this spurious peak to the frequencies containing the watersurface reflections might then dominate the water reflection. To monitor this difference, the reflection of the secondary peak was sometimes also processed and recorded along with the timeseries of the direct water reflections.

Table 5.1 lists the measurement number and the averaged microwave backscatter for the cases analysed so far, with a monochromatic generated wave of  $f = .375$  Hz and amplitudes and wind speeds as indicated. The first number refers to the VIERS reference numbering. A number of measurements could not be analysed by the standard procedure, either, because a new digitization of DAT backup recordings will have to be made, or because the original header file was corrupted due to the DMA errors during the acquisition as mentioned above.

As was to be expected,  $\overline{\sigma^0}$  is larger for VV than for HH polarization under similar circumstances. Furthermore it increases with increasing wind speed. With low mechanically

$u_*$ (m/s)	pol	Upwind looking radar							
		no wave		.30 meter		.6 meter		1.0 meter	
		no.	$\overline{\sigma^0}$	no.	$\overline{\sigma^0}$	no.	$\overline{\sigma^0}$	no.	$\overline{\sigma^0}$
0	HH			421	-37.8				
0	VV			420	-37.5				
$\approx .15$	HH	433	-31.48	438	-30.39	424	-29.13	458	-25.08
	VV	434	-27.26	441		422	-25.25	467	
$\approx .33$	HH	432	-25.37	443	-26.39	425	-25.91	460	-23.16
	VV	471	-	444	-21.12	426	-20.53	464	
$\approx .41$	HH	435	-22.98	440		427	-22.35	459	-19.75
	VV	470	-18.40	442	-18.11	423	-17.83	469	-16.72

Table 5.1: Overview 9 minute averaged  $\overline{\sigma^0}$ 

generated waves (wave height .30 m) the backscatter is sometimes lower (432) and sometimes larger (438, 442) than without. The changes are very small and hardly significant especially because of the uncertainty introduced by the extrapolation procedure that was needed to calculate the friction velocity at the water surface (see 5.2). For the higher waves, .6 meter and 1 meter height, the average backscatter is generally larger than for the wind only cases.

The timeseries of the radar backscatter served as input for many post-processing data analysis programs. In the next few paragraphs a number of these application programs will be described.

### Power spectral density functions

Movement of the watersurface causes a constant re-orientation of the scatterers and therefore a time dependence of the normalized backscattered power  $\sigma^0(t)$ , see also fig. 5.4. Studying the spectral distribution of  $\sigma^0$  provides information on the timescales of these re-orientations and the resulting decorrelation of the microwave backscatter.

Power spectral density estimates were obtained of  $\sigma^0$  as follows. Timeseries of  $\sigma^0(t)$  obtained as described in paragraph 5.1 were split into 25 blocks of each 2048 samples (20.48 seconds). Each block was detrended (subtraction of any linear trend), multiplied with a Hanning window, Fourier transformed and multiplied with the complex conjugate of the Fourier transform. The resulting spectra of all 25 blocks were then averaged to obtain a more accurate estimate of the power spectral density of  $\sigma^0$ . The frequency resolution in the spectra was 48.8 mHz with a maximum frequency of 50 Hz. The spectra are calibrated

in such a way, that:

$$\text{total variance} = \sum_{i=1}^{1024} PSD(f_i). \quad (5.1)$$

Figure 5.6 (page 126) shows one such spectrum of VIERS measurement 425. It was recorded with HH polarization at  $45^\circ$  incidence angle, upwind directed. The friction velocity  $u_*$  was 0.33 m/s, the dominant wave was 11.05 meter long (0.375 Hz) with a height of 0.6 m. The spectrum has been plotted on a double logarithmic format to show the full dynamic range.

*De Loor* [13] in a first inventarisation of this type of spectrum distinguished 2 regions: region "A" around the frequency of the dominant wave and region "B", also called the plateau region. Both regions are indicated in fig. 5.6. The sensitivity of the microwave backscatter to the long wave modulation of the surface can clearly be seen at  $f = .375$  Hz. This modulation effect will be dealt with in more detail in paragraph 5.4.

The drop-off spectral density beyond 30 Hz indicates that the surface components causing the backscatter remain correlated for at most  $\approx 30$  ms under these environmental and instrumental conditions.

Figure 5.7 (page 127) shows power spectra for three different wind speeds ( $u_* = .155, .33$  and  $.41$  m/s), HH polarization, upwind,  $45^\circ$  incidence angle, wave: monochromatic,  $f = .375$  Hz, height = .6 m. The spectral shape of the middle and high windspeed are -apart from the spectral level- very similar. The low wind speed spectrum shows a slightly higher sensitivity to the harmonics of the dominant wave and it shows a lower cut-off frequency indicating a longer decorrelation time.

Figure 5.8 (page 128) shows 4 PSD's for the same scatterometer parameters as fig. 5.7, and a friction velocity of  $u_* \approx 0.33$  m/s and four different wave heights (0.0, 0.3, 0.6 and 1.0 m.) with a fixed wavelength of 11.05 m. (.375 Hz). The increasing modulation of the dominant wave with wave height can clearly be seen at  $f = .375$  Hz. The high frequency tails of the three lower wave heights show a large similarity. For some unknown reason in the case of the highest wave the tail is around 4-6 dB higher than the other cases.

Finally, figure 5.9 (page 129) shows the dependence of the power spectral density on the polarization for a measurement with  $u_* = .33$  m/s and a generated wave with a length of 11.05 m and a height of .3 m. Especially in the medium (1-10 Hz) and high ( $> 10$  Hz) frequency ranges there are clear differences between both polarizations. The amount of energy in the medium range is much less for HH than for VV polarization. The VV spectrum tends to fall off at lower frequency than HH, indicating a shorter decorrelation time for VV, which is in agreement with the observations of *de Loor* [13].

### Autocorrelation functions of the microwave backscatter

As is well known, the power spectral density and the autocorrelation functions are Fourier pairs:

$$\text{autocorrelation} \xrightarrow{\text{inverse Fourier}} \text{PSD} \quad (5.2)$$

So the autocorrelation function can easily be determined from the PSD by applying an Fourier transform and proper normalization. The autocorrelation approach is the more convenient for the determination of the fast decorrelation time of the microwave backscatter.

Figure 5.10 (page 130) shows the autocorrelation function of the VV polarized signal from figure 5.9. Along with *de Loor* [1984] we now distinguish three regions:

- I a region of fast decorrelation, associated with the relatively fast reorientation of the principle scatterers, the Bragg waves.
- II a "plateau" region which can possibly be attributed to facets on the long wave slope.
- III a region associated with long wave slopes.

De Loor in his report distinguishes two different decorrelation times:

1. the short time  $t_1$ , which he determined by fitting a line through region I and taking the time at a correlation level of 0.5.
2. an intermediate time  $t_2$  which is the time where the decorrelation function has decreased to half the value of the plateau region II.

In this report we will determine only the fast decorrelation time for the cases with a monochromatic dominant wave. The reason for this is, that the second time  $t_2$  is already heavily influenced by the long wave. The scales of region II and III are insufficiently separated.

Figure 5.11 (page 131) shows the autocorrelation function for varying wind speed, fig. 5.12 (page 132) for varying wave height and fig. 5.13 (page 133) for different polarizations. Table 5.2 lists the decorrelation times  $t_1$  for the measurements processed so far. One can observe almost no effect of the short decorrelation time by long wave height, a slight decrease of  $t_1$  with increasing wind speed and a strong polarization dependence.

Furthermore -in agreement with the analysis of in situ measurements by *de Loor*- the correlation level in the "plateau region II" is much lower for VV than for HH polarized signals.

$u_*$ (m/s)	pol	Upwind looking radar							
		no wave		.30 meter		.6 meter		1.0 meter	
		no.	$t_1$	no.	$t_1$	no.	$t_1$	no.	$t_1$
0	HH			421					
0	VV			420					
$\approx .15$	HH	433	62	438		424	100	458	
	VV	434	32	441		422		467	
$\approx .33$	HH	432	43	443	40	425	45	460	50
	VV	471		444		426	32	464	
$\approx .41$	HH	435	30	440		427	42	459	
	VV	470		442		423		469	

Table 5.2: Overview of the short decorrelation time  $t_1$ 

The overall comparison of the autocorrelation functions with de Loo's in situ measurements shows remarkably similar qualitative behaviour. The decorrelation times however, are much longer than the in situ values (7 and 9 ms for respectively VV and HH polarization). A possible explanation for this might be, that under the moderate circumstances in the "de Voorst" flume, the lack of wave breaking causes the surface to remain much longer "intact" and thus correlated.

In the future more measurements than the presently described subset will be analysed. Simulations of simplified surface models will be used to analyse the autocorrelation function.

## 5.2 Meteo data

KNMI obtained a total of 147 runs, most of them of 10 minutes each.

The new data system proved to be a great asset. Not only was there no loss of data, but the relevant quantities of all runs had been converted to useful physical values within a few days after the treatment of the data was started, due to their improved accessibility.

As stated earlier, the basic atmospheric quantity we needed is the friction velocity  $u_*$ , defined by

$$u_*^2 = - \langle u'w' \rangle \quad (5.3)$$

where  $u'$  and  $w'$  are the instantaneous values of the fluctuations in, respectively, the horizontal along wind and vertical wind speed.  $u'$  is defined as

$$u' = u - U \quad (5.4)$$

in which  $u$  is the instantaneous and  $U$  the mean value of the wind speed in the horizontal along wind direction.  $w'$  is defined in the same way for the vertical wind and the brackets indicate a mean value, which, in our case is the time average over a ten minute run.  $\langle u'w' \rangle$  is the value of the vertical momentum transport in a turbulent flow. For more details see [1], chapter 3.1.2.

The conversion of the measured data, however, did not provide us with the  $u_*$  values needed, because of the complexities introduced by the relatively large distance between the water surface and the wind meter.

In a wave flume the momentum of the flow is not only transported to the water, but also lost to the walls. This manifests itself in a variation of  $u_*$  (or  $\langle u'w' \rangle$ ) with the distance to the water surface. The quantity we need is the value of  $u_*$  at the water surface, so we had to develop a method to extrapolate the measured values of  $u_*$  at the position of the PA sensor head to the water surface. Our basic assumption for this extrapolation is a linear relation between the momentum flux and the distance to the water surface (or the ceiling of the flume). This assumption is based on both experimental and theoretical considerations and confirmed by the final results. A detailed description of our method is presented in Annex D.

The first step in the calculations is to determine the wind profile, the relation between the mean wind speed and the distance to the water surface. With the characteristic parameters derived for the wind profile the momentum flux at the water surface can be calculated. The  $u_*$  values at the water surface which we calculated in this way were both internally consistent and in the expected range, which further improved our confidence in the method. The final results for the whole experiment are presented in table 6.4.

## 5.3 Discussion

### 5.3.1 Modulation of the microwave backscatter by the long waves

The primary objective of the 'de Voorst' experiment was to investigate the modulation of the microwave backscatter signal by the long, gravity wave, especially the modulation by the long wave slope (tilt modulation) and the hydrodynamic modulation.

An analysis has been made on the modulation of the microwave backscatter by the long mechanically generated waves. Wave slope signals were measured by means of the Reflective Slope Gauge at approximately the same footprint as the microwave measurements. A time synchronization of 40 ms was achieved between both types of measurements. A correction has been applied for the small (25 cm) misalignment of the footprint of the LSG and the center of the scatterometer footprint.

Sixteen lines out of each RSG image, positioned in the center approximately along the line of movement of the reflected light spot, have been digitized. After averaging over four images, a Gauss curve was fitted to the resulting slope distribution. The mean and standard deviation of this distribution are a measure of the long wave slope and small waves mean square slope. Timeseries of 5:46 minutes were obtained with a sampling frequency of 6.25 Hz. The slope data are accurate enough to extract the frequency and phase of the long wave slope, but care is needed in the interpretation of the signal strength because of many non-linear imaging distortions have not been taken care of. Since the analysis presented here concerns only regular waves, the frequency and phase of the long wave suffice.

Processing of the scatterometer signals as described in par. 4.1 resulted in time series of the microwave backscatter from the water surface with a resolution of 10 ms and a duration of 8:52 minutes per measurement. In order to reduce the amount of data and to facilitate further processing the radar data was re-sampled at a frequency of 6.25 Hz, i.e. the same frequency as the RSG. At this frequency (6.25 Hz) about 16-17 individual measurements of the radar backscatter were obtained over each long wave, which means a phase accuracy of around 20 degrees. This is of the same order as the phase uncertainty introduced by the radar footprint size (around 1 meter). Signals of around 200 long waves were recorded for each measurement.

Frequency and phase of the long wave were estimated from the RSG timeseries by means of a Fourier transform on the RSG timeseries. The frequency of the regular long wave was  $f_{max} = 0.375 \text{ Hz}$ , which corresponds to a long wave wavelength (deep water dispersion relation) of 11.08 meter. The phase of the long wave slope was estimated using

$$phase(f_{max}) = \arctan2(\text{imaginary part}/\text{real part})_{f=f_{max}} \quad (5.5)$$

Comparison of the measured slope signals with simulated signals based on the estimated frequency and phase, showed that the frequency and phase were accurate enough to use for comparison with the radar signal.

The phase of the long wave could now be evaluated for each individual backscatter measurement. Figure 5.15-5.19 (page 135-139) show backscatter distributions in 10 degree bins. Table 5.3 lists the measurement conditions. The abscissa of the plots is the phase of the long wave. The trough of the long wave is at ninety degrees; 180 degrees corresponds to the 'up-going' zero crossing of the wave (see fig. 5.14, page 134). As was to be expected,

Fig.	$u_*$ m/s	Long wave height (m)	Polarization HH/VV	'look' direction Up/Down	Viers no.
1	.355	1.0	HH	Up	460
2	.32	0.6	HH	Up	425
3	.34	0.6	VV	Up	426
4	.30	0.30	HH	Up	443
5	.30	0.30	VV	Up	444

Table 5.3: Backscatter modulation measurements analysed so far.

the radar backscatter is lowest around 0-90 degrees, i.e. between the trough and the down-going zero crossing of the wave. Maxima are found between the up-going zero-crossing (180 degrees, minimal local incidence angle) and the crest.

### 5.3.2 Comparison with models.

A preliminary comparison has been made with the tilt modulation model and the model for hydrodynamic modulation as described by *Alpers* [11].

For the simple 1-dimensional configuration in the "Delta" tank, one can easily write down the equations for the Bragg scattering cross section, for HH polarization:

$$\sigma^{oHH}(\theta, \psi, \lambda) = 4\pi k_{bragg}^4 \cos^4(\theta + \psi) g_{\perp}^2(\theta + \psi) \times E_0(k_{bragg}) \quad (5.6)$$

and for VV polarization;

$$\sigma^{oVV}(\theta, \psi, \lambda) = 4\pi k_{bragg}^4 \cos^4(\theta + \psi) g_{\parallel}^2(\theta, \psi) \times E_0(k_{bragg}) \quad (5.7)$$

with:

$$k_{Bragg}(\theta, \psi, \lambda) = \frac{4 * \pi i}{\lambda_{e.m.}} \sin(\theta + \psi) \quad (5.8)$$

$$g_{\perp}(\theta, \psi) = \frac{\epsilon - 1}{[\cos(\theta + \psi) + (\epsilon - \sin^2(\theta + \psi))^{1/2}]^2} \quad (5.9)$$

and:

$$g_{||}(\theta, \psi) = \frac{(\epsilon - 1)[\epsilon(1 + \sin^2(\theta + \psi)) - \sin^2(\theta + \psi)]}{[\epsilon \cos(\theta + \psi) + (\epsilon - \sin^2(\theta + \psi))^{1/2}]^2} \quad (5.10)$$

$\theta$  = the incidence angle (45 degrees)

$\psi$  = the tilt angle of the long wave.

$E_0$  = the energy density spectrum of the short waves.

$\epsilon$  = dielectric constant of water (48-35i at X-band).

Figure 5.15-5.19 show the results of the calculation of the tilt modulation (5.6)+(5.7) as the dashed lines. A wavenumber spectrum proportional to  $k^{-4}$  has been assumed. A correction has been made for the varying footprint size due to the tilting of the long waves. This is why the tilt modulation is not exactly symmetric around 180 degrees. The model curves were fitted to the measured data around a phase angle of 180 degrees.

Besides tilt modulation, also a comparison with a model for the hydrodynamic modulation has been carried out. The model used was developed by *Alpers and Hasselmann* [12]. The modulation is described by a complex modulation transfer function  $R^{hydro}(\omega)$ , which describes the modulation of the backscatter as:

$$\sigma = \sigma^0 [1 + |R^{hydro}| A \cos(k_{l.w.} x - \omega_{l.w.} t + \delta)] \quad (5.11)$$

where  $\sigma^0$  is the mean radar cross section, A is the long wave amplitude,  $\omega_{l.w.}$ ,  $k_{l.w.}$  are respectively the long wave frequency and wavenumber, and  $\delta$  is the phase angle of the modulation transfer function.

For a short wave spectrum  $E_0 \propto k^{-4}$  the hydrodynamic modulation can be written as:

$$R^{hydr} = -4.5k\omega \frac{\omega - i\mu}{\omega^2 + \mu^2} \quad (5.12)$$

$\mu^{-1}$  has the dimension of time and is called the 'relaxation time constant'. However, as Alpers mentions in his paper, it is not really a constant, but probably some -unknown- function of the windspeed. For  $\mu=0$ , the maximum of this hydro-dynamic modulation occurs at the crest of the wave, for  $\mu \neq 0$  a phase shift occurs towards the up-going zero crossing. Figure 5.20 (page 140) shows the modulation of the cross section in dB with respect to the mean as a function of the phase angle of the long wave for 4 different values of the relaxation parameter  $\mu$  and for a single long wave with frequency 0.375 Hz and an height of 50 cm. One can see that for larger values of  $\mu$ , the modulation decreases and the maximum backscatter shifts from 270 degrees (crest) toward 200 degrees.

Fig.	Wind speed m/s	Long wave height ( $m_{pp}$ )	Polarization HH/VV	modulation dB	max angle	min angle
1	.355	1.0	HH	20	220	15
2	.32	0.6	HH	12.5	245	15
3	.34	0.6	VV	5	215	0
4	.30	0.30	HH	6.25	175	30
5	.30	0.30	VV	3	185	65

Table 5.4: Backscatter modulation depth and phase.

The total modulation (tilt and hydrodynamic) has been calculated for two cases with  $\mu=0$  and  $\mu = 0.5$ . The curves are plotted in figure 5.15-5.19 as the dotted ( $\mu = 0$ ) and dash-dot ( $\mu = 0.5$ ) lines. This simple model for the hydrodynamic modulation is only applicable for smooth water surfaces, where nonlinear effects like wave breaking have a minor influence. Effects of the waves on the wind and vice versa are *not* taken into account.

### 5.3.3 Conclusion

All data show a large dependence on the phase angle as was to be expected. Maximum backscatter can be found somewhere between the upgoing zero crossing (180 degrees) and the crest, the minimum is located somewhere between 0 degrees and the trough. It is interesting to see the minimum shift from 0 degrees in fig. 5.15 (HH, 1.0 meter wave) to 70 degrees in fig. 5.19 (VV, .30 meter wave), which means the minimum shifts more with decreasing tilt modulation, probably under influence of hydrodynamic modulation.

The magnitude of the modulation is much larger for HH polarizatoin than for VV polarization, as could be expected on basis of the tilt modulation. To give an indication, table 5.4 lists the approximated modulation and the phase angles for the maximum and the minimum.

The 'tilt' modulation model gives a good qualitative and quantitative description of the modulation especially for the HH polarized signals at phase angles between 0 and 180 degrees (fig. 5.15,5.16,5.18). It has been assumed that the short wave spectrum falls off as  $k^{-4}$ . A different coefficient has some influence on the amount of tilt modulation but the best fit was obtained with a coefficient of -4.

Above 180 degrees the HH data is generally underestimated by the tilt model, indicating that other types of modulation (e.g. hydrodynamic modulation) are of importance there.

At VV polarization (fig. 5.17,5.19), the tilt modulation is much smaller than for HH polarization, therefore the effects of hydrodynamic modulation become more visible as the hydrodynamic modulation is polarization independent. The tilt modulation model alone now underestimates the total modulation in the microwave backscatter. Inclusion of hydrodynamic modulation does give some improvement, especially for the small amplitude case (fig. 5.19).

For HH-polarized signals, the hydrodynamic modulation as calculated by Alpers' model does not quantitatively agree with the increased backscatter between the 'upward going' zero crossing and the crest of the long wave (see fig 5.15,5.16). Of even more importance is a strange phenomenon in fig. 5.15: the modulation of the microwave backscatter becomes larger than the backscatter itself, causing negative received powers! Obviously for these steep waves the model is used outside its validity range.

The effect of the shift of the minimum backscatter toward 70 degrees is qualitatively predicted by the combined tilt/hydrodynamic model. For the small wave VV-polarized measurement (fig.5.19) even quite good quantitative agreement is reached.

More single wave data will have to be analysed before any conclusions can be drawn on the value of these models. The simple tilt modulation describes the magnitude of the total modulation of the radar backscatter rather well, but especially around the crest sometimes more backscatter is measured than can be explained by tilting alone. The tilt+hydrodynamic model does give qualitative improvement, but cannot explain all modulation, especially at HH-polarization around the crest.

It should be mentioned here that effects of the wind on the waves and vice versa are *not* implemented in the hydrodynamic modulation model. Some of these wind-wave interaction effects have been noticed in the KNMI pressure anemometer data. Therefore further study on this interaction is needed.

## Chapter 6

# Concluding remarks

### 6.1 The 'Delft' experiment

The mean microwave backscatter values as measured in the 'Delft' wind/wave tank experiment show a wind dependence which is not a simple power law. Two regions could be distinguished, one of large growth of backscatter with increasing wind speeds (for a wind speed range upto 10 m/s) and one with much more moderate growth for the higher wind speeds. The polarization ratio between HH and VV polarization suddenly decreases for wind speeds above 10-11 m/s (fig. 2.3, 95).

The incidence angle dependence and the azimuthal variation of the microwave backscatter show a behaviour very similar to 'field' measurements.

The data were compared with model calculations on the basis of a two-scale model with input of parameterized wave measurements from three of the wave sensors employed: the imaging wave gauge, the laser slope gauge and the wave wire (LWG). The results with the two-scale model (fig. 3.19-3.21, pages 113-115) are very encouraging, they provide a good basis on which we can build further. The comparison between model and measurements also shows some weak points of the model which need to be improved in later versions:

1. at wind speeds above 10 m/s the VV model cross section predictions are too large. This error is most probably caused by the fact that the surface roughness in these cases becomes too large to use the 'Bragg' (small perturbation) approximation for radar scattering.
2. the model exaggerates the difference between VV and HH polarized scatter (especially at high wind speeds). This is a well-known feature of the Bragg scatter model.

To develop an improved scatter algorithm we intend to study test cases with more exact theoretical models as the Rayleigh method.

3. the model backscatter at small incidence angles highly depends on the choice of a cut-off parameter that shields a model singularity at zero incidence angle. The cut-off parameter is an undesired ad-hoc element in the theory. We intend to use the Holliday model as an alternative for small incidence angles and to analyze the singularity with the help of the Rayleigh method.
4. the difference between the upwind and downwind scatter should be explained through an upwind-downwind asymmetry in the waves. The wave data have been searched for such an asymmetry, but as yet nothing has been found.

The weak points mentioned above are caused by the backscatter module, since the wave modules consist of parameterized measured data.

In the near future other scattering modules (Holliday-first iteration and Rayleigh model) will be implemented in the model and tested. A model which calculates the short wave spectrum on the basis of the energy balance equation, including a non-linear wave interaction term, is under development and will be tested soon.

## 6.2 The 'de Voorst' experiment

In March 1989 the second wind/wave flume experiment was conducted in the 'Delta' tank of Delft Hydraulics in the noordoostpolder. This experiment has been very successful. Microwave backscatter, wind and wave measurements were conducted under controlled conditions for wind and waves with almost real sized mechanically generated waves. The measurements were done as a function of wind speed (0 till 10 m/s), wave height (zero up to  $1m_{pp}$ ) and wave spectrum (monochromatic, 11 meter wave length and JONSWAP spectrum) with the radar at a fixed incidence angle looking either upwind or downwind.

Preliminary analysis of the radar measurements in 'de Voorst' show a weak dependence of the backscatter on the wave height such, that for large wave heights the cross section increases.

The power spectral density and the autocorrelation functions of the microwave backscatter are very similar to those measured at sea by de Loor [13]. However, the short decorrelation time  $t_1$  of the backscatter as defined by de Loor is much longer in the case of the flume measurements. This may be explained by the lack of breaking waves and consequently slower surface decorrelation in the flume. This topic needs further study with more cases than the ones processed so far.

The analysis of the modulations of the microwave backscatter by the monochromatic waves show that 'tilt' modulation gives a good qualitative and quantitative description of the modulation especially for the HH polarized signals at phase angles between 0 and 180 degrees (fig. 5.15,5.16,5.18). Above 180 degrees the HH data is generally underestimated by the tilt model, indicating that other types of modulation (e.g. hydrodynamic modulation) are of importance there.

At VV polarization (fig. 5.17,5.19), the tilt modulation is much smaller than for HH polarization, therefore the effects of hydrodynamic modulation become more visible as the hydrodynamic modulation is polarization independent. The tilt modulation model alone now underestimates the total modulation in the microwave backscatter.

Extension of the tilt model with a module for hydrodynamic modulation by Alpers and Hasselmann [12] does not give significant improvement for most of the cases examined so far.

It should be mentioned that interactions between the wind and the waves and vice versa are *not* implemented in the hydrodynamic modulation model. Some of these wind-wave interaction effects have been noticed in the KNMI pressure anemometer data.

The 'de Voorst' wave measurements consisted of wave slope measurements done at the radar footprint and simultaneous with the radar measurements. These measurements have been analysed and were used to determine the radar backscatter with respect to the long wave slopes. Also high resolution wave images were made with a so-called reflective slope gauge. These images were recorded to determine the short wave spectrum as a function of the long wave slopes. However at the moment the image processing algorithms available are not sufficient to perform this task.

In the near future all remaining radar measurements will be analysed in the same way as the selected measurements presented in this report. A literature search will be performed toward more sophisticated hydrodynamic modulation models than the one from Alpers and Hasselmann. Furthermore the interaction between wind profile and water surface will be examined using the wind profile measurements as performed with the KNMI pressure anemometer.

### **6.3 The field experiment at MeetPost Noordwijk.**

The next step in the VIERS-1 experimental programme, to take place in the late fall of 1990, is a field experiment, in which the conclusions resulting from the interpretation of the Delft experiment and the de Voorst experiment, as well the theoretical insights obtained in the studies of the modelling group will be confronted with the harsh reality of the North

Sea. The experiment will be performed from Meetpost Noordwijk (MPN, Measuring Station Noordwijk) of Rijkswaterstaat, an offshore platform 5 seamiles (9 km) off the Dutch coast, near the seaside resort of Noordwijk, which by some strange coincidence is also the town where ESTEC has its abode.

During the field experiment we will again do measurements on the atmosphere, the waves and the radar reflectivity of the sea surface to provide information on the way the radar return and the transport coefficients depend on the meteorological and oceanographic situation. The emphasis is on the measurement of the radar return in relation to the wind field and the sea state (especially the two dimensional wave field in the centimeter range).

In another part of the experiment, the flux experiment, the dependence of the transport of momentum, exemplified by  $u_*$ , on wind speed, sea state and stability will be investigated. This will again be done using the eddy-correlation method. The flux experiment can be viewed as a follow-up of the international HEXMAX experiment, which took place in 1986 in the same area. Improvements compared with the 1986 situation consist of a better knowledge of a number of environmental parameters, especially the wave field, the surface current and the water vapor concentration.

Finally another new technique will be tested in which the transport of gases (among them  $\text{CO}_2$ ) through the water surface is derived from radar backscatter. This technique has been developed at the University of Heidelberg and this will be its first application at sea.

Several radars will be mounted on MPN to measure the normalized radar cross section ( $\sigma^0$ ) of the sea surface under various environmental conditions. Their data will not only be used to obtain remotely sensed wind fields, but also to measure both surface currents and waves.

Simultaneously the oceanographic and meteorological measurements will be performed from one or more outriggers, attached to the platform. Central to the experiment are measurements of

- the directional wave slope spectrum up to a frequency of about 10 Hz by optical methods;
- wind speed and direction, humidity,  $\text{CO}_2$  concentration and temperature values and their fluxes, the fluxes to be obtained by the eddy correlation method, using in situ sensors specially developed for use at sea.
- measurement of the current with radar, using the newly developed FEL-TNO SHIRA system.

There is a possibility that more (foreign) groups will participate.

#### **6.4 After the field experiment.**

After the launch of ERS-1 ESA will put a number of sets of  $\sigma_o$  values, measured during the calibration/validation phase of the spacecraft, and the corresponding wind speeds and directions, calculated with the standard method of ESA, at the disposal of the VIERS-1 group. At a somewhat later stage these will be completed with in situ data of the wind, measured at the same time and place as the  $\sigma_o$  values. Both the ESA results and the in situ data will then be compared with winds calculated with the VIERS-1 algorithm.

## Acknowledgements

The contribution of the Dutch Laboratories was supported by the Netherlands Remote Sensing Board. The cooperation with the Institute for Environmental Physics of the Heidelberg University was supported by a grant of the state Baden-Württemberg and the European Community.

The VIERS-1 team gratefully acknowledges the activities of the KNMI construction bureau, especially those of mr. Louis van der Woerd, for the design and realization of the wind tunnel on top of the Delta tank at "de Voorst".

In this context we also want to thank mr. Ed Worrell of the KNMI Oceanographic Division for the accomplished way in which he performed the supervision of both the planning and the execution of this project.

Mr. Laméris of the Research Institute for Road Vehicles TNO is gratefully acknowledged for the generation of wind in the Delta flume and his constructive and enthusiastic contribution to the 'de Voorst' experiment.

The reduction in the processing time of the KNMI data from months to days and the greatly improved ease of their administration are due to the impeccable functioning of the new data logging system, for which we thank mr. Cor van Oort.

The authors would like to thank Dr. P. Lobemeier for lending to them the high frequency wave wire.

One of the authors (BJ) would like to thank especially Mr's D. Wierzimok, Th. Billen, R. Fischer, K. Riemer and P. Libner who have greatly contributed to the success of the experiments during various phases of the preparation and the actual measurements.

Last but not least we thank the staff of the Delta tank for the way in which they supported the rather unusual way in which we utilized their excellent facility.

# Bibliography

- [1] D. van Halsema et al. *progress report on the VIERS-1 project*. Technical Report bcrs-89-24, BCRS, 1989.
- [2] M.A. Donelan and W.J. Pierson Jr. Radar scattering and equilibrium ranges in wind-generated waves with application to scatterometry. *Journal of Geophysical Research*, 92:4971-5029, 1987.
- [3] G.R. Valenzuela. Theories for the interaction of electromagnetic and oceanic waves - a review. *Boundary Layer Met.*, 13:61-85, 1978.
- [4] K. Hasselmann et al. *Deutsch. Hydr. Zeit.*, A12:, 1973.
- [5] S.A. Kitaigorodskii. *J.Phys.Oc.*, 13:816-827, 1983.
- [6] O.M. Phillips. *J. Fluid Mech.*, 156:505-531, 1985.
- [7] H. Lamb. *Hydrodynamics*, 6th ed., 1945.
- [8] W.J. Plant. *J. Phys. Oc.*, 10:1340-1352, 1980.
- [9] P.M. van den Berg. Reflection by grating, rayleigh methods. *Journal of the Optical Society of America*, 71:1224-1229, 1981.
- [10] B. Jaehne and K.S. Riemer. Two-dimensional wave number spectra of small-scale water surface waves. *Journal of Geophysical Research*, 95:11531-11546, 1990.
- [11] Alpers et al. On the detectability of ocean surface waves by real and synthetic aperture radar. *J.Geophys. Res.*, C7:6481-6498, 1981.
- [12] Alpers and K. Hasselmann. *Bound. Layer Meteor.*, 13:215-230, 1978.
- [13] G.P. de Loor. *Project Noordwijk, part V: Analysis of the fading component of the radar backscatter*. Technical Report PHL 1984-21, FEL-TNO, 1984.

## Appendix A Presentations

On January 25, 1990 a VIERS-1 workshop was held at KNMI, de Bilt, which was experienced as very inspiring by the participants. Among those present were Dr.A.Ramamonjiarisoa of the Institut de la Mécanique Statistique de la Turbulence (IMST) in Marseille, Dr.S.Zecchetto of the Istituto per lo Studio della Dinamica delle Grandi Masse (ISDGM) in Venice, both working in the field of radar scatterometry and Dr.A.Long of ESTEC, responsible for the ESA ERS- 1 scatterometer algorithm. The day's programme is shown on the next page:

**9.30 Opening of the Workshop**

Session 1: the "Delft" Experiment

- 9.45 W.A.Oost (KNMI):  
Description of the experiment and wind measurements.
- 10.00 B. Jähne (Scripps/Heidelberg):  
Wave measurements.
- 10.15 D. van Halsema (FEL-TNO):  
Radar measurements
- 10.30 Discussion

**Coffee break****Session 2: the "De Voorst" Experiment**

- 11.00 D. van Halsema (FEL-TNO):  
Description of the experiment
- 11.15 P. Snoeij (TU Delft):  
Radar measurements
- 11.30 B. Jähne (Scripps/Heidelberg):  
Wave measurements
- 11.45 W.A. Oost (KNMI):  
Wind measurements
- 12.00 Discussion

**Lunch****Session 3: Modelling Results**

- 14.00 C. Calkoen (Delft Hydraulics):  
The VIERS-1 model
- 14.30 J.A.M. Janssen (KNMI):  
The air-sea interaction module of the VIERS-1 model
- 14.45 J. Vogelzang (RWS-DGW):  
Several microwave backscatter models
- 15.00 Discussion

**Tea Break****Session 4: the Future of VIERS-1**

- 15.45 W.A. Oost (KNMI):

- The field experiment**
- 16.00 C. Calkoen (Delft Hydraulics):  
Goals of the modelling effort
- 16.15 Discussion

## Other publications:

van Halsema, D., B.Jähne, W.A.Oost, C.Calkoen and P.Snoei,ij,

*First results of the VIERS-1 experiment.*

In: Radar scattering from modulated wind waves,

G.J.Komen and W.A. Oost eds.,

Kluwer 1989, 49-57.

van Halsema, D., B.Jähne, W.A.Oost, Ch.Calkoen and P.Snoei,ij,

*Comparison of X-band radar backscatter measurements with area extended wave slope measurements made in a large wind/wave tank.*

Proc. IGARSS '89, Vol. 5, 2997-3000.

van Halsema, D., Ch.Calkoen, B.Jähne, W.A.Oost, P.Snoei,ij and S.Waas,

*Progress Report on the VIERS-1 project*

*Part-1: The Delft Wind/Wave Experiment*

BCRS contract report, BCRS-89-24, November 1989.

Snoei,ij, P., Ch.Calkoen, J.Vogelzang, W.A. Oost, D.van Halsema and B.Jähne

*Comparison of radar backscatter measurements and area extended wave slope measurements of wind generated waves in a large wind/wave tank with two-scale model predictions.*

Proc. of the URSI-F symposium, Signature Problems in Microwave Remote Sensing of the Surface of the Earth Hyannis USA 16-18 may 1990, K.6

Snoei,ij, P., Ch.Calkoen, J.Vogelzang, W.A.Oost, D.van Halsema and B.Jähne

*Dual-polarized scatterometer measurements of generated wind and gravity waves in a very large wind/wave tank.*

Proc. of IGARSS '90, Remote Sensing Science for the Nineties

Maryland USA 20-24 may 1990, vol. III, 2157-2160.

Halsema, D.van, P.Snoei,ij, Ch.Calkoen, J.Vogelzang, W.A.Oost and B.Jähne

*Comparison of two-scale model calculations with radar backscatter measurements and area extended wave slope measurements of wind generated waves in a large wind/wave flume.*

Conference: "Oceans from Space"

Venice, May 1990

Snoei,ij, P., J.Vogelzang, Ch.Calkoen, W.A.Oost, D.van Halsema and B.Jähne

*A high resolution scatterometer for radar backscatter measurements of wind generated waves in wind/wave tanks.*

Proc. of the 20th European Microwave Conference

Budapest Hungary, 10-14 september 1990, 881-886.

## Appendix B Organization and finances

The programme is run by a managing group consisting of representatives of the participating institutes and headed by a projectleader provided by KNMI, the prime contractor for the project. For the scientific progress of the project the group reports to ROWA. The relation between the NRSP and KNMI has been regulated in two contracts, the second of which is not yet definitive at the time of writing, mainly due to uncertainties about the amount of support available. The relation between KNMI and the secondary contractors (at present FEL-TNO, Delft Hydraulics and Delft Technical University) is regulated in a set of secondary contracts; these contracts too are not yet finalized for the second period, due to the situation with the primary contract. Meanwhile the activities have continued, based on a working arrangement between the VIERS-1 group and the BCRS programme bureau.

VIERS-1 has so far been supported by funds from the first phase of the NRSP supplemented with a considerable contribution from each of the participating institutes. Due to the limited size of these resources, the level of support has not been guaranteed at the required level for the initial stage of phase 3 of the programme. The projectleader therefore has been spending a large fraction of his time available for VIERS-1 to fund raising instead of stimulating the progress of the project. At the time of writing these activities have proven successful and the field experiment has received the required supplementary support from the National Research Programme "Global Air Pollution and Climate Change". It is hoped that this situation will not repeat itself for the activities after the field experiment.

The EC also supports VIERS-1 in the framework of the Twinning programme (contract ST2J-0451-C), a programme aimed at improving cooperation between scientists from different EC countries which mainly covers the extra expenses due to this international cooperation.

## Appendix C

## Two-Dimensional Wave Number Spectra of Small-Scale Water Surface Waves

BERND JÄHNE

Physical Oceanography Research Division, Scripps Institution of Oceanography, La Jolla, California

KLAUS S. RIEMER

Institut für Umweltphysik, University of Heidelberg, Im Neuenheimer Feld 366, D-6900 Heidelberg, Federal Republic of Germany

Two-dimensional wave slope spectra have been measured in the large Delft wind-wave facility using an imaging optical technique and digital image processing. The data cover wavelengths from 0.4 to 24 cm and wind speeds ( $U_{10}$ ) from 2.7 to 17.2  $\text{ms}^{-1}$ . The spectral densities of small gravity waves at higher wind speeds are proportional to  $k^{-3.5}$  and  $u_*$ . Capillary-gravity and capillary waves show features which clearly manifest that the energy balance for these waves is much different from that for gravity waves. The degree of saturation is approximately constant at a given wind speed, but strongly increases with friction velocity ( $\propto u_*^{2.5}$ ). A sharp cutoff, which is almost independent of the wind speed, occurs at a wavelength of about 7 mm.

## 1. INTRODUCTION

The complex two-dimensional propagation and interaction of small-scale wind waves on the ocean surface cannot adequately be measured with point measuring devices such as wire and laser slope gauges. Such instruments yield time series from which only the temporal characteristics can be derived. No insight is gained into the two-dimensional spatial structures of the wave field.

A more detailed knowledge of these properties, however, is crucial for a deeper understanding of small-scale air-sea interaction processes and active remote sensing of them with microwaves. From scale considerations it is clear, whatever the detailed mechanisms may be, that backscatter of electromagnetic waves is determined by structures on the water surface of the same scale as the incident wavelengths, i.e., by small-scale waves in the capillary-gravity range with wavelengths ranging from centimeters to millimeters.

The dependency of these small wavelets on the wind speed and friction velocity, is the basis of remote sensing of the wind speed and direction by measuring the radar backscatter cross section [Schroeder *et al.*, 1982; de Loor, 1983]. Yet, the mean spectral densities of the small-scale waves also depend on a number of other parameter as derived by recent studies of the radar backscatter. Keller *et al.* [1985] found a significant increase in the radar return with increasing atmospheric instability. Another important factor is the development of the wave field commonly expressed in the nondimensional wave age. Wind speeds determined by scatterometers and altimeters are considerably overestimated at high wave ages [Glazman *et al.*, 1988; Glazman and Pilorz, 1990]. Furthermore, surface active films significantly damp even small gravity waves with frequencies as low as 2 Hz [Alpers and Hühnerfuss, 1989].

Of equal importance is the modulation of the small-scale waves by larger-scale features such as large-scale gravity waves, internal waves, tidal currents, and bottom topography [Komen and Oost, 1989]. Through these interactions, large-scale features can be made visible by imaging radar systems such as synthetic aperture radars (SAR).

A more detailed investigation of all these effects depends entirely on knowledge of the small-scale structures on the sea surface. There are virtually no laboratory and at-sea measurements of wave number spectra available for waves in the capillary-gravity and capillary range. Previously published measurements are limited to larger wavelengths and include rather sporadic and limited data, but no systematic study over a wide range of parameters.

Banner *et al.* [1989] report wave number spectra based on stereophotogrammetric determination. Their measurements were obtained from an oil platform and covered a wavelength range from 0.2 to 1.6 m and wind speeds from 7 to 13.3 ms<sup>-1</sup>. Because of the coarse resolution of only 33 × 33 pixels, only one-dimensional wave number spectra, i.e., projections of the two-dimensional spectra are discussed.

During the TOWARD experiment, Shemdin *et al.*

[1988] also used stereophotography to derive two-dimensional wave number spectra. The stereo images were taken from an image sector of 2.5 m × 2.5 m and were evaluated manually with a resolution of about 300 × 300 pixels. The wave number spectra, calculated from 8–10 frames per condition, include wavelengths between 0.02 and 1 m and cover wind speeds from 1.5–5.0 ms<sup>-1</sup>.

The results of these two investigations disagree: While Shemdin *et al.* [1988] found that the spectral densities go with  $k^{-3.6}$  and increase with wind speed, Banner *et al.* [1989] obtained a  $k^{-4.0}$  dependency and no significant change with wind speed. For further interpretation, more data are needed since both papers include only a few spectra. Furthermore, the wind speed ranges of the investigations do not overlap.

Very recently, in the course of the SAXON-I field experiment at the Chesapeake Light Tower, stereo and Stilwell-type [Stilwell, 1969] image sequences have been taken [Shemdin and McCormick, 1989]. Thus, in the near future more field data should be available. However, the new data will not include capillary waves, since it is estimated that only waves down to wavelengths of 1 cm and 2 cm will be resolved with the stereo and Stilwell technique, respectively.

In conclusion, considerable progress in the experimental technique and data analysis of wave images is still necessary to produce instruments which (1) can resolve the smallest wave scales; (2) can operate under a wide range of conditions in the field; and (3) allow a systematic study of the spatial wave characteristics.

We chose a step by step approach to this difficult matter, starting with the relative easy indoor environment of a wind/wave facility and going to the much more demanding environment at sea. This seems to be the most efficient way to develop the measuring technique. A description of the optical wave measuring technique envisaged is given by Jähne and Waas [1989].

The experiments reported in this paper were performed in the well-controlled indoor Delft wind/wave facility within the first phase of the VIERS project, an international and multidisciplinary cooperation to forward the understanding of microwave backscattering and small-scale water surface waves [van Halsema *et al.*, 1989]. The measuring program focused on synchronous recording of the backscatter cross section with an X-Band FM/CW radar (9.6 GHz) and of wave image sequences at the same footprint on the water surface (van Halsema *et al.*, in preparation, 1990)

Meanwhile, a second experiment took place in March 1989 in the even larger outdoor 250 m long and 5 m deep Delta flume, where full-scale gravity waves could be generated. As last step, an experiment is planned from the Noordwijk research platform in the North Sea.

This paper discusses two-dimensional wave number spectra and consists of four sections: The first section briefly discusses the present theoretical knowledge about wave number spectra of small-scale waves. Sections 3 and 4 cover the experimental techniques and the processing of the wave images. The experimental results are discussed in section 5.

## 2. SLOPE WAVE NUMBER SPECTRA

### 2.1. Wave Slope

Since we performed wave slope measurements, we start with a discussion of the wave slope and its relation to the wave height. The wave slope is the gradient of the water surface deflection  $a(\mathbf{x}, t)$

$$\mathbf{s}(\mathbf{x}, t) = \nabla a(\mathbf{x}, t). \quad (1)$$

It is a two-dimensional vector function with two components, the along-wind component,  $s_1$ , and the cross-wind component,  $s_2$ . The relation between the slope and amplitude power spectra can easily be deduced from the Fourier transform of the water surface deflection

$$\hat{a}(\mathbf{k}, \omega) = \int \int \int_{x_1, x_2, t} a(\mathbf{x}, t) \exp[-i(\mathbf{k}\mathbf{x} - \omega t)] d\mathbf{x} dt, \quad (2)$$

where  $\hat{a}(\mathbf{k}, \omega)$  is the complex-valued amplitude function. The slope spectra (along-wind  $S_1$ , cross-wind  $S_2$ , and total  $S = S_1 + S_2$  as the sum of both) are given by

$$\begin{aligned} S_1 &= k_1^2 |\hat{a}(\mathbf{k}, \omega)|^2 = k^2 \cos^2 \Theta A(\mathbf{k}, \omega) \\ S_2 &= k_2^2 |\hat{a}(\mathbf{k}, \omega)|^2 = k^2 \sin^2 \Theta A(\mathbf{k}, \omega) \\ S &= k^2 |\hat{a}(\mathbf{k}, \omega)|^2 = k^2 A(\mathbf{k}, \omega) \end{aligned} \quad (3)$$

where  $\hat{A}(\mathbf{k}, \omega) = |\hat{a}(\mathbf{k}, \omega)|^2$  is the directional wave number-frequency spectrum of the wave amplitude and  $\Theta$  the angle between the wind direction and the propagation direction of the wave.

### 2.2. Wave Number Spectra

Single images of the waves on the water surface yield only the spatial structures and thus only wave number spectra can be calculated. The wave number spectra are obtained from the directional wave number-frequency spectrum by integration over all frequencies contributing to a single wave number, i. e., by a projection of the 3-D spectrum onto the wave number plane.

$$\begin{aligned} F(\mathbf{k}) &= \int_{\omega} \hat{A}(\mathbf{k}, \omega) d\omega \\ S_1(\mathbf{k}) &= k^2 \cos^2 \Theta \int_{\omega} \hat{A}(\mathbf{k}, \omega) d\omega \\ S_2(\mathbf{k}) &= k^2 \sin^2 \Theta \int_{\omega} \hat{A}(\mathbf{k}, \omega) d\omega \\ S(\mathbf{k}) &= k^2 \int_{\omega} \hat{A}(\mathbf{k}, \omega) d\omega, \end{aligned} \quad (4)$$

These relations mean that the total slope wave number spectrum  $S$  can directly be derived from the height wave number spectrum  $F$  and vice versa:

$$F(\mathbf{k}) = k^{-2} S(\mathbf{k}), \quad S(\mathbf{k}) = k^2 F(\mathbf{k}) \quad (5)$$

This relation gives free choice to measure either the slope or the height of the waves. If slope measurements are chosen, it is important to measure the total slope spectrum, i. e. both the along- and cross-wind compo-

nents. If only one component is available, waves traveling perpendicularly to the corresponding direction do not contribute to the spectral densities and are lost because of the angular weighting factors  $\cos^2 \Theta$  and  $\sin^2 \Theta$  for along- and cross-wind components (4).

### 2.3. Saturation Range and Representation of Spectra

The simplest concept of an upper-limit asymptote of the spectrum, the saturation range, goes back to the early work of Phillips [1958]. He postulated that dissipation (e. g., by wave breaking) imposes an upper limit on the spectral densities. If this limit is independent of the energy input by the wind and depends only on the restoring gravity and capillary forces,  $g$  and  $\gamma = \sigma/\rho$ , respectively, ( $\sigma$  denotes the surface tension) a simple dimensional analysis

$$\begin{aligned} [F(\mathbf{k})] &= L^{-4} & [S(\mathbf{k})] &= L^{-2} \\ [g] &= LT^{-2} & [\gamma] &= L^3 T^{-2} \end{aligned} \quad (6)$$

yields

$$\begin{aligned} F(\mathbf{k}) &= \beta f(\Theta) k^{-4} \\ S(\mathbf{k}) &= \beta f(\Theta) k^{-2} \\ S_1(\mathbf{k}) &= \beta \cos^2 \Theta f(\Theta) k^{-2} \\ S_2(\mathbf{k}) &= \beta \sin^2 \Theta f(\Theta) k^{-2} \end{aligned} \quad (7)$$

where the dimensionless function  $f(\Theta)$  describes the angular spread of the waves, which, of course, cannot be derived from dimensional analysis alone. Since the saturation range does not explicitly depend on the restoring force, the wave number spectra for capillary and gravity waves show the same spectral shape, although the constant  $\beta$  may be different.

The saturation spectrum (7) corresponds to a wave field which, statistically, shows spatial discontinuities in the slope, i. e., the first spatial derivative. This simple fact emphasizes that the slope is a basic parameter for the waves. Indeed, the slope of the wave is the parameter which describes the nonlinearity of waves in the Navier-Stokes differential equation [Kinsman, 1965]. From the experimental point of view, slope measurements offer a significant advantage over height measurements since the slope signal has a much smaller dynamic range. Clearly, the concept of a saturation range is an oversimplification. It is very helpful, however, in representing spectral densities. All spectra in this paper are represented as a dimensionless function, the "degree of saturation"  $B(\mathbf{k})$ , as proposed by Phillips [1985]

$$B(\mathbf{k}) = F(\mathbf{k}) k^4 = S(\mathbf{k}) k^2 \quad (8)$$

A different train of thought leads to the same representation for wave spectra. The starting point is the fact that real-world data are obtained from discrete grids. A Cartesian wave number grid, which results from the discrete Fourier transform of an image, is not an optimum choice. The relative wave number resolution in the wave spectra is not constant, but increases proportional to the wave number to unnecessarily high levels well below 1%. Moreover, it is costly and cumbersome to extract the angular dispersion, profiles in a certain direction, or the dependency of the spectral density on the absolute wave number from the Cartesian grid.

These demands are much better met by a discrete grid in a  $(\ln k, \Theta)$  space, which preserves a constant relative  $k$  resolution and allows easy extraction of the angular dispersion and  $k$  profiles. Actually, these features are directly visible in such a representation, while it is hardly possible to compare angular dispersions of different wave numbers in a Cartesian grid. The transition from a  $(k_x, k_y)$  grid to the  $(\ln k, \Theta)$  grid for the spectral densities is given by

$$S(\mathbf{k})dk_1dk_2 = S'(\mathbf{k})d\ln kd\Theta \quad (9)$$

Using  $dk_1 = kd\Theta$ ,  $dk_2 = kd\ln k$  and (8) yields

$$S'(\mathbf{k}, \Theta) = k^2 S(\mathbf{k}, \Theta) = B(k) \quad (10)$$

On a  $(\ln k, \Theta)$  grid the slope spectrum is directly expressed as the degree of saturation  $B$ . The multiplication by  $k^2$  reflects the fact that the area of the grid cells increases with  $k^2$ . Representation of the wave number spectra in a  $(\ln k, \Theta)$  grid, instead of a Cartesian grid, also yields considerable data compression.

#### 2.4. Energy Balance in Small-Scale Waves

The key to a deeper understanding of the wave spectra lies in the determination of the energy balance of the waves. In a stationary wave field, the spectral densities adjust in such a way that the different sources and sinks balance each other in the mean. Basically there are three terms [Phillips, 1985]: (1) energy input by the turbulent wind field; (2) transfer of energy between waves of different wave numbers by nonlinear wave-wave interaction; and (3) dissipation of energy by wave breaking, viscous dissipation, and turbulent diffusion.

Even for small gravity waves there is a considerable lack of knowledge. While the input of energy by wind is known best, the mechanisms and magnitude of the wave dissipation term is quite uncertain [Plant, 1989]. Recently, two models have been proposed, both yielding an increase in the degree of saturation with  $k^{1/2}$  and  $u_*$  on quite different assumptions. Phillips [1985] assumed that all three fluxes sketched above are of equal importance. Balancing these terms locally, he obtained

$$\begin{aligned} F(\mathbf{k}) &= \beta g^{-1/2} f(\Theta) u_* k^{-7/2} \\ B(\mathbf{k}) &= \beta g^{-1/2} f(\Theta) u_* k^{1/2} \end{aligned} \quad (11)$$

In contrast, Kitaigorodskii [1983] proposed the existence of a Kolmogoroff-type energy cascade in which the wind input primarily occurs at the energy-containing large scales and dissipation at small scales. As a consequence, the spectral energy flux in the intermediate wave numbers is constant, and he also obtained (11).

For capillary-gravity and capillary waves, several new aspects, which make a theoretical treatment of the energy balance even more difficult, come into play:

**Strong nonlinear wave-wave interaction.** Resonant nonlinear wave-wave interaction in the gravity range takes place between quartets of waves. This is a "weak" process in the sense that the characteristic time scale is hundreds of wave cycles [Kinsman, 1965]. In contrast, resonant interactions between capillary-gravity waves occur in triplets and are much stronger; the third wave

component is excited in less than five cycles of the interacting waves [McGoldrick, 1965].

**Energy transfer over a wide range of wave numbers.** Steep gravity waves generate ripples at their crests. This mechanism transfers energy over a wide wave number range. In contrast the standard perturbation theory for nonlinear wave-wave interaction deals only with waves of similar wavelengths. To the knowledge of the authors, no estimates are available comparing these different modes of energy transfer.

**Viscous cutoff.** Towards high wave numbers, viscous dissipation should become dominant, since it is proportional to the wave number squared [Phillips, 1980]. It is generally believed that viscous dissipation sets the upper limit for waves which can be generated on the water surface. In order to estimate the viscous cutoff, Donelan and Pierson [1987] balanced the wind input and viscous dissipation term and argued that wave numbers for which the wind input term is smaller than the viscous dissipation can not be generated. Their calculations (Figure 4 of their paper) lead to a cutoff wave number which strongly increases with the wind speed, due to an increase of the wind input term, and less strongly with temperature, due to a decrease of the kinematic viscosity. The cutoff wave numbers range from about  $200 \text{ m}^{-1}$  ( $\lambda = 3 \text{ cm}$ ) at  $2.7 \text{ ms}^{-1}$  wind speed to about  $1100 \text{ m}^{-1}$  ( $\lambda = 0.57 \text{ cm}$ ) at  $12 \text{ ms}^{-1}$ .

**Turbulent wave dissipation and interaction with shear currents.** A closer review of this term is lacking. Only recently, Rosenthal [1989] proposed that turbulent diffusion yields a nonlinear mechanism for wave dissipation which agrees in the order of magnitude with the measured spectral densities. Damping of capillary waves by turbulence is, of course, governed by eddies of much smaller scales. The damping mechanisms may be quite different, since the penetration depth of these waves,  $\lambda/2\pi$ , is of the same order as the wind driven shear current in the viscous boundary layer. Thus, these waves propagate in a strongly sheared layer. These effects became important in research on air-sea gas exchange, in order to explain the strong enhancement of the air-sea gas transfer rate in the presence of waves [Jähne et al., 1987]. Since the gas transfer is controlled by a layer which is considerably thinner than the aqueous viscous boundary layer, it is a sensitive indicator for turbulence very close to the water surface.

**Surface films.** Besides wave breaking, viscous and turbulent dissipation, waves are also dissipated by monomolecular surface films. This fact makes the wave field dependent on a variety of chemical and biological parameters. Despite this complexity, the basic relations between the damping factor and the viscoelastic properties of the surface films are well established [Alpers and Hühnerfuss, 1989].

The many parameters influencing small-scale waves are a challenge for more detailed measurements. Such experimental data could help to sort out predominant mechanisms and to guide further theoretical research.

### 3. EXPERIMENTAL TECHNIQUE

#### 3.1. Slope Measurements by Light Refraction

The imaging of the wave slope is based on light refraction at the water surface. The same principle has been used for laser slope gauges [Cox, 1958; Tober *et al.*, 1973; Hughes *et al.*, 1977; Lange *et al.*, 1982; Jähne, 1989b; Jähne and Waas, 1989]. The water surface is observed by a CCD camera mounted at the ceiling of the facility, 4 m above the water level.

A submerged illumination system similar to the device constructed by Keller and Gotwols [1983] is used. It was modified to visualize both the along- and cross-wind slopes of the waves (compare section 2.2.). It replaces one of the 2 m × 2 m × 0.3 m concrete plates which cover the bottom of the end section of the water channel in the Delft facility (Figure 1). The illumination system fits smoothly into the bottom of the facility and does not cause any disturbance of the flow and waves in the water tank.

A row of six 150-W Osram HQI metal vapor lamps is located at the down- and cross-wind side walls of a 1.4 m × 1.4 m × 0.2 m glass box containing an aqueous suspension of Dow Latex particles with a diameter of 0.4 μm (Serva Feinbiochemica). The particles are used to scatter the light in the box. Double glass windows at the bottom and top of the scattering volume act as a light guide by total reflection. Only one of the two rows of lamps is used at a time. This simple setup should — according to first-order scattering theory — result in an exponential decrease of the brightness  $I$  in the direction perpendicular to the corresponding row of lamps

$$I(X) = I_0 \exp(-X/\bar{X}) \quad (12)$$

If the water surface is flat, the CCD camera observes a horizontally or vertically changing intensity. The measured profiles show close agreement. The along-wind profile (Figure 2a) is approximately exponential, with  $\bar{X}$  being roughly equal to the illuminated width of the image, while the cross-wind profile is constant (Figure 2b). When the water surface is inclined by waves, the light beam received by the CCD-camera comes from a place in the illumination source which is more or less bright. In this way, the intensity gradient is modulated by the slope of the waves.

It is important to note that focusing and defocusing caused by the lens effects of surface curvature cannot occur with this setup. The "ripple at the bottom of the tank effect" is only observed when a bundle of parallel light or convergent light, emitted from a point source, illuminates the water surface. The illumination source used in the imaging slope gauge is quite different. It is large, and the light is emitted in a wide cone, limited only by total reflection at the glass-air interface at the upper double glass window of the scattering volume. It is shown below that the illumination cone is wide enough even for high wave slopes.

#### 3.2. Wave Slope and Image Intensity

A quantitative relation between the intensity modulation and the wave slope can be derived by ray tracing (Figure 3) assuming that the light source radiates light

isotropically in all directions. In the following considerations emphasis is put on a careful estimate of the various nonlinearities related to the refraction law and the exponential intensity profile.

For the sake of simplicity, dimensionless coordinates  $(x, y) = (\tan \epsilon_1, \tan \epsilon_2)$  are used to denote the position on the image plane. Three-dimensional world coordinates are indicated by capital letters  $(X, Y, Z)$ . The optical axis of the system is aligned along the  $Z$  axis.

The horizontal position  $(X, Y)$  in the light source corresponding to a point  $(x, y)$  on the image plane is then given by (compare Figure 3)

$$\begin{pmatrix} X \\ Y \end{pmatrix} = (Z_a - H) \begin{pmatrix} x \\ y \end{pmatrix} + (Z_w + H) \begin{pmatrix} \tan \gamma_1 \\ \tan \gamma_2 \end{pmatrix} \quad (13)$$

where  $Z_a$  and  $Z_w$  are the distances from the camera to the mean water level and from the mean water level to the light source, respectively, and  $H$  is the wave height. Since the intensity changes in only one direction, we need to consider only one component of (13); we take the along-wind component.

Next, the relation between the slope  $s_1 = \tan \alpha_1$  of the water surface and the refraction angle  $\gamma_1$  is considered in order to eliminate  $\gamma_1$  from (13) (Figure 3). Elementary trigonometry and the law of refraction yield

$$s_1 = \tan \alpha_1 = \frac{n_w \sin \gamma_1}{n_w \cos \gamma_1 - \cos \epsilon_1} = \frac{\sin \epsilon_1}{n_w \cos \gamma_1 - \cos \epsilon_1} \quad (14)$$

Introducing the image coordinate  $x = \tan \epsilon_1$  yields

$$s_1 = \sqrt{1+x^2} \left( \frac{n_w \tan \gamma_1}{n_w \sqrt{1+x^2} - \sqrt{1+\tan^2 \gamma_1}} - \frac{x \sqrt{1+\tan^2 \gamma_1}}{n_w(1+x^2) - \sqrt{1+\tan^2 \gamma_1}} \right) \quad (15)$$

Clearly, the dependence of  $\tan \gamma_1$  on the wave slope  $s_1$  and the image coordinate  $x$  is nonlinear. A third-order Taylor expansion in  $x$  and  $\tan \gamma_1$  yields the following approximation after some lengthy calculations (using  $n_w = 4/3$ )

$$\tan \gamma_1 = \frac{1}{4} s_1 \left[ 1 + \frac{3}{2} x^2 - \frac{3}{32} (s_1 + 3x)^2 \right] + \frac{3}{4} x \left[ 1 - 2x^2 - \frac{5}{32} (s_1 + 3x)^2 \right] \quad (16)$$

The refraction angle  $\gamma_1$  equals only about a quarter of the wave slope (if  $s_1 = 1, \gamma_1 = 13^\circ$ ). Thus  $\gamma_1$  covers only a small range. Consequently, the use of the Taylor expansion in  $\tan \gamma_1$  and the assumption of an isotropic light source (section 3.1.) are justified. Substituting this equation into (13) yields  $X$  as a function of the wave

slope  $s_1$  and the position in the image plane  $x$

$$X = (Z_a - H)x + \frac{Z_w + H}{4} \left\{ s_1 \left[ 1 + \frac{3}{2}x^2 - \frac{3}{32}(s_1 + 3x)^2 \right] + \frac{3}{4}x \left[ 1 - 2x^2 - \frac{5}{32}(s_1 + 3x)^2 \right] \right\} \quad (17)$$

The shift in position of the illumination source  $\Delta X$  from a flat water surface ( $s_1 = H = 0$ ) to a wavy surface is given by

$$\Delta X = \frac{Z_w + H}{4} s_1 \left[ 1 + \frac{21}{32}x^2 - \frac{3}{32}s_1^2 - \frac{9}{16}s_1x \right] - \frac{H}{4}x - \frac{3Z_w}{4}x \left[ \frac{5}{32}s_1^2 + \frac{30}{32}s_1x \right] \quad (18)$$

The shift in position  $\Delta X$  is essentially proportional to the wave slope  $s_1$ . The wave height  $H$  causes a sensitivity shift. Ripples at the crest of large waves are imaged more sensitively than at the trough. In our experiments with pure wind waves, the wave height was at most 5 cm. Since the mean distance to the light source was 85 cm, the effect is only about 6%. The effect on mean wave number spectra is much less, since only an uneven distribution of the ripples would cause a bias in spectral densities.

Equation (18) contains the effects of the nonlinearity related to the refraction law. These effects are of third order in the wave slope  $s_1$  and the image coordinate  $x$ . In order to reduce the nonlinearities, it is essential to keep  $x$  small, i. e., by putting the camera as far away from the water surface as possible. In our setup,  $x$  was always smaller than 0.1. Then the position-dependent nonlinearities are 6.2% for  $s_1 = 1$  and 2.3% for  $s_1 = 0.3$  at the edges of the image. In the mean, the effects are much lower, since the largest term  $3/32s_1x$  is linear in the position and thus cancels when integrated over the whole image. A bias of only 0.3%, which is caused by the term quadratic in  $x$ , remains. The nonlinearities which depend only on the wave slope are larger. The slope signal is 9.4% and 0.8% lower than expected from a linear relation for  $s_1 = 1$  and  $s_1 = 0.3$ , respectively.

The second term in (18) causes a zero-point shift for the slope signal. The effects are small and therefore negligible. A wave height of 5 cm causes a slope shift of 0.0063 at the edge of the image. The position-dependent shift is 0.028 and 0.009 at the edge of the image for slopes of 1 and 0.3, respectively, while the slope itself results in a zero shift of 0.047 and 0.004, respectively.

Finally, the intensity change is related to the wave slope by expanding (12) in a Taylor series, using (18) to substitute  $\Delta X$

$$\Delta I = I(s) - I(0) = -\alpha I(0)s_1 \left[ 1 - \frac{1}{2}\alpha s_1 + \left( \frac{1}{6}\alpha^2 - \frac{3}{32} \right) s_1^2 - \frac{9}{16}s_1x \right] \quad (19)$$

with

$$\alpha = \frac{Z_w + H}{4X} \quad (20)$$

$I(0)$  denotes the intensity which would be obtained for a flat water surface at the same point. The exponential intensity profile introduces a quadratic nonlinearity into the slope/intensity relation. However, the effects on the wave number spectra are small. As an example for a wave with  $s_1 = 0.5$ , a secondary peak will show up in the spectrum at twice the wave number with an amplitude of only 0.4% of the spectral density at the actual wave number. Even if the slope spectrum drops rapidly with the wave number, say proportional to  $k^{-4}$ , the spectral densities will only be in error by 6%.

Summarizing, we can say that the slight nonlinearities of the whole system do not affect the spectral densities to such an extent that it would be worthwhile to correct them. Likewise, it is not necessary to compensate for the sensitivity decrease proportional to the intensity  $I(0)$  in (19), since it acts as a windowing function which is applied to the images anyway, before performing the Fourier transform (see section 4.3.).

Though only either the along- or cross-wind slope of the waves is made visible, the images contain the directionality of the waves. A wave with the slope  $s_0$  traveling at an angle  $\Theta$  to the wind speed direction, shows along- and cross-wind slope components,  $s_0 \cos \Theta$  and  $s_0 \sin \Theta$ , respectively. In an angular sector of  $\pm 60^\circ$  the amplitude damping in the corresponding slope signal is less than a factor of 2.

### 3.3. Image Acquisition and Digitization

The images were acquired with a Siemens K230 interline transfer CCD camera. In order to obtain sharp images, the exposure time was limited to 1.7 ms by a chopper wheel rotating in front of the camera lens synchronously with the video signal. During the experiments the wave image sequences were recorded on a Umatic video tape recorder.

The images were digitized with a spatial resolution of  $512 \times 512$  pixels and 256 grey values (one byte per pixel), using an Imaging Technology FG100 image processing board in a 10 MHz PC-AT compatible personal computer. Since a full frame consists of two half frames which are individually illuminated with a time difference of 20 ms, only half frames with a horizontal (along-wind) and vertical (cross-wind) resolution of 512 and 256 pixels, respectively, were processed. The further features of the digitized images are summarized in Table 1.

### 3.4. Spatial Resolution

The spatial resolution of the images is limited by two effects. The first factor is the overall spatial transfer function of the electro-optical system from the camera lens, the CCD chip, and the videorecorder to the video signal processing prior to digitization. Measurements with test images containing fine lines yielded a steep cutoff at a wave number of  $1250 \text{ m}^{-1}$ , which is slightly more than half of the Nyquist wave number  $k_0$  (Table 1). The second factor is the blurring of the images

by the motion of the waves. If it is assumed that the intensity is constant during the exposure time  $\Delta t$ , the wave image sequence  $s(\mathbf{x}, t)$  is convolved along the time coordinate with a rectangular function  $\Pi$  of the width  $\Delta t$ .

$$s'(\mathbf{x}, t) = s(\mathbf{x}, t) * \Pi\left(\frac{t}{\Delta t}\right) \quad (21)$$

Consequently, the frequency spectrum is multiplied by the Fourier transform of  $\Pi$ , the sinc-function

$$\hat{s}'(\mathbf{k}, \omega) = \hat{s}(\mathbf{k}, \omega) \cdot \frac{\sin(\pi\Delta t\nu)}{\pi\Delta t\nu} \quad (22)$$

The sinc-function falls off to one half at a frequency  $\nu_c \approx 0.6033/\Delta t$ , which reduces to 355 Hz for the chosen exposure time of 1.7 ms. Even if we assume phase velocities as large as  $1 \text{ ms}^{-1}$  for these small waves (by advection with the orbital velocities of large waves), the corresponding wave number cutoff starts only at  $2230 \text{ m}^{-1}$ , which is just about the along-wind Nyquist wave number.

These simple estimates are supported well by measurements made without the mechanical chopper, i.e., an exposure time of 40 ms. The observed cutoff in the spectral densities was found to be in good agreement with (22).

It can be concluded that the spatial resolution is limited rather by the total transfer function of the setup than by the velocity smearing. Waves down to a wavelength of 0.5 cm can be measured without significant damping.

### 3.5. Calibration

The imaging slope gauge was calibrated with a "frozen wave" built from a thin transparent foil, which was bent into a sinusoidal shape by a surrounding frame. The whole device is put onto the water surface in such a way that the space below the foil is filled with water. This calibration wave has a wavelength of  $0.130 \pm 0.002 \text{ m}$  and a slope amplitude of  $0.484 \pm 5\%$ . Its size of  $74 \text{ cm} \times 103 \text{ cm}$  is large enough to fit into the largest sector to be measured. Figure 4 shows an intensity profile averaged over all lines with the wave aligned in the along-wind direction.

### 3.6. Nonlinearity

The overall nonlinearity of the imaging slope gauge was estimated by processing a sequence of images with the sinusoidal calibration wave. The second and third harmonics were found to be 0.3% and 0.018%, respectively, of the spectral densities of the main peak in the power spectra, which is in good agreement with the estimates discussed in section 3.1.

### 3.7. Noise Level

Data obtained as images contain only a low dynamic range because of the limited resolution, typically 8 bits. Thus, the information is easily corrupted by noise or artifacts in the images. Besides the electronic noise of the imaging CCD sensor, the video recording equipment, and the video analog-digital converter, there is another noise source, which is very difficult to handle:

small particles floating in the water and sedimenting onto the glass plate of the illumination source. As long as parts of the water surface are flat, these particles become visible and increase the noise level. When the water surface becomes rough they are no longer visible. Thus this noise source is signal-dependent and unpredictable. Consequently, the detection of ripples with low slopes at low wind speeds is the most critical issue. It turned out that the most reliable indicator is a direct comparison of the wave number spectra with the slope frequency spectra simultaneously obtained with the laser slope gauge (see section 5.2.).

Another problem is fixed patterns in the images. Even faint patterns which are not detectable by eye, can cause spikes in the spectrum. We observed spurious sensitivity changes from line to line in the image which resulted in peaks in the spectrum in the cross-wind direction.

## 4. WAVE IMAGE PROCESSING

Evaluation of image data involves the handling of huge amounts of data. Thus it is crucial to work with efficient data structures and algorithms. This section details all steps from the raw image data to the two-dimensional wave number spectra.

### 4.1. Noise Reduction by Median Filtering

It turned out that the digitized images contained a kind of gray-level-dependent "salt and pepper" noise which was caused by a small defect in the analog digital converter of the frame buffer. This effect could be detected only after contrast enhancement but caused an increase in the noise level in the spectra. Since it is basically white noise, it shows up as an increase  $\propto k^2$  in the degree of saturation of the spectra (Figure 5a).

A  $3 \times 3$  median filter was used to reduce this type noise efficiently. Unlike a linear convolution-type filter which simply multiplies the Fourier transform by some factor, a median filter is especially suitable to remove isolated distorted pixels in an image which increase the white noise level in the spectrum. Though the median filter is not directionally sensitive, it basically filters out the increasing spectral densities at high wave numbers in the cross-wind direction, which are reduced by almost a decade; in the along-wind direction, however, the spectral density is damped at most by 40%. (Figure 5b). This result clearly demonstrates that the median filter effectively removes the noise, but does not significantly damp high wave numbers. The damping by 40% is thus only an upper limit, since the median filter probably also removed some noise in the along-wind direction.

### 4.2. Subtraction of Least Squares Plane

The images contain waves with wavelengths larger than the imaged sector. Without any corrections, spectral leakage into the low wave number range would occur. In order to diminish this effect, each image was fitted by a plane with a least squares algorithm. The fitted plane was subtracted from the image. In this way, a zero-mean image is obtained, and the mean slope of large scale waves and the intensity gradient due to the

illumination is compensated for.

#### 4.3. Windowing

Windowing is especially important for two-dimensional data, since a rectangular window results in a star-like pattern in the spectra along the principal axes. We used a cos window (Hanning window).

#### 4.4. Two-Dimensional FFT

Because the intensity levels in the images are quantized with only 8-bit resolution, a 16-bit integer FFT algorithm provided sufficient accuracy. Whenever overflow occurred, the data were scaled down by a factor of 2 (block-floating). A separable radix-two FFT algorithm was used, which first transformed the rows and then the columns. The algorithm transforms the image in the frame buffer of the image processing system and is vectorized in the sense that all rows and columns are transformed simultaneously [Jähne, 1989a]. This procedure significantly reduces the overhead of the algorithm and thus avoids any trivial multiplication by checking the multiplication factor for trivial values such as 1, -1,  $i$ , or  $-i$ , before the butterfly operation is applied to a vector. The whole image evaluation including the steps described in sections 4.1–4.4. took about 1 min per image.

#### 4.5. Remapping the Power Spectra on a $(\ln k, \Theta)$ Grid

The mean power spectra are remapped on the  $(\ln k, \Theta)$  grid, which was introduced in section 2.3. The mapping itself is done by bilinear interpolation of the spectral densities between the four nearest neighbors on the Cartesian grid.

#### 4.6. Addition of Along- and Cross-Wind Slope Spectra

The last step yields the total slope spectrum by addition of the along- and cross-wind slope spectra according to (4). Figure 6 shows that there are actually cross-wind traveling waves present which would have been lost without measuring the cross-wind slope spectrum.

## 5. RESULTS

### 5.1. Summary

All measurements were obtained in the large wind-wave facility of Delft Hydraulics at a fetch of 100 m, 14°C water temperature, and neutral stability of the air flow. The friction velocities have been measured by KNMI with a pressure anemometer [Oost, 1983]. The experimental conditions are summarized in Table 2. From the measured friction velocities, equivalent wind speeds at a height of 10  $\text{ms}^{-1}$ ,  $U_{10}$ , have been calculated. In the following we refer to these values. Two-dimensional wave number spectra are available at seven wind speeds from 2.7 to 17.2  $\text{ms}^{-1}$ . Wave slope frequency spectra were obtained simultaneously with a laser slope gauge (Figure 7). These data are discussed in another paper (B. Jähne, in preparation, 1990) and are used here only to be compared with the two-dimensional wave number spectra. The vertical lines in Figure 7 indicate the sector of the spectrum which corresponds to the wave number spectra. All wave number spectra are summarized in Figure 8. The wave number spectra are

shown in a three-dimensional plot on a  $(\ln k, \Theta)$  grid and with a logarithmic scale for the degree of saturation  $B(k)$ . The plots cover wave numbers from 26.5 to 1701  $\text{m}^{-1}$  (wavelengths from 23.6 cm down to 0.36 cm) and an angular range of  $\pm 90^\circ$ . The full angular range of 360° cannot be resolved from single images, since they contain a 180° ambiguity, i. e., waves traveling with and against the wind direction cannot be distinguished.

At the lowest wind speed (Figure 8a) of 2.7  $\text{ms}^{-1}$ , the dominant wave is just within the measured wave number range. The frequency spectrum (Figure 7) gives a peak frequency of 2.8 Hz. Using the linear dispersion relation, this results in a wavelength of 20 cm in agreement with the position of the peak in the wave number spectrum. While the angular dispersion of the dominant wave is narrow it widens considerably towards smaller wavelengths. It is quite flat over a range of about  $\pm 45^\circ$  with a clear tendency towards a bimodal distribution. Beyond a wavelength of 6 cm, the spectral densities drop steeply until they reach a plateau with spectral densities about 1.5 decades lower. Again, the smallest waves show a smaller angular dispersion peaking in the along-wind direction, very similar to that of the dominant wave. The different spikes at  $\pm 90^\circ$  are remaining artifacts as discussed in section 3.7.

At higher wind speeds, the dominant wave is no longer contained within the measured wave number range. The features found at the lowest wind speed gradually change with increasing wind speed. The bimodal angular dispersion first becomes more pronounced, but then changes into a unimodal distribution which becomes continuously wider. The spectral densities for wavelengths between 0.5 and 3 cm strongly increase with wind speed and finally exceed the levels at larger wavelengths at the highest wind speed. Here, the angular dispersion is very wide. Cross-wind traveling waves show spectral densities not less than half of the values for along-wind waves.

After this general overview, a more specific and quantitative analysis of the data follows, based on  $k$  or  $\Theta$  profiles extracted from the two-dimensional data.

### 5.2. Wave Number Dependence

Figure 9 shows profiles at 0°, 30°, and 60° to the wind direction and one integrated over all angles, i. e., the unidirectional  $k$  spectrum. At low wind speeds, the spectral shape is governed by a strong decrease towards higher wave numbers, especially in the along-wind direction (Figure 9a). The profiles also show that the dominant peak is included only at the lowest wind speed of 2.7  $\text{ms}^{-1}$ . At moderate wind speeds, only the decrease from the dominant peak is observed, while at the highest wind speeds a small gravity wave range has obviously been established. The spectral peak at 17.2  $\text{ms}^{-1}$  is located at a frequency of 1 Hz in the frequency slope spectrum (Figure 7), corresponding to a wavelength of 1.56 m. Thus the dominant wave is separated by about one decade from the small gravity wave range at wavelengths from 5 to 20 cm. This should be a sufficient separation of the small gravity wave range from the dominant wave, though at sea it typically has a ten

times larger wavelength.

In the small gravity range, the degree of saturation increases. This increase depends on the propagation direction. While it is approximately proportional to  $k^{0.6}$  for the along-wind component, it is only  $\propto k^{0.35}$  in the unidirectional  $k$  spectrum. This means that these data support a  $k^{-3.5}$  height spectra for wavelengths between 3 cm and 24 cm, rather than a constant degree of saturation.

In a wave number range of about  $200\text{--}800\text{ m}^{-1}$  (0.75–3 cm wavelength), a plateau is reached where the degree of saturation is basically constant in the along-wind direction. At the lowest wind speeds of  $2.7\text{ ms}^{-1}$  and  $3.9\text{ ms}^{-1}$ , this plateau is obviously influenced by the noise level. While in the slope frequency spectra measured with the laser slope gauge the spectral densities continue to decrease even at the lowest wind speeds (Figure 7), they do not do so in the wave number spectra. In contrast to the plateau in the along-wind direction, the spectral densities at  $30^\circ$  and  $60^\circ$  decrease slowly with increasing wave number. This means that the angular dispersion is getting narrower towards higher wave numbers. The unidirectional spectra (Figure 9d) show the same trend.

Beyond a wave number of  $800\text{ m}^{-1}$ , the spectral densities fall off steeply. This cutoff is nearly independent of the wind speed. It seems to occur only at the lowest wind speeds, at a slightly higher wave number of  $1000\text{ m}^{-1}$ . The discussion in section 3.4. has shown that the resolution limit of the images lies at  $1250\text{ m}^{-1}$ . Thus, the strong decrease of the spectral densities beyond  $800\text{ m}^{-1}$  seems to be a real effect, although the shape of the cutoff may be influenced by the limited resolution and the median filtering. The hypothesis of a cutoff independent of the wind speed is also supported by the slope frequency spectra (Figure 7). Here the cutoff frequency increases only slightly with wind speed from about 65 Hz at  $7.3\text{ ms}^{-1}$  to about 100 Hz at  $17.2\text{ ms}^{-1}$ . This comparison also shows that a cutoff at  $k = 800\text{ m}^{-1}$  is reasonable, since it leads to mean phase velocities of  $50\text{ cms}^{-1}$  and  $78\text{ cms}^{-1}$ , respectively. These values, including the increase in the phase velocity, are reasonable since at higher wind speeds the orbital velocities advecting the small scale waves are significantly larger.

### 5.3. Wind Speed Dependence

The wind speed dependence of the degree of saturation shows a remarkable change with the wave number (Figure 10). Small gravity waves are much less dependent on the wind speed than are gravity-capillary and capillary waves. The unidirectional spectral densities for 6.3-cm and 12.5-cm waves are independent of the friction velocity up to a friction velocity of about  $0.3\text{ ms}^{-1}$ , where they start increasing, in approximate proportion to the friction velocity (Figure 10c). The same pattern can be observed for the along-wind component, with the exception that the 12.5-cm waves decrease first (Figure 10a). This effect is related to the fact that at low wind speeds the 12.5-cm wave comes closer to the along-wind traveling dominant wave.

In contrast, the spectral densities of capillary-gravity and capillary waves in the wavelength range of 0.7–3 cm strongly increase with friction velocity (Figure 10b and Figure 10d). The curves are S-shaped, with the steepest increase roughly  $\propto u_*^3$  at medium friction velocities. The mean exponents (disregarding the two lowest and the highest wind speed) are  $2.5 \pm 0.2$  and  $2.4 \pm 0.2$  for along-wind and unidirectional spectral densities, respectively. Very similar results have been found for slope frequency spectra in different wind-wave facilities, including the Delft facility [Jähne, 1989b].

### 5.4. Angular Dispersion

Finally, the two-dimensional wave number spectra allow us to investigate the angular dispersion of the waves. The significant deviations from the usually assumed  $\cos^p$ -type angular distributions have already been pointed out in the qualitative discussion of the two-dimensional spectra (Figure 8) in section 5.1. The deviations are most pronounced at low wind speeds (Figure 8a). At  $2.7\text{ ms}^{-1}$  the dominant wave shows a narrow angular dispersion around the along-wind direction, while small gravity waves of about 6 cm wavelength establish a bimodal distribution peaked at about  $\pm 45^\circ$ . Except for the higher background due to the higher noise level, the angular dispersion of the capillary waves is very similar to that of the dominant wave.

These features in the angular dispersion suggest that two processes determine the wave number spectra at this wind speed. First, the capillary waves seem to be generated by steep dominant gravity waves than directly by the wind. The observation that capillary waves occur as bursts of short, steep wave trains [Jähne, 1989b] supports this hypothesis. Secondly, the bimodal distribution of small gravity waves indicates that the dominant waves decompose by a two-dimensional instability process.

At higher wind speeds, the angular dispersion gradually becomes more uniform. At  $5.4\text{ ms}^{-1}$  there are still some indications of a bimodal distribution now shifted towards larger wavelengths (Figure 8c). In the gravity-capillary range the distribution is still flatter than with a  $\cos^p$ -type distribution.

## 6. CONCLUSIONS AND OUTLOOK

Viewed against the background of the theoretical discussion in section 2.4., the wave number spectra show a number of interesting and surprising features:

1. In the small gravity range (3–24 cm wavelength) and at higher wind speeds, the spectral densities behave approximately as expected from theories balancing the different terms of the energy flux in the gravity wave field. The height wave number spectrum goes approximately with  $k^{-3.5}$  and  $u_*$ . However, this does not mean that the data verify these theories. Inferring the energy balance from the spectral densities is rather an underdetermined inverse problem as is shown by the coinciding results of the theories based on quite different assumptions [Phillips, 1985 and Kitaigorodskii, 1983]. At lower wind speeds the dominant waves have wavelengths too short, even in the 100-m Delft facility. Thus the small gravity wave range is "contaminated" by them, and an

equilibrium range is not established.

2. The wave number spectra change significantly for waves shorter than 3 cm ( $k \approx 200 \text{ m}^{-1}$ ). Then the height wave number spectra goes with  $k^{-4}$  and strongly depends on the friction velocity ( $\propto u_*^{2.5}$ ). It is worthwhile to note that these changes do not occur right at the transition from gravity to capillary waves at  $\lambda = 1.73 \text{ cm}$  or  $k = 363 \text{ m}^{-1}$ , respectively, but at a wave number less than  $150 \text{ m}^{-1}$ . The significant change in the dependence on the friction velocity is a clear indicator that the energy balance for these shorter waves differs from the energy balance for gravity waves. The  $u_*^{2.5}$ -dependence comes close to the  $u_*^3$ -dependence of the wind input term. Consequently, the dissipation term seems to be only weakly dependent on the mean spectral energy density in this range.

3. The wind speed independent cutoff is another remarkable feature. This experimental fact stands in clear contrast to the assumption that the cutoff is determined by a balance between the wind input and viscous dissipation as discussed in section 2.4. Since all energy fluxes increase with wind speed except for viscous dissipation, a wind-speed-independent cutoff indicates that viscous dissipation seems to play only a minor role.

There is one direct observation from the wave images that were obtained supporting this idea. While at low wind speeds wave trains of capillary waves may be 10–20 wavelengths long, they range over only a few wavelengths at higher wind speeds [Jähne *et al.*, 1987]. Thus, the energy flux is very large at small wavelengths and the overall attenuation rate at high wind speeds is certainly higher than 0.3. In comparison, viscous dissipation is a weak process even at these small wavelengths. A wave with a wavelength of 7 mm has an attenuation rate of about 0.01 and 0.03 at a clean and a surface film covered surface, respectively [Phillips, 1980]. This rate is very low compared to the observed attenuation of the wavelets. This obvious discrepancy directs attention to other dissipation mechanisms such as turbulent damping. Especially important are more detailed studies on the propagation of capillary waves in the highly sheared current of the viscous boundary layer.

4. The data at low wind speed indicate that direct generation of capillary waves by steep unstable gravity waves seems to be a significant energy transfer mechanism. By its very nature, as a single-step process, it should be more efficient than a multistep cascade process.

In conclusion, the two-dimensional wave number spectra give some first insight into the energy balance of small scale waves, but it is not readily and unambiguously deferrable. By analyzing only mean wave number spectra, most information contained in the images is disregarded. Actually, image sequences from the waves contain the complete spatiotemporal information on the wave field, except for the limitations imposed by the size of the images. Thus, a promising research avenue opens up for other kinds of image sequence processing to investigate directly the energy cycling in the wave field. Tracing of individual wavelets should be one way to determine their mean lifetime and coherency lengths,

parameters that are not only of importance for a better understanding of water wave physics, but also to the radar remote sensing community. Digital image processing nowadays offers the tools for such detailed investigation of wave image sequences.

*Acknowledgments.* The authors would like to express their sincere thanks to their Dutch colleagues for the excellent and efficient cooperation in the frame of the VIERS project. The following organizations participated: The Royal Netherlands Meteorological Institute (KNMI), the Physics and Electronics Laboratory of the Netherlands Organization for Applied Research (TNO), the Technical University of Delft, and Delft Hydraulics. Financial support by the State of Baden-Württemberg (Federal Republic of Germany), the German Science Foundation, the European Community (twinning contract), and the Director's office of Scripps Institution of Oceanography is gratefully acknowledged. Part of the data evaluation has also been supported by a grant from the California Space Institute. The authors would also like to thank two anonymous reviewers for their detailed and helpful comments.

B. Jähne, Scripps Institution of Oceanography, Physical Oceanography Research Division, University of California, San Diego, La Jolla, CA 92093.

K. S. Riemer, Institut für Umweltphysik, University, Im Neuenheimer Feld 366, D-6900 Heidelberg, Federal Republic of Germany.

(Received August, 1989;  
accepted February 5, 1990.)

Copyright 1990 by the American Geophysical Union.

Paper number 90J00510  
0148-0227/90/JC-00510\$05.00

TABLE 1. Summary of the Features of the Digitized Wave Images

Feature	Horizontal Direction (Along-Wind)	Vertical Direction (Cross-Wind)
Size	66.35 cm	47.28 cm
Pixels	512	256
Spatial resolution	1.30 mm	1.85 mm
Maximum wave number	2424 m <sup>-1</sup>	1701 m <sup>-1</sup>

TABLE 2. Summary of the Evaluated Two-Dimensional Wave Number Spectra Measured in the Delft Wind-Wave Facility at a Fetch of 100 m

Reference Wind Speed $U_r$ (ms <sup>-1</sup> )	Friction Velocity $u_*$ (ms <sup>-1</sup> )	Wind Speed 10 m $U_{10}$ (ms <sup>-1</sup> ) <sup>a</sup>	Number of Frames <sup>b</sup>
2.12	0.073	2.7	95, 38
3.08	0.100	3.9	138, 113
4.20	0.140	5.4	116, 130
5.62	0.205	7.3	115, 109
6.78	0.269	8.9	104, 122
9.06	0.424	12.2	119, 119
12.4	0.722	17.2	152, 135

<sup>a</sup>Estimated from the measured friction velocities assuming a logarithmic wind profile.

<sup>b</sup>First figure along-wind, second cross-wind slope spectra.

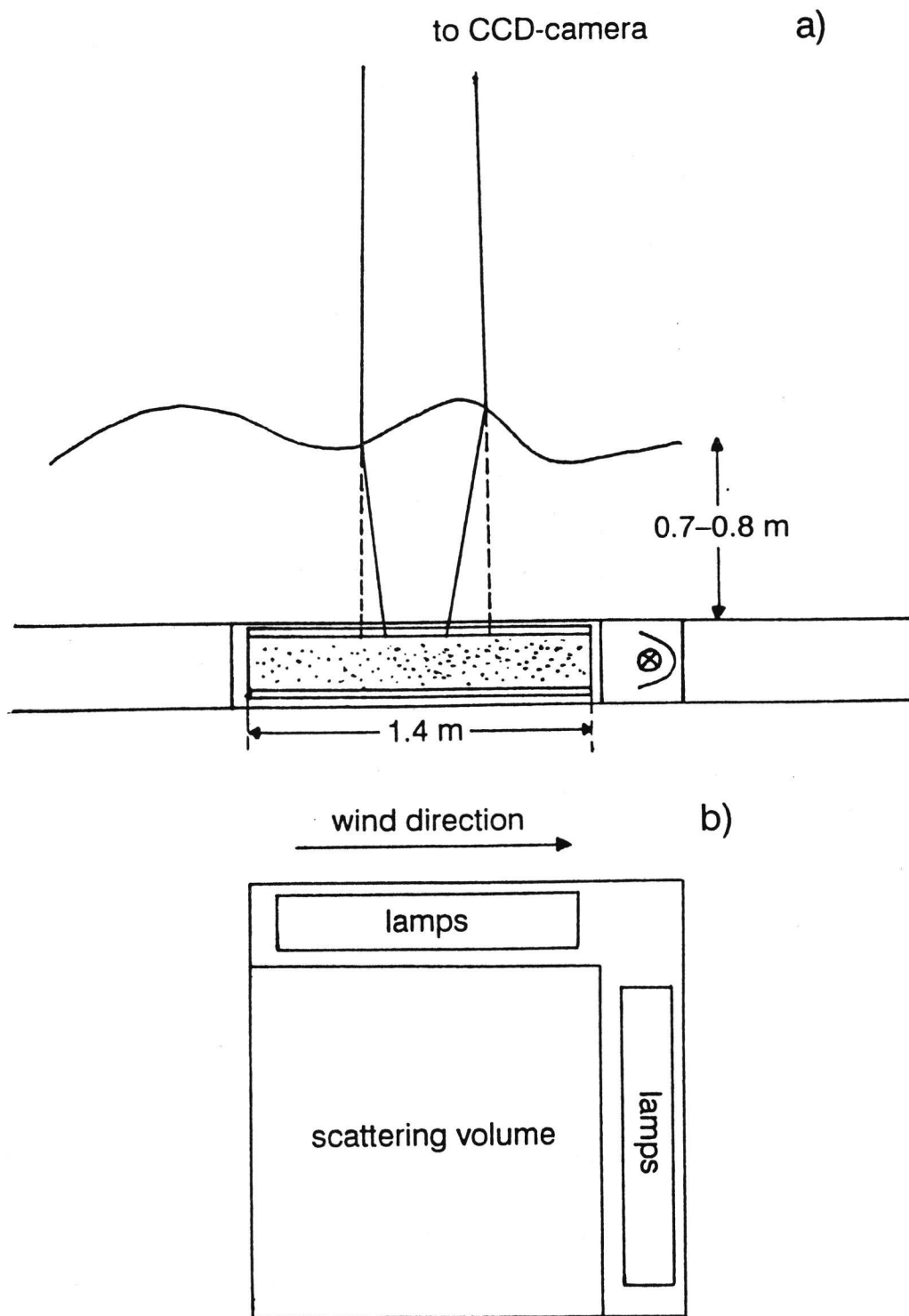


Fig. 1: Set up of the imaging slope gauge in the Delft wind-wave facility; a) cross section in wind direction; b) view onto the submerged illumination system from above.

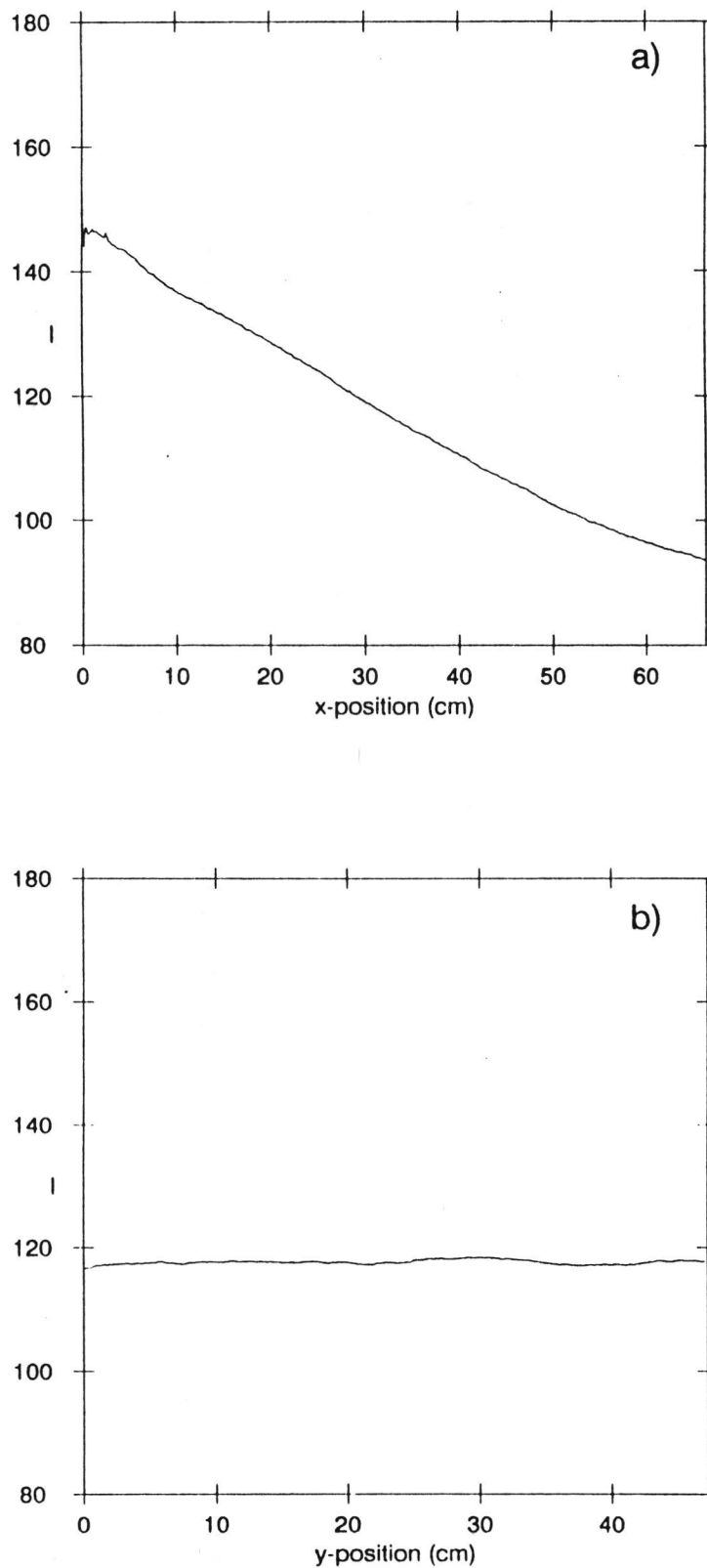


Fig. 2: Intensity profile in the image at a flat water surface with an along-wind illumination gradient; a) along-wind profile; b) cross-wind profile.

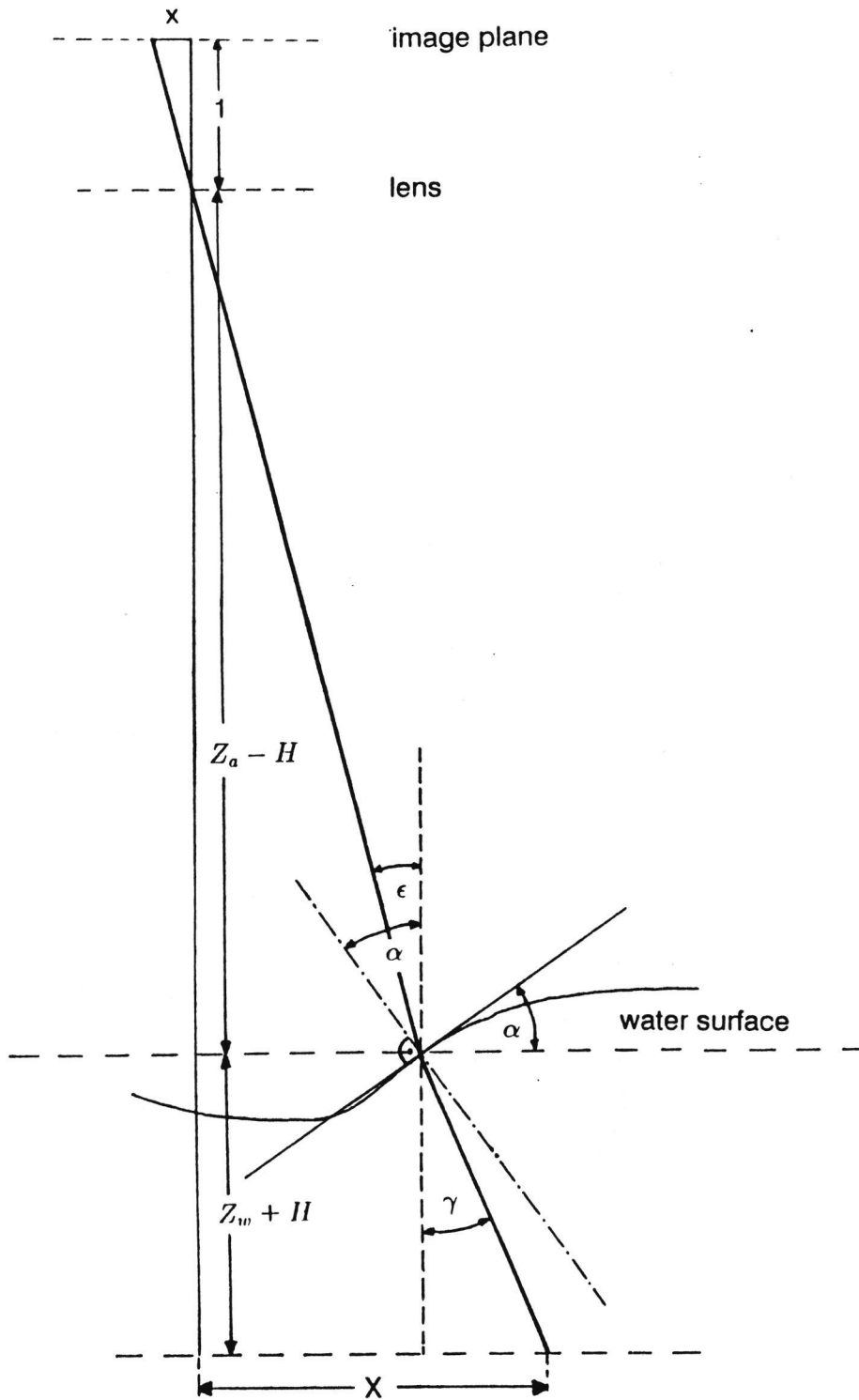


Fig. 3: Optical geometry of the imaging wave slope gauge.

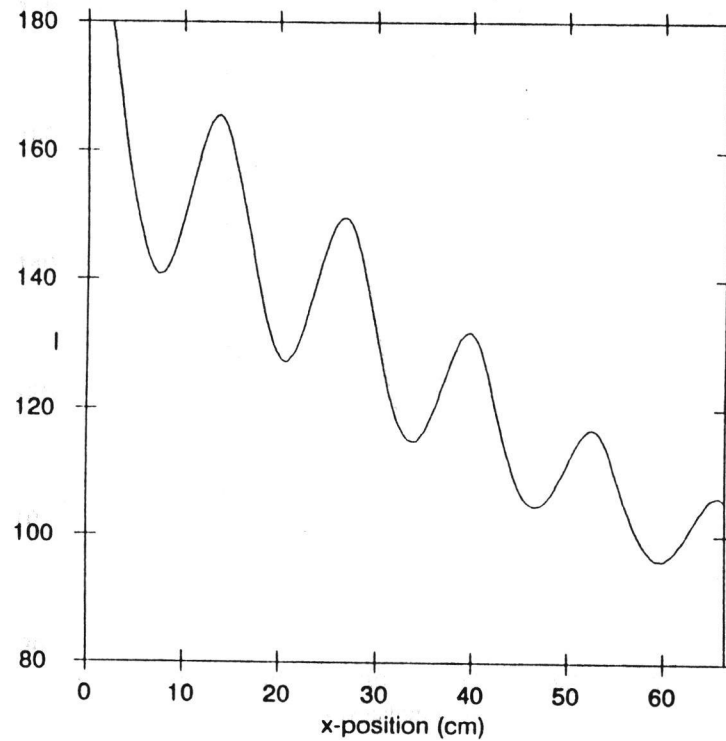


Fig. 4: Intensity profile of the calibration object, an artificial wave with  $\lambda = 13$  cm and a slope amplitude  $s_0 = 0.484$ . The wave and the illumination gradient are orientated along-wind.

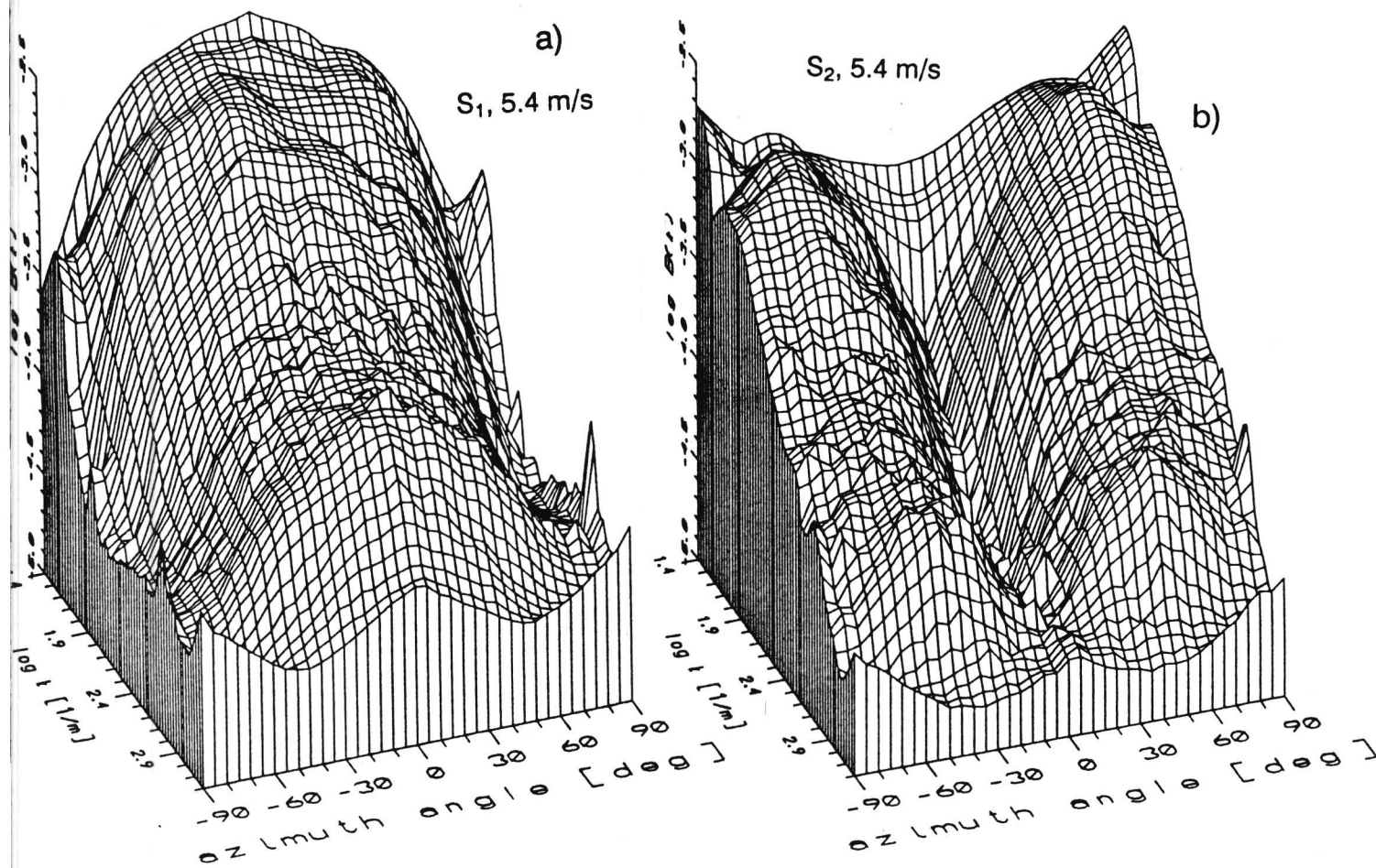


Fig. 6: a) Along- and b) cross-wind slope spectra at 5.4 m/s wind speed. The corresponding total slope spectrum as the sum of both is shown in Figure 8c.

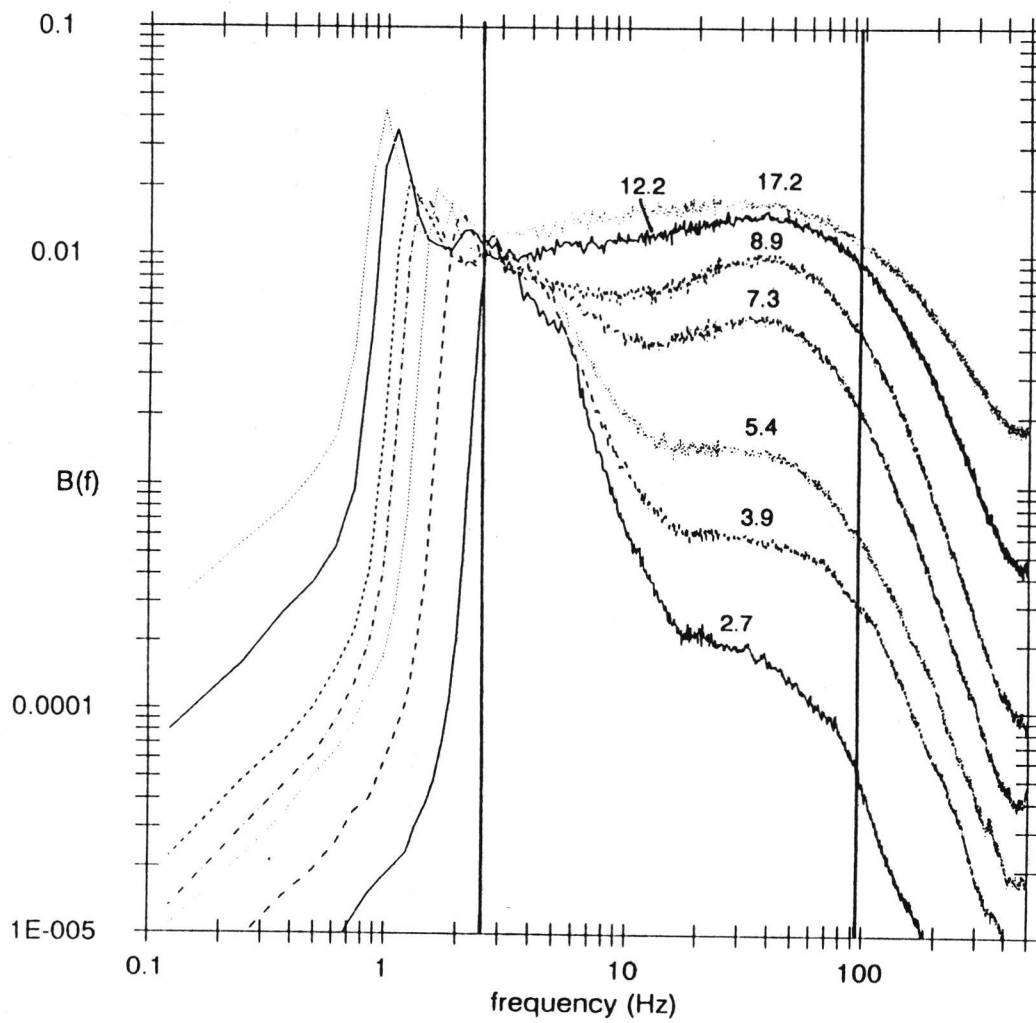


Fig. 7: Wave frequency spectra measured at the same wind speeds and about 90 m fetch with the laser slope gauge. The vertical lines mark the approximate range contained in the wavenumber spectra.

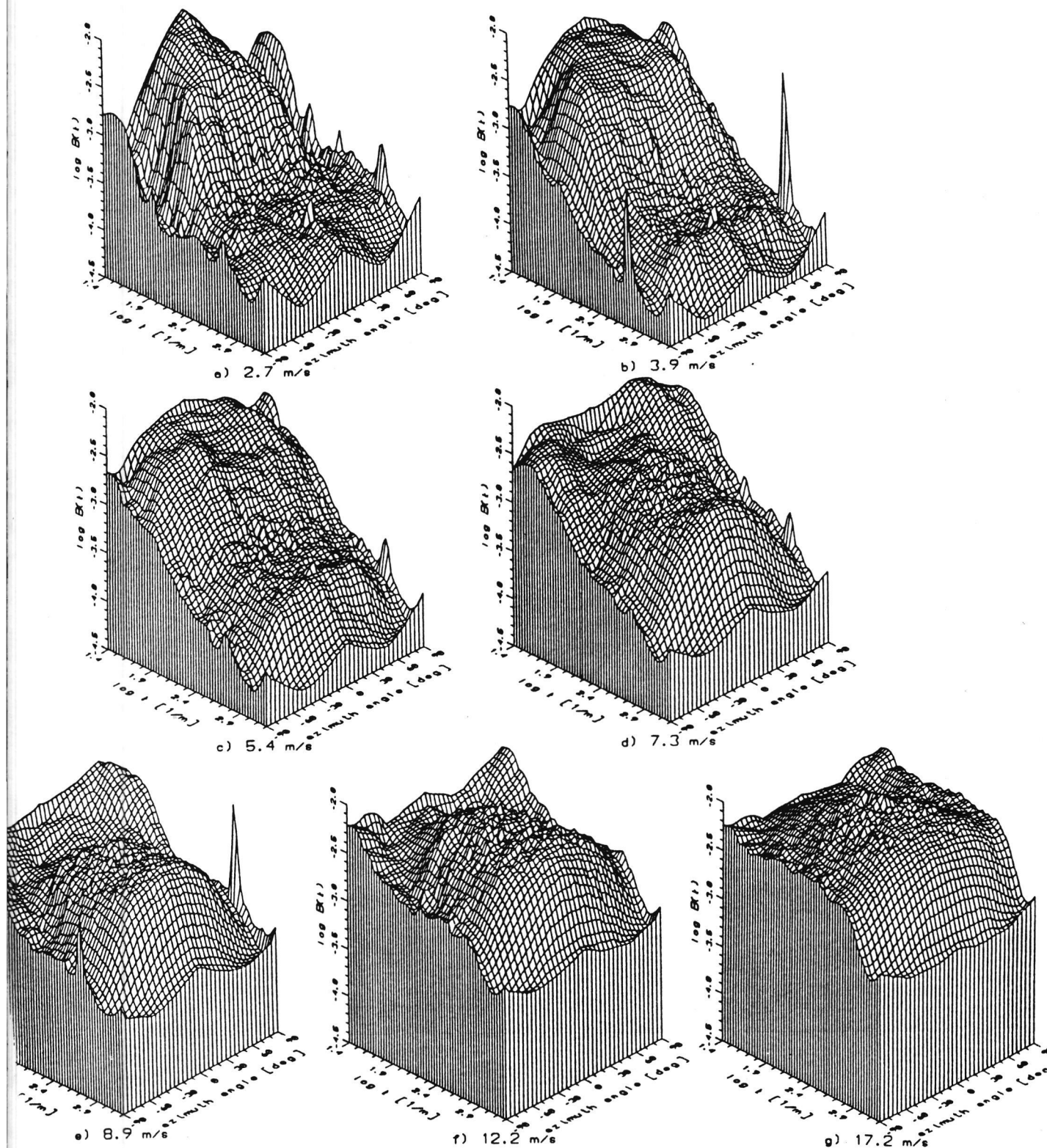


Fig. 8: Collection of all 2D-wavenumber spectra measured at 100 m fetch and represented as degree of saturation in a  $(\ln k, \Theta)$ -grid at wind speeds as indicated.

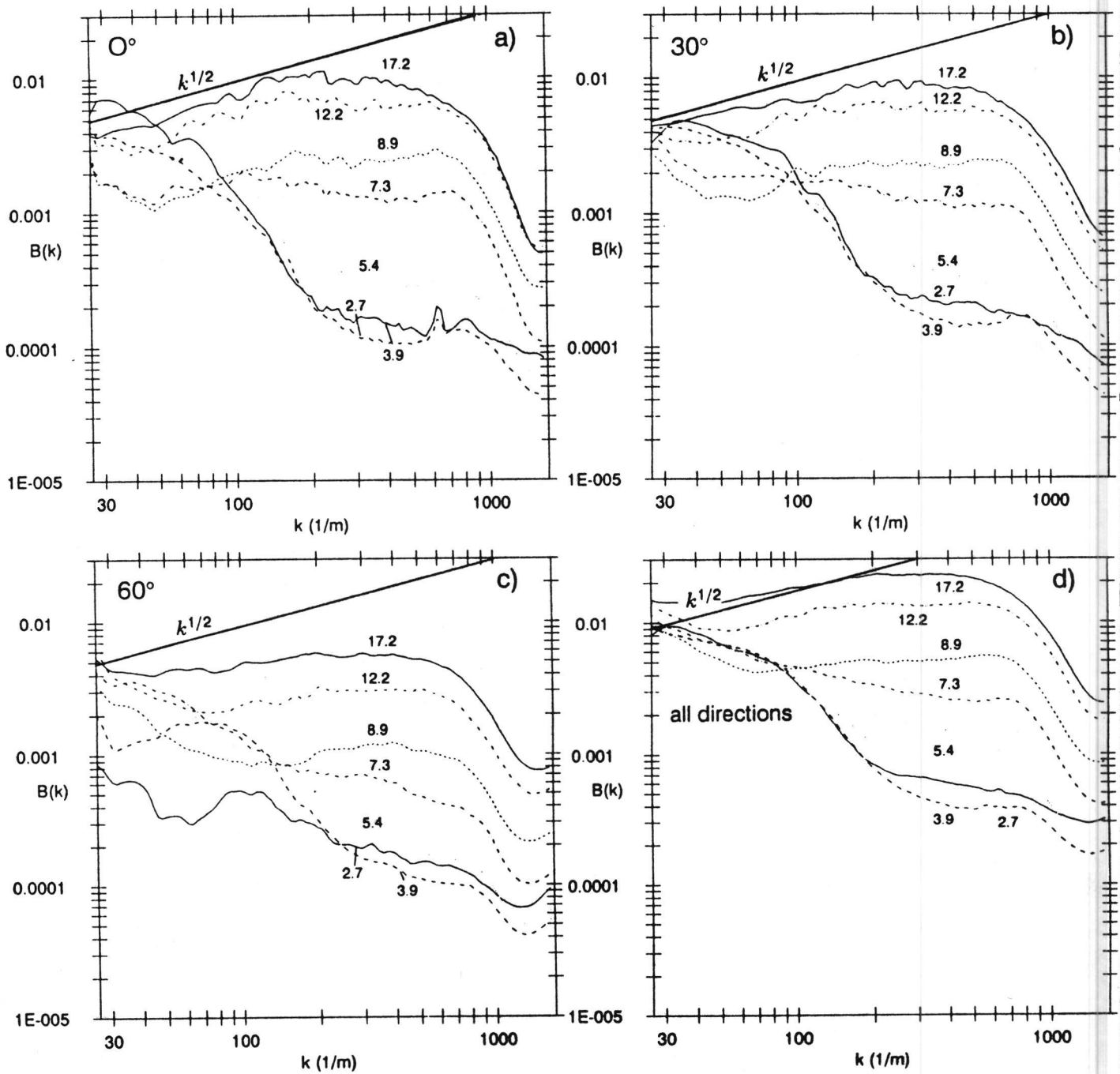


Fig. 9: Wavenumber spectra in different directions: a) along-wind ( $\pm 5^\circ$ ); b)  $30 \pm 5^\circ$ ; c)  $60 \pm 5^\circ$ ; d) unidirectional spectra integrated over all angles; wind speeds ( $U_{10}$  in m/s) as indicated.

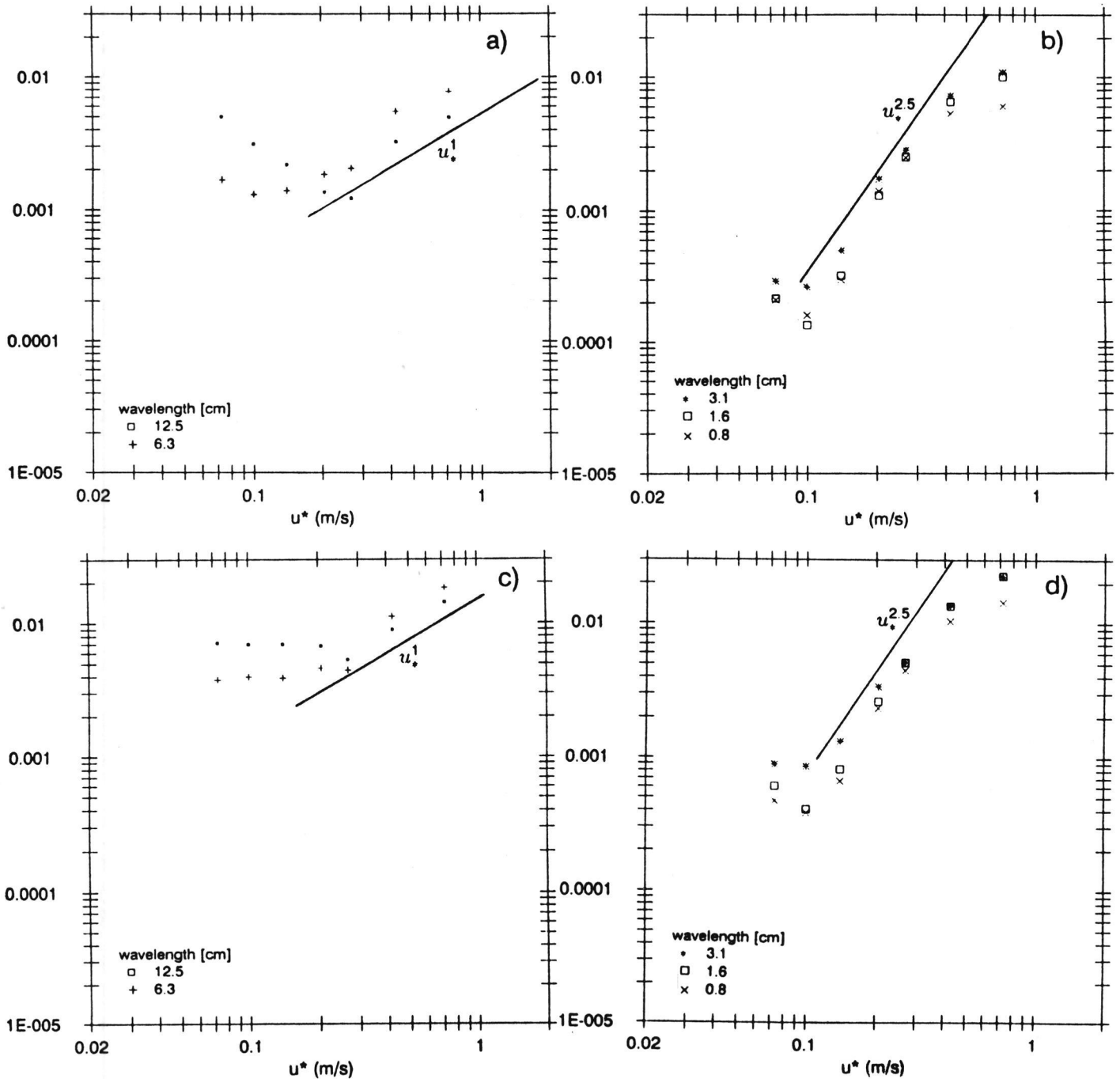


Fig. 10: Dependence of spectral densities on the friction velocity in different wavenumber ranges as indicated; a) small gravity waves, along-wind; b) gravity-capillary waves and capillary waves, along-wind; c) small gravity waves, unidirectional; d) gravity-capillary waves and capillary waves, unidirectional.

## Appendix D

### The Wind Profile in a Wave Tank

by

W.A. Oost

## THE WIND PROFILE IN A WAVE FLUME

BY  
W.A.OOST,

## 1. Introduction.

The study described in this paper arose from a program aimed at an improved understanding of the processes involved in the measurement of wind from space by radar scatterometry, especially from the scatterometer on board the European Remote-sensing Satellite, ERS-1. The program is called VIERS-1, a Dutch hybrid acronym for Preparation (Dutch: Voorbereiding) Interpretation ERS-1.

The program consists of two laboratory experiments, a field experiment and the development of an algorithm for the interpretation of scatterometer data. This paper discusses a problem we ran into in the course of the second laboratory experiment. This experiment took place in a large wave tank, the Delta flume of Delft Hydraulics, which is 230m long, 5m wide and 5m deep. We needed this large facility to study the influence of large waves (swell) on the radar reflective properties of the water surface (hydrodynamic modulation), which required "life size" waves. The Delta flume can produce waves with a height of up to 3 m, but it is an open wave tank with no wind facility. To convert it into a wind flume we covered the tank over a length of 150 m with a hood, taking care to make the inside as smooth as possible, and mounted two large wind machines, each with a maximum capacity of 100 m<sup>3</sup>/sec, at one end of the hood and an inlet-grating at the other. The machines could pull the air through this rather improvised wind tunnel at a speed of almost 10 m/s.

The basic atmospheric quantity for our experimental program is the turbulent flux of momentum from the mean air flow to the waves, embodied in the friction velocity  $u_*$ . We use the eddy-correlation method in which this momentum flux is measured as the mean value of the product  $u'_1 u'_3$ ,  $u'_1$  and  $u'_3$  being the turbulent fractions of respectively the horizontal and vertical wind component. In a conventional Cartesian coordinate system  $\langle -u'_1 u'_3 \rangle$  is positive (the angular brackets indicate a mean value) and  $u_*$  is defined by

$$u_*^2 = \langle -u'_1 u'_3 \rangle$$

The subject of this paper is a problem that arises when the anemometer to measure the flux is mounted at some distance from a wind tunnel wall (or floor, or ceiling) and the flux at that wall is needed. The flux cannot be considered as equal to the one at the wall when the distance is more than a few percent of that to the opposite wall, because the momentum flux has the opposite sign at each wall. We were forced to mount our anemometer (a pressure anemometer, see Oost, 1983) sufficiently far from the water surface, to protect it from being hit continuously by the waves.

Due to this requirement the distance from the mean water surface to the anemometer was indeed a fairly large fraction of the height of the flume, so we had to develop the method outlined below to calculate the properties of the flow at the water surface from our data.

## 2. The model.

To find a functional relation between the momentum flux and the distance to the wall we write down the momentum equation for a non-viscous fluid, and neglecting stability and Coriolis effects:

$$\frac{\partial U_i}{\partial t} + \frac{\partial}{\partial x_j} \left[ U_i U_j + \langle u'_i u'_j \rangle \right] = - \frac{1}{\rho} \frac{\partial P}{\partial x_i} + g_i$$

with  $U_i$  a component of the mean wind speed,  $t$  the time,  $x_j$  a Cartesian coordinate,  $\rho$  the air density,  $P$  the atmospheric pressure,  $g_i$  ( $= (0, 0, g)$ ) the gravity vector and the  $u'_i$  as before. In a stationary situation with no vertical wind we have for  $i=1$  and  $j=3$

$$\frac{\partial}{\partial x_3} \langle u'_1 u'_3 \rangle = - \frac{1}{\rho} \frac{\partial P}{\partial x_1}$$

which, assuming a constant downwind pressure gradient, leads to

$$u_*^2 = \langle u'_1 u'_3 \rangle = A x_3 + B,$$

a linear relation between the momentum flux to the wall and the distance.

In the literature on momentum flux measurements in wind tunnels we found two classical German publications by Reichart (1933, 1938), in which the author, making an ingenious use of hotwire measurements and photographic techniques (for his data registration), showed that in a rectangular wind tunnel the momentum flux outside the viscous boundary layer indeed varies linearly with the distance to the wall. Although his results were obtained in a wind tunnel with four identical walls, whereas we have different materials for the ceiling (plywood) and the floor (water), we nevertheless decided to check whether our data showed the same behavior:

$$u_* |u_*| = A z + B \quad (1)$$

in which  $z$  is the distance to the undisturbed water surface. The instruments were mounted at approximately equal distances from the side walls of the tunnel, so cross-stream effects should be small. We note here that near the walls, where viscous effects become important, (1) does not apply. Therefore, when we determine what we call " $u_*$  at the surface", we in fact calculate a hypothetical friction velocity for a non-viscous air flow. In the real situa-

tion a viscous sublayer prevents the air velocity from going to minus infinity at the wall, but this has no effect on the momentum transport outside that layer.

We also note that  $A < 0$  and  $B > 0$ , so  $u_*^2$  changes sign for

$$z = z_m = -B/A.$$

This is as expected: in the upper part of the flume the momentum flux is directed upward (the - turbulent - boundary layer of the ceiling), in the lower part downward (to the water). If the roughness of the water and that of the ceiling are not extremely different  $z_m$  is of the order of  $0.5 H$ , so  $A H / B = -H / z_m \cong -2$  (as stated already we tried to make the walls of the flume as smooth as possible). A consequence of the change of sign of (1) is that we have to make separate calculations for the lower ( $Az+B > 0$ ) and upper ( $Az+B < 0$ ) part of the flume.

The data were grouped according to the following characteristics:

- Horizontal position of the anemometer  
We used two different positions, one upwind and one downwind from the measuring section for the radar.
- Air-water temperature difference  $\Delta T$   
Four categories:  $\Delta T < -4$ ,  $-4 < \Delta T < 0$ ,  $0 < \Delta T < 4$ ,  $\Delta T > 4$
- Wave height and type of wave field  
Regular waves of 0, 0.3, 0.6 and 1 m height with a period of 11 sec.;  
Jonswap type spectrum at 3 energy levels.
- Wind speed (according to PA)  
4, 7 and 10 m/s.
- Vertical position of the anemometer  
0.6, 1 and 1.4 m above mean water level.

From sets of runs with the same characteristics, but for the vertical position of the anemometer, we found the change with height of  $u_*^2$ . These data indeed showed a height dependence that could well be approximated by a linear function as illustrated by figs. 1A and 1B. Extrapolation of the regression lines to the water surface provided us with the desired  $u_*$  values at the surface.

To find a relation between  $u_*$  at the surface and the wind speed measured at some height above the water we need a wind profile, characterized by a maximum wind speed  $v_{max}$  and a functional relationship between the wind speed and the distance to the water or a wall.

For this we assumed a mixing length relation between  $u_*$  and the mean wind speed gradient:

$$-u_*'w' = u_*^2 = \left( \ell \frac{dv(z)}{dz} \right)^2 \quad (2)$$

in which  $\ell$  is the mixing length and  $v(z)$  the mean wind speed at level  $z$ .

We now need  $\ell$  as a function of  $z$ . An acceptable formula for this relationship has to make allowance for both the lower and the upper boundary. We therefore used

$$\ell = \kappa \frac{z (H - z)}{H} \quad (3)$$

in which  $\kappa$  is the von Kármán constant (we use  $\kappa = 0.4$ ), and  $H$  the distance between the mean water level and the ceiling (3.4 m). In the limit for small  $z$  this approximates the usual formula for  $\ell$

$$\ell = \kappa z, \quad (z \ll H)$$

and near the ceiling

$$\ell = \kappa (H - z) \quad (z \cong H).$$

The combination of (1), (2) and (3) for  $z < z_m$  leads to

$$(A z + B)^{1/2} = \kappa \frac{z (H - z)}{H} \frac{dv}{dz} \quad (4)$$

or, with  $\xi = (A z + B)^{1/2}$  and  $B' = -(A H + B)$ :

$$v = \frac{2 H A}{\kappa} \int \frac{\xi^2 d\xi}{(B - \xi^2)(B' + \xi^2)} \quad (5)$$

This can be integrated analytically to

$$v = \frac{B^{1/2}}{\kappa} \left[ 2 \{-(1 + HA/B)\}^{1/2} \arctan \left\{ \frac{1 + Az/B}{-(1 + HA/B)} \right\}^{1/2} + \ln \left\{ \frac{1 - (1 + Az/B)^{1/2}}{1 + (1 + Az/B)^{1/2}} \right\} \right] + C$$

which, remembering that  $B^{1/2}$  is equal to the value of  $u_*$  at the surface,  $u_{*,0}$ , can be written as

$$v = \frac{u_{*,0}}{\kappa} \left[ 2 (H/z_m - 1)^{1/2} \arctan \left\{ \frac{1 - z/z_m}{H/z_m - 1} \right\}^{1/2} + \ln \left\{ \frac{1 - (1 - z/z_m)^{1/2}}{1 + (1 - z/z_m)^{1/2}} \right\} \right] + C. \quad (6A)$$

In the limit of small  $z$  the first term between the square brackets and the denominator of the logarithmic term become constants, which can be absorbed in  $C$ .  $v$  can then be approximated as

$$v = \frac{u_{*,0}}{\kappa} \ln z + C \quad (z \ll z_m, H),$$

the familiar formula for a logarithmic profile.

As stated, (6A) is valid for  $0 < z \leq z_m$ , the lower part of the flume, where the momentum flux is directed toward the water surface. The simplest way to derive a formula for the profile in

the upper part  $z_m \leq z < H$ , (where  $A z + B < 0$ , momentum flux toward the ceiling), is to use a new coordinate system, indicated with primes, in which  $z' = H - z$ ,  $u'^2 = -u^2$  and  $v'(z) = -v(z)$

In this system all equations are the same as in the unprimed one and

$$A' = A ; B' = -(A H + B)$$

so

$$v' = - \frac{B'^{1/2}}{K} \left[ 2 \{-(1 + H A' / B')\}^{1/2} \arctan \left\{ \frac{1 + A' z' / B'}{-(1 + H A' / B')} \right\}^{1/2} + \ln \left\{ \frac{1 - (1 + A' z' / B')^{1/2}}{1 + (1 + A' z' / B')^{1/2}} \right\} \right] - C'$$

which can be transformed into

$$v = \frac{u_{*,0}}{K} \left[ 2 \arctan(z/z_m - 1)^{1/2} + (H/z_m - 1)^{1/2} \ln \left\{ \frac{(H/z_m - 1)^{1/2} - (z/z_m - 1)^{1/2}}{(H/z_m - 1)^{1/2} + (z/z_m - 1)^{1/2}} \right\} \right] + C' \quad (6B).$$

Near the ceiling ( $z \approx H$ ) (6B) reduces again to a logarithmic profile. What remains is to calculate and interpret the coefficients  $C$  and  $C'$ . From (4) it is clear that  $dv/dz = 0$  for  $z = z_m = -B/A$ , so for  $z = z_m$  we find the maximum wind speed. If we introduce  $z = z_m$  in (6A) and (6B) we find  $v = C$ , respectively  $v = C'$ , so our conclusion is that

$$C = C' = v_{\max} \quad (7)$$

is the maximum wind speed.

### 3. Comparison with data

We tested the validity of the profile just derived by comparing it with our measurements. To this end we used the same grouping of the data as for fig. 1. For groups of runs with all parameters equal except the height of the anemometer above the water we calculated  $v(z) - C$  with (6A) and (6B), using the  $B$ 's and  $A$ 's derived earlier. From  $v(z) - C$  we calculated  $C$  with the measured values of  $v(z)$ .

If the tunnel had always been running at exactly the same speed for all runs of a group, the value of  $C$  should have been the same for all runs of that group. Slight differences in the wind speed during different runs introduced some variation. This we took care of by taking the mean value  $C_{\text{mean}}$  for the group and making (small) linear corrections to  $v(z)$  according to

$$v(z) = C_{\text{mean}} \times v(z)_{\text{meas}} / C_{\text{ind}}$$

in which  $v(z)_{\text{meas}}$  is the measured value of  $v(z)$  and  $C_{\text{ind}}$  the value of  $C$  calculated for that individual run. Strictly speaking the momentum fluxes should be corrected as well, but the corrections in  $C$  were sufficiently small to neglect this variation, as they would have led to changes in  $u_{*,0}$  well within the experimental error. The results of our calculations are shown in figures 2A and 2B for cases with regular waves. These cases were selected because they offered an full range of variations, as in both cases we had results available for three different anemometer heights for each curve and three groups of data as well.

#### 4. Conclusion

Figures 2A and B show an excellent correspondence between the measured wind speeds and the calculated profiles. This is quite satisfactory, as the basic parameters for the profiles were obtained from the turbulence measurements, whereas we now compare with the mean velocities, which were derived independently. Our conclusion therefore is that the new profile offers a useful and consistent framework for the interpretation of data in a wind tunnel with two different types of walls.

The results presented in figures 2A and B are for regular waves (wavelength 11 m) and unstable conditions ( $-4 < \Delta T < 0$ ). For these circumstances only we had sufficient data available viz. measurements with three categories of wave fields (wind waves, wind waves with 30 cm mechanical waves and wind waves with 1 m mechanical waves), at three levels above the water surface and at three nominal wind speeds (4, 7 and 10 m/s). We also used this data set for a regression calculation on both wave height  $H$  and mean wind speed  $U$ :

$$u_*^2 = D * H * U + E * U + F * H + G$$

With  $H$  in m and  $U$  in m/s we found  $D = -0.0005$ ,  $E = 0.025$ ,  $F = 0.021$  and  $G = -0.098$ . From these values we drew the inference that the wave dependence and the wind dependence of  $u_*^2$  are not independent, otherwise  $D/E$  would have had to be equal to  $F/G$  and  $D/F$  to  $E/G$ . We put the coefficients to good use, even though they have no direct physical meaning, by applying them to data obtained under different circumstances (different stability, wave field or horizontal position), to test their sensitivity to differences in the environmental conditions. In almost all cases the calculated  $u_*$  values showed a good correspondence with the measured ones. The only instance where we found large discrepancies was for irregular waves. This indicates that the transport of momentum under these conditions is different from that with regular waves, which is as expected because the drag of the air flow over the water surface is the result of a complex interaction process in which both small and large waves play their rôle (Janssen, 1989). Whether this would affect the relation between distance to the surface and momentum transport is a matter which we cannot check thoroughly with the available data. It does seem probable, though, in view of the already very different roughnesses of the ceiling and the water in our flume, that the assumption of linearity remains valid and that our asymmetric profile is generally applicable for the air flow in wave flumes.

## REFERENCES

- Oost, W.A., 1983: The pressure anemometer - an instrument for adverse circumstances. *J. Climate Appl. Meteor.*, 22, 2075-2084.
- Janssen, P.A.E.M., 1989: Wave-induced stress and the drag of air flow over sea waves. *J. Phys. Ocean.*, 19, 745-754.
- Reichart, H., 1933: Die quadratischen Mittelwerte der Längsschwankungen in der turbulenten Kanalströmung, *Zeitschr. f. angew. Math. und Mech.*, 13, 358-361.
- Reichart, H., 1938: Messungen turbulenter Schwankungen, *die Naturwissenschaften*, 24/25, 404-408.

## FIGURE CAPTIONS

Figure 1A. The momentum flux  $u_*|u_*|$  as a function of height above the water surface. The wave field consisted of wind waves and mechanical waves of 30 cm height and a wave length of 11 m. Data are shown for three wind speeds: squares : 4 m/s; "+" signs : 7 m/s; diamonds: 10 m/s. Lines are least squares fits.

Figure 1B. As figure 1A, for a fixed wind speed of 7 m/s and three wave fields. Wave heights: squares: only wind waves; "+" signs: wind waves and 30 cm mechanical waves; diamonds: wind waves and 1 m mechanical waves. The mechanical waves had a wavelength of 11 m.

Figure 2A. Wind profiles calculated according to (6A) and (6B) and experimental values for the mean wind speed. All data are for 30 cm mechanical waves with a length of 11 m. Wind speeds: squares: 4 m/s; diamonds: 7 m/s; "x" signs: 10 m/s.

Figure 2B. As figure 2A, but with data for a nominal wind speed of 7 m/s. Wave heights: squares: only wind waves; diamonds: wind waves and 30 cm mechanical waves; "x" signs: wind waves and 1 m mechanical waves.

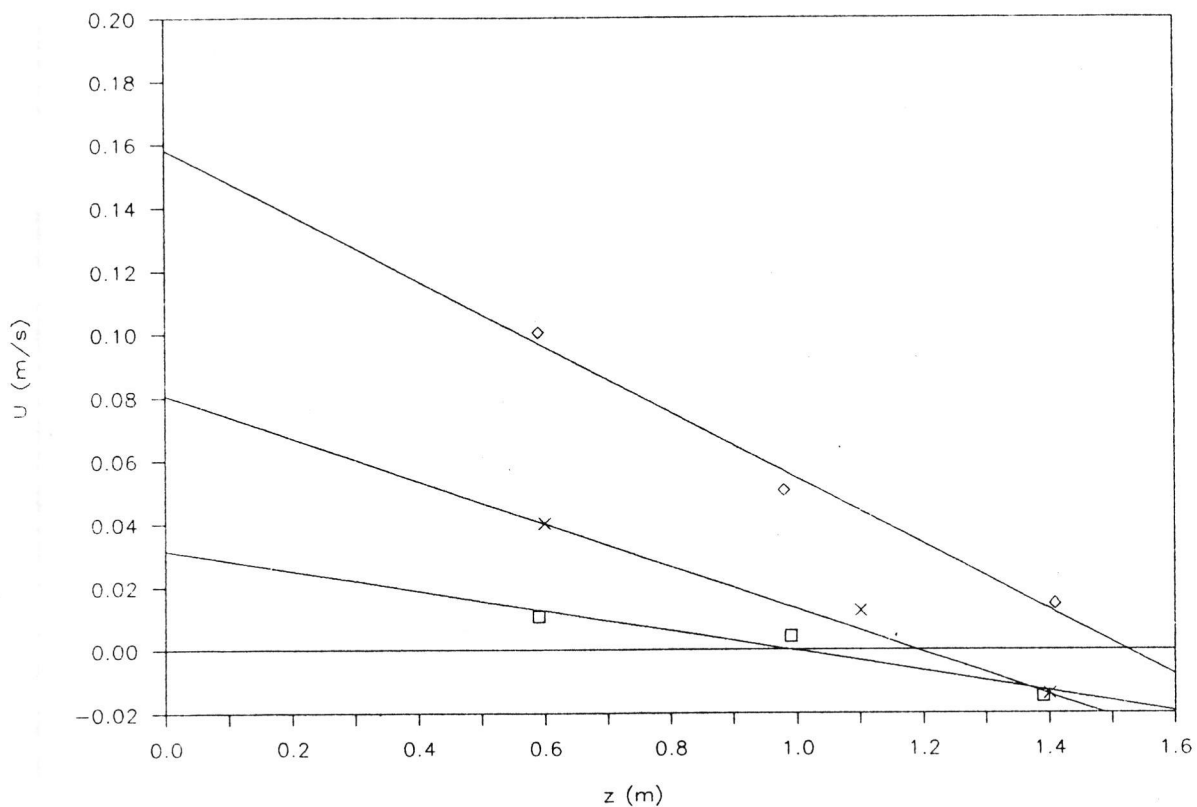


Figure 1A

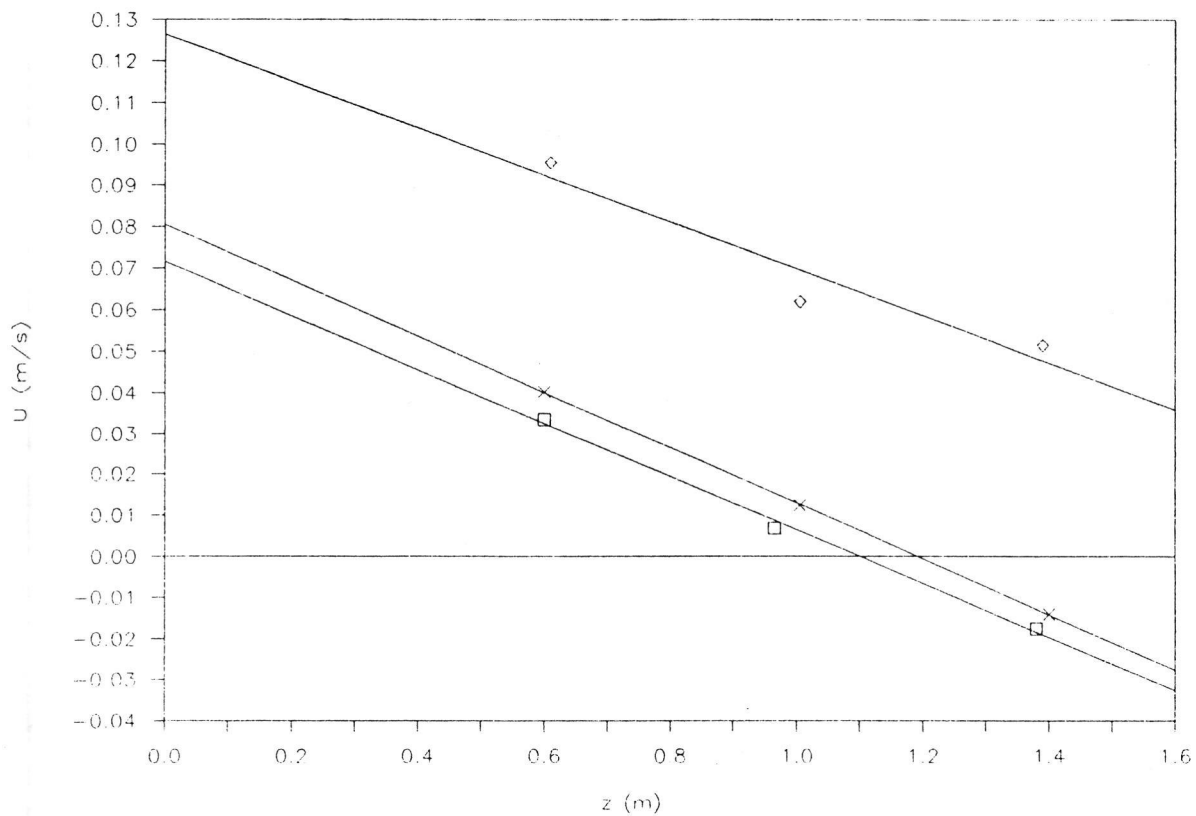


Figure 1B

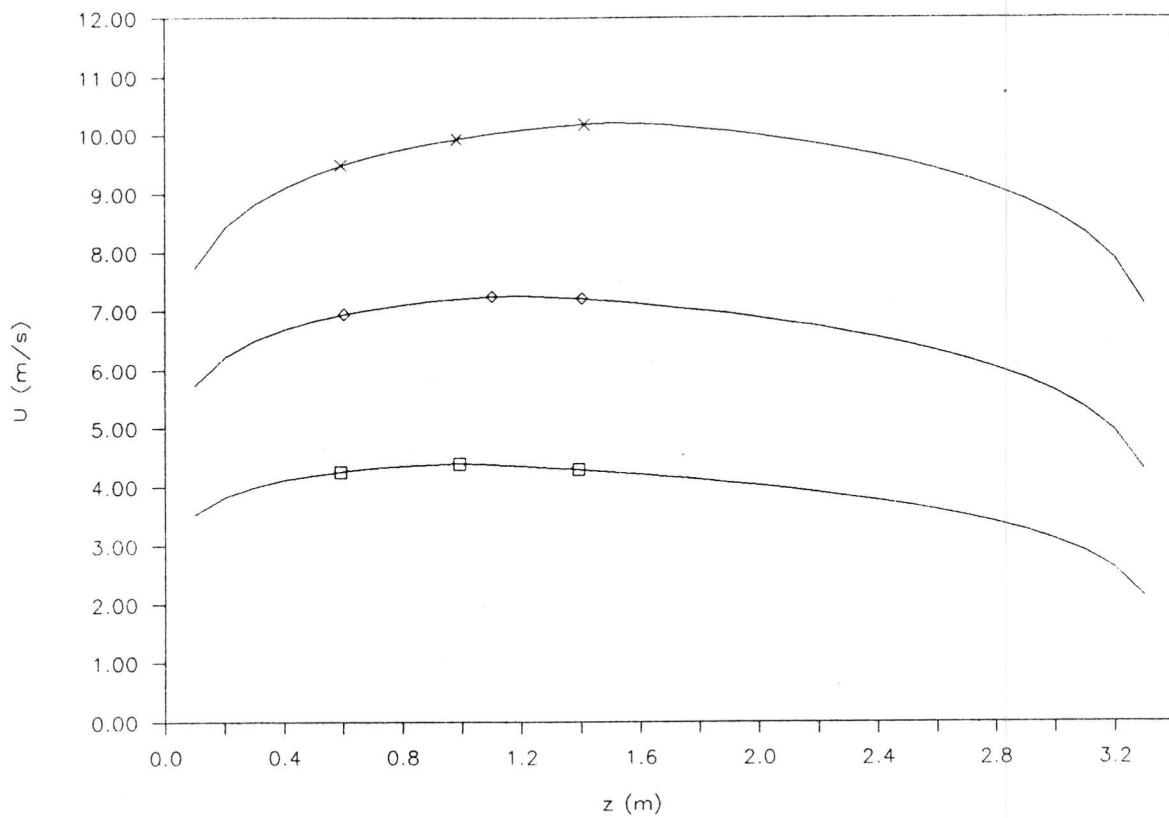


Figure 2A

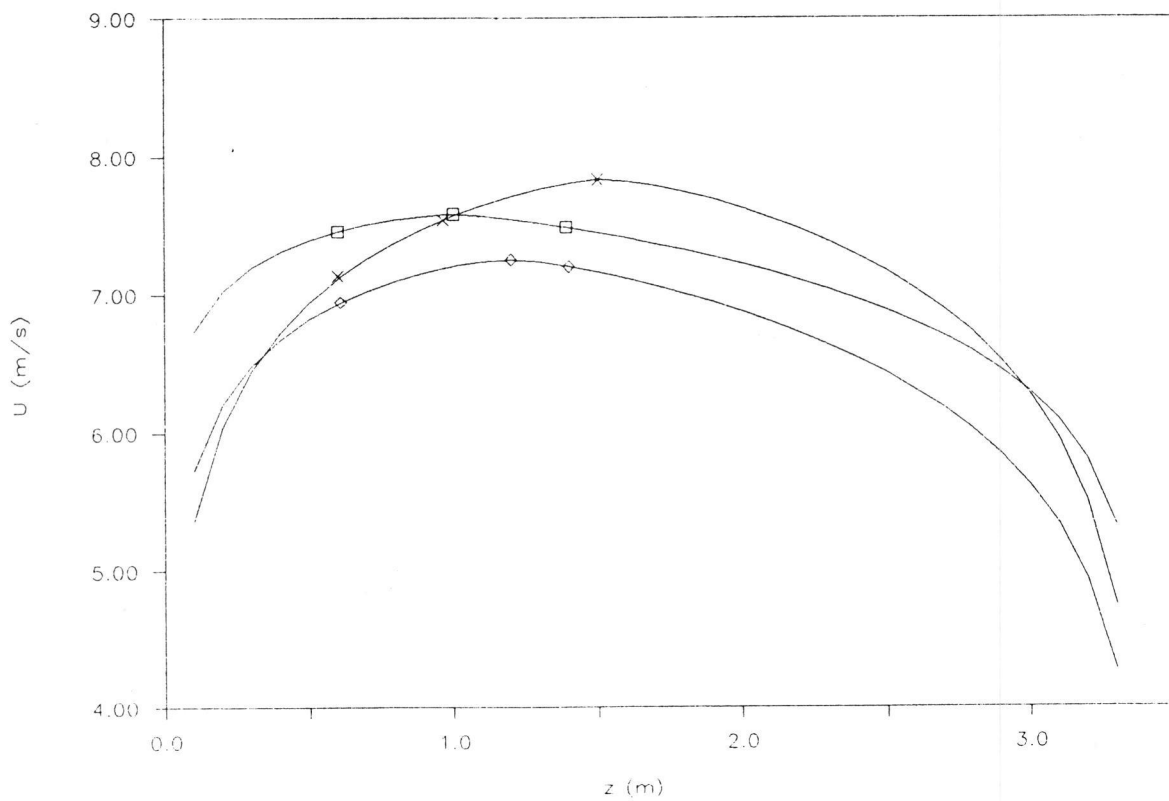


Figure 2B

## Appendix E

### Conditions for 'de Voorst' measurements

TABLE 1 RESULTS METEO MEASUREMENTS DE VOORST

KNMI RUN: Run number meteo data  
TNO RUN : Run number radar data  
CUP1, CUP2, DANT: Wind speeds as measured by respectively two cup anemometers (mounted at fixed places) and a Dantec Flowmaster wind meter, mounted beside the Pressure Anemometer (PA) and at the same level.

Ta : Air temperature  
Tw : Water temperature  
Q : Relative humidity  
P : Atmospheric pressure (outside the flume).  
WHGT : Wave height (nom=nominal value in meters, m=measured mean value, also in meters).  
WLNG : Wave length  
Hpa : Distance from sensor head PA to the ceiling of the flume.  
Upa : Wind speed as measured by the PA  
Zpa : Distance from sensor head PA to the undisturbed water surface.  
Vs,0 : Maximum wind speed, calculated from the measurements and the model wind profile.  
u\* : Friction velocity at the water surface.  
Cd : Drag coefficient relative to the Vs,0.

KNMI RUN	TNO RUN	DATE	CUP1 m/s	CUP2 m/s	DANT m/s	Ta C	Tw C	Ta-Tw C	Q %	P hPa	WHGT nom.	WHGT m.	WLNG m	Hpa m	Upa m/s	Zpa m	Vs,0 m/s	u* m/s	Cd *1000
3	401	10/03/89	4.24	4.21	4.86	12.20	8.37	3.83	66	1020	0.60	0.71	11	2.00	4.36	1.38	4.49	0.163	1.32
4	401	10/03/89	4.24	4.25	4.73	12.40	8.39	4.01	65	1020	0.60	0.71	11	2.50	4.31	0.88	4.32	0.150	1.20
6	402	10/03/89	4.31	4.25	4.89	13.20	8.26	4.94	64	1019	0.00	0.04	0	2.00	4.42	1.39	4.42	0.111	0.63
7	402	10/03/89	4.32	4.20	4.77	13.30	8.26	5.04	63	1019	0.00	0.03	0	2.50	4.40	0.89	4.49	0.117	0.68
9	403	10/03/89	6.49	6.38	7.76	13.50	8.34	5.16	63	1019	0.60	0.72	11	2.00	7.48	1.38	7.48	0.315	1.78
10	403	10/03/89	6.03	6.51	7.45	13.50	8.35	5.15	64	1019	0.60	0.73	11	2.50	7.41	0.88	7.62	0.321	1.78
11	403	10/03/89	6.34	6.34	7.11	13.30	8.39	4.91	65	1019	0.60	0.72	11	3.00	7.17	0.39	7.92	0.332	1.76
12	403	10/03/89	6.23	6.34	7.09	12.00	8.60	3.40	73	1019	0.60	0.73	11	3.00	7.12	0.41	7.94	0.333	1.76
15	405	13/03/89	4.01	4.36	4.69	9.18	9.03	0.15	75	1004	0.00	0.04	0	2.00	4.30	1.37	4.30	0.096	0.50
16	406	13/03/89	6.32	6.76	7.45	8.30	9.16	-0.86	84	1004	0.00	0.07	0	2.00	7.63	1.38	7.71	0.306	1.58
17	407	13/03/89	8.42	9.03	9.71	8.52	9.15	-0.63	79	1006	0.00	0.10	0	2.00	10.40	1.37	10.42	0.402	1.48
20	409	13/03/89	3.99	4.39	4.73	8.07	9.06	-0.99	77	1010	0.30	0.37	11	2.00	4.38	1.39	4.47	0.140	0.99
21	410	13/03/89	5.99	6.66	7.15	6.65	9.15	-2.50	90	1010	0.30	0.36	11	2.00	7.25	1.40	7.30	0.298	1.67
22	411	13/03/89	8.14	8.69	9.77	6.25	9.17	-2.92	96	1011	0.30	0.38	11	2.00	10.00	1.41	10.03	0.395	1.55
24	413	13/03/89	6.43	6.90	7.64	6.91	9.14	-2.23	89	1012	1.00	1.17	11	2.00	7.59	1.39	7.96	0.345	1.88
26	415	13/03/89	6.45	6.98	7.59	7.75	9.13	-1.38	77	1013	J10	0.49	0	2.00	7.61	1.38	7.61	0.269	1.25
28	417	13/03/89	8.02	8.59	9.65	7.67	9.15	-1.48	75	1015	J5	0.27	0	2.00	9.82	1.39	9.89	0.333	1.13
34	422	14/03/89	4.13	4.47	0.00	9.20	8.63	0.57	67	1016	0.60	0.71	11	2.00	4.47	1.38	4.49	0.163	1.32
35	-	14/03/89	4.11	4.45	0.00	9.31	8.63	0.68	66	1016	0.60	0.71	11	2.40	4.46	0.98	4.37	0.154	1.24
36	-	14/03/89	4.16	4.45	0.00	9.72	8.58	1.14	66	1016	0.60	0.71	11	2.80	4.45	0.59	4.39	0.155	1.25
37	423	14/03/89	8.09	8.61	0.00	9.70	8.54	1.16	67	1015	0.60	0.70	11	2.40	10.10	1.00	10.22	0.407	1.59
38	-	14/03/89	8.07	8.62	0.00	9.96	8.55	1.41	65	1015	0.60	0.69	11	2.80	9.85	0.60	10.49	0.415	1.57
39	424	14/03/89	3.96	4.23	0.00	10.20	8.53	1.67	63	1015	0.60	0.71	11	2.80	4.17	0.61	4.39	0.155	1.25
40	-	14/03/89	4.01	4.28	0.00	10.10	8.54	1.56	61	1015	0.60	0.72	11	2.40	4.27	1.01	4.37	0.154	1.25
41	425	14/03/89	6.36	6.77	0.00	10.10	8.58	1.52	61	1015	0.60	0.72	11	2.40	7.43	1.02	7.63	0.321	1.77
42	-	14/03/89	6.43	6.86	0.00	10.10	8.57	1.53	60	1014	0.60	0.72	11	2.80	7.49	0.62	8.01	0.335	1.75
44	426	14/03/89	6.41	6.81	0.00	10.40	8.53	1.87	55	1014	0.60	0.72	11	2.80	7.54	0.63	8.01	0.335	1.75
45	-	14/03/89	6.04	6.83	0.00	10.40	8.56	1.84	55	1014	0.60	0.72	11	2.40	7.54	1.04	7.63	0.321	1.77
46	427	14/03/89	8.01	8.44	9.58	9.65	8.63	1.02	61	1013	0.60	0.71	11	2.40	9.97	1.05	10.22	0.407	1.59
47	-	14/03/89	7.88	8.37	9.41	9.52	8.65	0.87	60	1012	0.60	0.71	11	2.80	9.87	0.66	10.49	0.415	1.57
53	432	16/03/89	6.25	6.27	7.17	3.81	9.02	-5.21	99	998	0.00	0.07	0	2.80	7.52	0.54	7.76	0.308	1.58
54	432	16/03/89	6.32	6.34	7.40	4.16	8.95	-4.79	98	998	0.00	0.07	0	2.40	7.63	0.93	7.66	0.304	1.58
55	432	16/03/89	5.95	6.09	7.63	4.72	8.91	-4.19	97	998	0.00	0.07	0	2.00	7.62	1.33	7.67	0.305	1.58
56	433	16/03/89	3.92	4.08	4.42	5.18	8.88	-3.70	96	997	0.00	0.04	0	2.80	4.56	0.54	4.73	0.141	0.89
57	433	16/03/89	3.88	4.00	4.56	5.34	8.86	-3.52	96	997	0.00	0.03	0	2.40	4.58	0.94	4.62	0.130	0.80
58	434	16/03/89	3.86	4.02	4.46	5.49	8.86	-3.37	96	997	0.00	0.04	0	2.80	4.58	0.54	4.73	0.141	0.89
59	434	16/03/89	3.87	4.04	4.57	5.68	8.87	-3.19	95	997	0.00	0.04	0	2.40	4.63	0.94	4.62	0.131	0.80
60	435	16/03/89	7.91	8.07	8.94	5.76	8.84	-3.08	94	997	0.00	0.10	0	2.80	9.89	0.53	10.57	0.406	1.48
61	435	16/03/89	8.03	8.23	9.45	5.69	8.85	-3.16	94	997	0.00	0.10	0	2.40	10.10	0.92	10.19	0.394	1.50
64	438	17/03/89	3.95	4.18	4.69	6.07	8.69	-2.62	86	1003	0.30	0.37	11	2.80	4.38	0.58	4.38	0.132	0.91
65	438	17/03/89	3.98	4.02	4.74	6.01	8.68	-2.67	86	1003	0.30	0.37	11	2.40	4.45	0.98	4.32	0.127	0.86
66	439	17/03/89	7.97	8.19	9.57	5.52	8.69	-3.17	87	1004	0.30	0.38	11	2.40	10.00	0.98	10.21	0.401	1.54
67	440	17/03/89	7.79	7.91	9.48	5.58	8.69	-3.11	86	1004	0.30	0.38	11	2.40	9.87	0.99	10.21	0.401	1.54
68	440	17/03/89	7.65	7.78	9.17	5.75	8.70	-2.95	85	1004	0.30	0.38	11	2.80	9.59	0.59	10.41	0.407	1.53
69	441	17/03/89	3.73	3.81	4.50	6.08	8.68	-2.60	83	1005	0.30	0.36	11	2.80	4.11	0.60	4.38	0.132	0.90
70	441	17/03/89	3.69	3.81	4.57	6.34	8.64	-2.30	83	1005	0.30	0.37	11	2.40	4.18	1.00	4.32	0.127	0.86
71	442	17/03/89	7.67	7.98	9.55	5.88	8.59	-2.71	80	1007	0.30	0.37	11	2.40	9.92	0.98	10.21	0.400	1.54
72	442	17/03/89	7.65	7.86	9.32	6.16	8.55	-2.39	76	1007	0.30	0.37	11	2.80	9.74	0.58	10.41	0.407	1.52
73	443	17/03/89	5.88	6.16	7.18	6.59	8.53	-1.94	74	1008	0.30	0.35	11	2.80	7.14	0.59	7.37	0.301	1.66
74	443	17/03/89	5.85	6.17	7.27	6.71	8.51	-1.80	75	1008	0.30	0.35	11	2.40	7.20	1.00	7.15	0.292	1.66
75	444	17/03/89	5.06	5.74	7.15	6.20	8.52	-2.32	79	1009	0.30	0.35	11	2.40	7.00	1.01	7.15	0.292	1.66
76	444	17/03/89	5.68	5.91	7.06	6.65	8.51	-1.86	72	1009	0.30	0.35	11	2.80	6.96	0.61	7.37	0.301	1.66
77	446	17/03/89	5.84	6.21	7.20	6.85	8.40	-1.55	59	1010	J3	0.16	0	2.80	7.12	0.57	7.41	0.254	1.18
78	446	17/03/89	5.94	6.20	7.29	6.63	8.40	-1.77	59	1010	J3	0.17	0	2.40	7.15	0.97	7.16	0.246	1.18
79	446	17/03/89	5.85	6.16	7.42	6.51	8.40	-1.89	58	1011	J3	0.16	0	2.00	7.09	1.38	7.16	0.245	1.17
80	447	17/03/89	5.79	6.09	7.39	6.16	8.39	-2.23	64	1015	J3	0.17	0	2.40	7.10	0.98	7.16	0.246	1.18

KNMI RUN	TNO RUN	DATE	CUP1 m/s	CUP2 m/s	DANT m/s	Ta C	Tw C	Ta-Tw C	Q %	P hPa	WHGT nom.	WHGT m.	WLNG m	Hpa m	Upa m/s	Zpa m	Vs,0 m/s	u* m/s	Cd *1000
81	447	17/03/89	5.75	5.98	7.17	5.86	8.43	-2.57	71	1015	J3	0.16	0	3.00	6.92	0.38	7.45	0.256	1.18
82	448	17/03/89	7.07	8.41	9.75	3.42	8.66	-5.24	82	1013	J5	0.26	0	2.80	10.20	0.58	10.50	0.349	1.10
83	448	17/03/89	7.76	8.49	9.93	3.38	8.67	-5.29	82	1014	J5	0.28	0	2.40	10.40	0.98	10.40	0.347	1.11
84	448	17/03/89	7.77	8.49	9.56	3.29	8.67	-5.38	82	1014	J5	0.27	0	3.00	9.91	0.39	10.59	0.351	1.10
85	449	17/03/89	7.68	8.42	9.87	2.94	8.68	-5.74	86	1014	J5	0.28	0	2.80	10.20	0.60	10.50	0.349	1.11
86	450	17/03/89	7.05	8.06	9.71	2.50	8.70	-6.20	89	1015	J5	0.26	0	2.80	10.20	0.61	10.50	0.349	1.10
87	450	17/03/89	7.51	8.24	9.82	2.54	8.71	-6.17	89	1015	J5	0.27	0	2.60	10.20	0.81	10.28	0.343	1.11
93	455	18/03/89	4.22	4.36	4.76	7.19	7.90	-0.71	63	1021	J10	0.46	0	2.80	4.54	0.58	4.65	0.138	0.88
94	455	18/03/89	4.25	4.39	4.99	7.08	7.88	-0.80	61	1021	J10	0.49	0	2.40	4.65	0.99	4.65	0.139	0.89
95	456	18/03/89	6.22	6.46	7.63	6.74	7.94	-1.20	57	1021	0.00	0.07	0	2.40	7.58	0.99	7.43	0.295	1.58
96	456	18/03/89	6.28	6.52	7.40	7.20	7.98	-0.78	53	1021	0.00	0.06	0	2.80	7.50	0.60	7.75	0.308	1.58
97	457	18/03/89	7.93	8.40	9.72	6.96	8.03	-1.07	55	1021	J10	0.49	0	2.80	10.20	0.60	10.79	0.360	1.11
98	457	18/03/89	7.93	8.40	9.92	7.23	8.05	-0.82	56	1021	J10	0.52	0	2.40	10.30	1.01	10.48	0.353	1.13
99	458	18/03/89	4.17	4.29	4.88	7.96	8.01	-0.05	51	1021	1.00	1.17	11	2.40	4.57	0.99	4.63	0.197	1.80
100	458	18/03/89	4.23	4.32	4.70	7.83	8.00	-0.17	50	1021	1.00	1.17	11	2.80	4.52	0.59	4.78	0.206	1.85
101	-	18/03/89	4.24	4.35	4.70	7.79	7.99	-0.20	51	1021	1.00	1.17	11	2.80	4.51	0.59	4.78	0.206	1.85
102	459	18/03/89	7.93	8.28	9.58	7.20	8.06	-0.86	53	1021	1.00	1.16	11	2.80	10.20	0.59	11.04	0.439	1.58
103	459	18/03/89	8.01	8.33	9.95	7.69	8.07	-0.38	54	1021	1.00	1.15	11	2.40	10.30	1.00	10.57	0.426	1.62
104	460	18/03/89	6.28	6.48	7.19	7.89	7.94	-0.05	52	1020	1.00	1.16	11	2.80	7.36	0.61	8.49	0.363	1.82
105	460	18/03/89	6.19	6.33	7.60	7.59	7.96	-0.37	53	1020	1.00	1.18	11	2.40	7.54	1.01	8.20	0.353	1.86
108	464	20/03/89	6.86	6.50	7.18	10.40	7.90	2.50	64	1006	1.00	1.15	11	2.80	7.26	0.58	8.01	0.346	1.87
109	464	20/03/89	6.08	6.40	7.51	10.80	7.85	2.95	63	1006	1.00	1.15	11	2.40	7.39	0.98	7.71	0.335	1.89
110	465	20/03/89	8.57	8.66	9.67	11.00	7.82	3.18	66	1005	J10	0.51	0	2.40	10.10	0.97	10.18	0.345	1.15
111	465	20/03/89	8.54	8.68	9.33	10.70	7.90	2.80	68	1005	J10	0.48	0	2.80	9.86	0.58	10.31	0.348	1.14
113	467	20/03/89	4.22	4.19	4.59	9.88	8.15	1.73	76	1005	1.00	1.18	11	2.40	4.26	0.98	4.27	0.174	1.65
114	467	20/03/89	4.14	4.25	4.36	9.80	8.15	1.65	76	1005	1.00	1.20	11	2.80	4.16	0.58	4.26	0.174	1.67
115	468	20/03/89	8.12	8.28	8.41	8.43	8.21	0.22	87	1005	1.00	1.17	11	2.80	9.14	0.58	10.20	0.416	1.66
116	469	20/03/89	8.41	8.59	8.98	7.18	8.42	-1.24	90	1006	1.00	1.17	11	2.80	9.77	0.57	11.04	0.439	1.58
117	469	20/03/89	8.42	8.57	9.43	7.12	8.42	-1.30	89	1006	1.00	1.18	11	2.40	9.84	0.97	10.57	0.427	1.63
118	470	20/03/89	8.38	8.51	9.44	7.14	8.44	-1.30	88	1005	0.00	0.10	0	2.40	9.93	0.96	10.19	0.394	1.50
119	471	20/03/89	6.34	6.53	7.16	7.25	8.43	-1.18	87	1005	0.00	0.06	0	2.40	7.22	0.94	7.43	0.295	1.57
122	475	22/03/89	6.67	6.84	7.33	11.40	8.13	3.27	85	1006	0.60	0.71	11	2.80	6.72	0.59	7.45	0.314	1.78
123	475	22/03/89	6.71	6.84	7.39	11.40	8.15	3.25	84	1006	0.60	0.72	11	2.40	6.81	0.99	7.12	0.301	1.79
124	476	22/03/89	8.77	8.90	9.66	11.50	8.18	3.32	83	1006	0.60	0.70	11	2.40	9.32	0.99	9.55	0.387	1.64
125	476	22/03/89	8.78	8.84	9.62	11.40	8.18	3.22	84	1006	0.60	0.70	11	2.80	9.19	0.60	9.82	0.395	1.62
126	477	22/03/89	6.73	6.82	7.36	11.70	8.15	3.55	83	1005	0.60	0.71	11	2.80	6.75	0.60	7.45	0.314	1.78
127	478	22/03/89	8.69	8.91	9.51	11.70	8.14	3.56	80	1004	0.60	0.70	11	2.40	9.20	1.01	9.55	0.387	1.64
128	478	22/03/89	8.51	8.55	9.37	11.60	8.16	3.44	80	1004	0.60	0.70	11	2.80	8.63	0.62	9.82	0.395	1.62
129	479	22/03/89	6.64	6.81	7.27	11.40	8.19	3.21	79	1004	J3	0.15	0	2.80	6.71	0.57	7.59	0.260	1.18
130	479	22/03/89	6.69	6.81	7.31	11.40	8.18	3.22	79	1004	J3	0.15	0	2.40	6.70	0.98	7.28	0.249	1.17
131	480	22/03/89	8.76	8.89	9.63	11.20	8.21	2.99	80	1004	J5	0.27	0	2.40	9.27	0.98	9.39	0.319	1.15
132	480	22/03/89	8.08	8.77	9.58	11.10	8.21	2.89	81	1003	J5	0.28	0	2.80	9.21	0.59	9.73	0.329	1.14
133	481	22/03/89	6.65	6.72	7.23	11.10	8.23	2.87	82	1003	J3	0.15	0	2.80	6.61	0.60	7.59	0.260	1.18
134	481	22/03/89	6.57	6.72	7.24	11.00	8.23	2.77	83	1003	J3	0.17	0	2.40	6.67	1.00	7.28	0.250	1.18
135	482	22/03/89	8.68	8.81	9.48	10.60	8.27	2.33	88	1003	J5	0.27	0	2.40	9.17	1.00	9.39	0.319	1.15
136	482	22/03/89	8.66	8.82	9.45	11.00	8.25	2.75	85	1003	J5	0.27	0	2.80	9.15	0.61	9.73	0.328	1.14
139	487	28/03/89	9.22	8.15	9.71	17.60	7.94	9.66	62	1012	J10	0.47	0	2.40	9.10	0.97	9.18	0.317	1.19
140	488	28/03/89	6.61	6.75	7.66	19.90	7.89	12.01	51	1013	J3	0.16	0	2.40	6.81	0.97	7.42	0.255	1.18
141	488	28/03/89	6.63	6.83	7.68	19.80	7.79	12.01	51	1013	J3	0.15	0	2.40	6.81	0.58	7.74	0.266	1.18
142	489	28/03/89	8.92	8.49	9.94	20.00	7.80	12.20	48	1013	J10	0.48	0	2.40	9.33	0.98	9.40	0.323	1.18
143	490	28/03/89	4.06	4.36	4.96	20.00	7.88	12.12	42	1013	0.60	0.70	11	2.40	3.90	0.61	3.90	0.110	0.79
144	490	28/03/89	4.57	4.31	4.95	20.00	7.89	12.11	42	1013	0.60	0.70	11	2.40	3.92	0.62	3.92	0.113	0.83
145	491	28/03/89	4.04	4.33	4.94	20.00	7.97	12.03	44	1013	0.60	0.71	11	2.40	3.92	0.62	3.92	0.113	0.83
146	492	28/03/89	8.09	8.69	9.74	19.00	8.07	10.93	54	1013	J5	0.25	0	2.40	8.88	0.57	9.23	0.314	1.16

## Appendix F.1

## Figures chapter 2

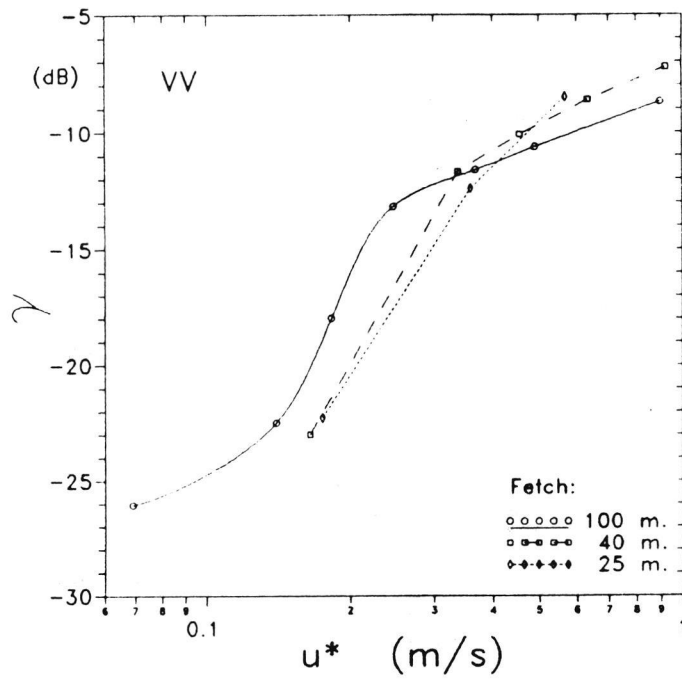


Figure 2.1: Dependence of the reflection coefficient  $\gamma$  on the friction velocity  $u_*$  for VV polarization. The incidence angle  $\phi = 45^\circ$ , azimuth  $\alpha = 0^\circ$ .  $\circ = 100$  m fetch,  $\square = 40$  m fetch,  $\diamond = 25$  m fetch.

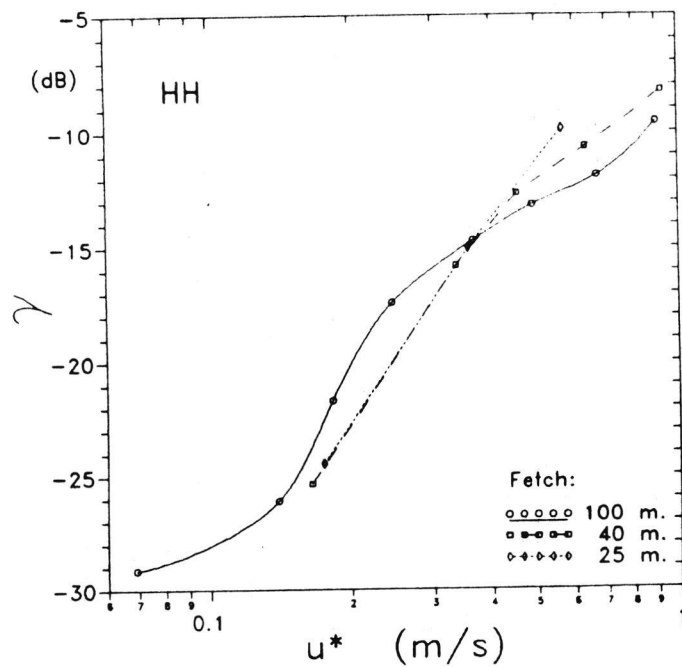


Figure 2.2: Dependence of the reflection coefficient  $\gamma$  on the friction velocity  $u_*$  for HH polarization. The incidence angle  $\phi = 45^\circ$ , azimuth  $\alpha = 0^\circ$ .  $\circ = 100$  m fetch,  $\square = 40$  m fetch,  $\diamond = 25$  m fetch.

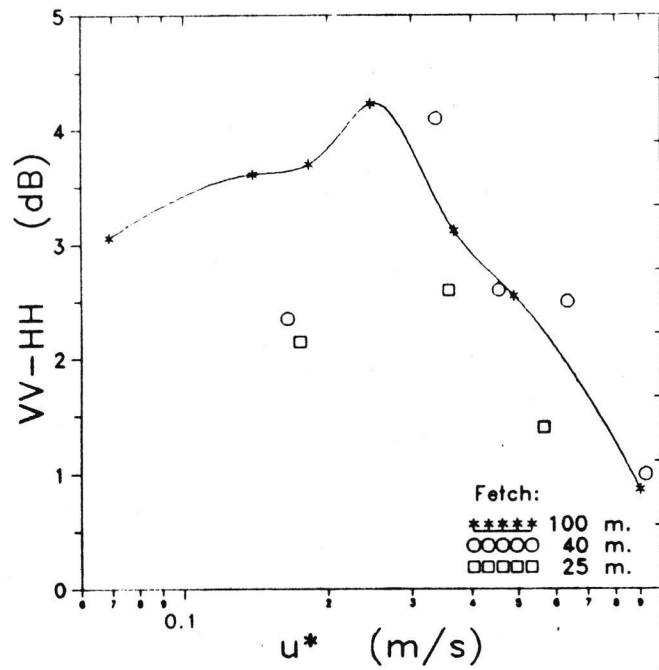


Figure 2.3: Ratio of VV and HH polarized reflection coefficient in dB's as a function of the friction velocity  $u_*$ . The incidence angle  $\phi = 45^\circ$ , azimuth  $\alpha = 0^\circ$ .  $\star = 100$  m. fetch,  $\circ = 40$  m fetch and  $\square = 25$  m fetch.

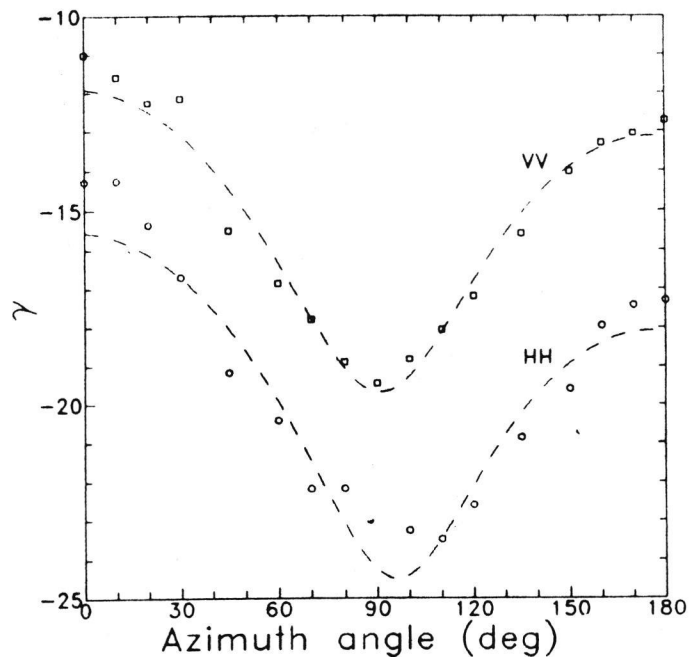


Figure 2.4: Azimuth dependence of the reflection coefficient. Incidence angle  $45^\circ$ , friction velocity  $u_* = 0.34$  m/s at a fetch of 100 m. The dashed lines are fits of the empirical model described by equation 2.1.

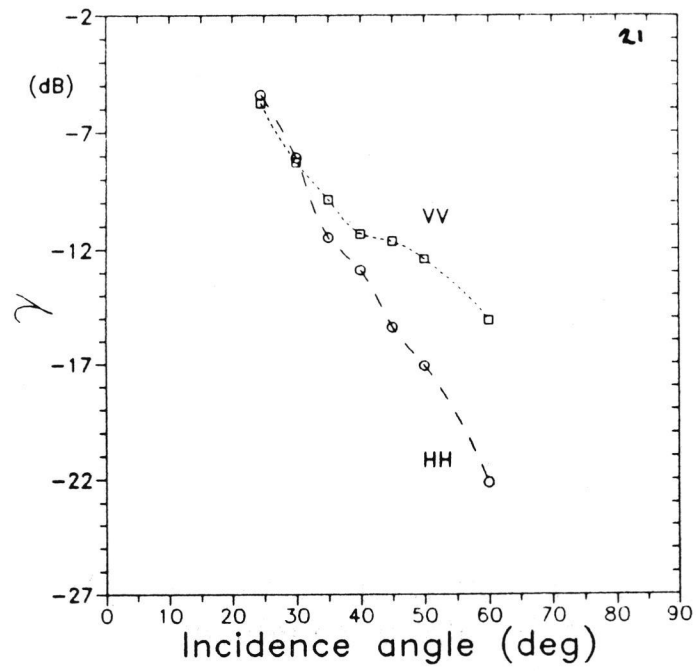


Figure 2.5: Incidence angle dependence of the radar reflection coefficient  $\gamma$  for HH and VV polarization.  $u_* = 0.34$  m/s, 100 m fetch,  $\alpha = 0^\circ$  (upwind).

## Appendix F.2

Figures chapter 3

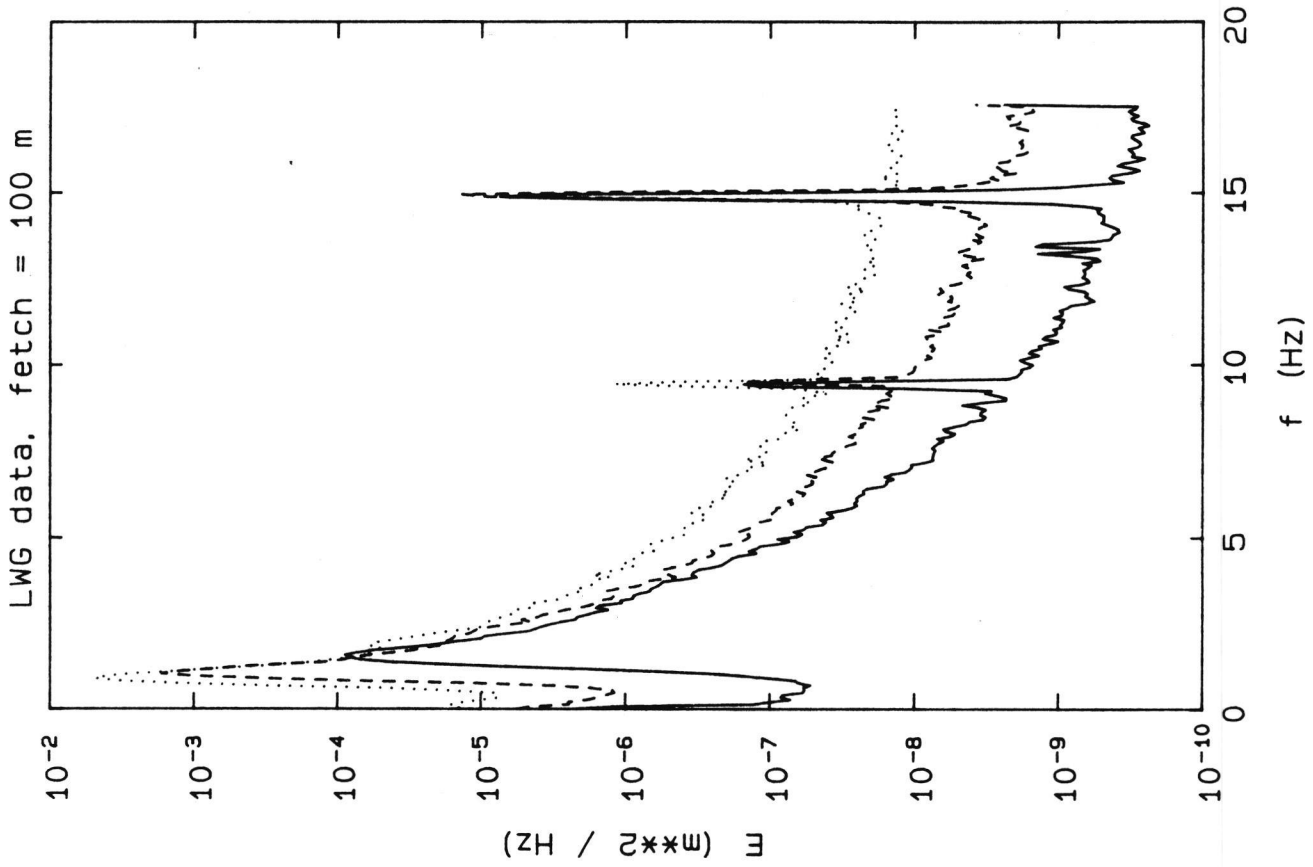


Figure 3.1: Lobemeier Wave Gauge spectra for  $U_{ref} = 8$  m/s and various fetches

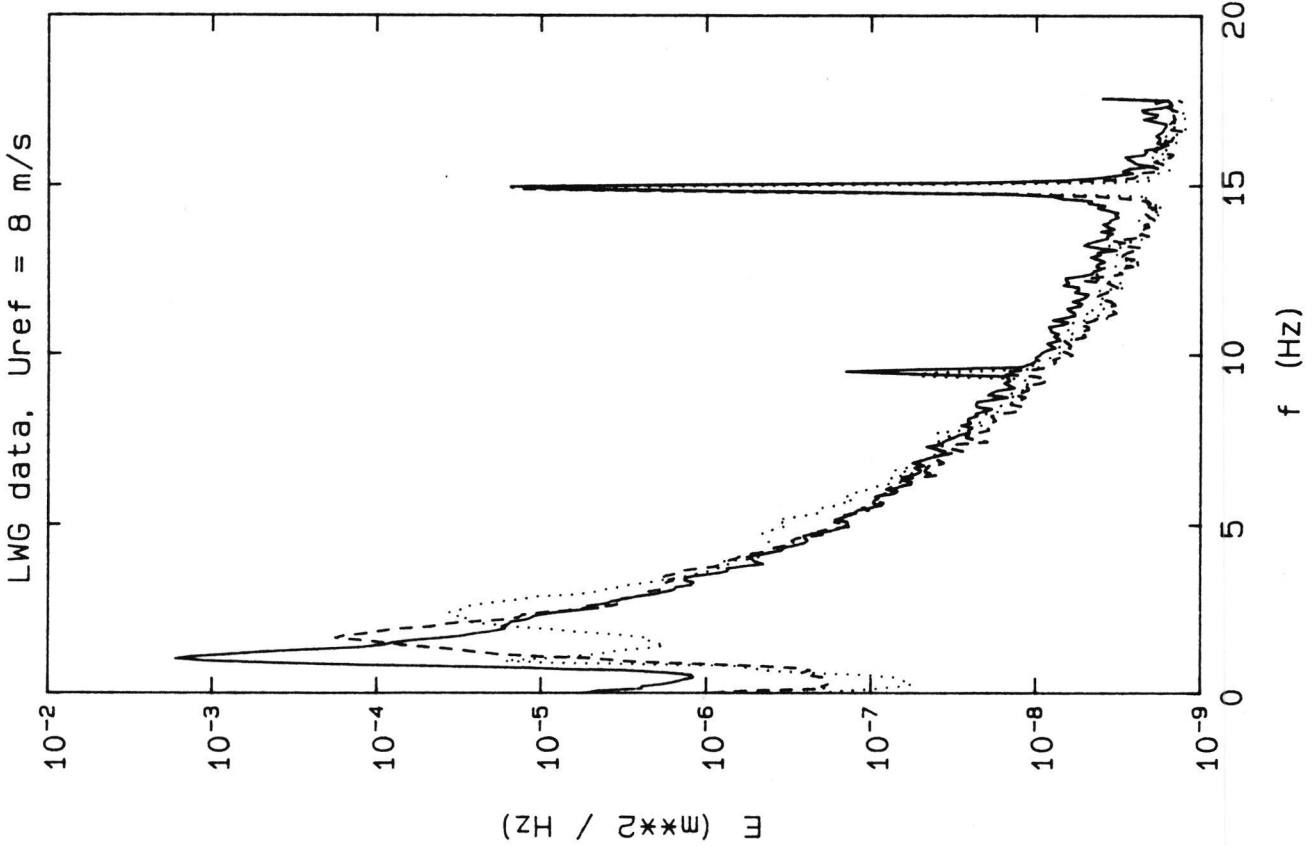


Figure 3.2: Lobemeier Wave Gauge spectra for 100 m fetch and various wind velocities

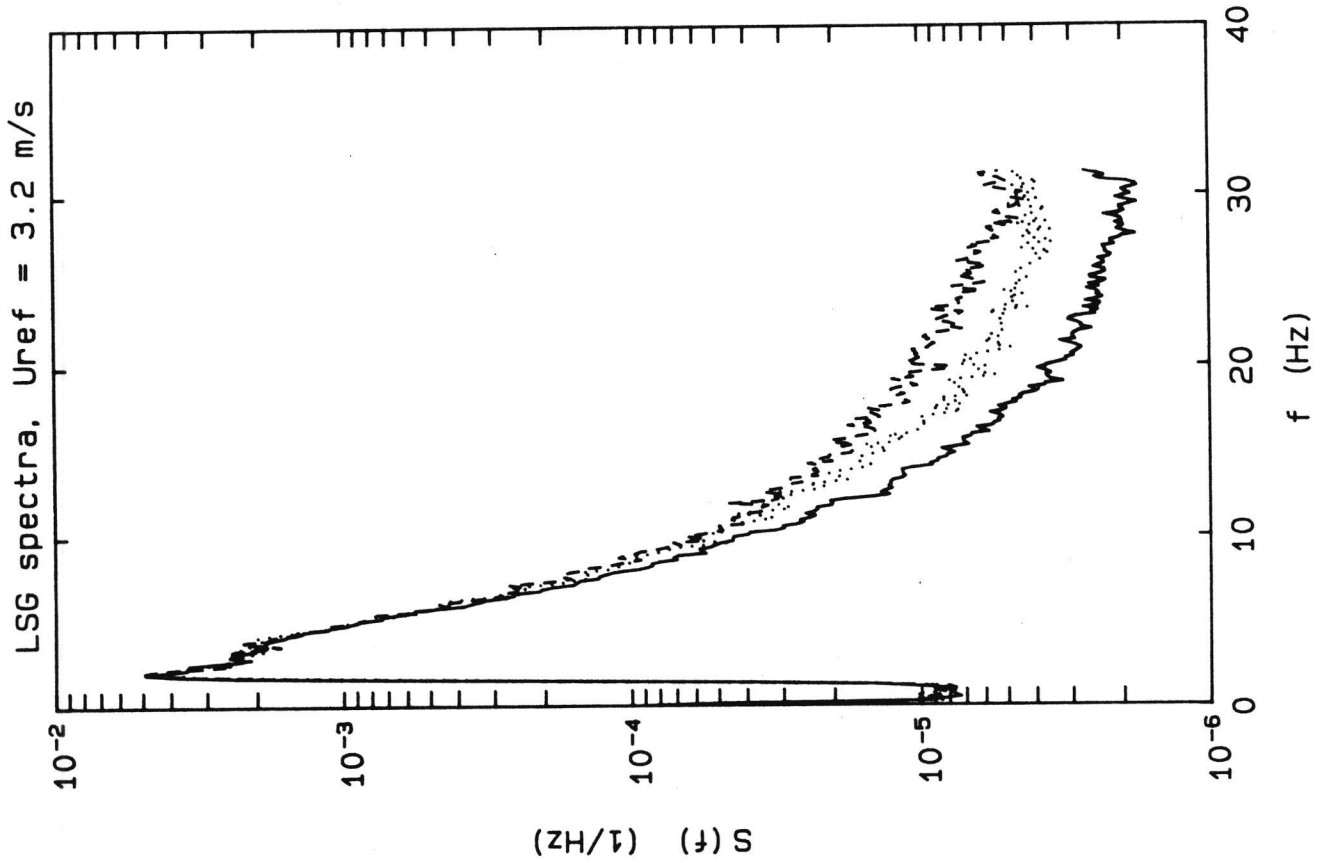


Figure 3.4: Reproducibility of LSG spectra for  $U_{ref} = 3.2$  m/s

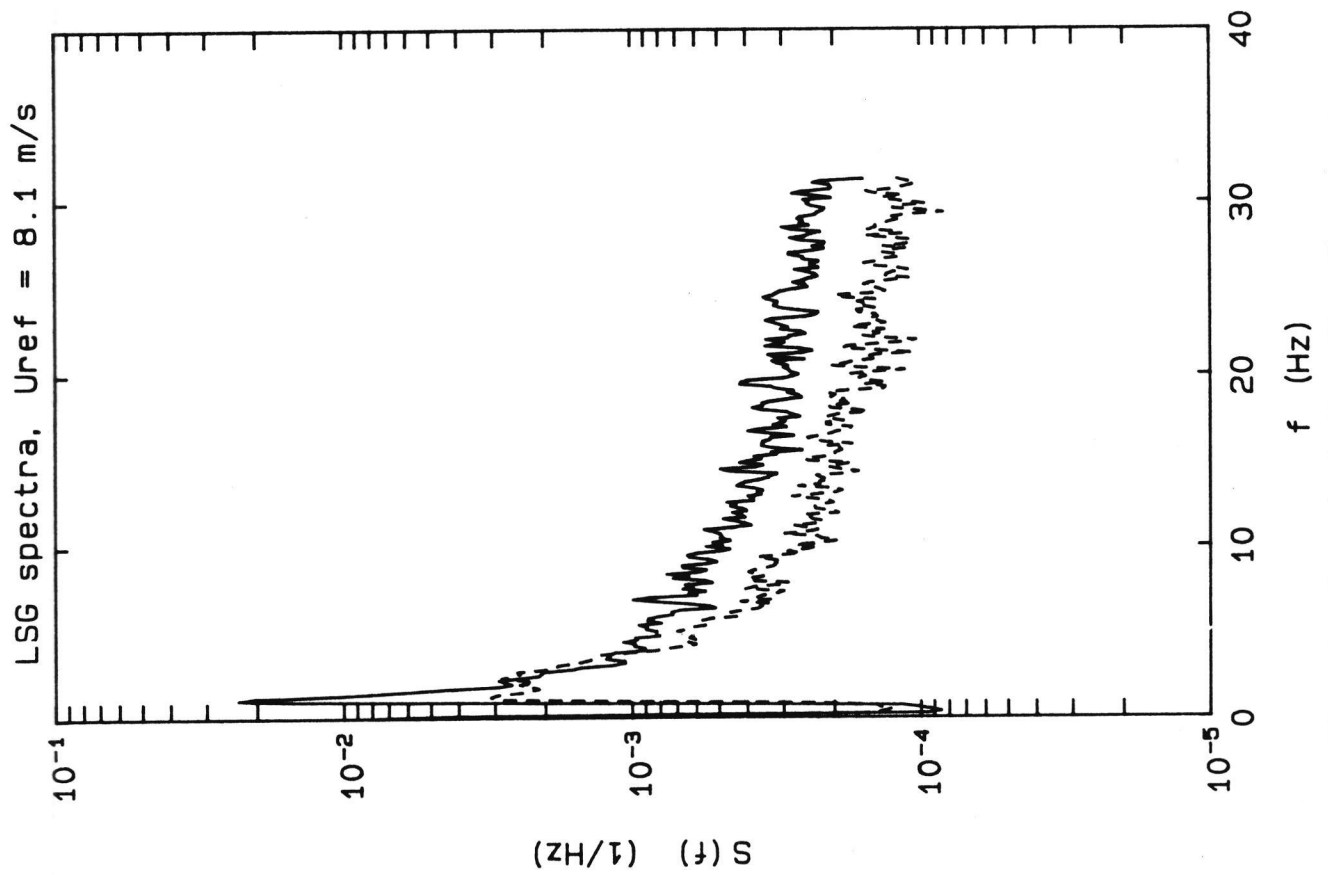


Figure 3.3: Example of a Laser Slope Gauge spectrum

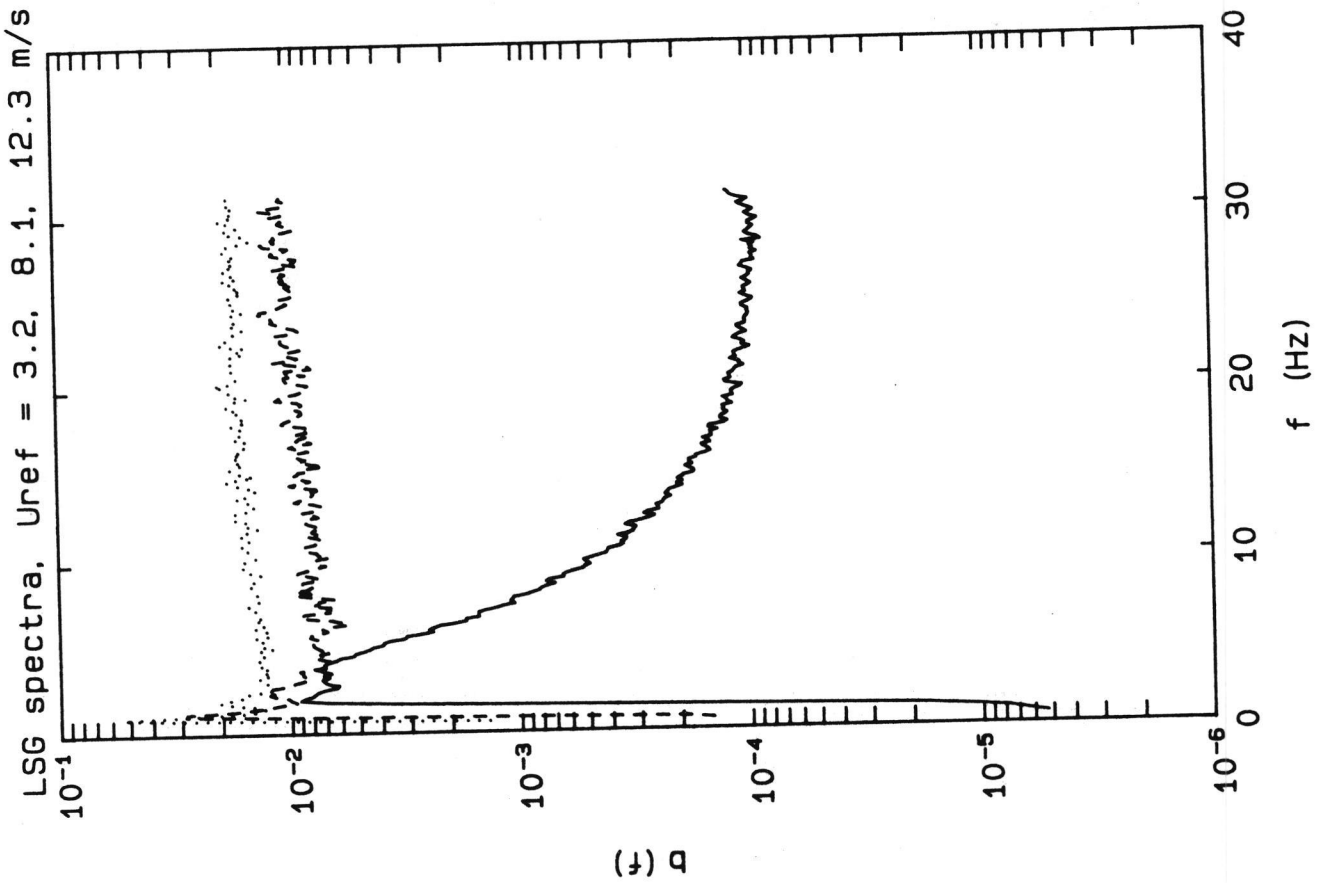


Figure 3.5: LSG spectra for  $U_{ref} = 3.2$  (drawn),  $8.1$  (dashed) and  $12.3$  (dotted) m/s

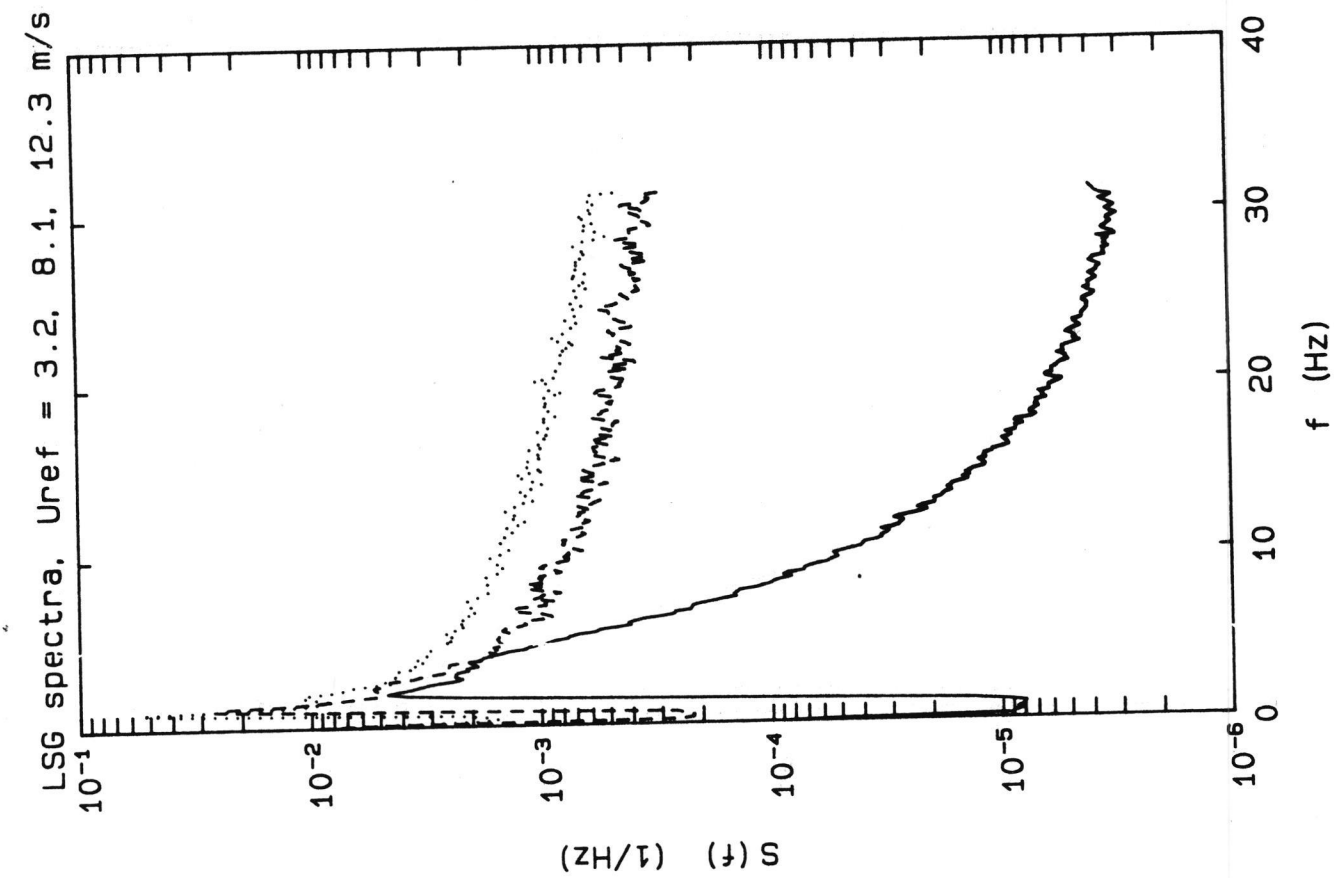
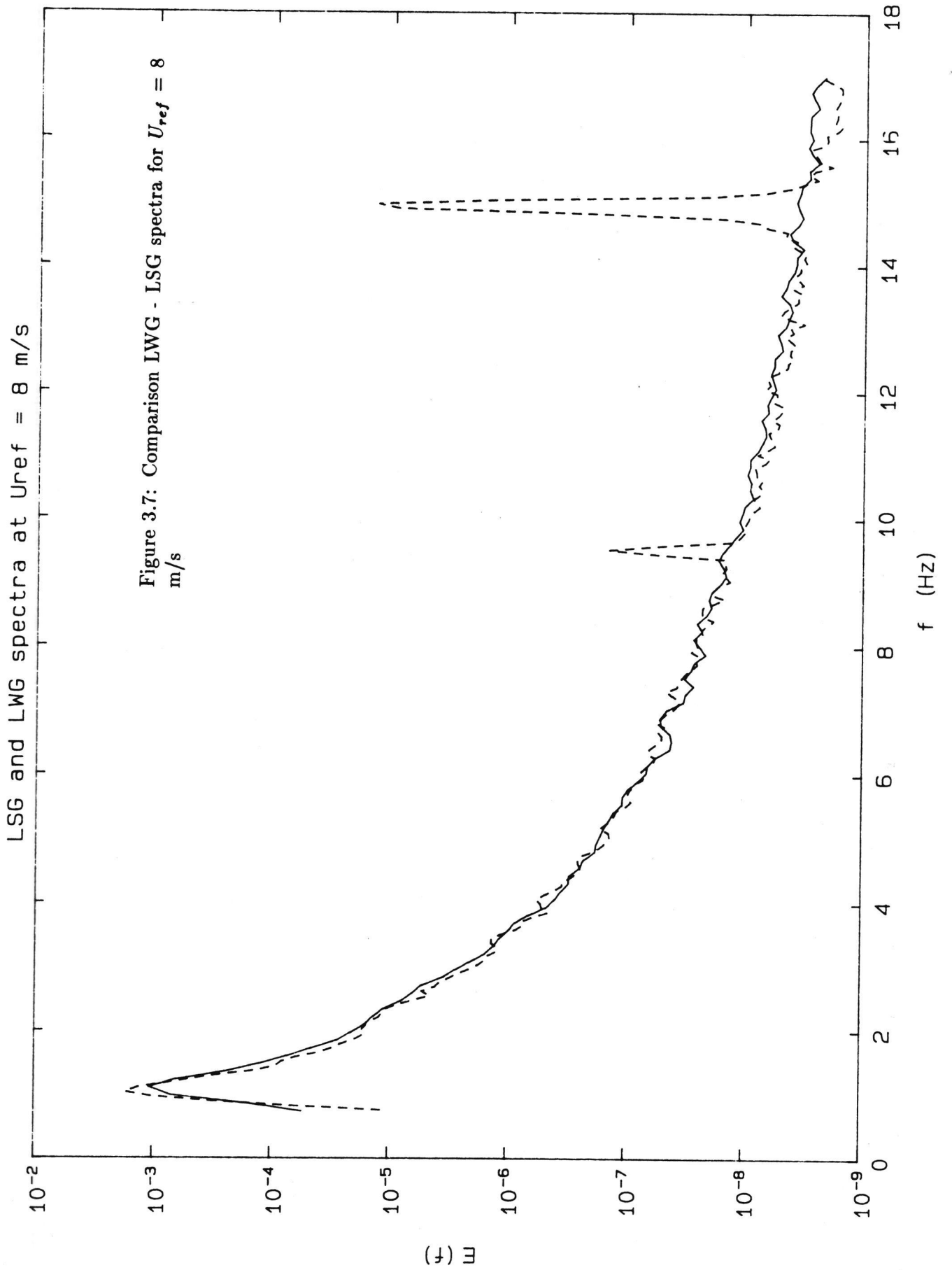


Figure 3.6: Saturation function  $b(f) = f * S(f)$  from LSG measurements



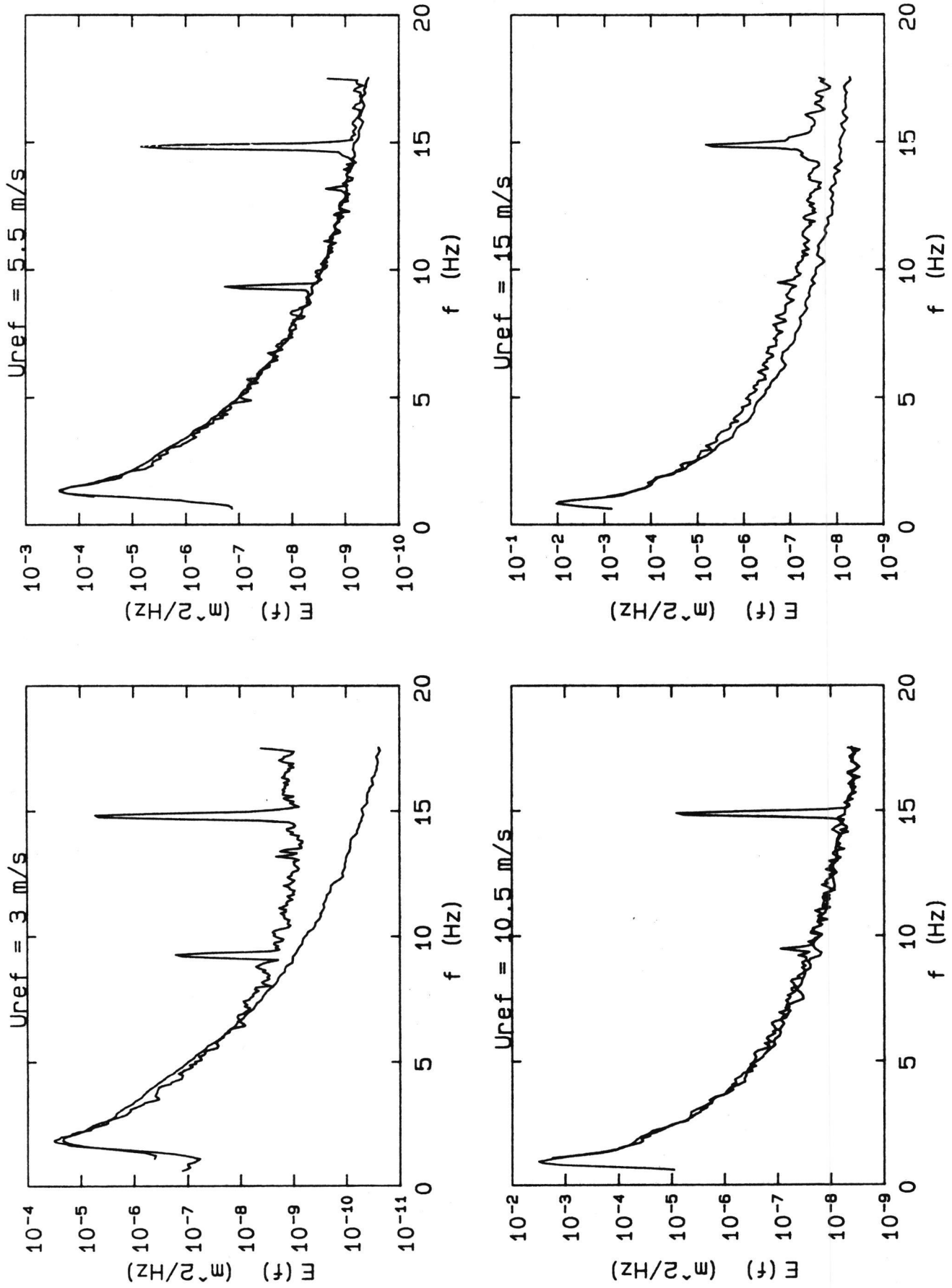


Figure 3.8: Comparison LWG - LSG spectra for various wind velocities

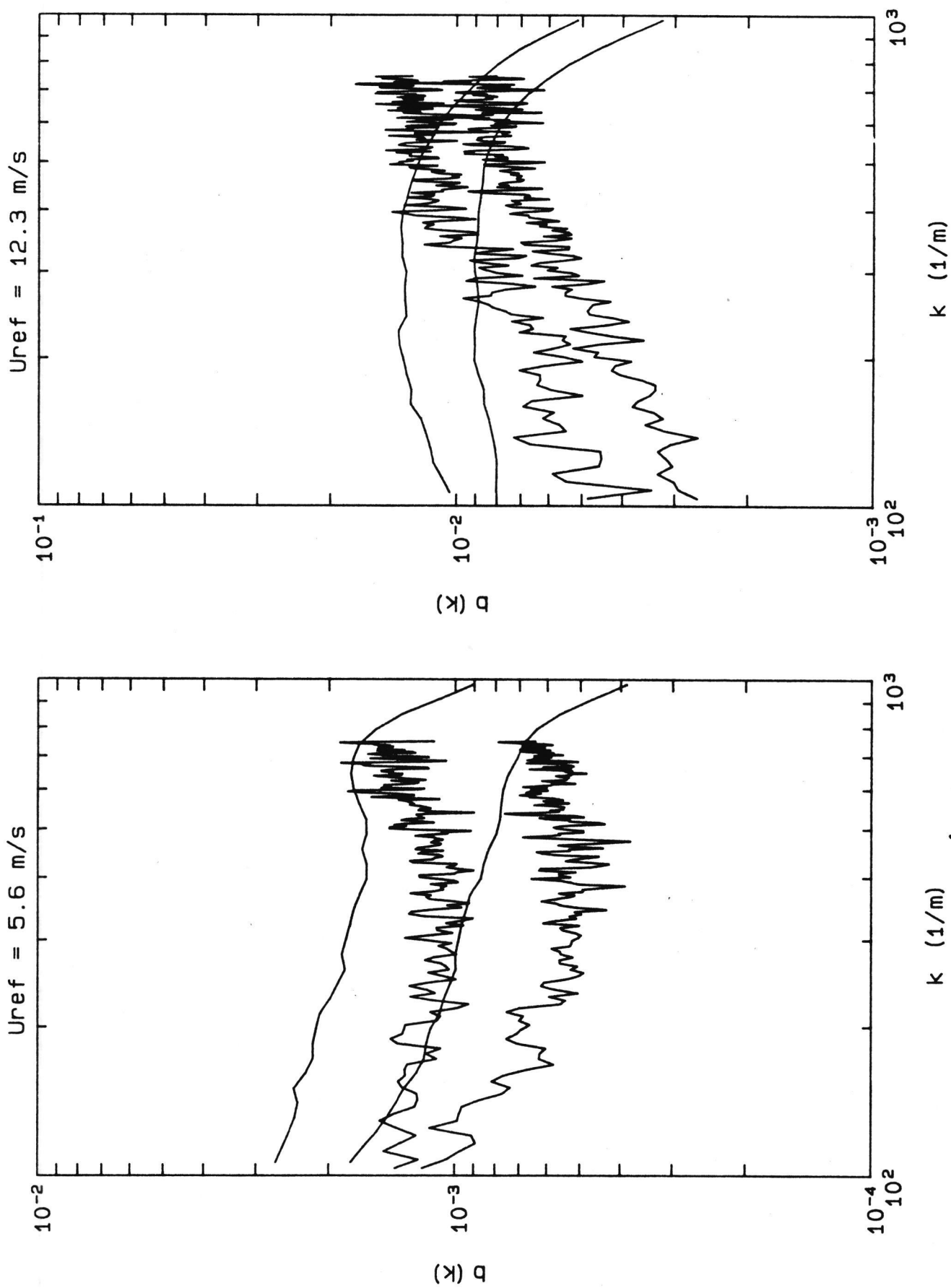


Figure 3.9: Comparison LSG - ISG saturation functions

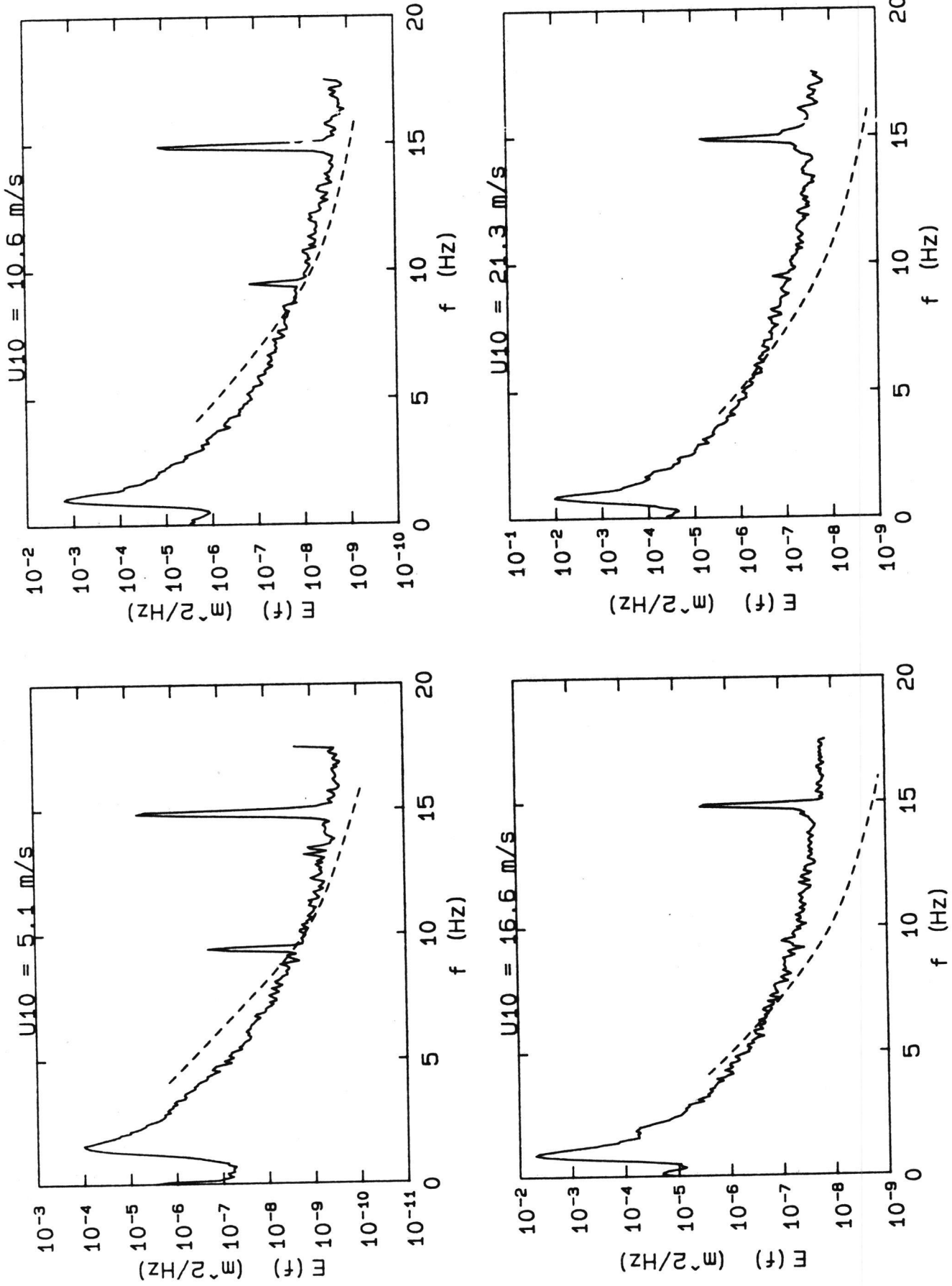


Figure 3.10: Comparison between LWG spectra and D&P wave model

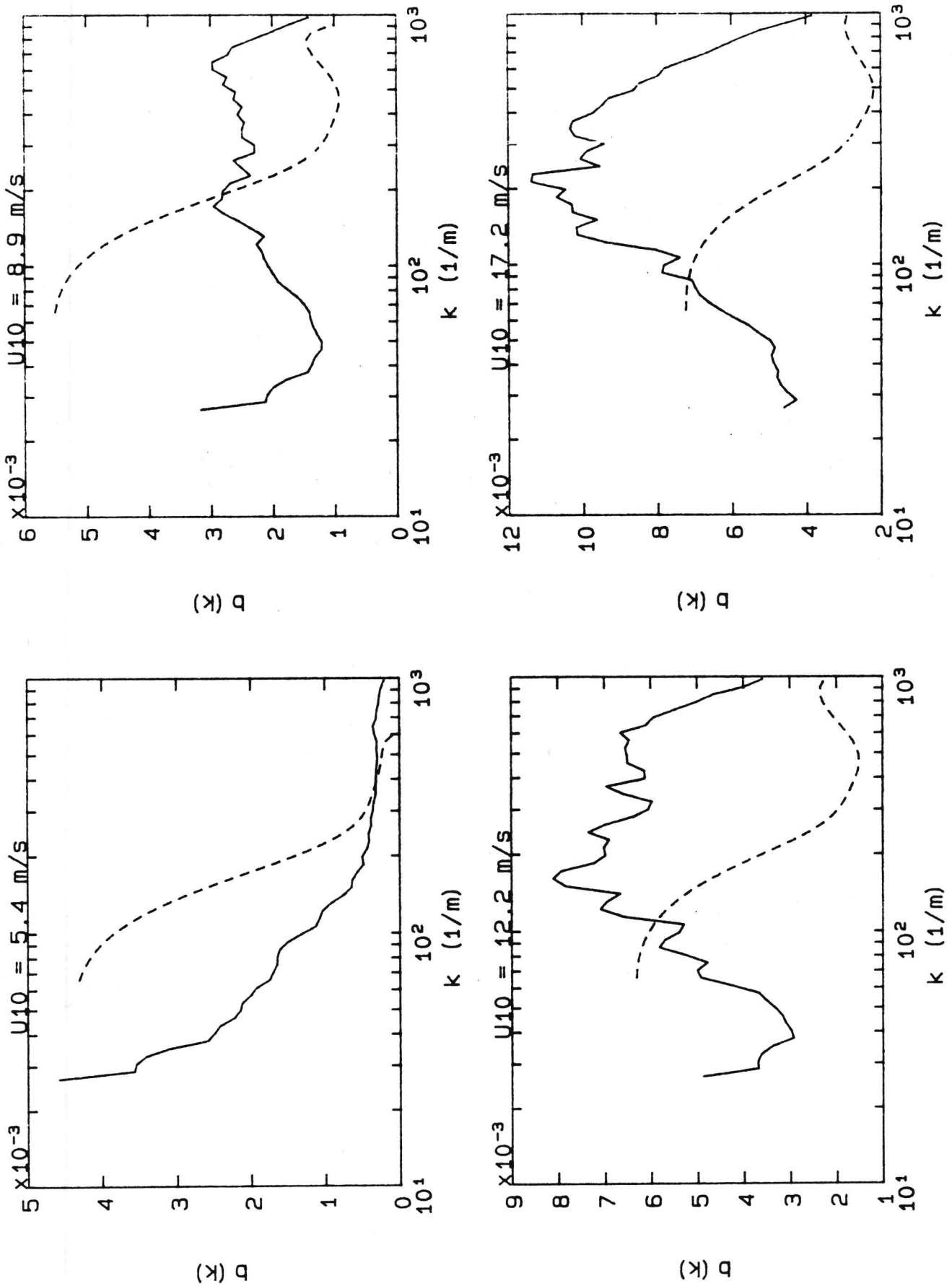


Figure 3.11: Comparison between ISG saturation functions and D&P wave model

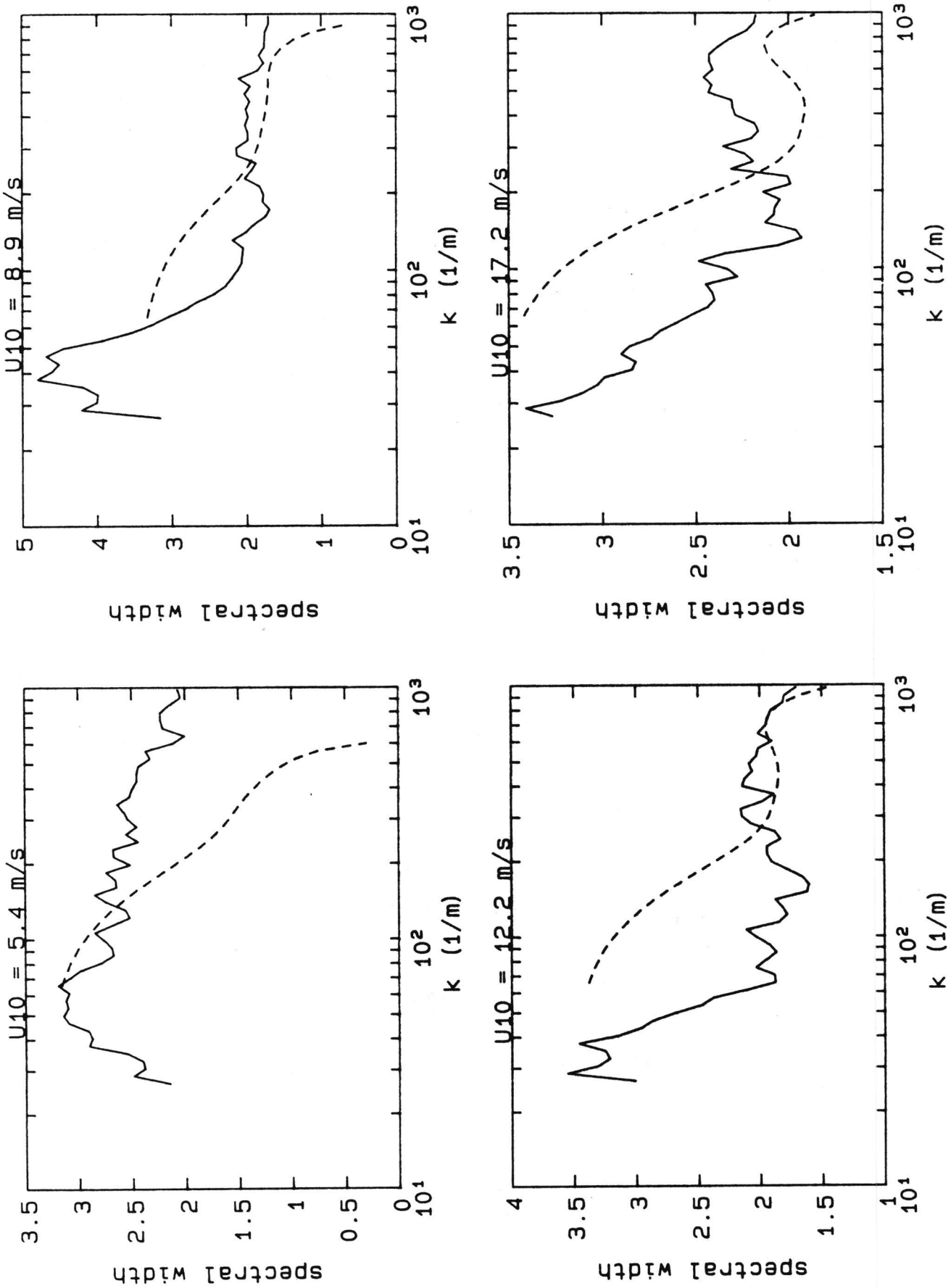
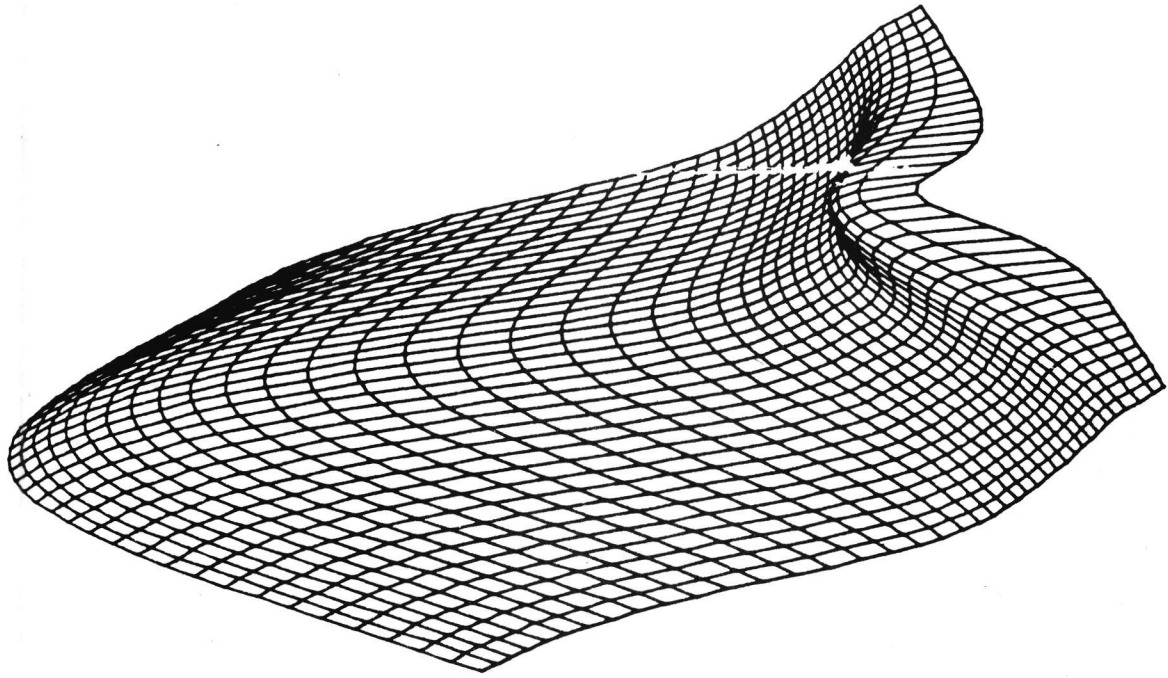


Figure 3.12: Comparison between spectral widths from ISG data and D&P wave model

b(k) from D&P model



b(k) from ISG data

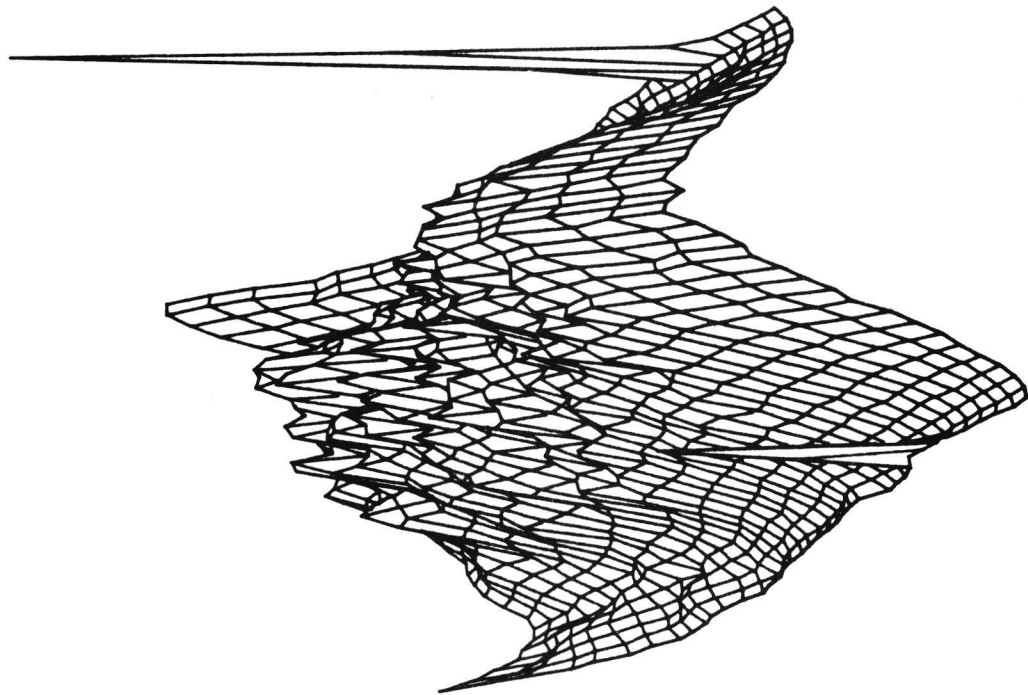


Figure 3.13: Examples of directional saturation functions: ISG data and D&P model

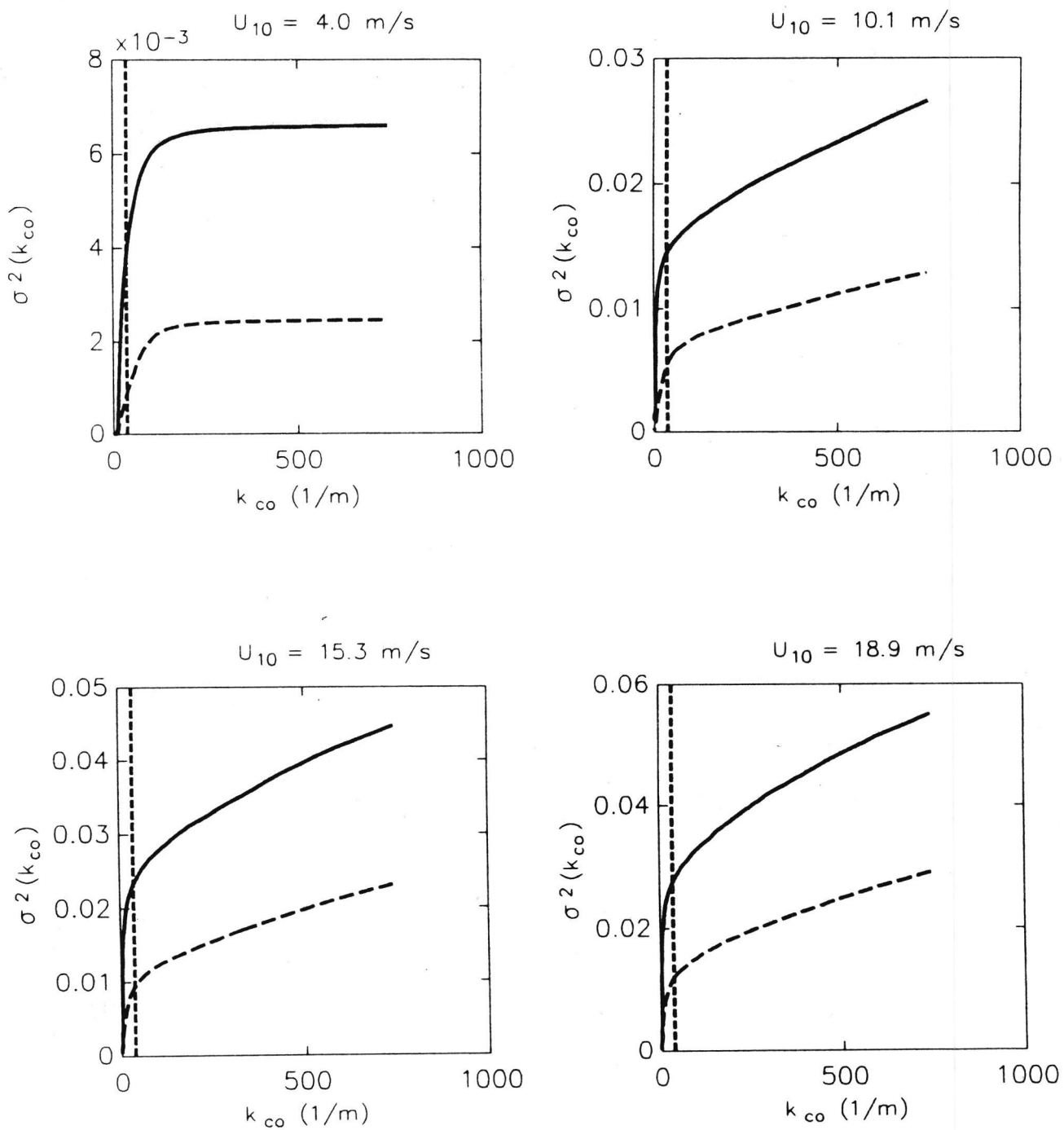


Figure 3.14: Long wave slope variances as a function of the cross-over wave number

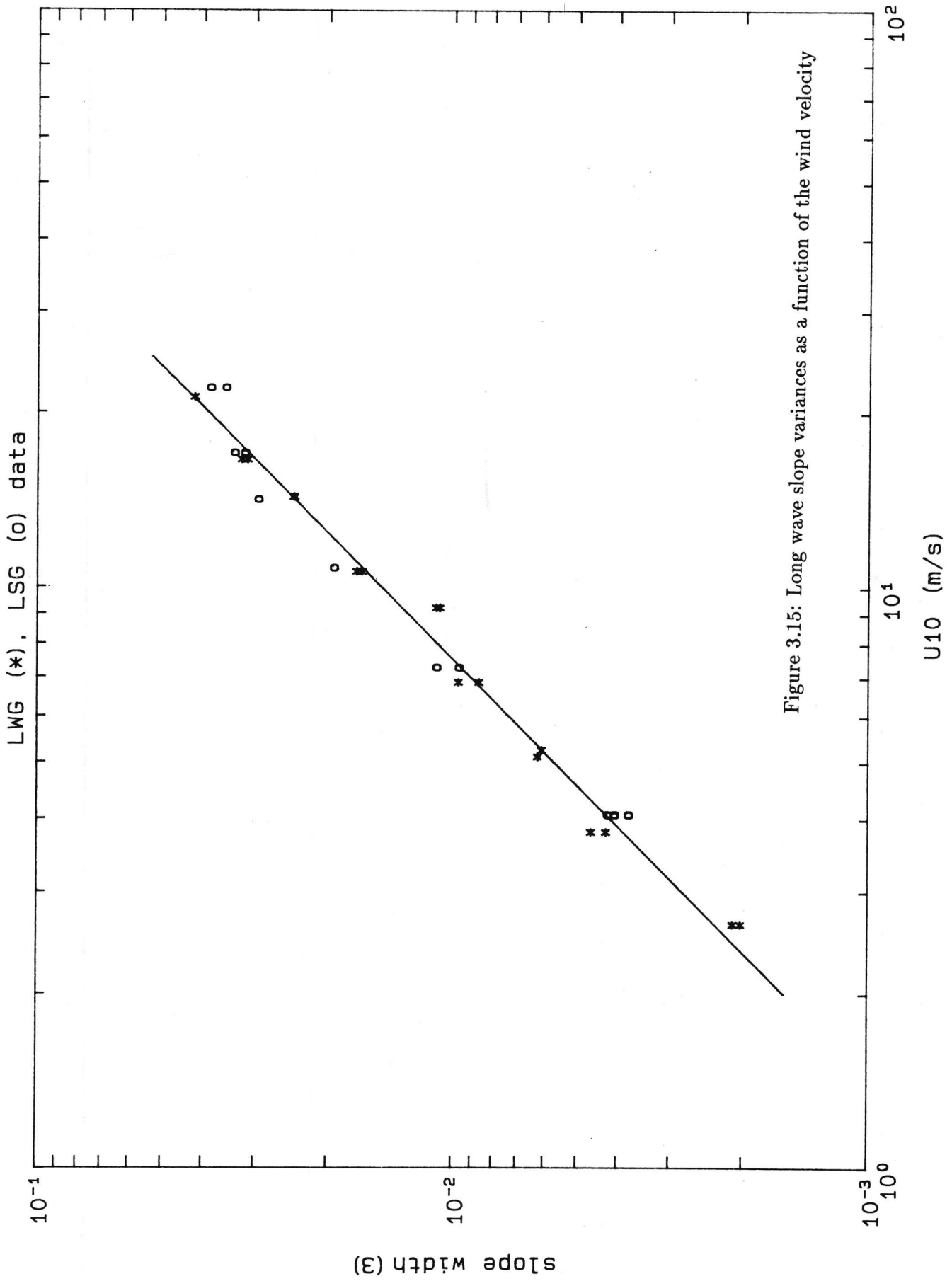


Figure 3.15: Long wave slope variances as a function of the wind velocity

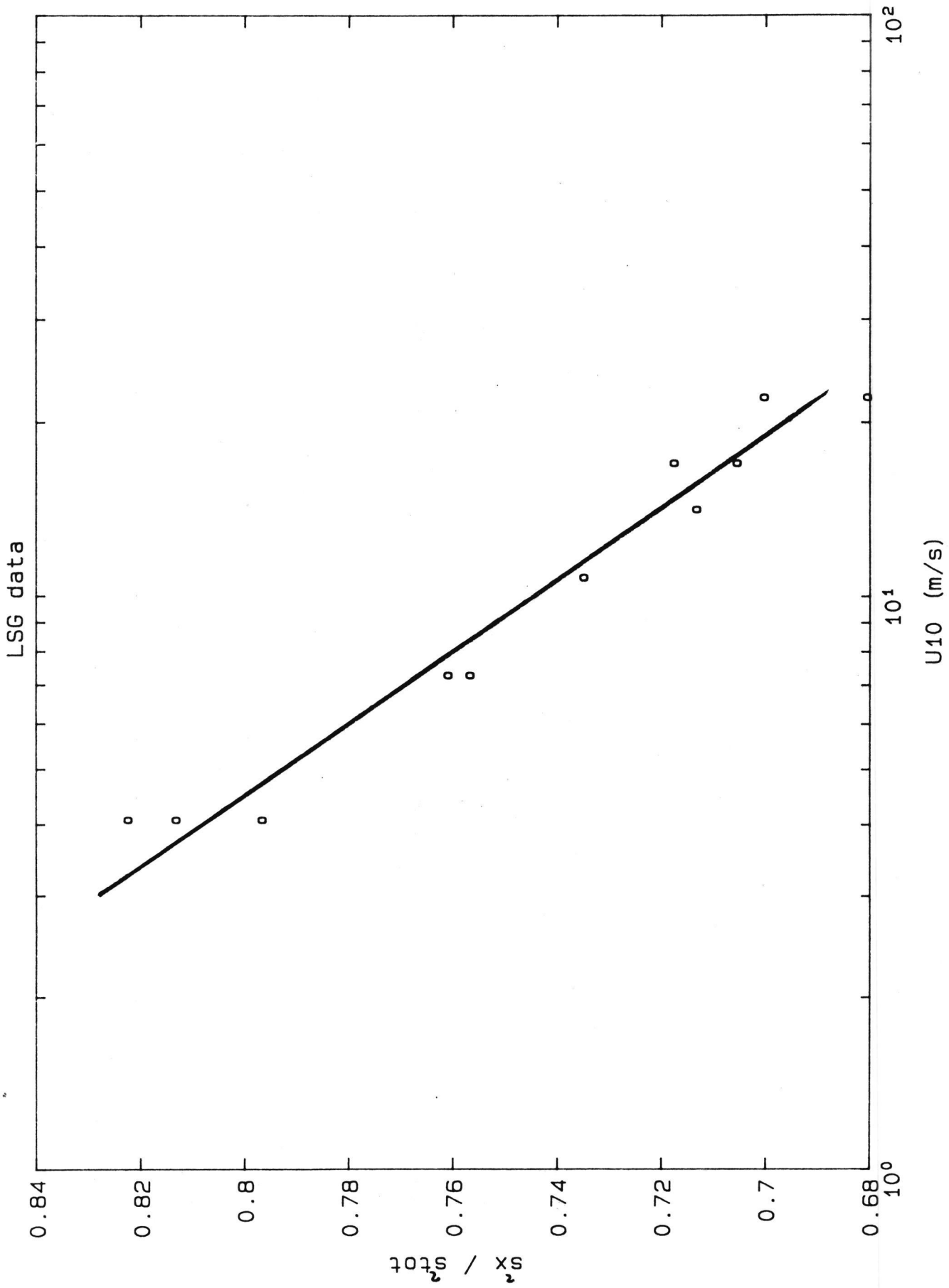


Figure 3.16: Fraction of the along-wind slope variance of the total variance versus the wind velocity

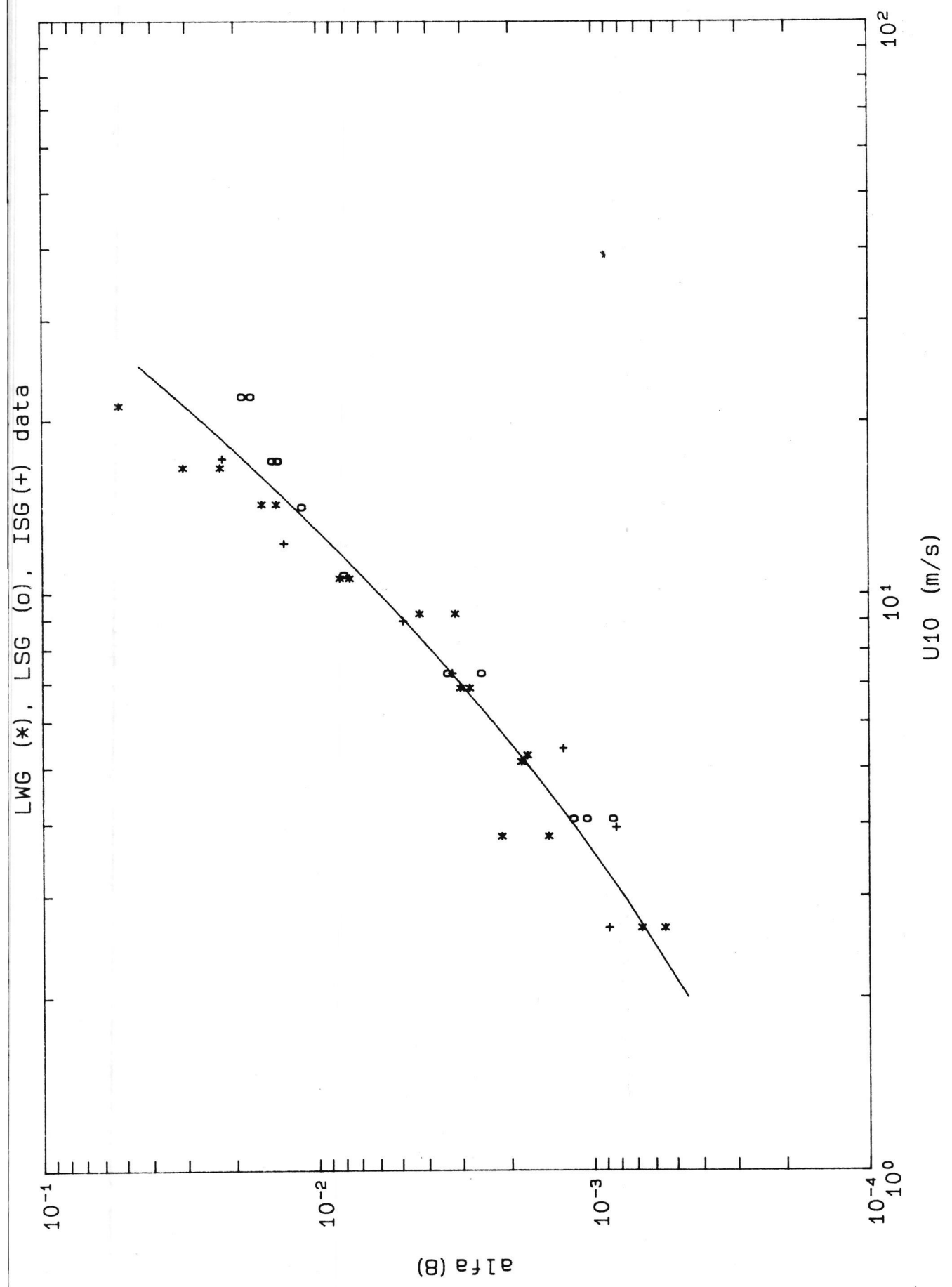


Figure 3.17: Tail parameter  $\alpha(8)$  as a function of the wind velocity

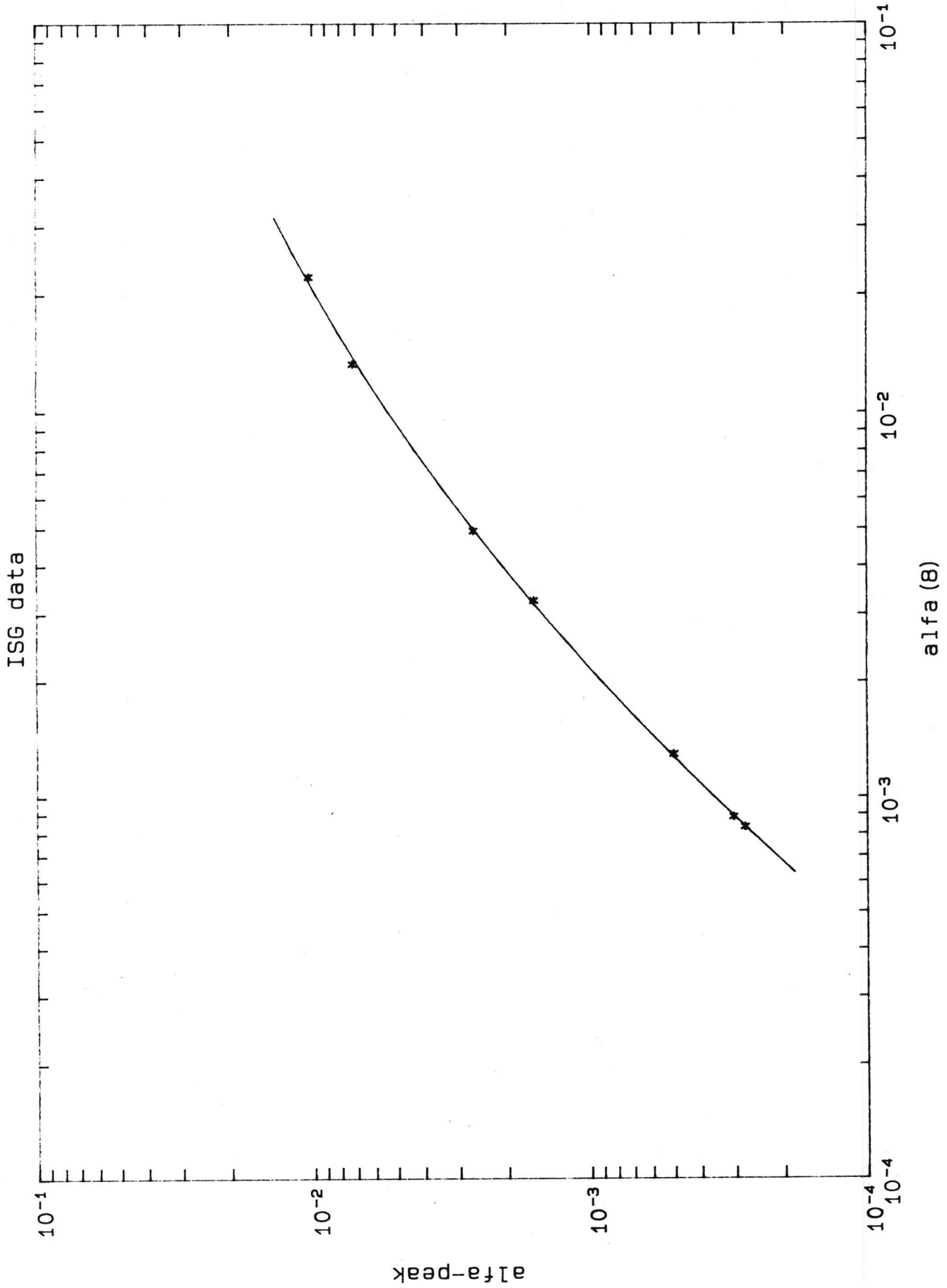


Figure 3.18: Fraction of the upwind tail parameter  $\alpha_u(8)$  of the total  $\alpha(8)$  versus the wind velocity

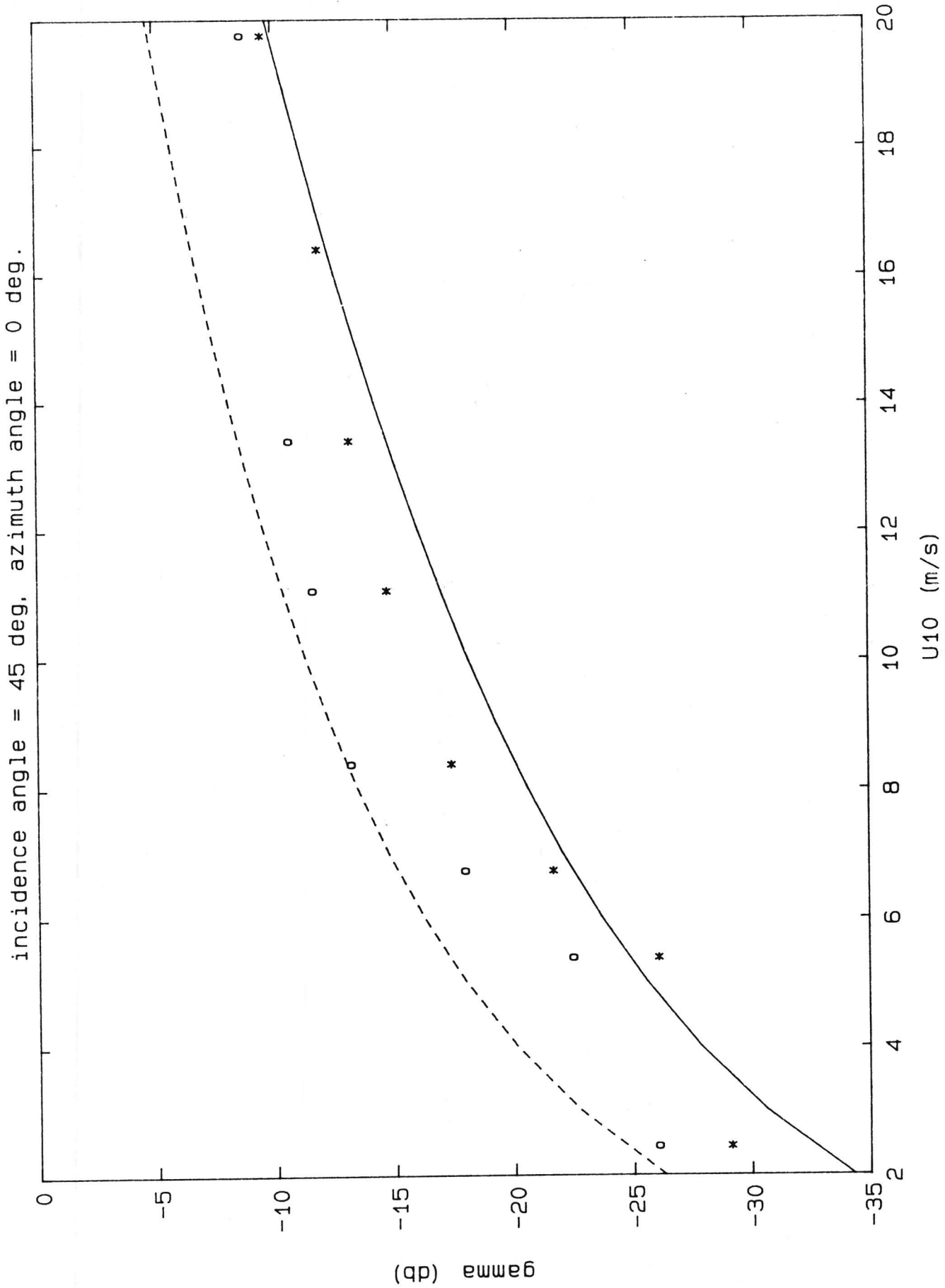


Figure 3.19: Comparison of measured radar data and VIERS-1 model versus wind velocity

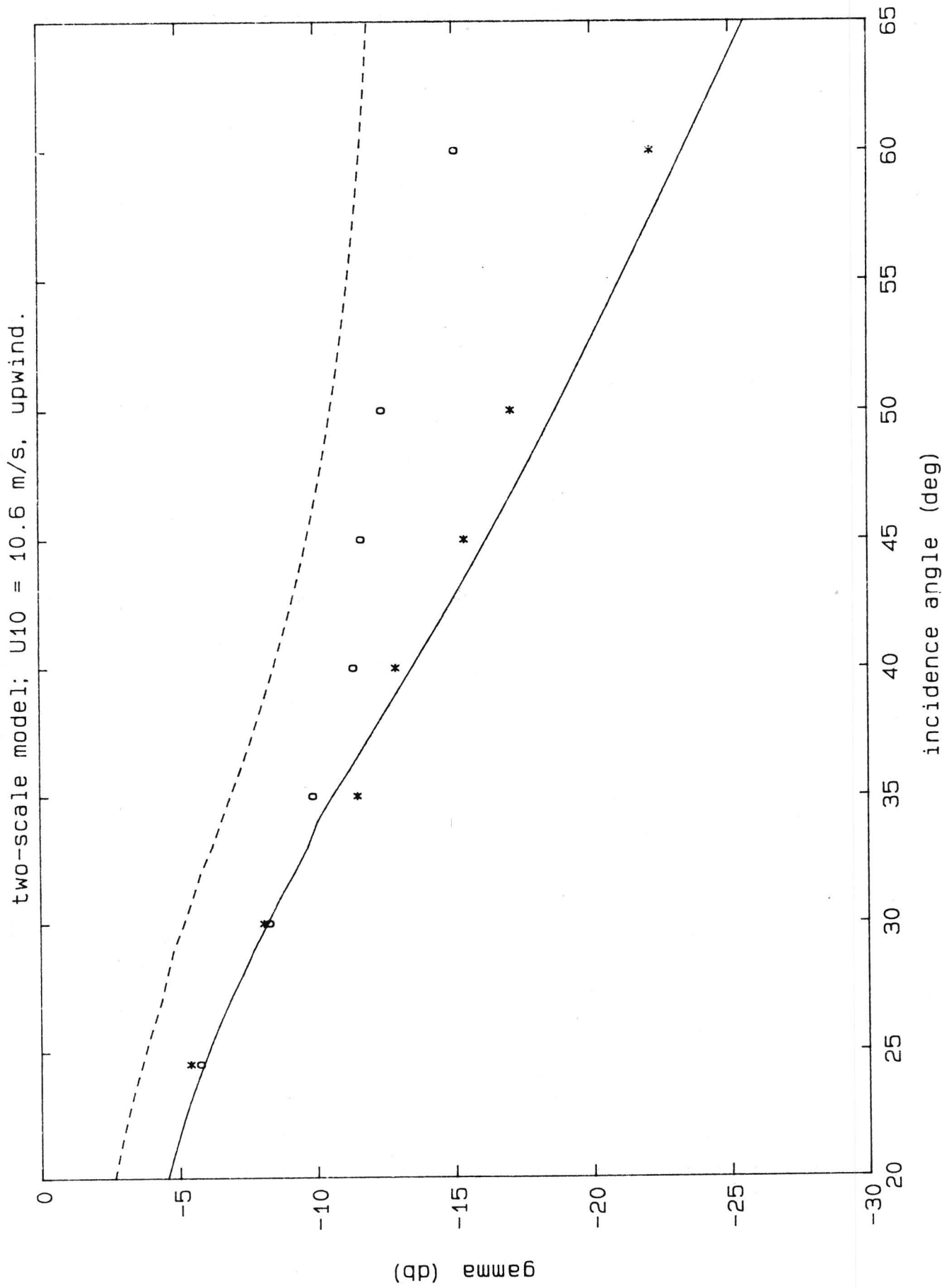
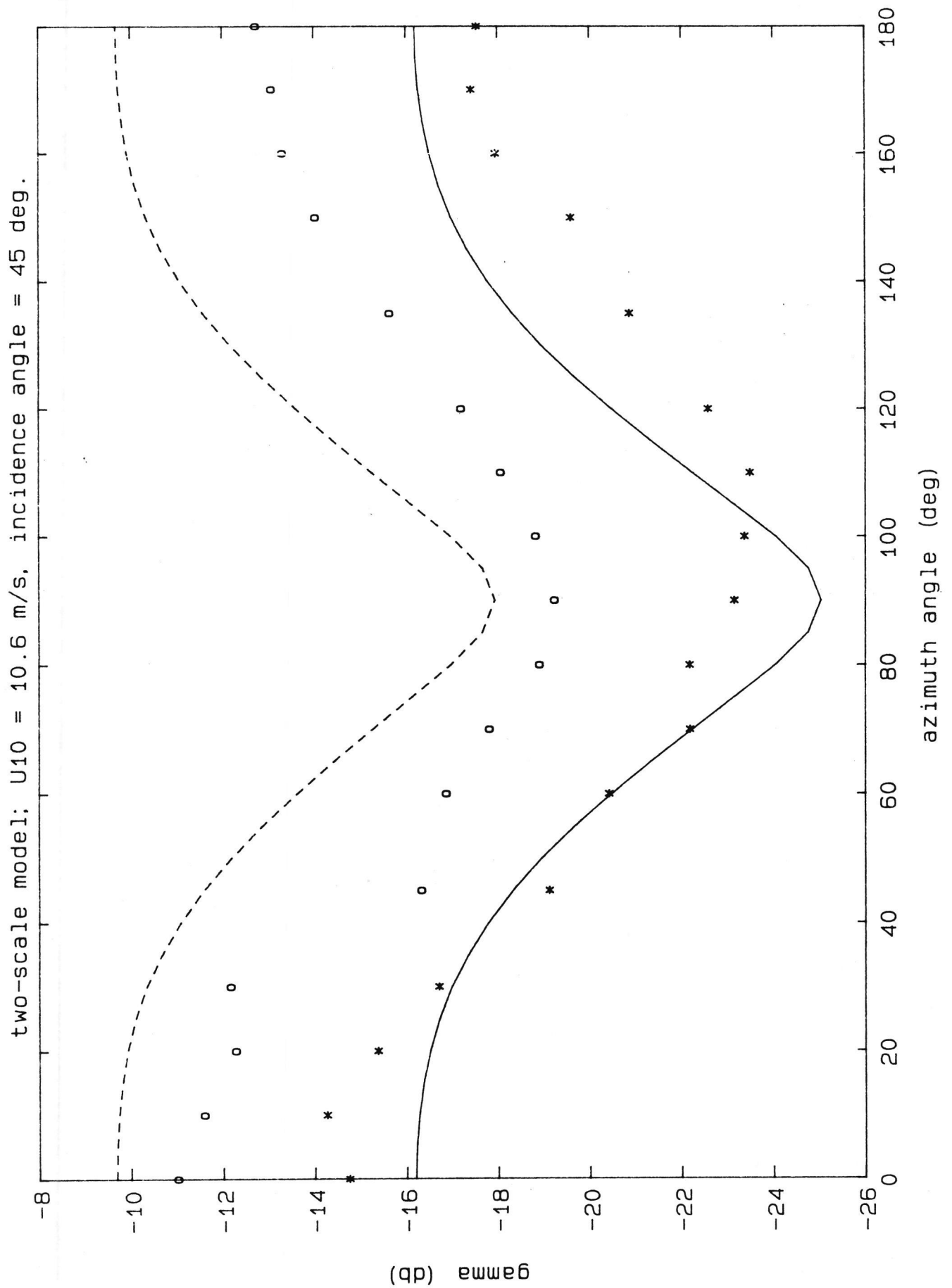


Figure 3.20: Comparison of measured radar data and VIERS-1 model versus incidence angle

Figure 3.21: Comparison of measured radar data and VIERS-1 model versus azimuth angle

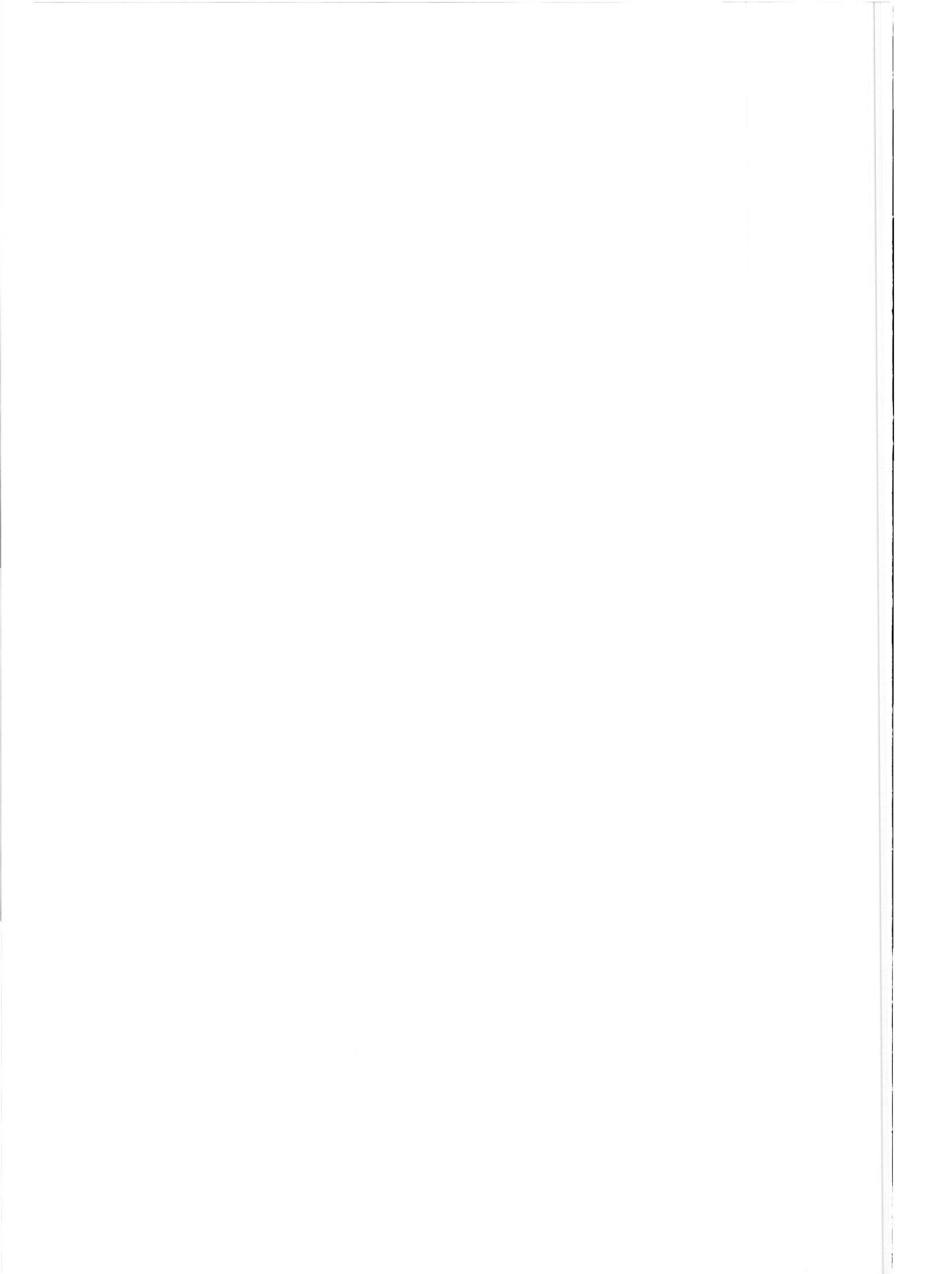


## Appendix F.3

Figures chapter 4



Figure 4.1: 'De Voorst' wave flume



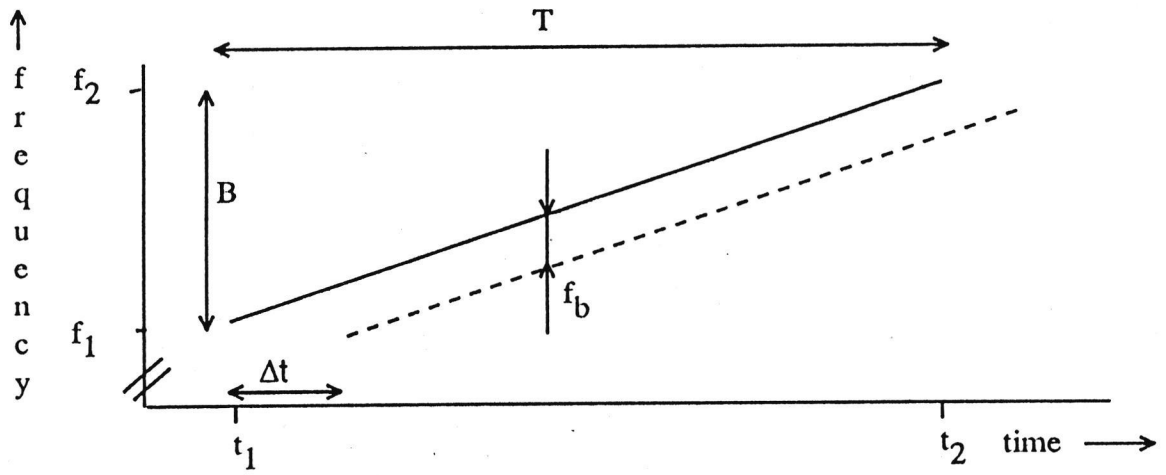


Figure 4.2: RF-frequency sweep for a FM/CW radar, see text

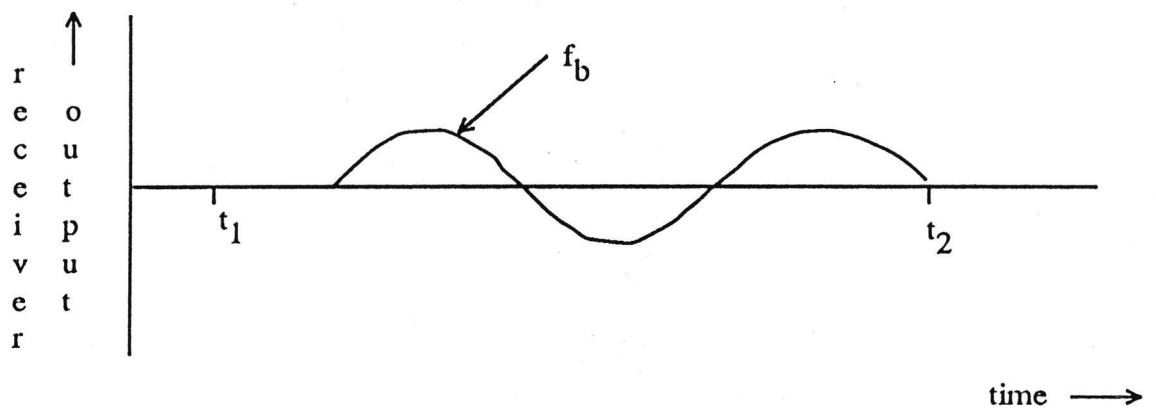
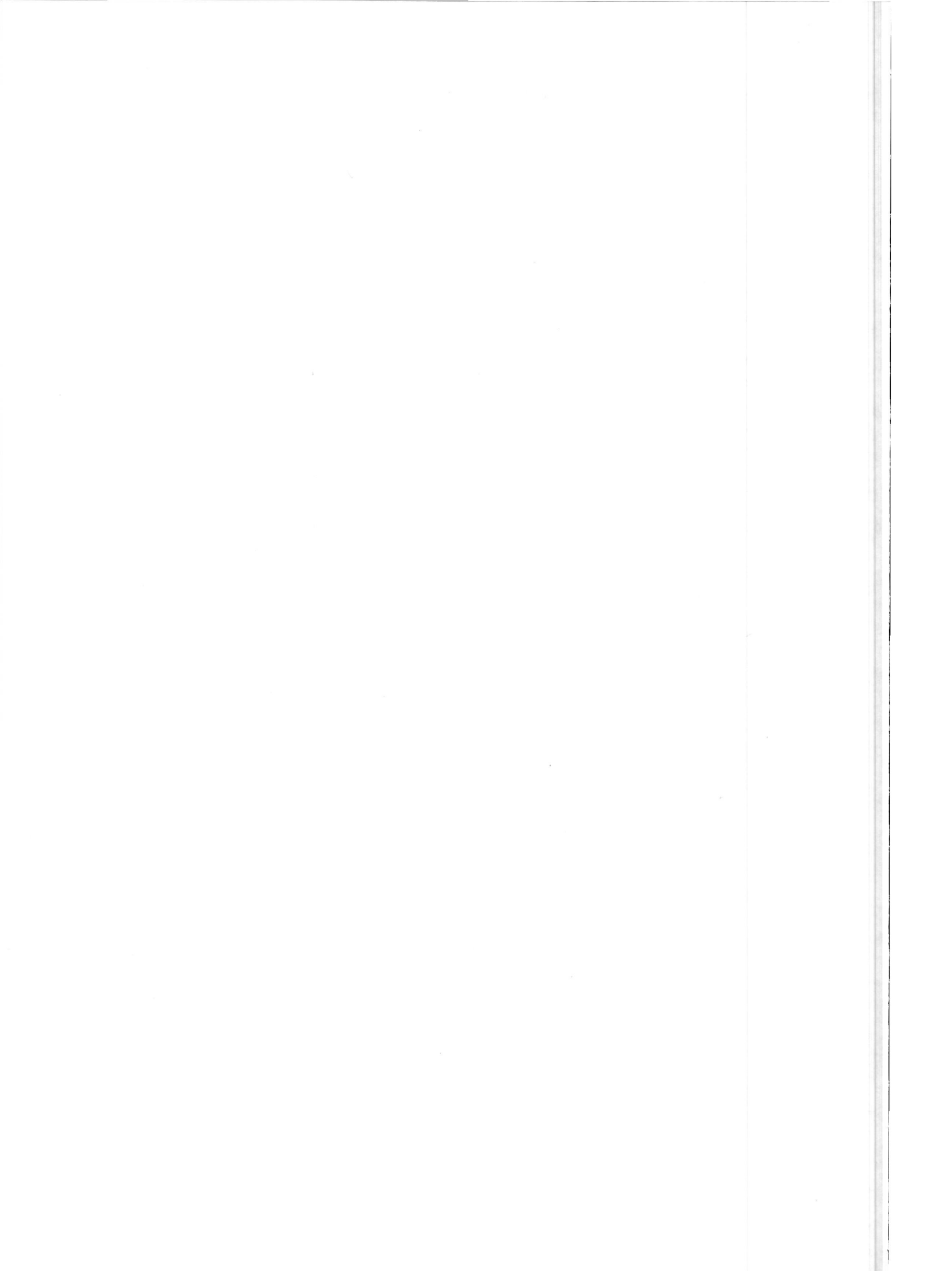


Figure 4.3: Beat signal for a point target



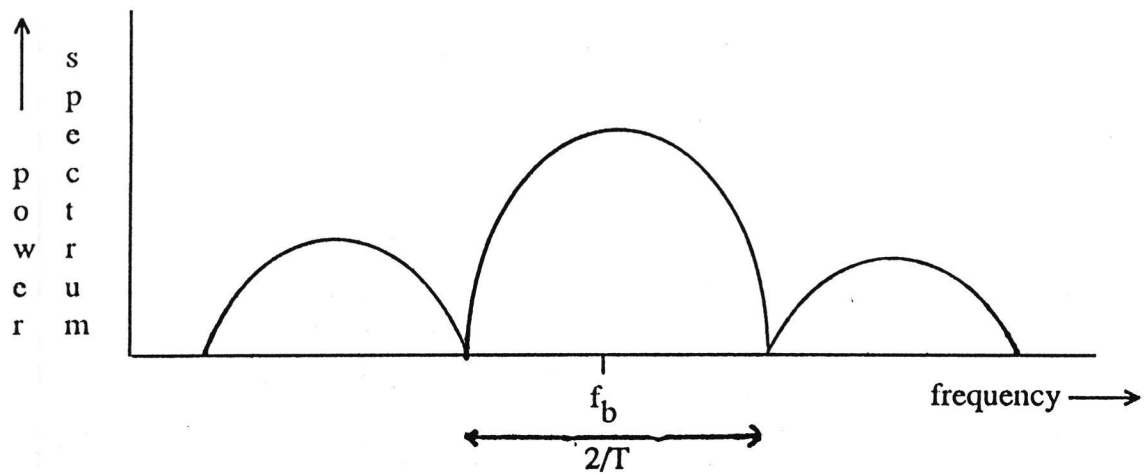


Figure 4.4: Frequency spectrum of the FM/CW beat signal.

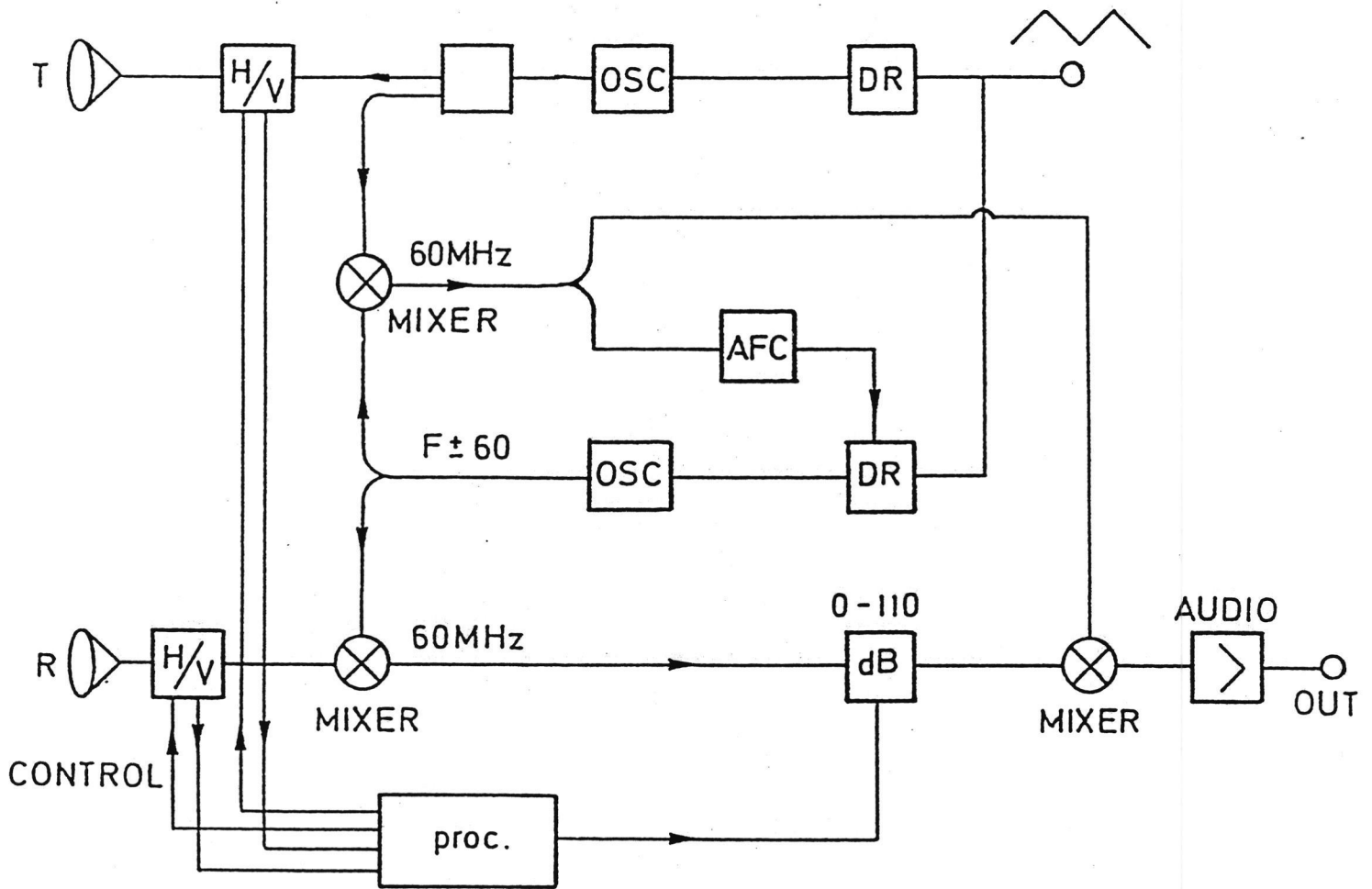


Figure 4.5: Schematic overview of the X-band FM/CW scatterometer used.

## Appendix F.4

Figures chapter 5

## Radar backscatter

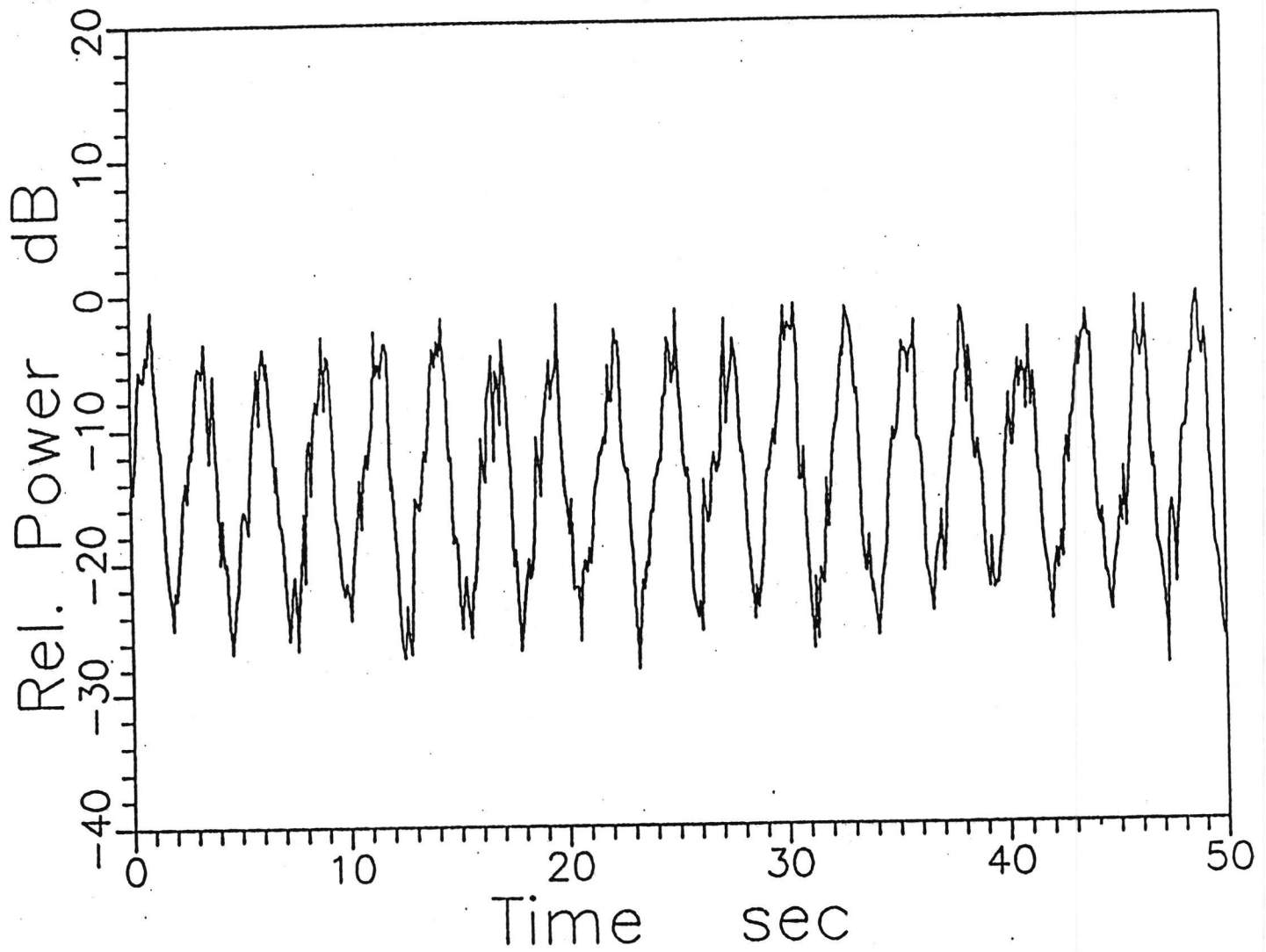


Figure 5.1: Timeseries of the microwave backscatter; HH; wave height: 1 m

## Radar backscatter

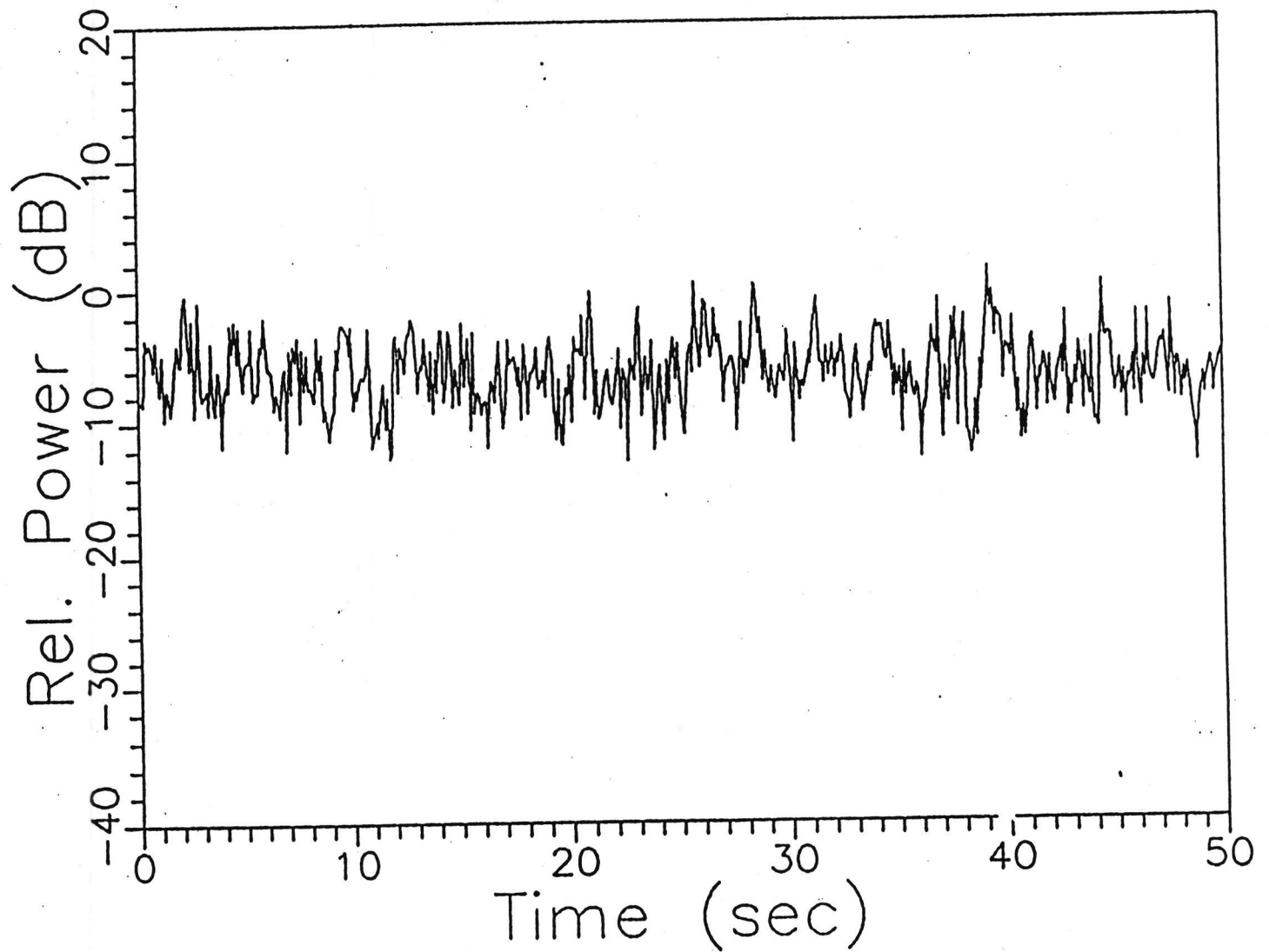


Figure 5.2: Timeseries of the X-band microwave backscatter; VV; wave height 0.30 m

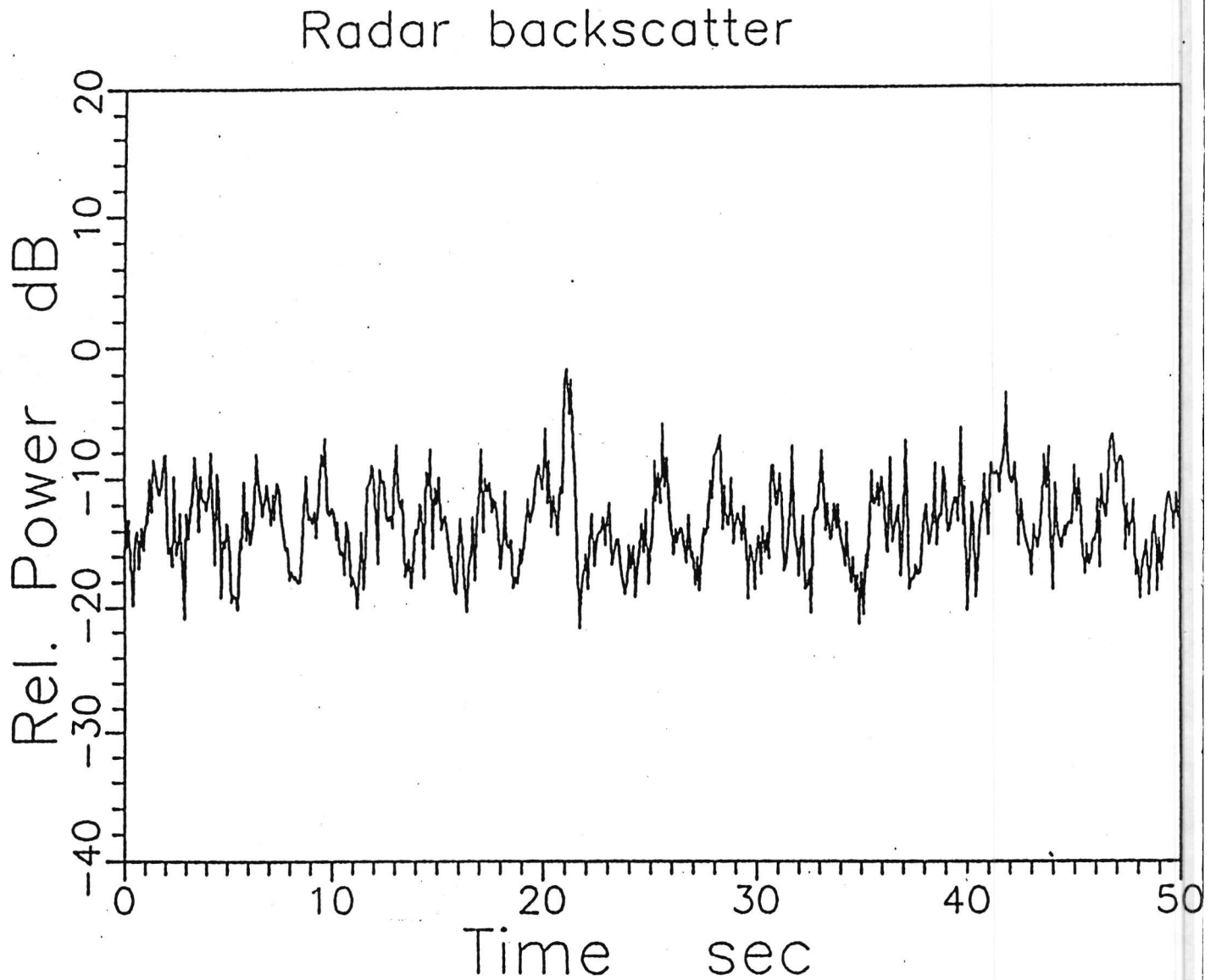


Figure 5.3: Timeseries of the X-band microwave backscatter; HH; wave height 0.30 m

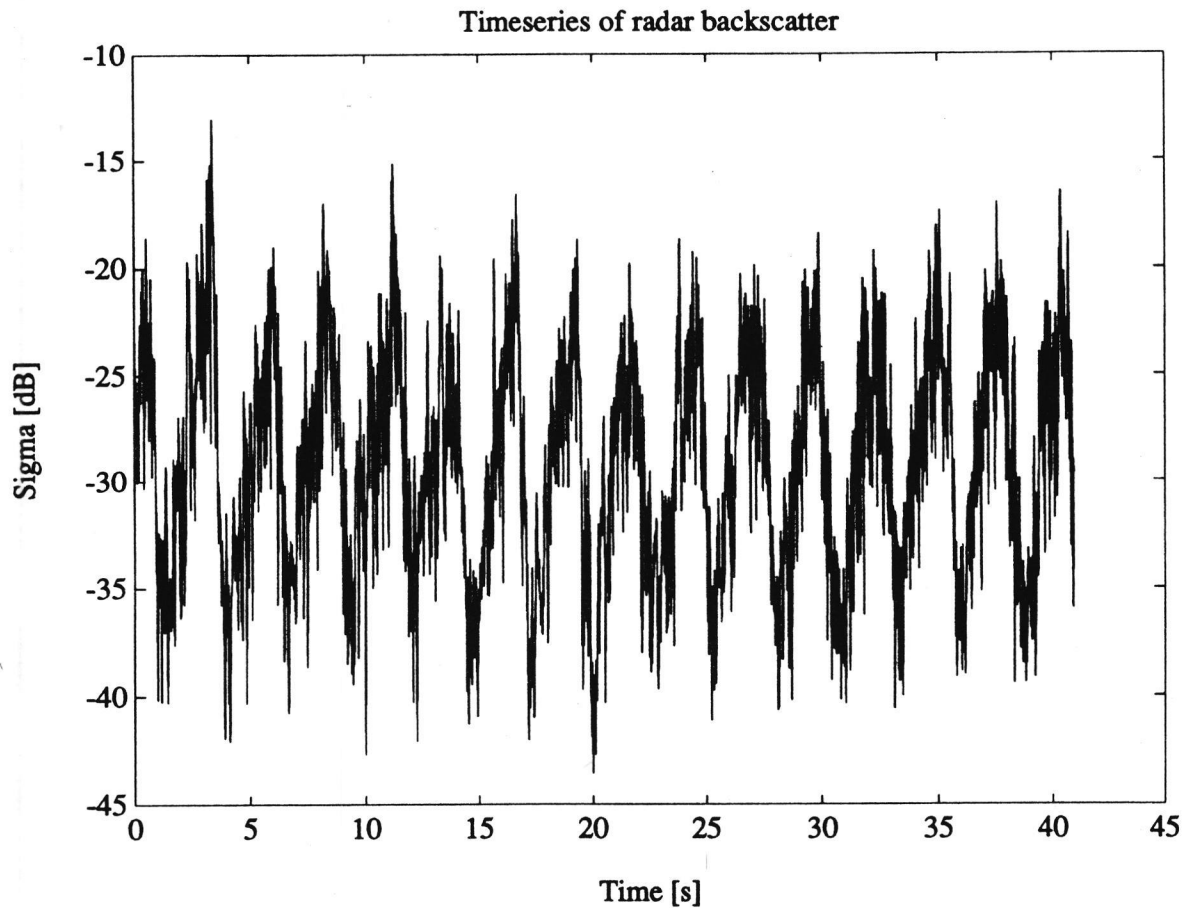


Figure 5.4: Timeseries of  $\sigma^0(t)$ , HH polarization,  $u_* = .33$  m/s, regular long wave ( $\lambda=11.05$ , height .6 m.)

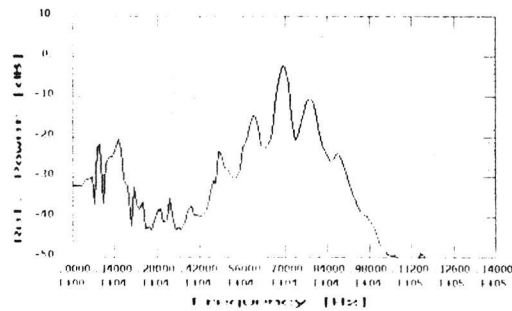


Figure 5.5: Range (frequency) spectrum of scatterometer

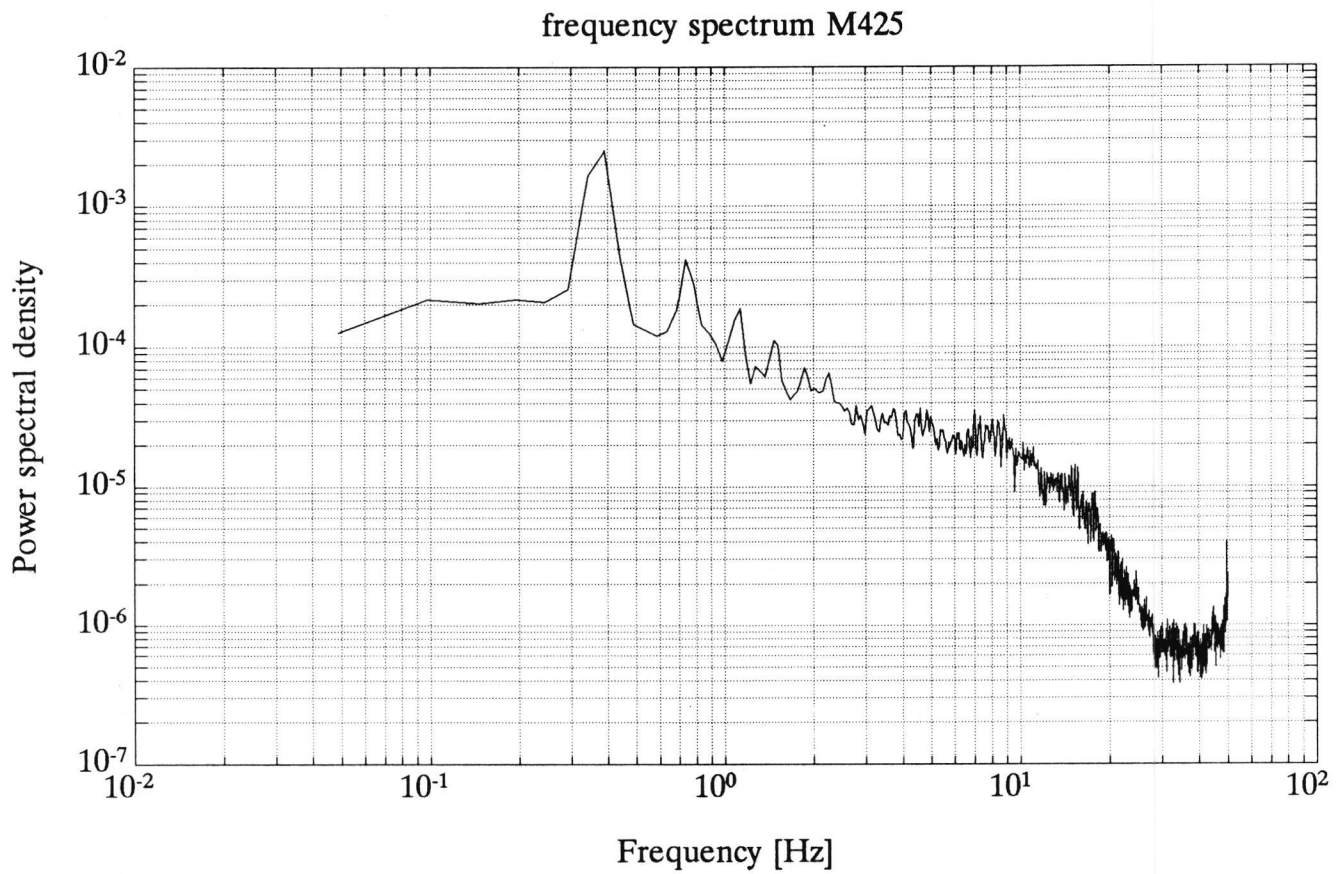


Figure 5.6: Power spectral density of microwave backscatter for measurement no. 425. The measurement conditions were: HH polarization, upwind,  $45^\circ$  incidence,  $u_* = .33$  m/s, monochromatic wave of  $\lambda = 11.05$  m., height .6 m.

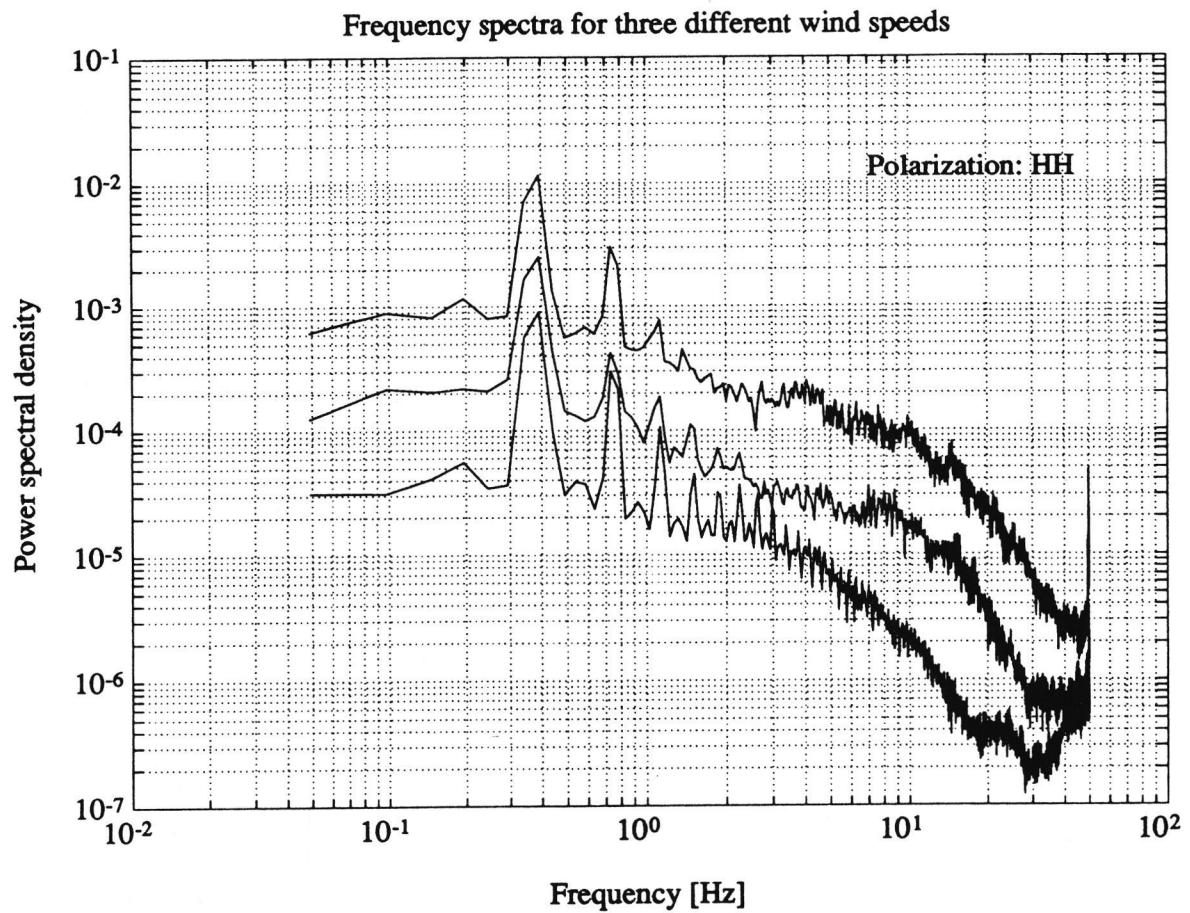


Figure 5.7: Power spectral density for three different friction velocities. Upper curve:  $u_* = .41$  m/s, middle:  $u_* = .33$  m/s, lower:  $u_* = .155$  m/s. HH polarization, upwind,  $45^\circ$  incidence angle, wave: monochromatic,  $f = .375$  Hz, height = .6 m.

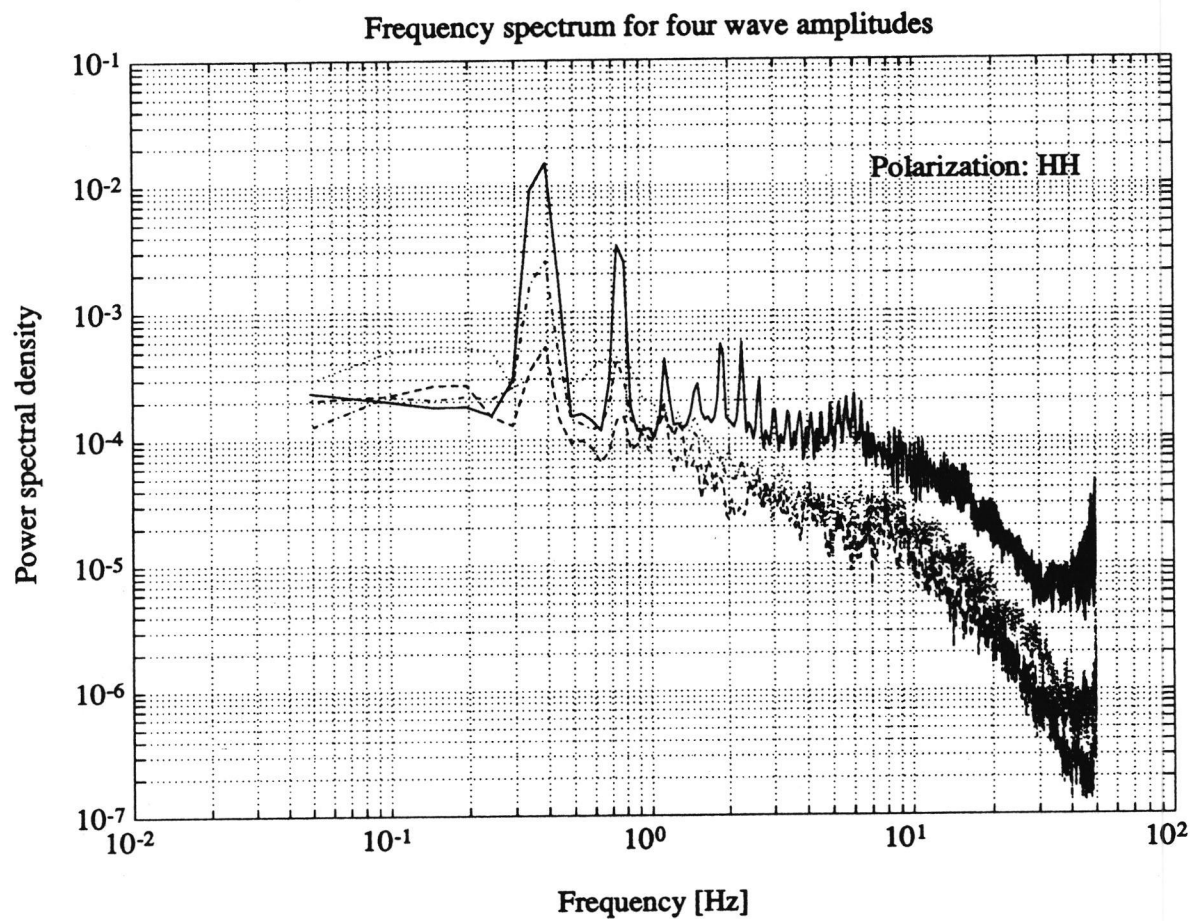


Figure 5.8: Power spectral density for four different wave heights. Drawn line: 1.0 m, dash-dot line: .60 m, dashed line: .30 m, dotted line: 0. m. HH polarization, upwind,  $45^\circ$  incidence angle,  $u_* = .30 \dots .33$  m/s

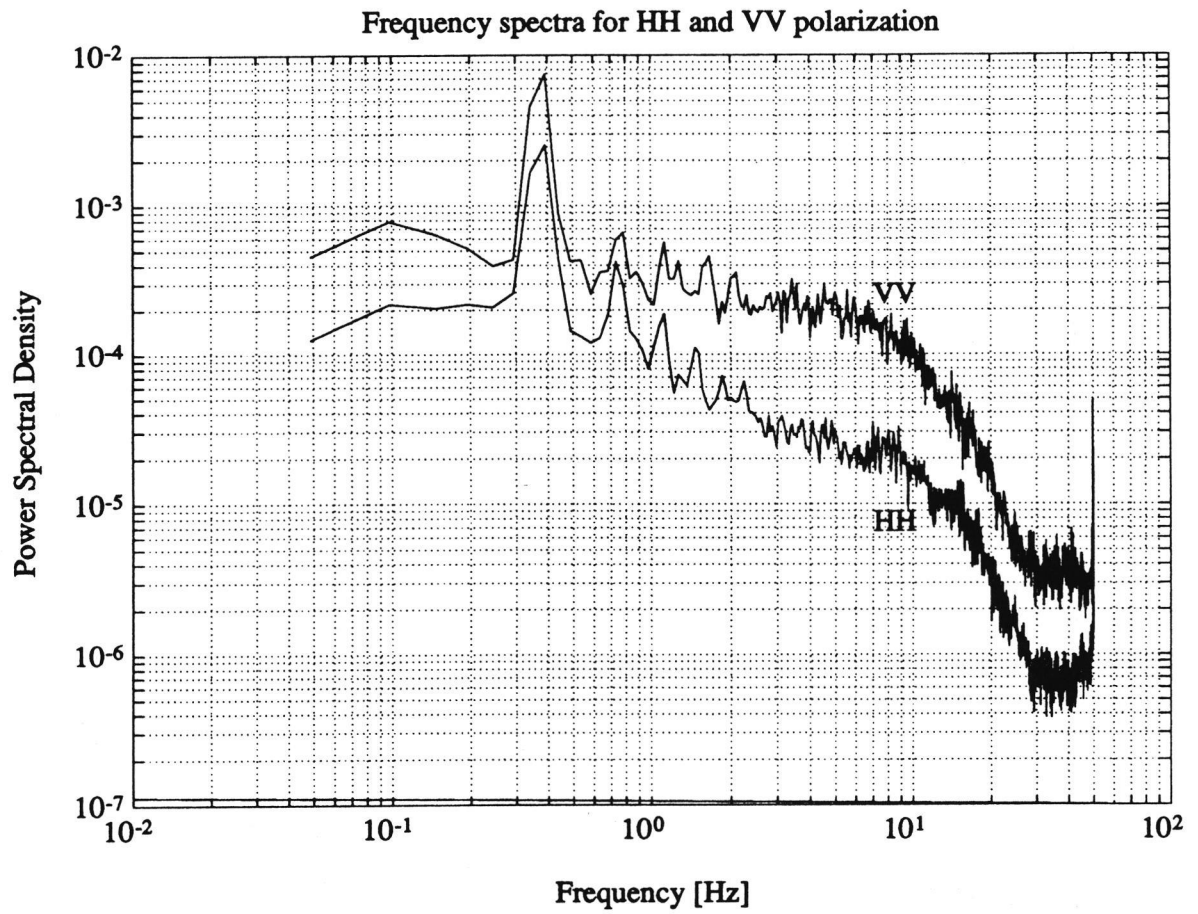


Figure 5.9: Power spectral density for HH and VV polarization,  $45^\circ$  incidence, upwind,  $u_* = .33$  m/s, wave: monochromatic,  $f = .375$  Hz, height .6 m.

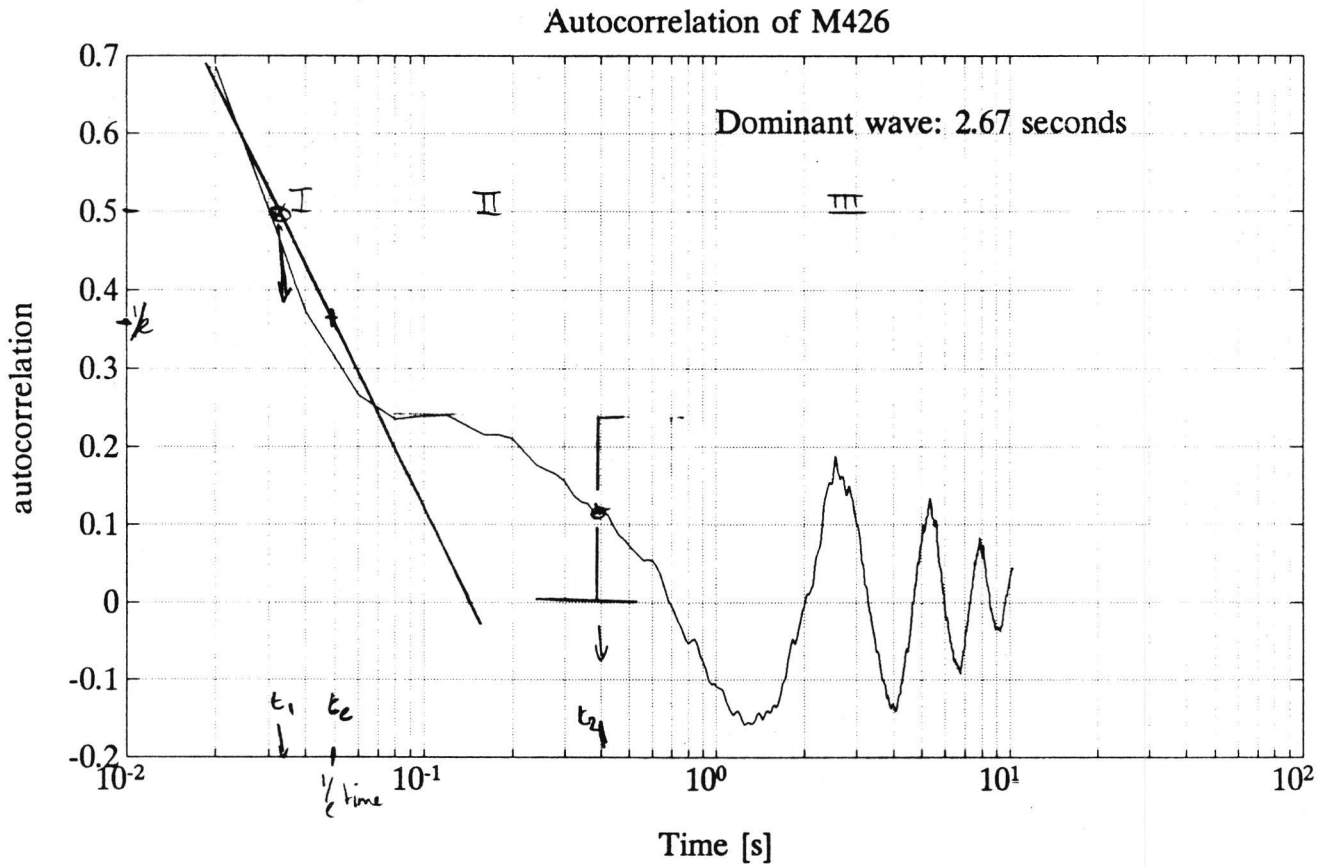
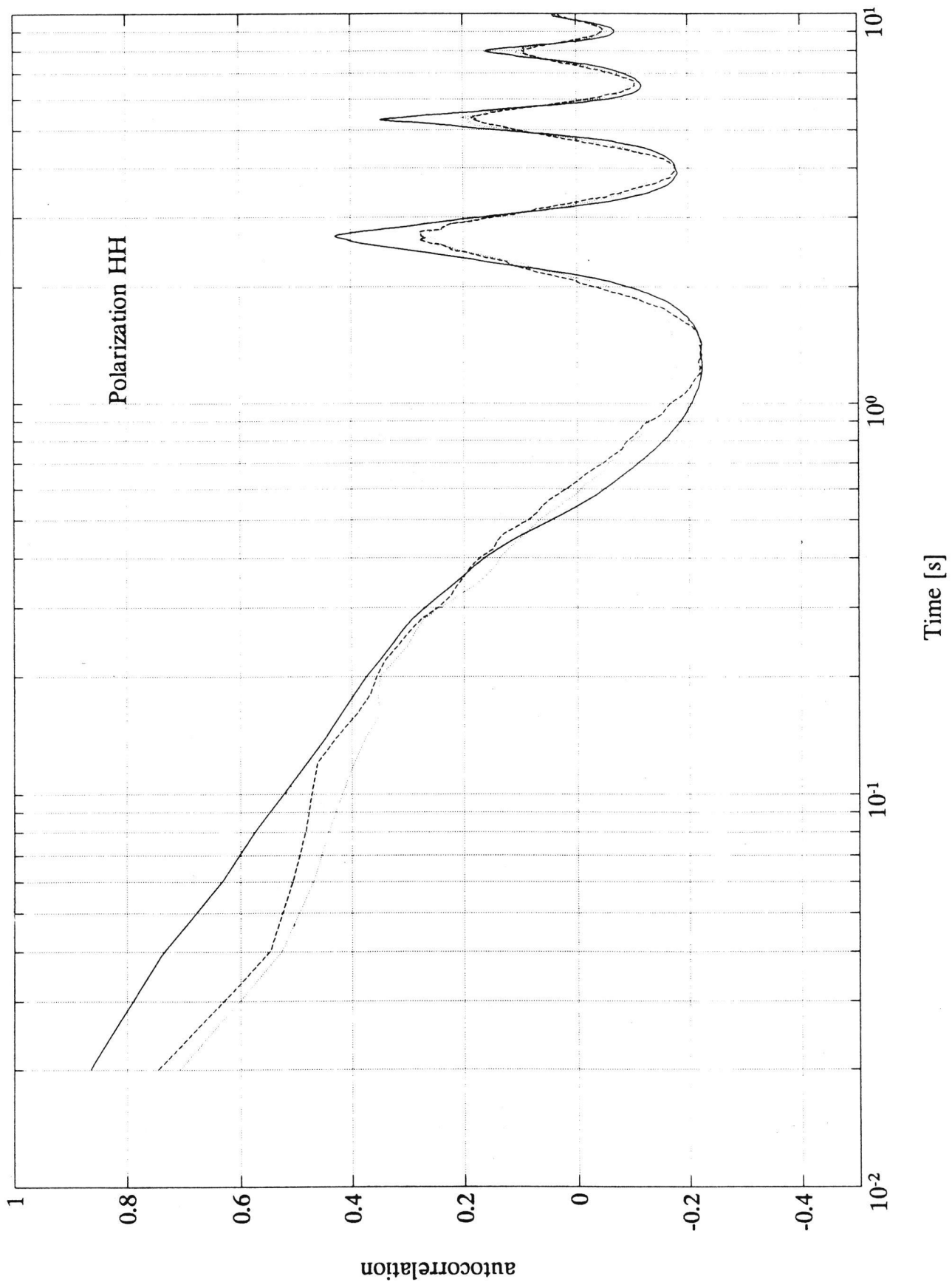


Figure 5.10: Autocorrelation function of the VV polarized signal

5.1.11 Autocorrelation for low, medium and high wind speed



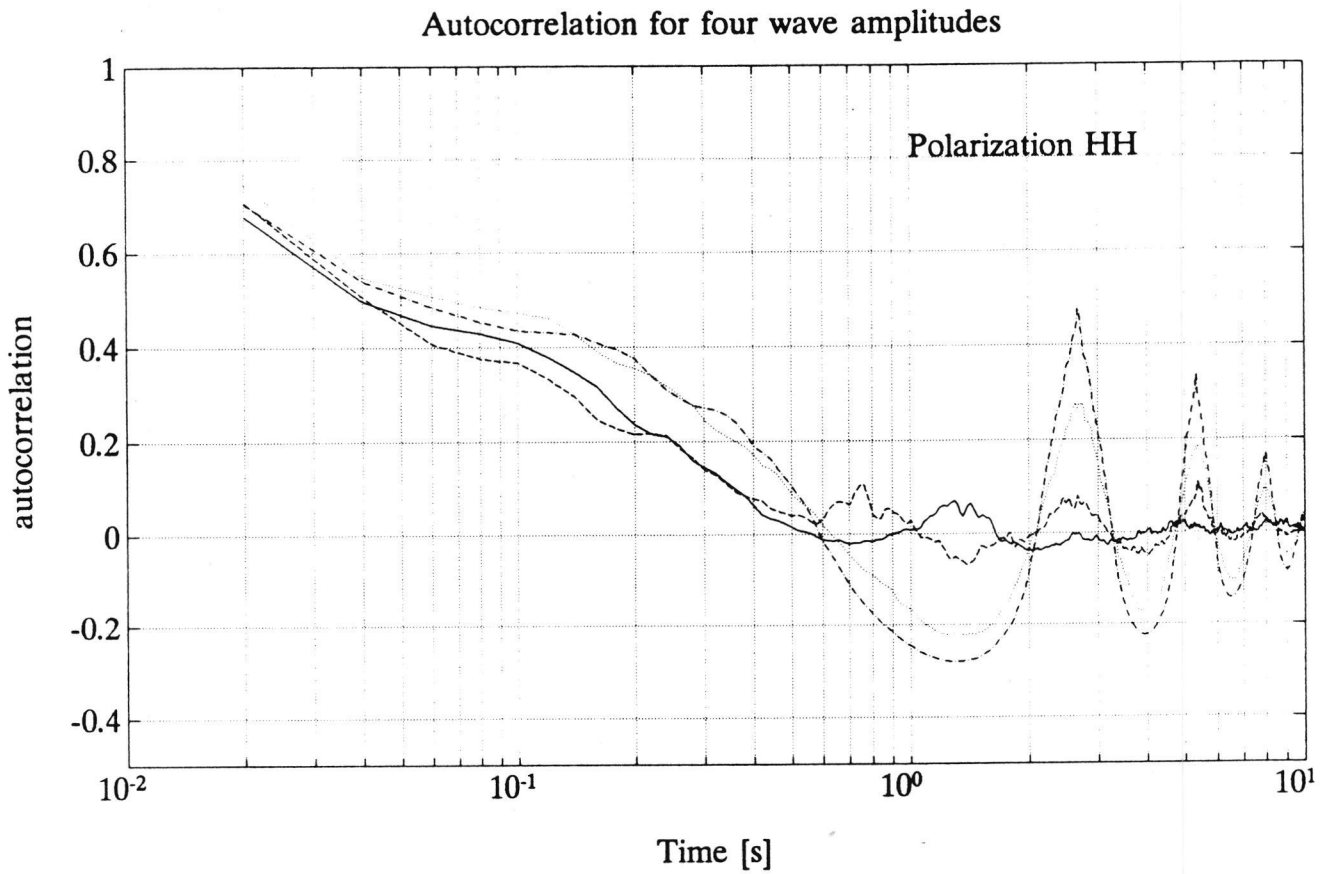
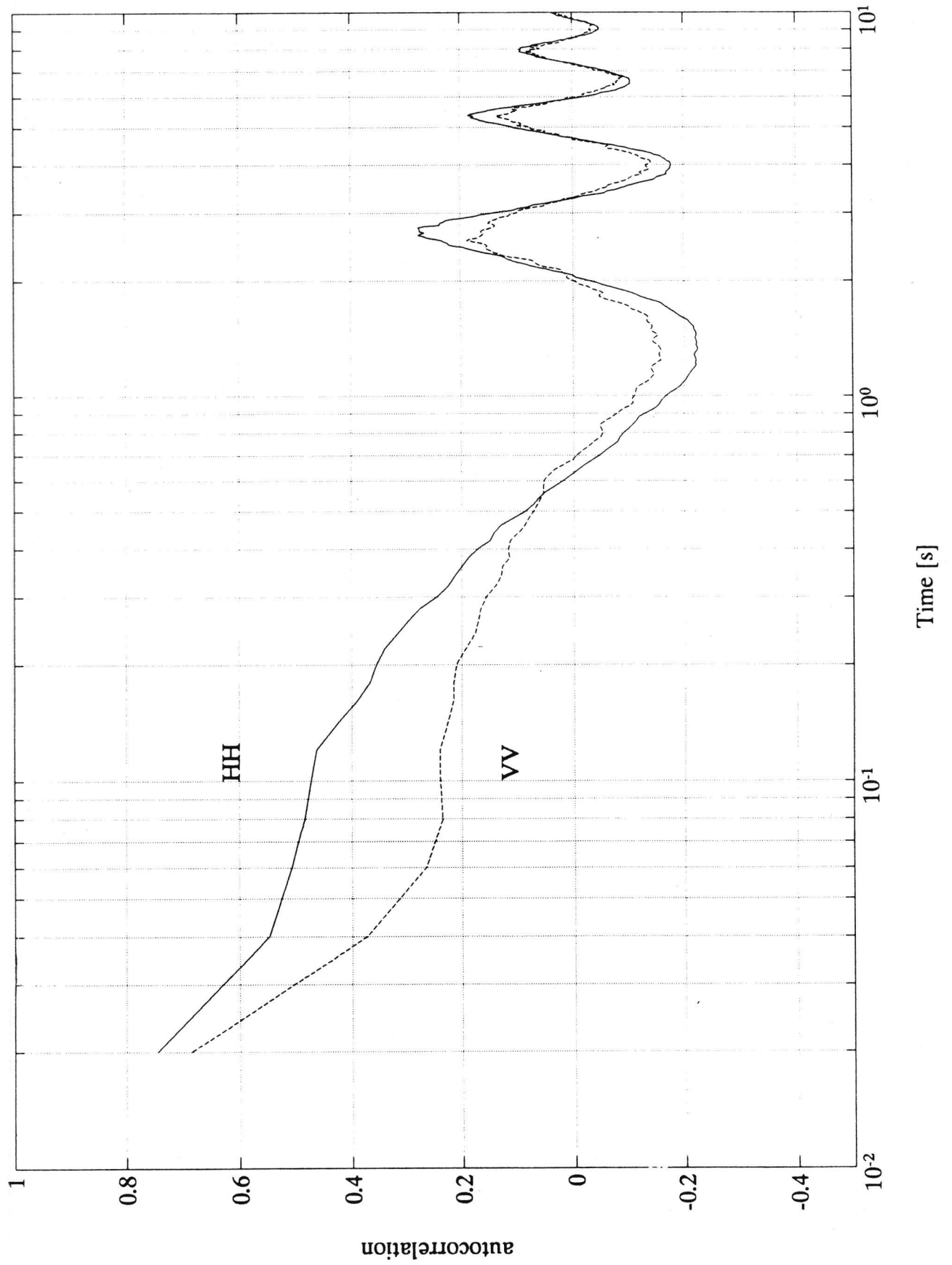


Figure 5.12: Autocorrelation of the microwave backscatter for different (monochromatic,  $f = .375$  Hz) wave heights, drawn line: only wind waves, dashed line: .30 m, dotted line: .60 m, dash-dotted line: 1.0 m; HH polarized, upwind,  $45^\circ$  incidence angle,  $u_* \approx .33$  m/s

5.13 Autocorrelation for HH and VV polarization



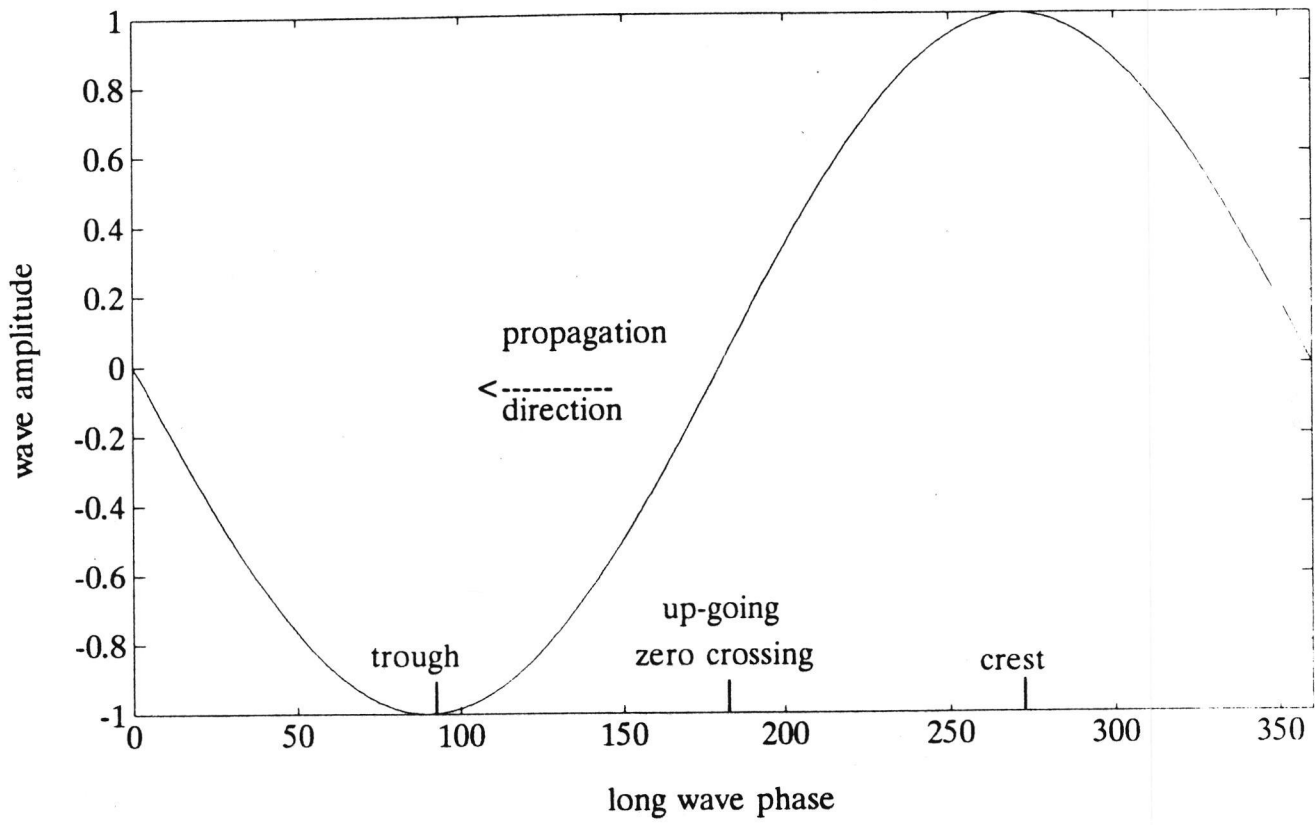


Figure 5.14: Definition of phase angle of the long wave

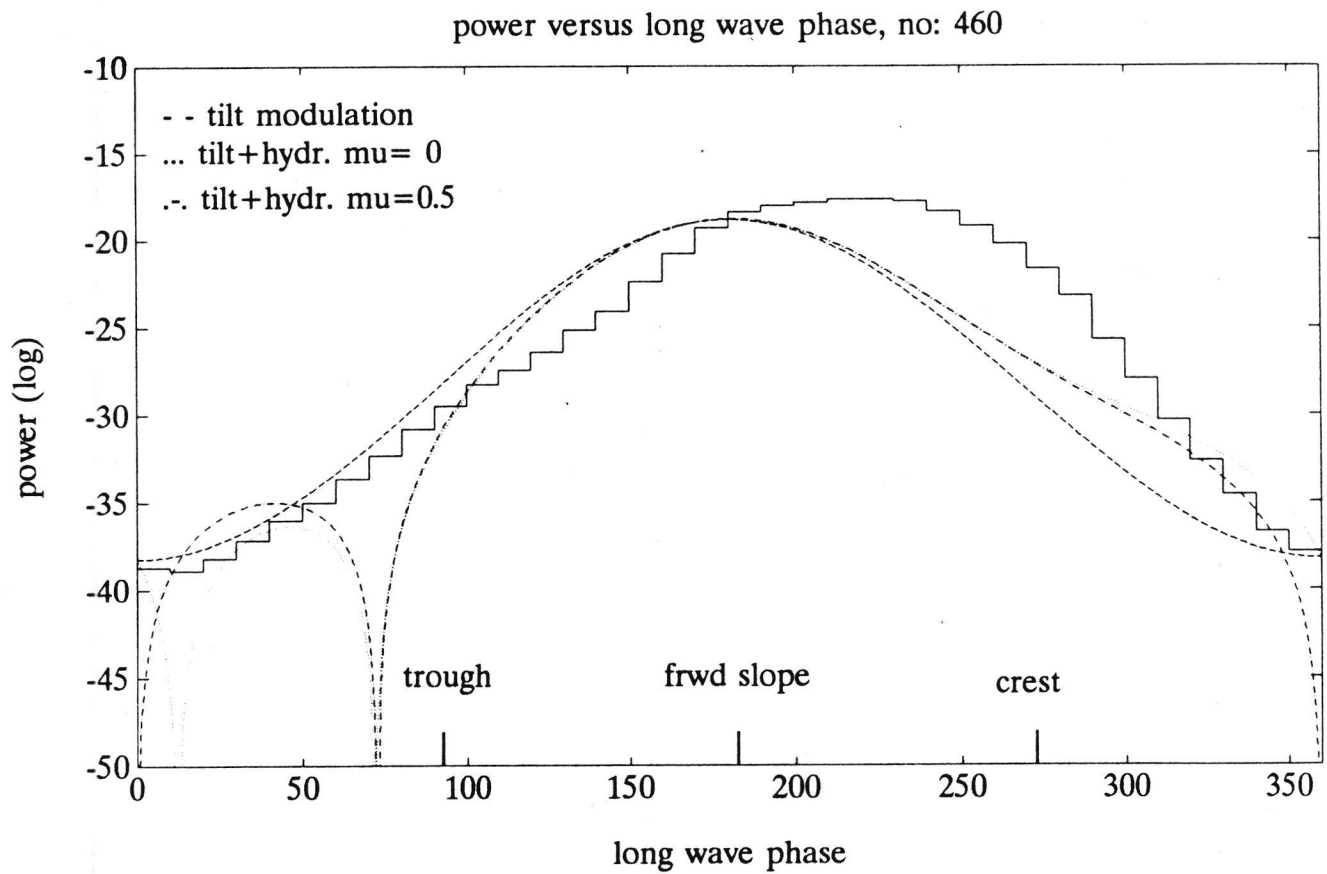


Figure 5.15: Microwave backscatter as a function of the long wave phase. Conditions: HH polarization,  $45^\circ$  incidence angle, upwind looking,  $u_* = .355$  m/s, mechanical wave:  $\lambda = 11.08$  m, height = 1.0 m

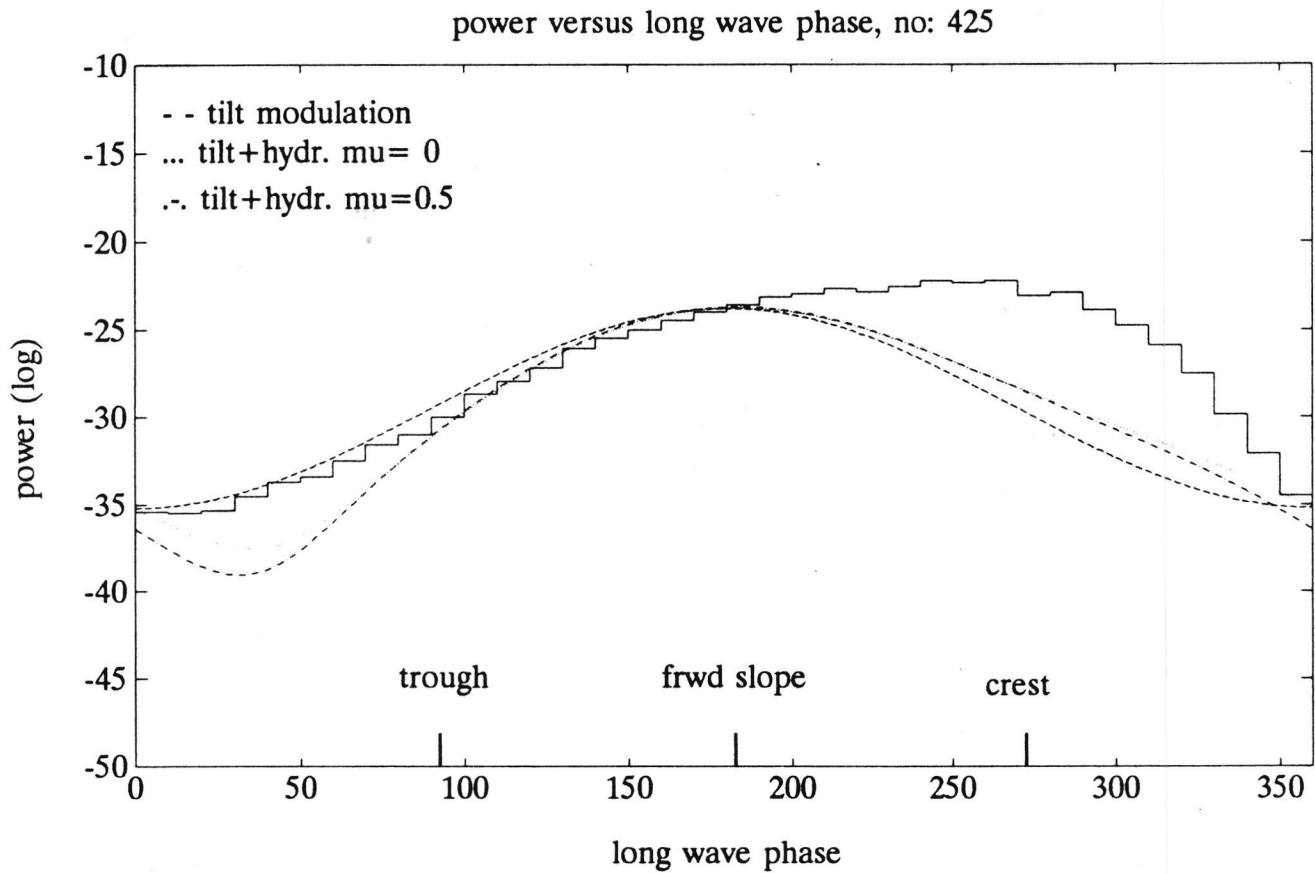


Figure 5.16: Microwave backscatter as a function of the long wave phase. Conditions: HH polarization,  $45^\circ$  incidence angle, upwind looking,  $u_* = .32$  m/s, mechanical wave:  $\lambda = 11.08$  m, height = .6 m

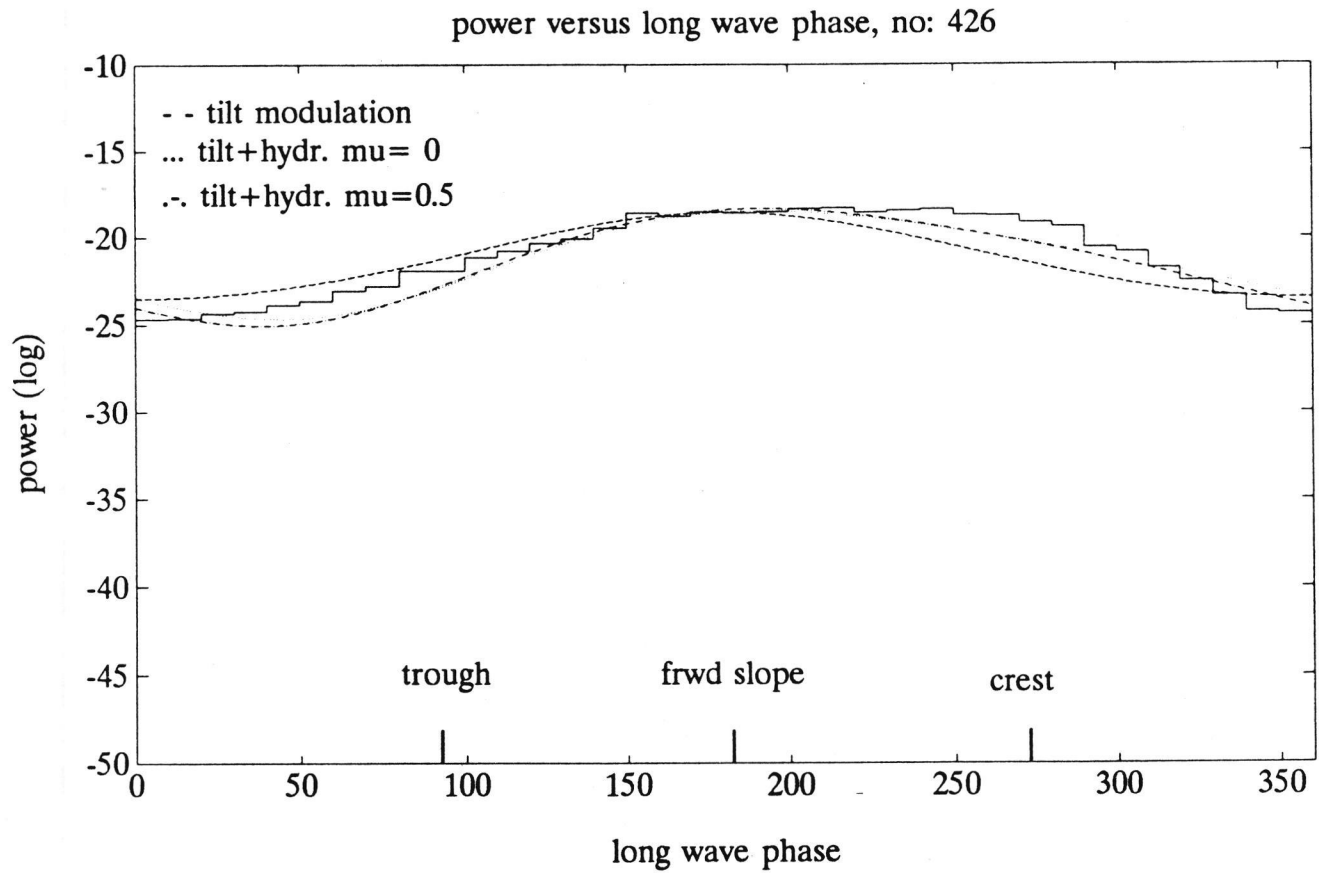


Figure 5.17: Microwave backscatter as a function of the long wave phase. Conditions: VV polarization,  $45^\circ$  incidence angle, upwind looking,  $u_* = .34$  m/s, mechanical wave:  $\lambda = 11.08$  m, height = .3 m

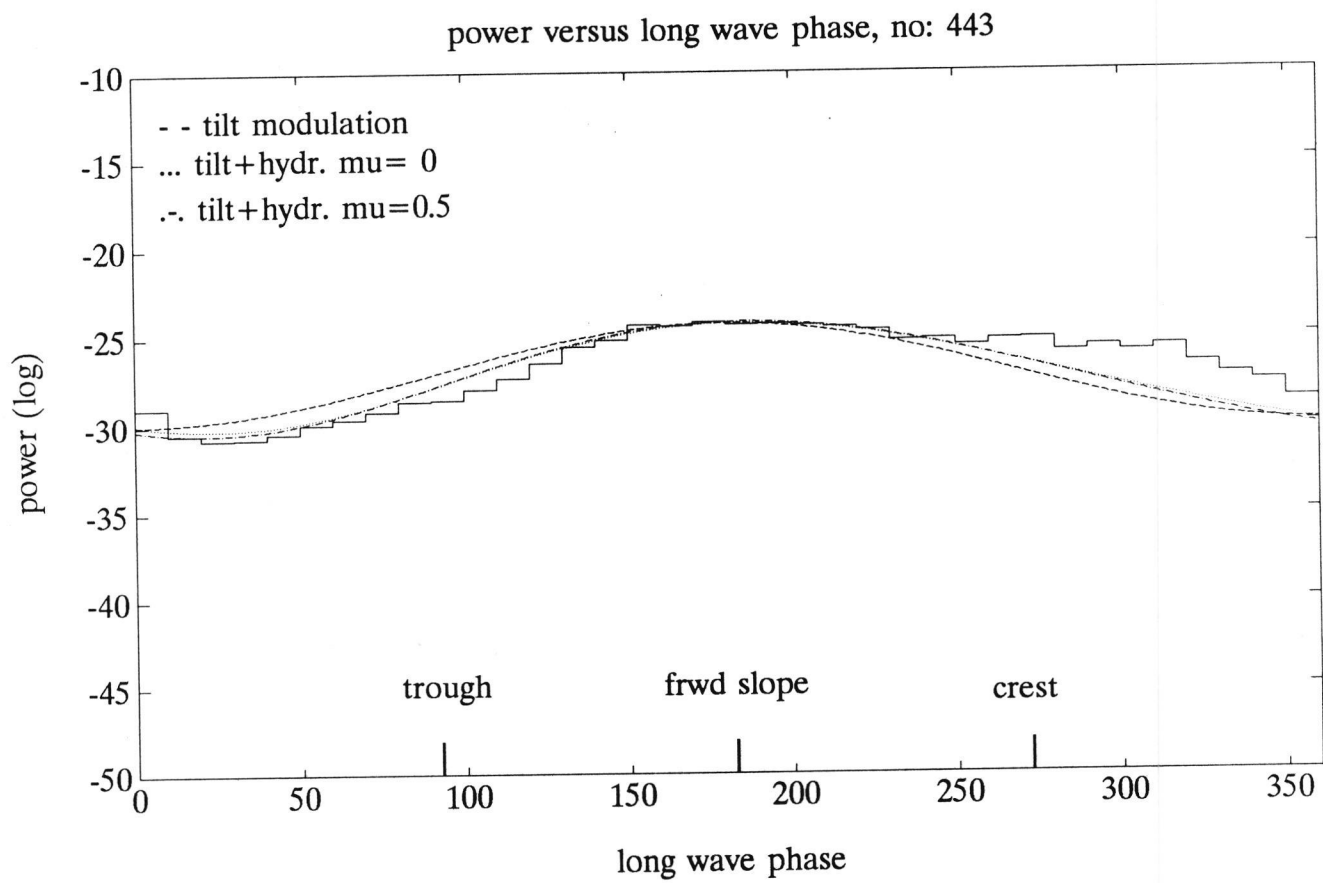


Figure 5.18: Microwave backscatter as a function of the long wave phase. Conditions: HH polarization,  $45^\circ$  incidence angle, upwind looking,  $u_* = .30$  m/s, mechanical wave:  $\lambda = 11.08$  m, height = .30 m

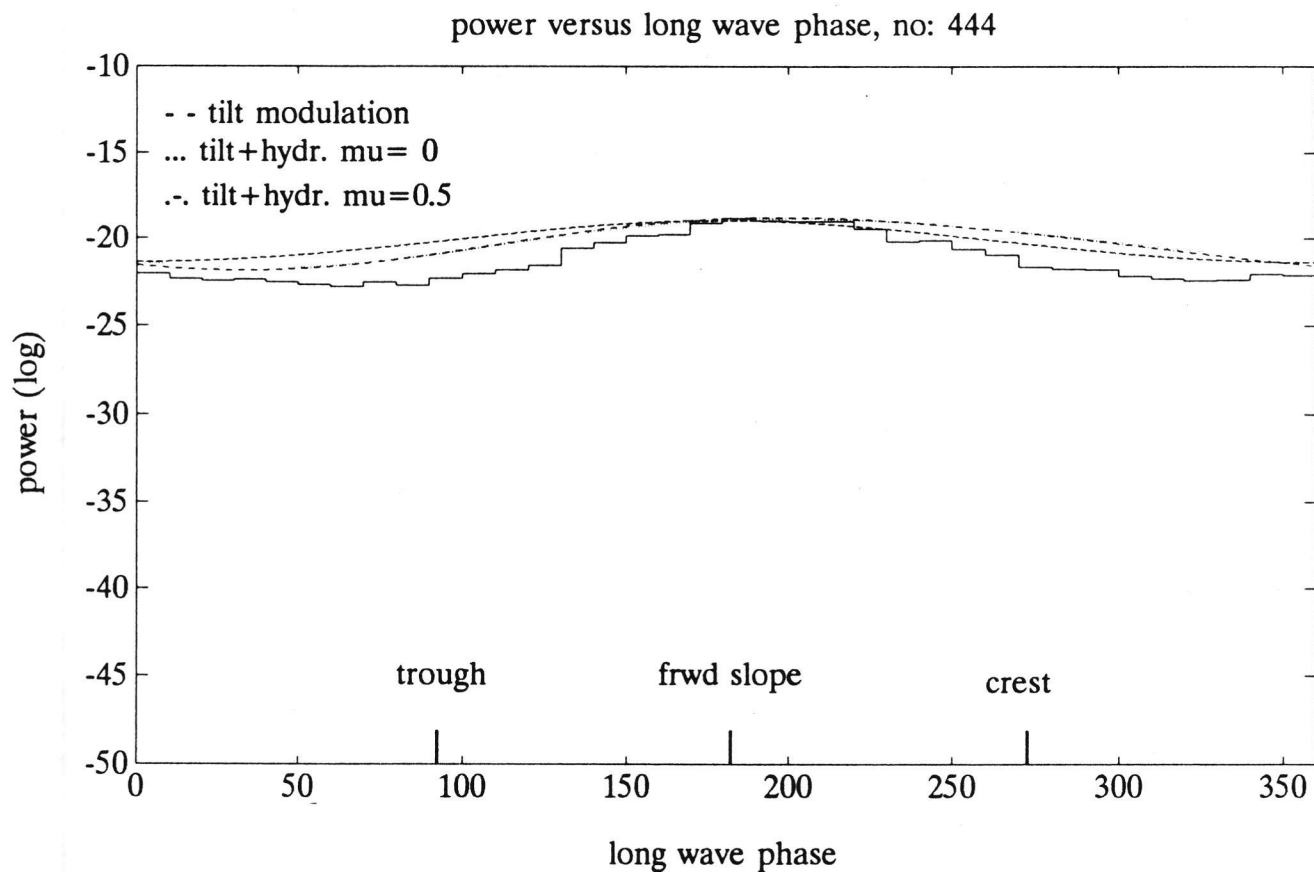


Figure 5.19: Microwave backscatter as a function of the long wave phase. Conditions: VV polarization,  $45^\circ$  incidence angle, upwind looking,  $u_* = .30$  m/s, mechanical wave:  $\lambda = 11.08$  m, height = .30 m

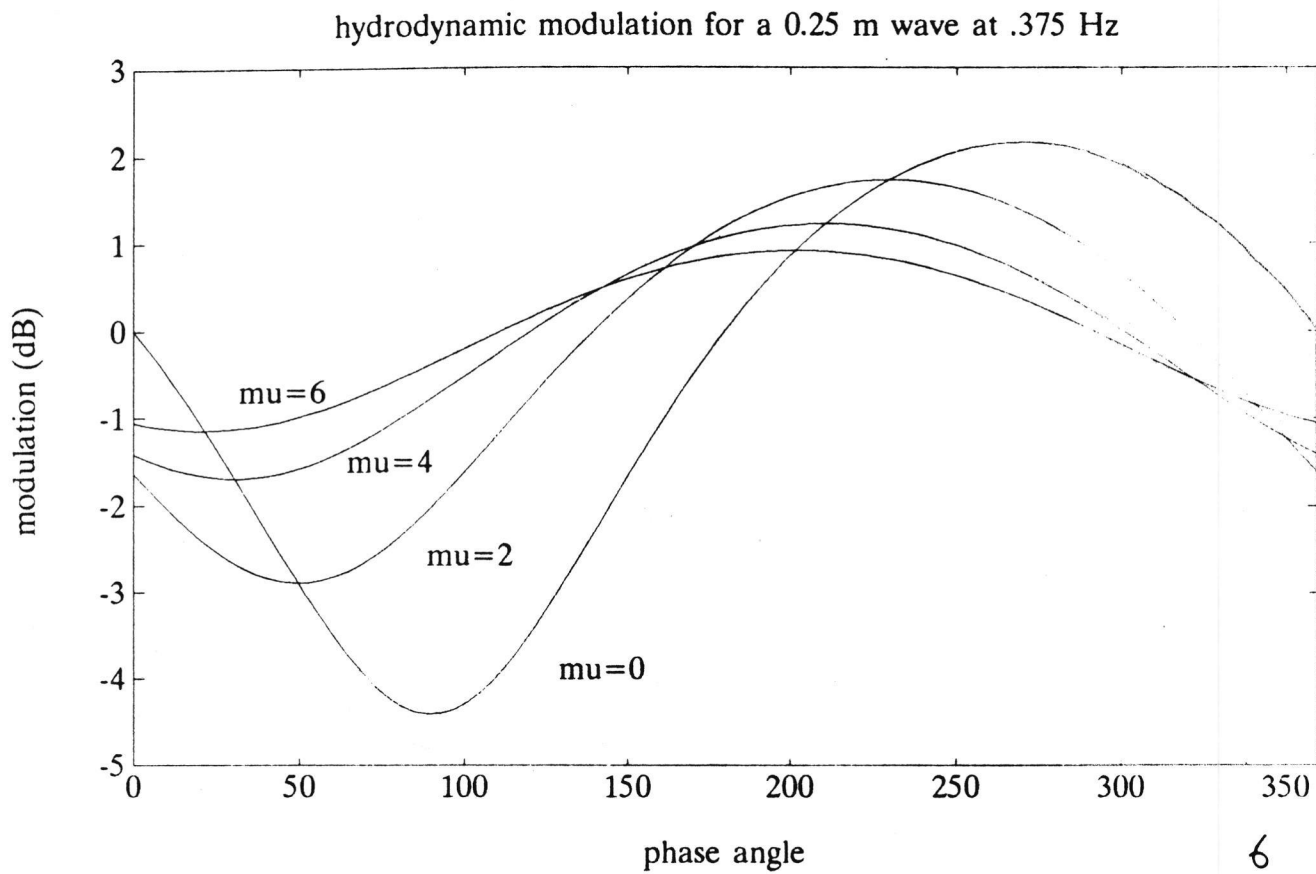


Figure 5.20: Total modulation of the radar cross section for 4 different values of the parameter  $\mu$